Optical and magneto-optical properties of purely two-dimensional electronic systems-graphene

Przemyslaw Leszczynski

To cite this version:

Przemyslaw Leszczynski. Optical and magneto-optical properties of purely two-dimensional electronic systems-graphene. Condensed Matter [cond-mat]. Université de Grenoble, 2014. English. NNT : 2014GRENY002 . tel-01558224

HAL Id: tel-01558224
https://tel.archives-ouvertes.fr/tel-01558224

Submitted on 7 Jul 2017

UNIVERSITÉ DE GRENOBLE

THÈSE

Pour obtenir le grade de

DOCTEUR DE L'UNIVERSITÉ DE GRENOBLE

Spécialité : **Physique de la Matière Condensée et du Rayonnement**

Arrêté ministériel : 7 août 2006

Présentée par

Przemysław Leszczyński

Thèse dirigée par **Marek Potemski**
et codirigée par **Clément Faugeras**

préparée au sein **Laboratoire National des Champs Magnétiques Intenses, CNRS, Grenoble, France**
et de **l'École Doctorale de Physique de Grenoble**

Propriétés optiques et magnéto-optiques de systèmes électroniques purement bidimensionnels – graphène

Thèse soutenue publiquement le **21 Février 2014**,
devant le jury composé de :

Dr. Jean-Yves Veuillen, docteur habilité
Directeur de recherche, Institut Néel-CNRS, Grenoble, France, Président

Dr. Stéphane Berciaud, docteur habilité
Maître de conferences, IPCMS - Département Magnétisme des Objets NanoStructurés (DMONS), Strasbourg, France, Rapporteur

dr hab. Andrzej Wysmołek, docteur habilité
Professeur, Faculty of Physics, University of Warsaw, Rapporteur

Prof. Luis Viña
Proffeseur, Departamento de Física de Materiales, Universidad Autónoma de Madrid Campus de Cantoblanco, Examinateur

Dr. Marek POTEMSKI, docteur habilité
Directeur de recherche, LNCMI-CNRS, Grenoble, France, Directeur de thèse

Dr. Clément Faugeras, docteur habilité
Chargé de recherche, LNCMI-CNRS, Grenoble, France, Co-Directeur de thèse

Acknowledgements

When I started my PhD project, in the Laboratoire des Champs Magnétiques Intenses in Grenoble, in the autumn 2010, I didn't yet realize how much it will change my life. Not only did it allow me to discover the fascinating world of the two dimensional crystals, and acquire the technical skills necessary to investigate them, but also it made me to grow and develop on the personal basis. The people I met in the laboratory during the last three years have left a permanent mark on my life, through their encouraging words, wise counsel and personal example. Without them, this work would not exist in its current form, therefore I would like to express my deepest gratitude to the following persons.

First of all I would like to thank my directeur de thése, Marek Potemski, for accepting me for the PhD studies. Thank you for all the help you showed me during my stay in France, especially in the beginning, when everything was new and strange for me. Thank you for encouraging me to learn French, which made my life here considerably easer. But most of all, thank you for all the scientific counsel you gave me during these years. Your experience and physical intuition never ceased to surprise me, and your ability to explain in a few simple words the complex physical phenomena helped me, many times, to progress in my work. Finally, thank you for proofreading this manuscript and the inexhaustible amounts of patience you had for me during the time I was writing it.

I would also like to thank my co-directeur de thése, Clément Faugeras, for the help shown me during the planing and execution of the experiments and for the readiness to explain me the details of the magneto-optical properties of graphene, sometimes over and over again. I thank you also for the time you spend on correcting this manuscript.

I owe much to Piotr Kossacki, who willingly spent a lot of time to explain me the theoretical models of the magneto-phonon resonance, greatly helped in developing the source code for modelling it, and always showed a great interest and support to my work. I greatly appreciate the help offered me by Paulina Płochocka, by introducing me to the subject of carbon based systems, teaching me in the laboratory, and showing me a great moral support during moments of doubt.

I have also profited a lot from the laboratory experience of Aurélien Nicolet and from theoretical knowledge of Gérard Martinez. None of my experiments would be possible without the technical skills and everyday enthusiasm of Ivan Breslavetz. Thank you for teaching me the techniques and instrumentation specific for the optical laboratory.

It is my pleasure to thank dr hab. Andrzej Wysmłek and Dr. Stéphane Berciaud for agreeing to be the referees of this manuscript, and to Prof. Luis Viña and Dr. Jean-Yves Veuillen for reading this manuscript and accepting to be members of the jury.

I strongly appreciate the cooperation with Vincent Bouchiat and Zheng (Vitto) Han from Intitut Néel, who provided us with the CVD grown graphene samples, and with Rashid Jalil from the University of Manchester, who made for us the graphene sample encapsulated between two boron nitride flakes. Many theoretical problems and dilemmas have been solved thanks to the fruitful discussions with Denis Basko.

The adaptation to the life in France, has been made considerably easier for me thanks to the helpfulness and kindness of all the administrative, IT, and technical staff of the laboratory. Whenever I needed some help, there were always people willing to assist me. Here, I would like especially firmly express my gratitude to Elisabeth Rochat, who often helped me to go through all the administrative paperwork, pushed me to uncover my hidden talents in speaking French, and who always created a kind and warm atmosphere in the laboratory.

During the time I spent in LNCMI, I had a pleasure to meet many other PhD students and post-doctoral fellows from CNRS laboratories, who added an important social aspect to my life. It is not possible to name them all, but I would like to thank in particular: Johannes Binder, Mateusz Goryca, Zheng (Vito) Han, Younnes Heni, Aleš Hrabec, Jan Kunc, Maciej Koperski, Petr Neugebauer, Karol Nogajewski, Michal Páleníček, Johannes Schneider and Petr Stepanov. I would also like to express my special gratitude to: Milan Orlita for the always stimulating discussions during the lunch time; Maciej Molas for teaching me a lot about physics and life; Matthias Kühne for encouraging me to learn ski, and always interesting discussions.

I am also very grateful to my friends in Poland: Artur Henrykowski, Bartek and Agnieszka Doleccy, and Kasia Woźniak, who constantly supported me, by keeping in touch, writing e-mails, calling, and always having time to meet whenever I was back in Poland.

Finally, I would like to thank my loving family: my parents and my brother, who were always supporting and motivating me. This work would not be possible without their unyielding belief in me.

Table of Contents

Résumé

Introduction (English)

Carbon is one of the most important elements on Earth, even the very existence of life depends on it. The importance of carbon stems from its ability to form uncountable number of various chemical compounds and in its pure form, to exist in many different allotropic forms. Amorphous carbon, graphite, diamond, carbon nanotubes and fullerenes exhibit largely different mechanical, electrical and optical properties. They represent objects that have three dimensional structure (graphite), quasi-one dimensional (nanotubes) and quasi-zero dimensional (fullerens). The allotropes that have the same dimensionality, can still differ due to different crystallographic arrangement of the atoms, like e.g. graphite, diamond and amorphous carbon. This cornucopia of carbon allotropes was recently enriched by discovering yet another form of carbon, a free standing, single plane of atoms arranged in a hexagonal lattice structure – the graphene.

Although graphene has been theoretically known for more than 60 years [1], and was widely used for describing properties of various carbon-based materials [2, 3, 4], its first isolation [5] came as a great surprise, since 2D crystals were considered to be thermodynamically unstable. The theory developed by *Landau* [6] and *Peierls* [7] predicted a divergent contribution of thermal fluctuations in low-dimensional crystal lattices, that would cause displacements of atoms on the scale comparable to interatomic distances at any finite temperature. These theoretical predictions were also supported by many experimental observations, such as: folding of the thin films with decreasing thickness, or segregation of atoms into islands at thicknesses of typically, dozens of atomic layers [8, 9]. However, a successful isolation of a single layer of graphene, but also MoS_2, $NiSe_2$ and $Bi_2Sr_2CaCu_2O$ [5, 10], proved that a whole new class of 2D materials was just waiting to be discovered.

Graphene is an outstanding material due to its unusual mixture of mechanical, electronic and optical properties. It is very strong, covalent sp^2 bonds are responsible for its excellent mechanical properties: the record high breaking strength (42 Nm^{-1}) and large Young modulus ($E = 1.0$ TPa) [11]. Because of that, graphene can be stretched elastically even up to 20%, this is more than any other crystal. In fact, the first commercially available applications of graphene are most likely to rely on its mechanical properties.

Nevertheless, up to now, the most explored aspect of graphene physics remains a study of its electronic properties. Graphene can be considered as a zero bandgap semiconductor

or a zero overlap semimetal, but many aspects of its electronic properties are unique and different from that of the other known solid state systems. There are several reasons for that. The first one, is the unusual linear electron dispersion close to the Fermi energy. Carriers exhibiting such dispersion cannot be described by the ordinarily used effective mass approximation and the standard Schrödinger equation. Instead they behave like a massless Dirac particles and their motion is ruled by a relativistic Dirac-like equation with an effective speed of light (called Fermi velocity) $v_F \approx c/300$.
The second reason for the graphene unusual electronic properties is that electrons in graphene propagate within a layer that is only one atom thick. This makes them susceptible to the proximity of other materials such as high-k dielectrics, superconductors, ferromagnetics, etc. This feature offers a possibility to tune the properties of graphene by a careful engineering its environment.
Thirdly, electronic states in graphene exhibit an astonishing robustness and quality. Its electrons can cover sub-micrometer distances without scattering, even in samples placed on an atomically rough substrate. The electron mobility can be as high as 2.5×10^5 cm^{2}V^{-1}s^{-1} at room temperature in exfoliated graphene encapsulated between two layers of BN [12], and it can reach even 10^7 cm^{2}V^{-1}s^{-1} in graphene flakes on the surface of graphite [13]. Thus, a ballistic transport, even at room temperatures, can be realized in this material and this high mobility of carriers make graphene an interesting candidate for replacing silicon in the high-performance integrated logic circuits.
Fourthly, as a result of the massless carriers and little scattering, the quantum effects in graphene are robust and can survive even at room temperature. Finally, the formal resemblance of quantum states of the quasi-particles in graphene to the relativistic particles described by a quantum electrodynamics (QED) offers a possibility to test some QED predictions in a workbench experiments. In the same time, the ~ 300 times lower value of the Fermi velocity, than that of the speed of light, the relativistic effects are expected to be ~ 300 times enhanced.
The optical properties of graphene are equally interesting as the electronic ones. The most distinctive feature is the universal optical absorption of light, which is frequency independent, given by just the fine structure constant α and equal to $\pi\alpha \approx 2.3\%$. Together with the good electrical conductivity and mechanical flexibility, this may predestine graphene to the use as a transparent, conductive electrode in the flexible light emitting devices.

Despite the massive attention that graphene has attracted in recent years, there are still many unanswered questions about its fundamental properties. In this work we present the results of a series of magneto-optical experiments performed on different graphene systems. The micro-Raman scattering spectroscopy was used as our method of choice, due to its non-invasive character, powerful characterization possibilities and high spatial resolution. The high magnetic fields were used to continuously tune the energy of inter-Landau level electronic excitations into a resonance with other excitations existing in the system. The magnetic field evolution of Raman active inter-Landau level excitations, and the details of the magneto-phonon resonance, gave us important information about the details of the electron-phonon interaction in graphene.
Three different types of graphene are studied in this work. The first one consists of graphene flakes that can be found on the surface of graphite. It is possibly the least

investigated graphene system, yet the one that shows the highest electronic quality. It offers a unique possibility to study the interband inter-Landau level electronic excitations in graphene, and to observe the fine effects of the electron-phonon interaction. The second studied system consists of a graphene flake encapsulated between two layers of atomically flat hexagonal boron nitride (hBN). It is a representative of a novel class of materials, where different 2D crystals, are stacked on top of each other in a predefined order, to modify some properties of its constituents. Depositing graphene on a thin layer of hBN is expected to largely improve its electronic properties, as compared to graphene deposited on Si/SiO$_2$. The last studied system is the CVD grown graphene flake with electrical contacts, which allowed us to tune the Fermi energy across different Landau levels, and to observe how switching off subsequent inter-LL electronic excitations influences the electron-phonon coupling.
This work is organized as follows:

- In **Chapter 1** the fundamental properties of graphene based materials are introduced. The electronic band structure of graphene is presented and the different approximations used in its derivation are shortly discussed. The effect of electron energy quantization due to external magnetic field is discussed in graphene, multilayer graphene and graphite.

- In **Chapter 2** the principles of Raman scattering spectroscopy are introduced. The main Raman scattering features in graphene are presented and the application of this experimental method for the characterization of graphene structure, strain and doping is shown.

- In **Chapter 3** the phonon dispersion in graphene is discussed, especially in relation to the Kohn anomalies and the effect of electron-phonon interaction on the Γ-point and K-point phonons. An existing model of a magneto-phonon resonance in graphene is briefly explained. The possibility to tune the effective strength of the electron-phonon interaction with Γ-point phonons is presented.

- In **Chapter 4** the theory of electronic excitations in graphene and bulk graphite is discussed. The selection rules in Raman scattering experiment are presented, for different interband inter-Landau level excitations.

- In **Chapter 5** we briefly describe each of the three different graphene systems that were studied in this work: graphene flakes on the surface of graphite, an exfoliated graphene flake, encapsulated between two layers of hBN and a gated, CVD grown graphene. Their main characteristics and production methods are discussed.

- In **Chapter 6** the details of our micro-magneto-Raman setup are presented

- In **Chapter 7** we present results of our magneto-Raman scattering experiments on the graphene flakes that can be found on the surface of graphite. Our method for locating these flakes with the use of magnetic field and without it is presented. The evolution of electronic excitations in magnetic fields is discussed. The effects of temperature, excitation wavelength and different coupling to the substrate are shown. We demonstrate that at high magnetic fields a fine-structure of the principal interband electronic excitation develops and discuss it in terms of doping and electron-hole asymmetry. A new type of a resonant electron-phonon interaction is observed, which involve an inter-valley carrier scattering and an emission of a K-point phonon. An analogous process for the phonons from the vicinity of the Γ point is observed.

- In **Chapter 8** the exfoliated graphene sample encapsulated between two layers of hBN is studied. We show how spatial mapping with Raman scattering technique can be used for characterization and selective visualization of each constituent of the complex, stacked structures. A first, clear observation of a magneto-phonon resonance and $L_{-1,1}$ electronic excitation in an intrinsic, exfoliated graphene is shown. The Fermi velocity dependence on the magnetic field is demonstrated. Also, the Fermi velocity and 2D band energy dependence on the substrate is observed and discussed in terms of dielectric screening of the electron-electron interaction.
- In **Chapter 9** we show the results of an experiment, where strength of the electron-phonon interaction in a gated, CVD grown, graphene was successfully tuned by the applied gate voltage. We compare these results with the theoretical calculations and show that the intra-band electronic excitations play an important role in the renormalization of the Γ phonon energy.

Introduction (français)

Le carbone est l'un des éléments les plus importants de la planète, l'existence même de la vie en dépend. L'importance du carbone provient de sa capacité à former un nombre incalculable de composés chimiques différents et, dans sa forme pure, d'exister sous plusieurs formes allotropiques différentes. Le carbone amorphe, le graphite, le diamant, les nanotubes de carbone et les fullerènes présentent des propriétés mécaniques, électriques et optiques extrêmement différentes. Ils représentent des objets qui ont une structure 3D (graphite), quasi-1D (nanotubes) et quasi-0D (fullerènes). Les formes allotropiques de même dimensionnalité, peuvent encore varier en raison de différents arrangements cristallographique des atomes, comme par exemple le graphite, le diamant et le carbone amorphe. Cette corne d'abondance de formes allotropiques du carbone a été récemment enrichie par la découverte d'une nouvelle forme de carbone stable, un plan unique d'atomes disposés en réseau hexagonal - le graphène.

Même si le graphène est connu théoriquement depuis plus de 60 ans [1], a été largement utilisé pour décrire les propriétés de divers matériaux à base de carbone [2, 3, 4], sa premier isolation [5] a été une grande surprise, car les cristaux 2D étaient considérés comme thermodynamiquement instables. La théorie développée par Landau [6] et Peierls [7] prédit une contribution divergente des fluctuations thermiques dans les réseaux cristallins de basse dimension. Cette divergence provoquerait des déplacements atomiques comparables aux distances interatomiques elles-mêmes, et ce à n'importe quelle température finie. Ces prédictions théoriques ont été également soutenus par de nombreuses observations expérimentales, telles que le repliement de couches minces avec la diminution de leur épaisseur, ou la ségrégation d'atomes dans des îlots d'épaisseurs des quelques dizaines de couches atomiques [8, 9]. Cependant, l'isolation d'une monocouche de graphène, mais aussi de MoS_2, de $NiSe_2$ et de $Bi_2Sr_2CaCu_2O$ [5, 10], ont prouvé que toute une nouvelle classe de matériaux 2D attendait juste d'être découverte.

Le graphène est un matériau remarquable en raison de son mélange inhabituel de propriétés mécaniques, électroniques et optiques. Il est très fort, les liaisons atomiques covalentes sp^2 sont responsables de ses excellentes propriétés mécaniques: résistance à la rupture record (42 Nm^{-1}) et un module d'Young très élevé ($E = 1.0$ TPa) [11]. A cause de cela, le graphène peut être étiré élastiquement jusqu'à 20%, ce qui est plus que tout autre cristal. De fait, les premières applications commerciales disponibles à base de graphène sont les plus susceptibles d'utiliser ses propriétés mécaniques.

Néanmoins, jusqu'à présent, l'aspect le plus exploré de la physique de graphène reste l'étude de ses propriétés électroniques. Le graphène peut être considéré comme un semiconducteur de bande interdite nulle ou un semi-métal avec un recouvrement nul, mais de nombreux aspects de ses propriétés électroniques sont uniques et différentes de celles des autres systèmes connus à l'état solide. Il y a plusieurs raisons à cela. La première, est la dispersion inhabituelle, linéaire des bandes électroniques proche de l'énergie de Fermi. Des porteurs de charge présentant une telle dispersion ne peuvent pas être décrits par l'approximation de la masse effective habituellement utilisée et par l'équation standard de

Schrödinger. Au contraire, ils se comportent comme des particules de Dirac sans masse et leur mouvement est gouverné par une équation, qui ressemble l'équation relativiste de Dirac, avec une vitesse effective de la lumière (appelée vitesse de Fermi) $v_F \sim$ de $c/300$. La deuxième raison pour les propriétés électroniques exceptionnelles du graphène est que les électrons dans le graphène se propagent dans une couche qui a l'épaisseur d'un seul atome. Cela les rend extrêmement sensibles à la proximité d'autres matériaux tels que les diélectriques high-k, les supraconducteurs, ferromagnétiques, etc. Cette fonctionnalité offre la possibilité d'ajuster les propriétés du graphène par une ingénierie attentive de son environnement.

Troisièmement, les états électroniques dans le graphène sont très robustes et de qualité, en terme de mobilité, étonnante. Ses électrons peuvent couvrir des distances micrométriques sans diffusion, même dans des échantillons placés sur un substrat rugueux à l'échelle atomique. La mobilité des électrons peut être aussi élevée que 2.5×10^5 cm^2 V^{-1}s^{-1} à température ambiante dans le graphène exfolié puis encapsulé entre deux couches de BN [12], et elle peut même atteindre les 10^7 cm^{2}V^{-1}s^{-1} dans des flocons de graphène à la surface du graphite [13]. Ainsi, un transport balistique, même à température ambiante, peut être réalisé dans ce matériau et cette grande mobilité des porteurs fait du graphène un candidat intéressant pour remplacer le silicium dans les circuits logiques intégrés de haute performance.

Quatrièmement, en raison de l'absence de masse des porteurs et de leur faible diffusion, les effets quantiques dans le graphène sont robustes et peuvent survivre même à température ambiante. Enfin, la ressemblance formelle des états quantiques des quasi-particules dans le graphène aux particules relativistes décrites par l'électrodynamique quantique (QED) offre la possibilité de tester certaines prédictions QED dans des expériences de laboratoire. En même temps, à cause de la valeur $\sim$ 300 fois plus faible de la vitesse de Fermi par rapport à celle de la vitesse de la lumière, les effets relativistes sont attendus être $\sim$ 300 fois exaltés.

Les propriétés optiques du graphène sont tout aussi intéressantes que ses propriétés électroniques. Sa caractéristique la plus distinctive est l'absorption optique universelle, indépendante de la fréquence dans une large gamme d'énergie, et déterminée uniquement par la constante de structure fine α, égale à $\pi\alpha \approx\sim 2.3\%$. Son excellente conductivité électrique et sa souplesse mécanique prédestinent le graphène à une utilisation en tant qu'électrode conductrice transparente dans les dispositifs flexibles pour l'émission ou la détection de la lumière.

Malgré l'attention massive que le graphène a attiré ces dernières années, beaucoup de questions concernant ses propriétés fondamentales restent sans réponse. Dans ce travail, nous présentons les résultats d'une série d'expériences de magnéto-optique effectuées sur des systèmes de type graphène différents. La spectroscopie de diffusion micro-Raman a été utilisée comme une méthode de choix, en raison de son caractère non invasif, des puissantes possibilités de caractérisation qu'elle offre, et de la haute résolution spatiale. Les champs magnétiques élevés ont aussi été utilisés pour permettre d'ajuster de manière continue l'énergie des excitations électroniques inter-niveau de Landau et de les amener en résonance avec d'autres excitations existant dans le système. L'étude de l'évolution

des excitations inter-niveau de Landau sous champs magnétique et les détails de la résonance magnéto-phonon, nous ont fourni des informations importantes sur les détails de l'interaction électron-phonon dans le graphène.
Trois types de graphène différents sont étudiés dans ce manuscrit. Le premier se compose de flocons de graphène qui peuvent être trouvés sur la surface de graphite. Il est peut-être le système de graphène le moins étudié, mais est celui qui présente la qualité électronique la plus élevé. Il offre une possibilité unique d'étudier les excitations inter-bande inter-niveau de Landau dans le graphène, et d'observer les effets fins de l'interaction électron-phonon. Le deuxième système étudié est constitué d'un flocon de graphène encapsulé entre deux couches de nitrure de bore hexagonal (hBN) plat à l'échelle atomique. Il est le représentant d'une nouvelle classe de matériaux, où les différents cristaux 2D, sont empilés les uns sur les autres dans un ordre prédéfini, pour modifier certaines propriétés de ses constituants. Déposer le graphène sur une mince couche de hBN améliore largement ses propriétés électroniques, en comparaison à du graphène déposée sur Si/SiO$_2$. Le dernier système étudié sont des flocons de graphène produit par croissance CVD, avec des contacts électriques, ce qui nous a permis d'ajuster l'énergie de Fermi parmi les différents niveaux de Landau, et d'observer comment l'extinction des excitations électroniques inter-LL affecte le couplage électron-phonon.

Ce travail est organisé de la manière suivante:

- Dans le chapitre 1, les propriétés fondamentales des matériaux à base de graphène sont introduites. La structure de bande électronique du graphène est présentée et les différentes approximations utilisées pour sa dérivation sont brièvement discutée. L'effet de la quantification de l'énergie des électrons sous champ magnétique externe est discuté pour le graphène, pour les multicouches de graphène et pour le graphite.

- Dans le chapitre 2, les principes de la spectroscopie de diffusion Raman sont introduits. Les principales caractéristiques de la diffusion Raman dans le graphène sont présentées et l'application de cette méthode expérimentale pour la caractérisation de la structure en fonction de la tension de grille et du dopage est présentée.

- Dans le chapitre 3, la dispersion des phonons dans le graphène est discutée, en particulier les anomalies Kohn et l'effet de l'interaction électron-phonon sur les phonons aux points Γ et K. Un modèle existant de la résonance magnéto-phonon dans le graphène est brièvement expliqué. La possibilité de régler la force effective de l'interaction électron-phonon impliquant les phonons au point Γ est présentée.

- Dans le chapitre 4 la théorie des excitations électroniques dans le graphène et dans le graphite est discutée. Les règles de sélection dans une expérience de diffusion Raman sont présentés, pour différents excitations inter-bandes inter- niveau de Landau.

- Dans le chapitre 5, nous décrivons brièvement chacun des trois systèmes de graphène qui ont été étudiés dans cet ouvrage: flocons de graphène sur la surface de graphite, un flocon de graphène exfolié, encapsulée entre deux couches de hBN et un flacon de graphène produit par croissance CVD. Leurs principales caractéristiques et les méthodes de production sont discutées.

- Dans le chapitre 6, les détails de notre dispositif expérimental micro-magnéto-Raman sont présentés.

- Dans le chapitre 7, nous présentons les résultats de nos expériences de diffusion magnéto-Raman sur les flocons de graphène qui peuvent être trouvés sur la surface de graphite. Notre méthode de localisation de ces flocons à l'aide ou non d'un champ magnétique est présenté. L'évolution des excitations électroniques dans des champs magnétiques est discutée. Les effets de la température, la longueur d'onde d'excitation et de couplage différent sur le substrat sont présentés. Nous démontrons que, pour des champs magnétiques élevés une structure fine des principales excitations électroniques inter-bande se développe, et est discutée en termes de dopage et d'asymétrie électron-trou. Un nouveau type de résonance électron-phonon est observée, qui implique une diffusion inter-vallée des porteurs et l'émission d'un phonon au point K. Un procédé analogue pour les phonons du voisinage du point Γ est observé.

- Dans le chapitre 8 l'échantillon de graphène exfolié puis encapsulée entre deux couches de hBN, est étudié. Nous montrons comment la cartographie spatiale associée à la technique de spectroscopie Raman peut être utilisé pour la caractérisation et la visualisation sélective des composants individuels et des structures complexes empilés. La première observation non ambiguë de la résonance magnéto-phonon et d'une excitation électronique ($L_{-1,1}$) dans du graphene exfolié neutre est présentée. Une dépendance de la vitesse de Fermi par rapport au champ magnétique est démontrée. En outre, la dépendance de la vitesse de Fermi et d'énergie de bande 2D sur le substrat est observée et discutée en termes de d'écrantage diélectrique de l'interaction électron-électron.

- Dans le chapitre 9, nous détaillons les résultats d'une expérience, où la force de l'interaction électron-phonon dans un échantillon de graphène avec une grille électrostatique, peut être ajustée, avec succès, par la tension de grille appliquée. Nous comparons ces résultats avec les calculs théoriques et nous montrons que les excitations électroniques intra-bande jouent un rôle important dans la renormalisation de l'énergie des phonons Γ.

Chapter 1

Fundamental properties of graphene

1.1 Graphene crystal lattice

Graphene, multilayer graphene and graphite are the different crystallographic forms formed by the carbon atoms. Carbon is a light element from the periodic table, that have atomic number $Z = 6$. Therefore it has 6 protons, 6 electrons and a various number of neutrons. However, the only naturally occurring isotopes on Earth are those with total number of nucleons A =12, 13 or 14. From those three, only A =12 and 13 are stable, while $A = 14$ isotope, also known as carbon-14 (C^{14}) is radioactive and due to its rather short half-time (5700 years) [14] occurs only in trace amounts (on average one C^{14} atom per 10^{12} other carbon isotopes). From the two stable isotopes C^{12} is by far the dominant one (98.9% of all isotopes) [14].

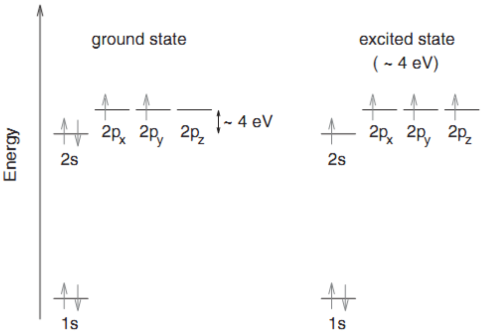

Figure 1.1: Electronic configurations for carbon in the ground state (left panel) and in the excited state (right panel). From ref. [15]

In the atomic ground state, the 6 electrons are found in the configuration $1s^2\ 2s^2\ 2p^2$, which means that the 2 electrons fill the inner shell $1s$, which is closely bound to the nucleus and does not participate in forming of the chemical bonds, while 4 electrons occupy the outer shells of $2s$ and $2p$ orbitals. The ground state of an isolated, single carbon atom consists of 2 electrons in the $2s$ orbital and only 2 of them in the $2p$ orbitals (see Fig. 1.1), because the $2s$ orbital has about 4eV lower energy than the $2p$ orbitals (2p$_x$, 2p$_y$, and 2p$_z$). However, when a carbon atom forms covalent bonds with other atoms around (like H, O, or other C atoms) it becomes energetically favourable to excite one electron from the $2s$ to the third $2p$ orbital (see Fig. 1.1). There-

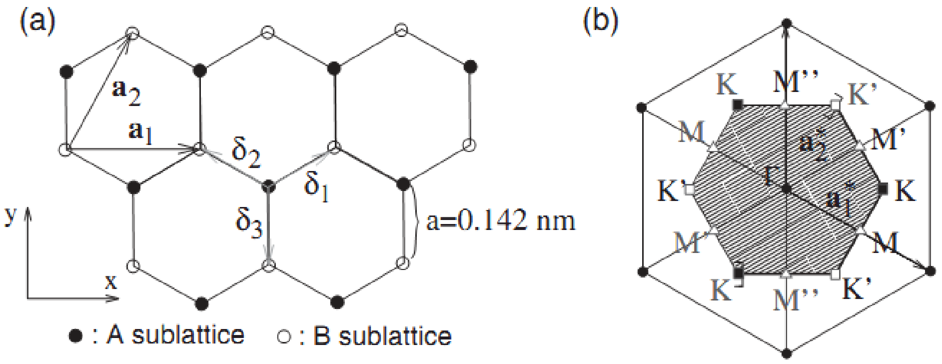

Figure 1.2: a) Arrangement of atoms in a graphene sheet. Open and filled circles denote atoms belonging to the two inequivalent sublattices A and B. The vectors $\mathbf{a}_1$ and $\mathbf{a}_2$ are basis vectors of the triangular Bravais lattice. b) Reciprocal lattice of the triangular lattice, with its primitive lattice vectors $\mathbf{a}_1^*$ and $\mathbf{a}_2^*$. The shaded region shows the first Brillouin zone (BZ), with its high symmetry points: the center at Γ, the two inequivalent corners at K and K', and three inequivalent points at M, M' and M'' points. From ref. [15]

fore, in the excited state there are four equivalent quantum-mechanical states, $|2s\rangle$, $|2p_x\rangle$, $|2p_y\rangle$, and $|2p_z\rangle$. A superposition of the state $|2s\rangle$ with n $|2p_i\rangle$ states is called sp^n hybridization, which play a main role in forming covalent bonds in carbon based materials. For instance, the sp^1 hybridization, plays an important role in forming triple bonds in some chains of hydrocarbons, such as alkynes. The sp^3 hybridization leads to the formation of diamond, a particular 3D allotrope of carbon. However in case of graphene, multilayer graphene and graphite it is the sp^2 hybridization that is responsible for formation of covalent bonds in those materials. The three sp^2-hybridized orbitals are oriented in the x-y plane and form an angle of 120° between each other. They form the strong σ bonds between atoms in the plane, and are responsible for the outstanding mechanical properties of graphene. On the other hand, the remaining unhybridized $2p_z$ orbital is perpendicular to the plane and forms the weak π bonds, that are responsible for the electronic properties at low energies ($< \pm 1$ eV from the charge neutrality point).

The rotational $\frac{2\pi}{3}$ symmetry of the sp^2 bonds results in carbon atoms arrangement in a honeycomb pattern in a graphene sheet. The hexagonal lattice, however, is not the Bravais lattice of graphene because two neighboring sites are inequivalent from a crystallographic point of view [1]. The actual Bravais lattice is triangular and has two atoms basis (see Fig. 1.2). Each of the two inequivalent atoms A and B belongs to its own triangular sublattice. This arrangement of atoms means that for each one belonging to the A sublattice its three nearest-neighbours belong to the B sublattice and are displaced from it by one of the vectors:

$$
\begin{aligned}
\boldsymbol{\delta}_1 &= \frac{a_0}{2}\left(\sqrt{3}\mathbf{e}_x + \mathbf{e}_y\right)\\
\boldsymbol{\delta}_2 &= \frac{a_0}{2}\left(-\sqrt{3}\mathbf{e}_x + \mathbf{e}_y\right)\\
\boldsymbol{\delta}_3 &= -a_0\mathbf{e}_y
\end{aligned}
\tag{1.1}
$$

Where $a_0 = 0.142$ nm is the nearest neighbour distance, sometimes also referred to as a lattice parameter. It has the same value as a bond length in a benzene ring which is in between the values of single (0.147 nm) and double (0.135 nm) σ bonds in carbon, which comes from its partially delocalized nature [16]. The Bravais lattice is spanned by the primitive vectors:

$$
\begin{aligned}
\mathbf{a}_1 &= \sqrt{3}a_0\mathbf{e}_x\\
\mathbf{a}_2 &= \frac{\sqrt{3}a_0}{2}\left(\mathbf{e}_x + \sqrt{3}\mathbf{e}_y\right)
\end{aligned}
\tag{1.2}
$$

The length of the basis vectors gives: the lattice spacing $\tilde{a} = \sqrt{3}a_0 = 0.24$ nm, and the area of the unit cell $A_{u.c.} = \frac{\sqrt{3}\tilde{a}_0}{2} = 0.051$ nm^2. The reciprocal lattice, which is defined with respect to the triangular Bravais lattice, is also a triangular lattice and is spanned by the vectors:

$$
\begin{aligned}
\mathbf{a}_1^* &= \frac{2\pi}{\sqrt{3}a_0}\left(\mathbf{e}_x - \frac{1}{\sqrt{3}}\mathbf{e}_y\right)\\
\mathbf{a}_2^* &= \frac{4\pi}{3a_0}\mathbf{e}_y
\end{aligned}
\tag{1.3}
$$

The first Brillouin zone (BZ, shaded region and border marked with thick lines of the hexagon in Fig. 1.2) represents all inequivalent points in the reciprocal space, i.e. all points that cannot be connected by any combination of reciprocal lattice vectors $n\mathbf{a}_1^* + m\mathbf{a}_2^*$, where n, m are integer numbers. The high symmetry points in BZ include the center of the zone – Γ point, two inequivalent points in the corners of the hexagon – K and K', and also points located in the middle of the K–K' line – M, M', and M''. Among them the K and K' points are of special interest to us since it is there where the valence and conduction bands touch each other in graphene. Those points are represented by vectors:

$$
\pm\mathbf{K} = \pm\frac{4\pi}{3\sqrt{3}a}\mathbf{e}_x \tag{1.4}
$$

The inequivalence of those two points is a direct property of the triangular Bravais lattice, and is therefore independent from the number of atoms in the base of the Bravais lattice. Instead, the presence of two sublattices A and B has an effect on the form of the electron wavefunction, which turns out to be described by a spinor.

1.2 Graphene band structure

There are several ways to calculate the band structure of graphene. The *ab initio*, $\mathbf{k}\cdot\mathbf{p}$ and tight binding approximation are the most frequently used ones. The last one is especially often used, due to its simplicity, analytic solutions and long track of successful predictions in the group of graphene based materials. It was originally used by *Wallace* to describe the band structure of graphite. The first step in his work was to calculate the band structure of graphene in the nearest-neighbour approximation [1]. Later on, this model was extended by including interactions with atoms lying further away and today is known as a *Slonczewski-Weiss-McClure* model of graphite [3, 2]. Then tight binding-approximation proved useful again to predict the band structure of carbon nanotubes [17, 18, 4, 19, 20]. Since exact derivation of tight binding model for graphene can be found in many review articles [15, 21, 22, 23] here we are going to show just the main idea behind this approach and the obtained results.

In a tight binding approximation the electron wavefunction $\Psi(\mathbf{k})$ can be written as a linear combination of two Bloch functions $\psi_A(\mathbf{k})$ and $\psi_B(\mathbf{k})$, which describe electrons on a sublattice A and B, respectively:

$$\Psi(\mathbf{k}) = c_A\psi_A(\mathbf{k}) + c_B\psi_B(\mathbf{k}) \tag{1.5}$$

Those Bloch functions $\psi_{A(B)}(\mathbf{k})$ are constructed from the $2p_z$ atomic orbital of the isolated carbon atom $\phi(\mathbf{r})$ and plane waves:

$$\psi_{A(B)}(\mathbf{k}) = \frac{1}{\sqrt{N}} \sum_{\mathbf{R}_{A(B)}} e^{i\mathbf{k}\cdot\mathbf{R_{A(B)}}} \phi\left(\mathbf{r} - \mathbf{R}_{A(B)}\right) \tag{1.6}$$

where $\mathbf{R}_{A(B)}$ is a vector pointing to a site on the sublattice A(B). Then this trial wavefunction is inserted into the stationary Schrödinger equation:

$$\hat{H}\Psi(\mathbf{k}) = E(\mathbf{k})\Psi(\mathbf{k}) \tag{1.7}$$

where $\hat{H}$ is the Hamiltonian of the system. Solving that equation gives a formal solution for the eigenenergies of the electron:

$$E(\mathbf{k})^{\pm} = \frac{-(-2E_0 + E_1) \mp \sqrt{(-2E_0 + E_1)^2 - 4E_2E_3}}{2E_3} \tag{1.8}$$

where $+(-)$ sign denotes the energy of the conduction (valence) band. The parameters E_0, E_1, E_2, E_3 are given by a combination of the matrix elements of the Hamiltonian $H_{IJ} = \langle\psi_I|\hat{H}|\psi_J\rangle$ and the overlaps between Bloch functions $S_{IJ} = \langle\psi_I|\psi_J\rangle$:

$$\begin{aligned} E_0 &= H_{AA}(\mathbf{k})S_{AA}(\mathbf{k}) \\ E_1 &= S_{AB}(\mathbf{k})H^*_{AB}(\mathbf{k}) + H_{AB}(\mathbf{k})S^*_{AB}(\mathbf{k}) \\ E_2 &= H^2_{AA}(\mathbf{k}) - H_{AB}(\mathbf{k})H^*_{AB}(\mathbf{k}) \\ E_3 &= S^2_{AA}(\mathbf{k}) - S_{AB}(\mathbf{k})S^*_{AB}(\mathbf{k}) \end{aligned} \tag{1.9}$$

nearest neighbour approximation

The main approximation in the tight binding method lies in substituting the infinite summation over $\mathbf{R}_{A(B)}$ vectors pointing to all the other atoms in the crystal, with just the few ones which give the major contribution to the matrix elements H_{IJ} and overlap integrals S_{IJ}. In case of graphene usually limiting oneself to counting only vectors pointing to the three nearest neighbouring atoms is enough to accurately capture the main features

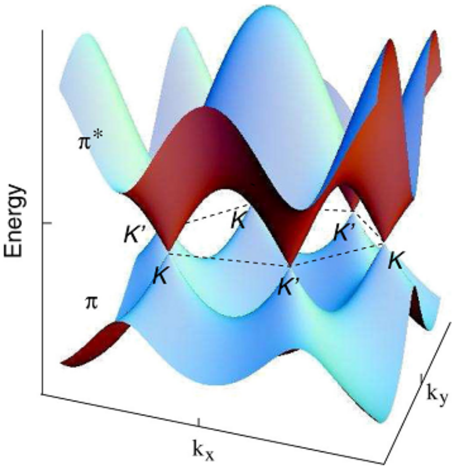

Figure 1.3: Energy dispersion in graphene as a function of the wavevector components k_x and k_y, obtained within the tight-binding approximation. Conduction and valence band meet at K and K' points. In the vicinity of those points their dispersion is linear. From ref. [15]

of the band dispersion. This approach to the tight binding method, which is also called nearest neighbours (nn) approximation, gives energy bands that are described by just one parameter $\gamma_0 \approx 2.8$ eV which is usually referred to as a carbon-carbon interaction energy, hopping parameter or tight binding integral. The electronic bands in the nn approximation have the following energy dispersion [21]:

$$E(\mathbf{k})^{\pm} = \pm\gamma_0\sqrt{3 + f(\mathbf{k})} \tag{1.10}$$

with function $f(\mathbf{k})$ defined as:

$$f(\mathbf{k}) = 2cos(\sqrt{3}a_0k_y) + 4cos(\frac{3a_0}{2}k_x)cos(\frac{\sqrt{3}a_0}{2}k_y) \tag{1.11}$$

The above energy dispersion is plotted over the whole first Brillouin zone in Fig. 1.3. In the nn approximation the conduction and valence bands are symmetric with respect to reflection by the $\Gamma - K - K'$ plane, which is called electron-hole symmetry. The peculiar feature of this dispersion is the fact that it displays characteristic valleys at the corners of the Brillouin zone, where the conduction and valence bands touch each other. The points where they meet are called Dirac points. In samples that are not strained, the Dirac points coincide with the K and K' points in the Brillouin zone. In a charge neutral sample the Fermi level lies exactly at the Dirac points, which gives graphene the semi-metallic properties. Moreover, in most of the optical and transport experiments, only states from the vicinity of the Fermi surface $E < E_F \pm 2$ eV are probed, which means that for all practical purposes the full band dispersion can be very well approximated by only two Dirac cones situated at the K and K' points. The energy dispersion around those points can be expanded for $k \ll K$ in the Taylor series, which gives a very simple and characteristic for graphene linear dispersion:

$$E(\mathbf{k})^{\pm} = \pm v_F\hbar|\mathbf{k}| \tag{1.12}$$

where wavevector $\mathbf{k}$ is measured with respect to the $K(K')$ point, parameter $v_F \approx 10^6$ m/s describes the slope of the band dispersion, has a dimension of a velocity and is called Fermi velocity. It is also proportional to the nn hopping integral γ_0[24, 25]:

$$v_F = \frac{3}{2\hbar} a_0 \gamma_0 \tag{1.13}$$

The linear energy dispersion in graphene implies that charge carriers in this material behave like relativistic particles with zero rest mass and constant velocity $v_F \sim 10^6$ m/s. They are often referred to as massless Dirac fermions, and with a good accuracy, their behaviour is described by the effective Hamiltonian [21, 24]:

$$\hat{H} = v_F \begin{pmatrix} 0 & p_x - ip_y \\ p_x + ip_y & 0 \end{pmatrix} = v_F \begin{pmatrix} 0 & \pi^\dagger \\ \pi & 0 \end{pmatrix} = v_F \boldsymbol{\sigma} \cdot \boldsymbol{p} \tag{1.14}$$

where $\boldsymbol{\sigma}$ is the Pauli matrix. This Hamiltonian is equivalent to the Hamiltonian in the Weyl equation for real relativistic particles with zero rest mass derived from the Dirac equation. Because of this formal similarity experiments in graphene can be used to answer some questions raised by quantum electrodynamics.

The density of states in such system with linear dispersion depends very differently on energy, as compared with the usual 2D system with massive particles. Instead of being constant, it rises linearly with energy like:

$$DOS(E) = \frac{g_s g_v |E|}{2\pi v_F^2 \hbar} \tag{1.15}$$

where $g_s = g_v = 2$ stands for the spin and valley degeneracies, respectively.

next nearest neighbour approximation

Despite its simplicity, graphene band structure obtained in a nearest neighbours approximation gives a very good description of quantum states in that system [26, 27, 28]. However, there are also instances when small deviations from the linear band dispersion are detected in the experiments [29] which invoke the need to describe the band structure with a greater accuracy. In the first step it can be achieved by including interaction with more than the closest neighbouring atoms, in the second step – by accounting for the electron-electron interaction. Here we limit ourself to demonstrate the result of including the interaction with the next nearest neighbours (nnn) when calculating the matrix elements and overlap integrals in Eq. 1.9. The resulting energy band dispersion is given by:

$$E(\mathbf{k})^{\pm} = \pm\gamma_0\sqrt{3 + f(\mathbf{k})} - \gamma' f(\mathbf{k}) \tag{1.16}$$

Where the γ' parameter describes the next nearest neighbours hopping energy. The *ab initio* calculations usually give γ' value in the range $0.02\gamma_0 < \gamma' < 0.2\gamma_0$ [21, 30], however its exact value is still debated. Here again we are mostly interested in the energy dispersion around Dirac cones, which is obtained from Taylor expansion of the above

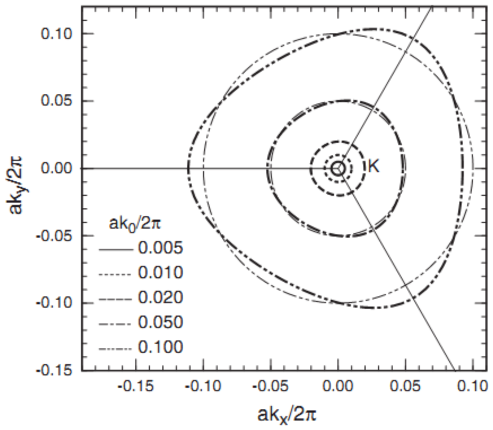

Figure 1.4: Constant energy cross-sections of the graphene band structure around $K(K')$ for chosen values of energy. The thin lines show the circular Fermi surface at energies $\epsilon = \hbar v_F k_0$. The thick lines shows the corresponding Fermi surface in the presence of trigonal warping. From ref. [20]

expression around K point:

$$E(\mathbf{k})^{\pm} = 3\gamma' \pm \hbar v_F|\mathbf{k}| - \left(\frac{9\gamma' a_0^2}{4} \pm \frac{3\gamma_0 a^2}{8} sin(3\theta_{\mathbf{k}})\right)|\mathbf{k}|^2 \tag{1.17}$$

where (1.18)

$$\theta_{\mathbf{k}} = arctan\left(\frac{k_x}{k_y}\right)$$

Above expression reveals two main effects of including the *nnn* in the tight binding calculations on the energy band structure. Namely, the electron-hole symmetry is broken by adding a positive, constant term $3\gamma'$ to the energy of carriers in both valence and conduction bands.

The other pronounced change is the breaking of the full rotational symmetry of Dirac cones, by introducing a term which depends on the direction in the reciprocal space and has a $2\pi/3$ rotational symmetry. This term causes warping of the Dirac cones, which is shown in Fig. 1.4 and makes the carrier angular momentum being defined up to a multiple of $\pm 3\hbar$. This effect is seen for instance in partial breaking of optical selection rules, which enables certain electronic excitations to be seen in polarization resolved Raman scattering experiments due to absorption of $\pm 3\hbar$ angular momentum by the crystal [31, 32] (see Chapter 4).

1.3 Energy dispersion of graphene multilayers and graphite

Graphene bilayer

Stacking graphene layers on top of each other changes the electron energy dispersion considerably. The graphene bilayer is the simplest example of a general class of graphene multi-layers and a building block of graphite.

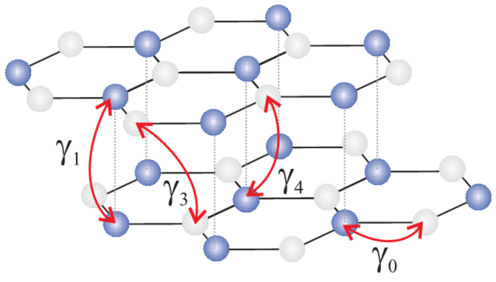

Figure 1.5: Crystal structure of the Bernal-stacked graphene bilayer with the corresponding SWM hopping parameters. From ref. [25]

Interest in the graphene bilayer started when *Novoselov et al.* demonstrated a characteristic quantum Hall effect and a Berry's phase of 2π seen in magneto-transport experiments in this system [33]. It turned out, that despite parabolic energy dispersion in bilayer graphene, charge carriers in this material do not behave exactly like a typical massive particles. This anomalous behavior, as evidenced by the quantum Hall effect, lead to naming those quasi-particles as *massive Dirac fermions.* Bilayer graphene band structure can be calculated analogously to the case of a monolayer, using for instance tight binding method. This approach was used as early as in the works of *Wallace* [1] and *Slonczewski, Weiss and McClure* (SWM) [2] who used the bilayer graphene to model the bandstructure of graphite. In this method several hopping integrals are introduced to describe interaction with different neighbouring atoms, both in the same and adjacent atomic plane. Those hopping integrals are shown in Fig. 1.5, and named following the standard SWM model designations. For the vast number of cases, it is enough to limit the number of parameters to just two hopping integral describing interactions with the nearest neighbouring atoms in plane γ_0 and across adjacent planes γ_1. The result of those calculations gives four parabolic energy bands at K and K' points, two of them (E_1 and E_2) in the valence and two (E_3 and E_4) in the conduction band. The highest one from the valence band and the lowest form the conduction band touch each other at K and K' points, and this is also the energy of the Fermi level in charge neutral samples. Their energy as a function of wavevector $\mathbf{k}$, obtained in this approximation is given by [25, 34]:

$$\begin{aligned}
E_1 &= -\left(\frac{\gamma_1^2}{2} + v_F^2\hbar^2|\mathbf{k}|^2 + \sqrt{\frac{\gamma_1^4}{4} + v_F^2\hbar^2\gamma_1^2|\mathbf{k}|^2}\right)^{1/2} \\
E_2 &= -\hbar\left(\frac{\gamma_1^2}{2} + v_F^2\hbar^2|\mathbf{k}|^2 - \sqrt{\frac{\gamma_1^4}{4} + v_F^2\hbar^2\gamma_1^2|\mathbf{k}|^2}\right)^{1/2} \\
E_3 &= -E_2 \\
E_4 &= -E_1
\end{aligned} \tag{1.19}$$

Where v_F is related to γ_0 in the same way as in Eq. 1.13.

Multilayer graphene

When more and more graphene sheets are stacked on top of each other their energy band structure becomes increasingly complex, with each addtional graphene plane adding one more pair of conduction and valence bands. However, *Koshino and Ando* have shown that

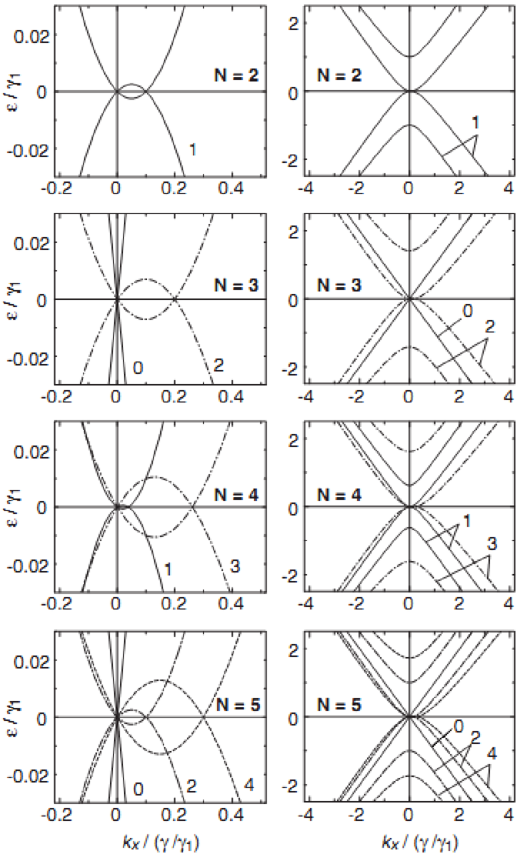

Figure 1.6: Band structures of multilayer graphenes ($N = 2, 3, 4, 5$) around the K point (taken as origin) along the k_x axis. Notice that subbands with linear dispersion appear for odd N. Right panel shows a zoom out of the left. From ref. [35]

a Hamiltonian of a multilayer graphene system with an arbitrary number of layers can be decomposed into those equivalent to the monolayer or bilayer graphene [35]. Using the $\mathbf{k}\cdot\mathbf{p}$ method to construct the Hamiltonian of a multilayer graphene for carriers around K(K') points, a Hamiltonian with a block matrix form has been obtained. Each of those blocks corresponds to the bilayer graphene Hamiltonian for a system that consist of an even number of layers. In systems that have an odd number of layers, an additional submatrix appears that has the form of a monolayer graphene Hamiltonian.

The resulting energy bands dispersions can be well described by the Eq. 1.19, but instead of using true γ_1 value, an effective ϵ_m parameter has to be used for each pair of bands. For a system with N layers, each of the N bands in the valence and each of the N bands in the conduction band is characterized by a quantum number m that change in the range $m = -(N-1), -(N-3), ..., N-3, N-1$. This number may be understood as a label of a momentum in the k_z direction, that is attributed to that graphene plane and equals

$$\kappa_m = \frac{\pi}{2} - \frac{m\pi}{2(N+1)} \tag{1.20}$$

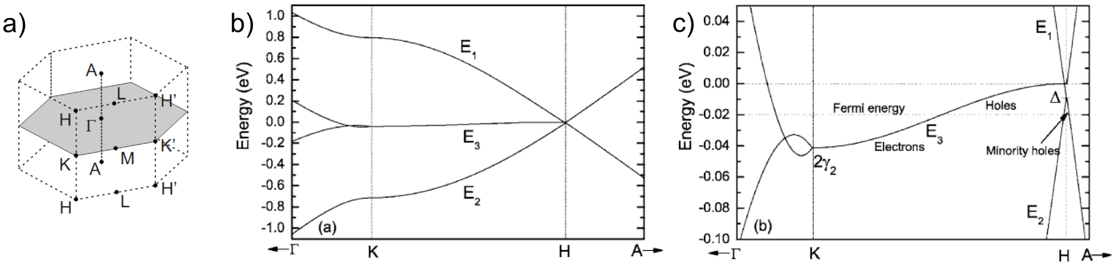

Figure 1.7: a) First Brillouin zone in graphite, with indicated high symmetry points. b) Energy band dispersion along the H-K-H line. c) magnification of the band dispersion around the Fermi energy. From ref. [23]

The value of the momentum in the k_z direction determines then the effective ϵ_m coupling constant:

$$\begin{aligned}\epsilon_m &= \lambda_{N,m}\gamma_1 \\ \lambda_{N,m} &= 2cos(\kappa_m)\end{aligned} \tag{1.21}$$

For odd numbers of N, the $m = 0$ appears among the other possibilities. Since $\epsilon_0 = 0$, the equation describing carriers dispersion in bilayer graphene (Eq. 1.19) simplifies to the form of corresponding equation for a monolayer sample (Eq. 1.12), and therefore a pair of bands with linear dispersion relation appears in samples with odd number of layers. The energy bands calculated using this effective bilayer method, for multilayer graphene stacks for $N \leq 5$ are shown in Fig. 1.6.

Graphite

The graphene band structure was already an object of active research as early as 1940s. As it was mentioned before, the works of *Wallace* [1] and *Slonczewski, Weiss and McClure* [2, 3], set the foundations for the tight binding model describing the band dispersion in this material. This model describes the band structure along the H-K-H line of the 3D Brillouin zone, which is responsible for most of the electrical and optical properties of bulk graphite. The SWM model is parametrized by six hopping integrals γ_0,...,γ_5, and an additional parameter Δ, usually called a pseudogap, which is related to the difference of the crystal field on atom-sites A and B. Graphite is a 3D material as contrasted with the 2D graphene, therefore in addition to the in-plane energy dispersion there is also a dispersion along the k_z direction – perpendicular to the atomic planes. This dispersion, shown in Fig. 1.7 reveals that there exist simultaneously two types of carriers in graphite – the massive carriers around K point and massless Dirac particles at H point. As one moves along the $H-K-H$ line, the nature of carriers changes slowly from massless to massive [23]. In fact, instead of using full complexity of the SWM model to describe the band structure of graphite, the effective bilayer model, which was introduced before, can be used to model the electronic bands around Fermi energy with satisfactory result. In this model, only the two most relevant hopping integrals γ_0 and γ_1 are taken into account. They describe the intra- and interlayer coupling to the nearest neighbours, respectively [36, 37]. It turns out that graphite Hamiltonian in this model is analogous to the Hamiltonian of a bi-layer graphene, and the carriers in-plane dispersion can be calculated using Eq. 1.19, where γ_1 hopping integral is substituted by the effective coupling constant $\lambda\gamma_1$. The λ parameter describes how the strength of the inter-layer coupling changes along the k_z direction:

$$\lambda = 2cos(\pi k_z) \tag{1.22}$$

The vanishing value of effective inter-layer coupling at H point (k_z=0.5) leads to linear in-plane energy dispersion that is characteristic for decoupled graphene flakes. As one moves along the k_z toward K point ($k_z = 0$), the effective interlayer coupling constant becomes larger, which induces the effective mass (curvature of the bands) of charge carriers.

There are nevertheless some differences between the massless carriers in graphite and graphene monolayer. Notably the twofold degeneracy of the valence and conduction band and the presence of a small gap determined by the parameter Δ.

1.4 Electronic states in magnetic field

Applying a magnetic field to a sample changes qualitatively the energy spectrum of its charge carriers. In case of an ordinary, massive, charged particles like a 2D electron-hole gas in semiconductor heterostructures applying a magnetic field **B** in the direction perpendicular to the 2D system exerts a Lorentz force $F = e\mathbf{v} \times \mathbf{B}$ on the charge carriers moving in the plane. In classical physics this leads to changing the carriers motion into circular orbits. The massive carriers precess with a characteristic frequency $\omega_C = eB/m$, which is given only by magnetic field strength B and particle effective mass m. The quantum mechanical treatment of the same problem, results in a quantization of the charged particle energy into a set of highly degenerated discrete levels. These energy levels, also called Landau levels (LLs), are equidistant in energy an rise linearly with the field $E = \frac{\hbar eB}{m}(n + 1/2)$.

Monolayer graphene

The fact that band dispersion in graphene cannot be approximated by the parabolic wavevector **k** dependence implies significant changes from a conventional LLs structure. For the energy bands described by the two Dirac cones (Eq. 1.12), the resulting LLs have a characteristic $\sqrt{B}$ dependence on magnetic fields and $\sqrt{n}$ dependence on the LL index n [38]:

$$E_n = sgn(n)v_F\sqrt{2e\hbar B|n|} \tag{1.23}$$

where levels with $n > 0$ are from the conduction band, those with $n < 0$ are from the valence band and the $n = 0$LL, is a special level that is shared by both types of carriers. In fact the existence of $n = 0$ is a purely quantum-mechanical effect that cannot be reproduced from any semi-classical quantization schemes [38], and it is responsible for the unusual sequence of the quantum Hall effect in graphene [39, 26]. In a neutral graphene $n = 0$ LL is half filled.

Each of those energy levels is highly degenerated, with the degeneracy given by:

$$\xi(B) = g_v g_s \frac{|eB|}{h} \tag{1.24}$$

On top of the usual degeneracy due to magnetic flux quantization, there is also the fourfold degeneracy of each level due to valley $g_v = 2$ and spin $g_s = 2$ degeneracy.
These quantized LLs can be probed experimentally, by investigating the inter-LLs excitations that can be produced when light couples to the charge carriers. This coupling can produce a series of dipole-allowed inter-LL transitions that have been observed in magneto-transmission experiments [40, 29, 41, 13, 42, 28, 43], while excitations following other selection rules were observed in magneto-Raman scattering experiments [44, 32, 45, 46].
The above simple formula describing LLs evolution in magnetic fields (Eq. 1.23) works surprisingly well in most of the cases. However, small deviations from the $\sqrt{B}$ dependence have been observed in a multilayer epitaxial graphene samples [29]. In order to explain them, LLs derived from a more precise band dispersion (Eq. 1.17) had to be used. The resulting LLs energy evolve in magnetic field, like [29, 15]:

$$E_n^{\pm} = \pm v_F \sqrt{2\hbar e B}\sqrt{n} + 3\frac{\gamma'}{\gamma_0} a_0 v_F e B n \mp \frac{3}{8} w^2 a_0^2 v_F \sqrt{\frac{2e^3 B^3}{\hbar}}\sqrt{n^3} \tag{1.25}$$

where w is a phenomenological parameter that takes into account corrections beyond the simplest tight-binding model [29, 20]. The overall result of those small corrections is to push slightly higher the LLs energies as compared with Eq. 1.23. The magnitude of this effect increases with LL index n.

Bilayer graphene

The parabolic electronic dispersion around K point in bilayer graphene leads to LLs structure qualitatively different from the one observed in the monolayer graphene. Since in bilayer graphene close to the Fermi energy, there are two parabolic branches in the conduction and two branches in the valence bands, when magnetic field is applied each of them gives rise to a set of LLs. Therefore each eigenstate of bilayer graphene Hamiltonian is uniquely described by a set of quantum numbers n, μ, s. Where n is the LL index, $s = +$ ($s = -$) represents the electron (hole) bands, while $\mu = \pm$ correspond to the higher and lower subbands in the limit of zero magnetic field. Often, in order to avoid confusion between s and μ, another notation is used where $\mu = H, L$. The LL structure in bilayer graphene for $n \geq 1$ is the given by [36]:

$$\epsilon_{n,\mu,s} = \frac{s}{\sqrt{2}}\left[\gamma_1^2 + (2n+1)E_1^2 + \mu\sqrt{\gamma_1^4 + 2(2n+1)\gamma_1^2 E_1^2 + E_1^4}\right]^{1/2} \tag{1.26}$$

where E_1 is defined as $E_1 = v_F\sqrt{2\hbar e B}$. For $n = 0$ there are two LLs in the higher subbands:

$$\epsilon_{0,H,s} = s\sqrt{\gamma_1^2 + E_1^2} \tag{1.27}$$

and one LL in the lower subbands $\epsilon_{0,L} = 0$. Contrary to monolayer graphene $n = -1$ is also allowed in bilayer, which gives additional zero energy LL $\epsilon_{-1,L} = 0$ (level $\epsilon_{-1,H}$ doeasn't exist).
Altogether the eightfold (8eB/h) degeneracy of the LL with $n = 0$ is twice higher than the degeneracy of all other levels and this produces a characteristic quantum Hall effect with the Berry phase of 2π [33, 47]. At energies around the neutrality point, the relevant

LLs are those from the lower subbands ($\mu = L$) in conduction and valence bands. At the low magnetic fields, their energies evolve practically linearly with B [36]:

$$\epsilon_{n,\mu,s} = s\frac{\hbar eB}{m^*}\sqrt{n(n+1)} \tag{1.28}$$

with effective mass defined as $m^* = \gamma_1/(2v_F^2)$ [47]. Nevertheless, departure from this linearity is seen at higher magnetic fields or at LLs with higher index n.

multilayer graphene

The effective bilayer model used to calculate the energy band structure in multilayer graphenes [23] can be also extended to calculate the Landau level structure in those materials [35, 36]. Representing the Hamiltonian matrix of such system in the form of block matrices, allows us to treat the multilayer graphene sample as an assembly of bi-layer type subsystems, each characterized by a quantum number m and effective inter-layer coupling constant $\lambda_m\gamma_1$. Therefore the resulting LLs structure is a sum of LLs from bilayer graphenes with different effective coupling constants. Eq. 1.26 can then be used for calculation of LLs in multilayer graphene, provided that γ_1 is substituted by an effective coupling constant $\lambda_m\gamma_1$. Fig. 1.8(Top) shows the LL structure of one bilayer-like subsystem as a function of the chosen κ momentum in the k_z direction(κ is related to the effective coupling constant through Eq. 1.21). LLs structure at $\kappa = \pi/3$ corresponds to a true bilayer case. Interestingly, at $\kappa = \pi/2$ LLs with the same index n, coming from the two subbands $\mu = H$ and $\mu = L$ have the same energy, which allows to reproduce the LL structure of a true monolayer graphene. The bottom panel in Fig. 1.8 shows which momenta κ and therefore effective coupling constants $\lambda_m\gamma_1$ are chosen in a multilayer graphene consisting of N layers. Characteristically, $\kappa = \pi/2$ corresponding to a monolayer-like energy bands appears in every multilayer with odd number of layers N.

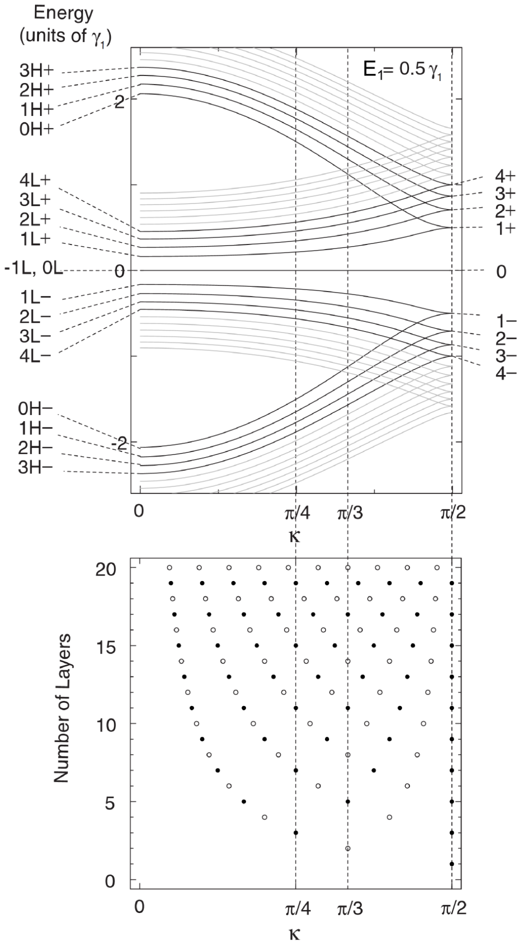

Figure 1.8: Top: Landau levels of the bilayer-type subbands as a function of κ. The magnetic field strength is taken as $E_1 = 0.5\gamma_1$ (B∼ 170 T) to show on the same scale all four subbands split due to Landau levels formation. Bottom: list of allowed κ values for each N-layer graphene. Empty and filled circles represent even and odd N's, respectively. From ref. [36]

Graphite

The structure of LLs in graphite may be calculated directly from the SWM model. However, introducing the magnetic fields expands the system Hamiltonian matrix to the infinite order [48], so its diagonalization becomes impractical. Therefore the calculations are done either by neglecting some of the hopping integrals [49, 50] which makes the Hamiltonian matrix of finite order, or by truncating the infinite matrix at some point and performing numerical calculations [51]. However, in magneto-optical experiments rarely a complete LLs dispersion along k_z direction is ever needed, since the main contribution to the optical response is provided just by the K and H points. At those specific points Landau bands become flat, which leads to singularities in the joint density of states and domination of carriers from that points in the optical response [36, 52]. Therefore a basic understanding of the complex magneto-optical response of bulk graphite [53], is possible just by taking into account massive carriers from the K point and massless carriers from H point. Thus, graphite can be modeled just by an effective graphene monolayer and an effective bilayer with a coupling strength enhanced twice in comparison to a true graphene bilayer. For calculations of LLs at the K point Eq. 1.26 is used after substituting γ_1 with $2\gamma_1$.

Surprisingly, this effective bilayer model that includes only two material parameters, γ_0 and γ_1, is able to catch the basic magneto-optical properties of bulk graphite, a complex 3D material.

Chapter 2

Raman scattering of graphene and its multilayers

2.1 Principles of Raman scattering

Interaction between light and matter is commonly used in solid state physics to probe properties of various materials in an non-invasive way. There exist a number of optical processes that can be used for that purpose. Among them absorption, reflection and, in some materials, luminescence are the most intense ones. Light scattering is the next one however, since it is second-order process, it is usually a weaker effect. Scattering can be generally divided into two groups. Firstly, the elastic processes during which energy of scattered light stays the same as the energy of incoming light, those are called Rayleigh scattering. The other group encompasses inelastic processes during which energy of the scattered light is lower (Stokes processes) or higher (anti-Stokes processes) than the initial one. This kind of light scattering is called either Brillouin or Raman processes, depending on the scale of the change in the photon energy. Historically for scattering with low energy acoustical phonons – term Brillouin scattering was used, while for optical phonons – Raman scattering. Since then however, scattering with many other elementary excitations has been observed, which energies could vary continuously in a large energy range [44]. Therefore Raman scattering term is nowadays in broader sense – regardless of the magnitude of change in the energy of scattered light.

This inelastic light scattering effect was originally discovered in 1928 independently by two groups of scientists: a pair of soviet physicists – G. Landsberg and L. Mandelstam and by a pair of Indian physicists – Ch. Raman and K. Krishnan [54]. However the effect is widely known by the name of just one of them, as a Raman effect. The significance of that discovery was quickly recognized by awarding Ch. Raman a Nobel Prize in 1930. However since intensity of the inelastically scattered light is about six orders of magnitude lower than intensity of the elastically scattered one, very strong sources of monochromatic light are needed to observe this effect. For this reason it wasn't until the development of lasers in 60' that Raman spectroscopy could reveal its full potential for both fundamental and applied research.

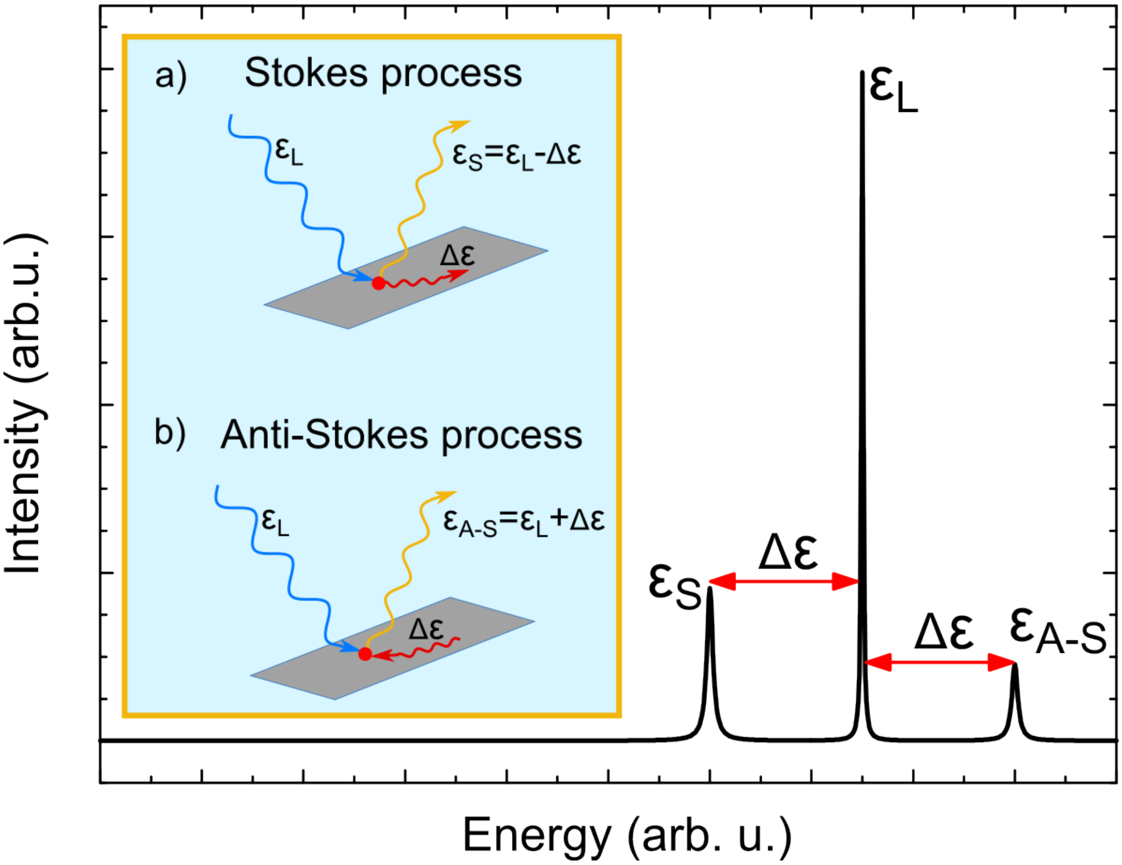

Figure 2.1: Sample of the Raman scattering spectrum. Insets show: a) Stokes process, b) Anti-Stokes process. ϵ_L-energy of the incident laser light, ϵ_S-energy of the scattered laser light in Stokes process, ϵ_{A-S}-energy of the scattered laser light in Anti-Stokes process, $\Delta\epsilon$-energy of the created/annihilated excitation. Intensities of Stokes and Anti-Stokes peaks are largely exaggerated to present them on the same scale as elastically scattered laser peak.

The Raman effect is based on an observation that when a monochromatic light is scattered from the investigated medium the additional frequency components are observed in the scattered light spectrum. This is illustrated in Fig. 2.1 where a theoretical scattered light spectrum is shown. In addition to the most intense central peak at the energy of incoming laser radiation (ϵ_L) two additional peaks occur, one at higher $\epsilon_{A-S} = \epsilon_L + \Delta\epsilon$ and one at lower $\epsilon_S = \epsilon_L - \Delta\epsilon$ energy. The energy difference between laser peak and one of those smaller peaks $\Delta\epsilon$ is called *Raman shift* and is characteristic for investigated material. This energy difference corresponds to the energy of an elementary excitation that was created or annihilated in the sample. In the former case it is called a Stokes process and it is illustrated in panel a) in Fig. 2.1. In such case the incoming photon looses part of its energy to create a new excitation (like e.g. phonon) in the system with energy $\Delta\epsilon$. Thus the scattered light has lower energy $\epsilon_S = \epsilon_L - \Delta\epsilon$. The opposite effect is also possible, assuming that some elementary excitation already exist in the system. Then interaction with incoming light leads to annihilation of that excitation (panel b) in Fig. 2.1) and the released energy is transfered to the scattered photon $\epsilon_S = \epsilon_L + \Delta\epsilon$.

Such processes are called – anti-Stokes. However their probabilities are proportional to the number of elementary excitations which already exist in the system. Since excitations number is governed by a distribution function, anti-Stokes processes are more probable at higher temperatures. On the other hand, the probability to create a new excitation doesn't depend on the number of already existing ones. So when working at low temperatures it is easier to observe Stokes peak than anti-Stokes. For this reason all results presented in this thesis focus on the Stokes processes.
The fact that Raman shift of scattered light corresponds exactly to the energy of created/annihilated excitation is simply a consequence of the energy conservation law. However there is also another quantity that needs to be conserved, as long as the crystal translational symmetry is not broken, namely the momentum or wavevector **k**. In such case:

$$\mathbf{k_i} = \mathbf{k_s} + \mathbf{q} \tag{2.1}$$

where $\mathbf{k_i}(\mathbf{k_s})$ indicate wavevector of the initial (scattered) light, while $\mathbf{q}$ wavevector of the created/annihilated excitation. It follows from Eq. 2.1, that the highest magnitude of created excitation wavevector $\mathbf{q} = |\mathbf{k_s} - \mathbf{k_i}|$ can be obtained in a backscattering geometry. However for the light in the visible range its wavevector $k = \frac{2\pi}{\lambda}$ is very small $k < 10^6$ cm^{-1}, as compared to the size of the first Brillouin zone. For instance, excitations from the zone edge would have a wavevector $q_{max} \approx \pi/a \approx 2 \cdot 10^8$ cm^{-1} (where $a = 0.142$ nm is the nearest neighbours inter-atomic distance in graphene). This is about two orders of magnitude larger than that of the incoming/scattered light. This, in turn, implies that the only excitations which can be created in the material due to first-order Raman scattering are those from the closest vicinity of zone center – Γ point. In graphene example of such process include a phonon from the highest optical branch at – Γ point. However this rule is strictly applicable only to the first order Raman processes. In case when more than one quasi-particle are created/annihilated during scattering, the process is called higher order Raman scattering, and the quasi-particle number determines the order of this process. In that case many excitations with even large wavevectors q_n may be created/annihilated in the scattering. Then the only condition is that their sum must add up to zero $\sum_n q_n = 0$.

Depending on the investigated system, different kinds of excitations can be probed using Raman scattering technique. Historically, it was first used to study excited electronic and vibrational levels in molecules. Later it was also successfully applied to the solid state systems, where it is now used to probe vibrational (phonons), electronic (excitons, plasmons) or spin (magnons) excitations. In this work we will discuss only the first two of them since they can be readily observed in graphene.
It is important to note that not all of the excitations that can exist in a given material can be detected using the Raman spectroscopy. In order to see them, an effective coupling between light and given excitation must exist. In case of phonons which are by large the most intensively studied excitations in solid state systems by the Raman spectroscopy, such coupling can be described in a semi-classical picture by changes in the system polarization. In that framework the incident monochromatic electro-magnetic wave $\mathbf{F}(\mathbf{r}, t) = \mathbf{F}(\mathbf{k}, \omega) cos(\mathbf{k} \cdot \mathbf{r} - \omega t)$ induces charge polarization $\mathbf{P}(\mathbf{r}, t) = \mathbf{P}(\mathbf{k}, \omega) cos(\mathbf{k} \cdot \mathbf{r} - \omega t)$

in the material. A relation between those two quantities

$$\mathbf{P}(\mathbf{r},t) = \chi(\mathbf{k},\omega,\mathbf{Q})\mathbf{F}(\mathbf{r},t) \tag{2.2}$$

is described by a second rank tensor known as electric susceptibility $\chi(\mathbf{k},\omega,\mathbf{Q})$. This tensor depends on the instantaneous lattice displacement $\mathbf{Q}$ which is described by a lattice vibration normal mode, i.e. a phonon:

$$\mathbf{Q}(\mathbf{r},t) = \mathbf{Q}(\mathbf{q},\omega_0)cos(\mathbf{q}\cdot\mathbf{r} - \omega_0 t)$$

To separate the static polarization effects which emerge from the χ described by atoms resting in equilibrium position χ_0 from those resulting from lattice vibrations, a Taylor expansion of electric susceptibility can be used:

$$\chi(\mathbf{k},\omega,\mathbf{Q}) = \chi_0(\mathbf{k},\omega) + (\partial\chi/\partial Q)_0\mathbf{Q}(\mathbf{r},t) + \frac{1}{2}(\partial^2\chi/\partial Q^2)_0\mathbf{Q}^2(\mathbf{r},t) + ...$$

So the resulting polarization $P(\mathbf{r},t,\mathbf{Q})$ yields terms proportional to the powers of lattice vibration $\mathbf{Q}(\mathbf{r},t)$. The zeroth order term describes the polarization that vibrates with the same frequency ω as the incoming electro-magnetic wave. The vibrating charge polarization becomes itself a source of radiation of the same frequency. Thus it is responsible for the Rayleigh scattering. The first order term however, proportional to $\partial\chi/\partial Q|_0\mathbf{Q}(\mathbf{r},t)$ oscillates with frequency $\omega - \omega_0$ and $\omega + \omega_0$. Thus it becomes a source of Stokes and anti-Stokes Raman peaks in the scattered spectrum. When light scattering analysis is limited only to this first order term, which is linear in lattice displacement, it is known as a dipole approximation. In that approximation all physics of interaction between light and crystal lattice is included in a quantity called a Raman tensor:

$$\mathbf{R} = \left.\frac{\partial\chi}{\partial Q}\right|_{Q=0}\frac{\mathbf{Q}}{|Q|} \tag{2.3}$$

That second order tensor is completely determined by the crystal lattice point group symmetry. *Loudon* tabulated those tensors for all 32 point groups [55]. Then it is possible to predict which phonons can participate in Raman scattering, since their symmetry must belong to the factor group of Raman tensor. If that is the case, the phonon is said to be *Raman active*, since it can be detected by Raman scattering. Moreover the intensity of a Raman peak corresponding to that phonon can be estimated for various experimental configurations of incident/scattered light direction and polarization. In that case one need only to contract Raman tensor $\mathbf{R}$ with unit vectors lying in the direction of incoming/scattered light polarization $\mathbf{\hat{e}_i}/\mathbf{\hat{e}_s}$:

$$I \sim |\mathbf{\hat{e}_i}\mathbf{R}\mathbf{\hat{e}_s}|^2$$

This leads to formulation of *selection rules* which describe which phonons are Raman active and in which experimental configuration they can be detected [56, 57].

The Raman tensor introduced above in a phenomenological way in a classical theory, appears also when a fully quantum mechanical treatment of Raman scattering problem is done [55, 58]. This approach highlights also one very important aspect of Raman scattering. Since direct coupling between light and atomic motion (phonons) is rather weak, the majority of Raman scattering intensity comes from a higher order term in the interaction described by the Hamiltonian $\hat{H}$. In the first step it involves interaction ($\hat{H}_{em-el}$) of electro-magnetic wave with the electronic subsystem of the crystal and creation of (virtual or real) electron-hole pair. In the next one the electron-hole pair interacts with the lattice through the electron-phonon interaction ($\hat{H}_{el-ph}$), which leads to the emission of phonon. Then the probability of such processes is calculated using the time-dependent perturbation theory, which gives the process matrix element:

$$\mathcal{M} \sim \sum_{s_0,\ldots,s_n} \frac{\langle i|\hat{H}_{em-el}|s_0\rangle\langle s_0|\hat{H}_{el-ph}|s_1\rangle\ldots\langle s_{n-1}|\hat{H}_{el-ph}|s_n\rangle\langle s_n|\hat{H}_{el-ph}|f\rangle}{(E_i - E_0 + 2i\gamma)(E_i - E_1 + 2i\gamma)\ldots(E_i - E_n + 2i\gamma)} \tag{2.4}$$

Here $|i\rangle$ denotes the initial state of the process i.e. one incident photon having energy E_i and no excitations in the crystal, $|f\rangle$ is the final state with one scattered photon and n phonons in the crystal. While s_k for $k = 0, ..., n$ stands for intermediate states with no photon present, but instead the electron-hole pair and k phonons that were created in the system. E_k are the energies of that intermediate states, while 2γ is the inverse carrier lifetime. Denominator of that matrix reveals that when the incident photon energy matches the energy of one of the intermediate states a resonance will be observed. This effect is indeed seen when the incident photon energy is tuned in resonance with the electronic bands of the system. In that case the virtual electron-hole intermediate state, becomes a real one and the divergence in denominator in Eq. 2.4 leads to the large increase in the observed Raman peaks. The resonant Raman scattering technique is based on this effect. Interestingly for graphene, due to its zero bandgap, for every energy of the incoming photon one can find a pair of states in the conduction and valence band that are separated by exactly this energy. Therefore independently on the used excitation wavelength, the two most intense phonon peaks in graphene originate always from the resonant Raman scattering processes (see Fig. 2.3a,e).

Finally we would like to stress that scattering from other elementary excitations than phonons is also possible, as long as the corresponding Raman scattering cross-section is non-zero. In Chapter 4 we introduce concept of Raman scattering on inter-Landau level excitons, while in Chapters 7 and 8 we present results of our magneto-Raman scattering experiments where such excitations were observed.

2.2 Main phonon peaks in graphene's Raman spectra

The Raman spectrum of graphene is very similar to that of bulk graphite, the major difference being the relative intensity of the two main peaks. So-called G-band appearing at ~ 1580 cm^{-1} and the 2D band at ~ 2700cm^{-1}, the latter one being also sometimes called a G′ band in the literature. From those two only the G-band results from a first order Raman scattering process, while 2D band together with other much less intense peaks appear as a result of higher order scattering processes. G-band is associated with the phonon from the highest optical phonon branch in the Γ point in the Brillouin zone. It is characterized by an E_{2g} symmetry and is doubly degenerate due to meeting of the in-plane longitudinal optical (iLO) and the in-plane transverse optical (iTO) branches at the Γ point. The energy dispersion of these branches around Γ point is determined by the electron-phonon interaction, resulting in the Kohn anomaly. This makes G-band energy sensitive to the Fermi energy, which is described in more details in Chapter 3.

The most intense Raman peak in graphene is the 2D band, which is seen around $\sim 2700\ \mathrm{cm}^{-1}$, but its exact energy depends on the used excitation laser energy. It originates from inter-valley scattering of carriers with phonons from iTO branch [60, 61] near the K point in Brillouin zone. In order to conserve momentum it requires scattering with two phonons having opposite momenta. However another process involving just one such phonon is also allowed, but then scattering with a defect, impurity or sample edge is needed to compensate the large momentum of the K point phonon [60, 61, 62]. Such scattering event leads to formation of a D-band at about half the energy of 2D band, which is seen only in defected samples or close to the sample edges (Fig. 2.2bottom). Both D-band and 2D band energy show dispersive behaviour, upshifting linearly with increasing excitation energy $E_{exc.}$. The former one at the slope of $\partial E_D/\partial E_{exc.} = 50\ \mathrm{cm}^{-1}$, while the latter one at about twice the speed of the D band i.e. $\partial E_{2D}/\partial E_{exc.} = 100\ \mathrm{cm}^{-1}$. This dispersive behavior is a hallmark of a double resonance process. In such case the energy of the photo-excited electron-hole pair determines the phonon wavevector q that participates in the scattering process, and since iTO phonon branch is strongly dispersive, it selects phonons with different energies. Another peculiar feature of D and 2D bands is that their energy slightly differ when observed in the Stokes and Anti-Stokes spectra. This in turn comes from the fact that phonon absorption and emission processes again select phonons with slightly different k-vectors, thus with slightly different energies.

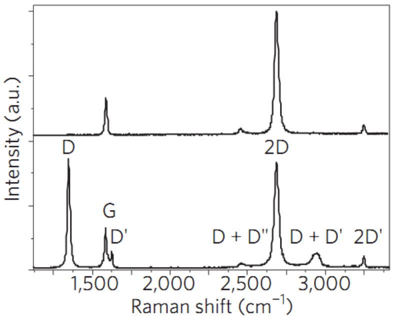

Figure 2.2: Raman spectra of pristine (top) and defected (bottom) graphene. From ref. [59]

Those effects were already observed in bulk graphite and in the past several models of the microscopic origin of D and 2D bands were proposed to explain them [65, 66, 67]. Finally the double resonance (DR) activation mechanism was proposed by *Thomsen and Reich* [62, 68] which proved to be most accurate and commonly accepted model. Raman scattering for Stokes process is shown schematically in Fig. 2.3d for the D band and in panel e) for 2D band. It consist of four steps among which at least two must be transitions between real electronic states. In the first one, an electron-hole creation occurs. While energy and wavevector of each quasi-particle $E_{e/h}$ are determined by the energy of the incoming laser radiation E_{laser}:

$$E_{e/h} = \frac{E_{laser}}{2}$$
$$|k_{e/h}| = \frac{E_{laser}}{2\hbar v_F}$$

The next step involves inter-valley scattering of one of the created quasi-particles with emission of phonon with wavevector $\vec{q} = \vec{K} + \vec{k'}$ ($\vec{k'}$ being small). The last two steps phonon is scattered back and recombines, exchanging in the process momentum $-\vec{q}$ with the environment. This process is realized differently for the D and 2D bands. In the

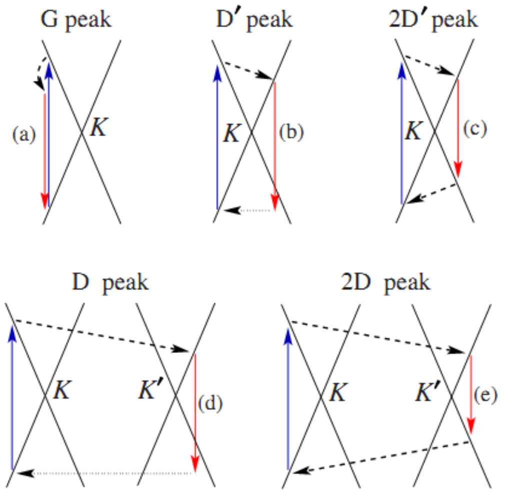

Figure 2.3: Role of the electron dispersion (Dirac cones, $\epsilon = \pm v_F|\mathbf{p}|$, shown by solid black lines) in Raman scattering: (a) intravalley one-phonon G peak, (b) defect-assisted intravalley one-phonon D' peak, (c) intravalley two-phonon 2D' peak, (d) defect-assisted intervalley one-phonon D peak, and (e) intervalley two-phonon 2D peak. Vertical solid arrows represent interband transitions accompanied by photon absorption (upward arrows) or emission (downward arrows). The photon wave vector is neglected. Dashed arrows represent phonon emission. Horizontal dotted arrows represent defect scattering. From ref. [63]

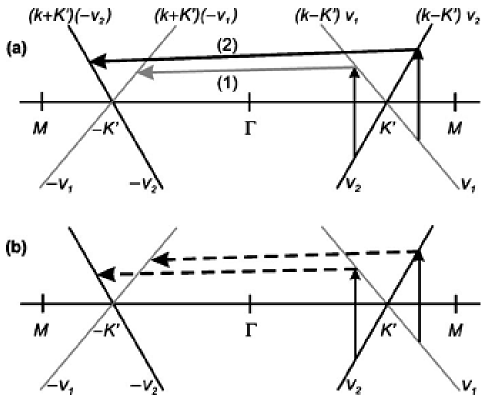

Figure 2.4: Double resonant scattering processes leading to D band in graphene/graphite. The electronic bands are assumed to be linear at K point with Fermi velocities v_1 and v_2. a) allowed processes, where scattering takes place across the Γ point within the same electronic band(opposite sign of the slopes), b) forbidden processes due to negative interferences between different bands (almost the same slopes). From ref. [64]

former case the carrier is first inelastically scattered by a defect which absorbs the additional momentum of scattered carrier, then electron and hole recombine. It means that existence of a defect, impurity or a sample edge close to the measured spot is a necessary condition to observe D band.

For the case of 2D band, another DR scattering process occurs with emission of phonon having wavevector $-\vec{q}$, followed by a recombination. So globally, momentum is conserved due to emission of two phonons with opposing momenta during the whole scattering process. This means that 2D band can be always observed in graphene, independently of its structure, existence of defects or sample edges.

It naturally follows from this model that, changing the excitations wavelength will select phonons with different wavevectors to meet the DR condition. Since iTO phonon branch is strongly dispersive in the $\Gamma - K$ direction, this leads to selection of phonons with different energies, and thus to the dispersive behaviour of 2D peak.

In principle in the DR process many different initial electronic states and phonons possessing different symmetries and wavevectors from the vicinity of the K point can satisfy the DR condition. However, due to: a) the existence of singularities in the density of phonon states which satisfy the DR condition, b) the angular dependence of the electron-phonon scattering matrix elements, and c) the destructive interference effects when the Raman transition probability is calculated, only a few specific DR processes contribute strongly to the Raman D and 2D bands [64]. So in order to calculate the correct Raman spectrum a full integration of the Raman cross-section has to be performed. However those calculations give a simple rule of a thumb for qualitative analysis of effects emerging from the DR conditions. They showed that destructive interference leads to cancellation of terms which involve scattering between bands having the same slope (Fig. 2.4b). So when one uses DR model in a simplified one-dimensional picture, to explain effects of D and 2D bands only transitions between bands of opposite slopes should be considered Fig. 2.4a) [64].

Inter-valley scattering processes described above can also occur between electronic states belonging to the same Dirac cone around K or K' point. In such case iTO phonons with small $\mathbf{q}$ wavevectors, coming from the vicinity of Γ point are involved in the scattering process. Those intra-valley modes are called D' and 2D' in analogy of the D and 2D inter-valley scattering processes (see Fig. 2.3b,c). However due to the higher energy of iTO phonon branch at Γ than in K point energies of D' and 2D' bands are higher than those of D and 2D bands. For instance, when using the 514 nm excitation D' mode and is observed at about 1620 cm^{-1}, while D band at 1360 cm^{-1}. Those intra-valley scattering processes share many similarities with previously discussed inter-valley scattering modes. One of them being the dispersive behavior with excitation wavelength. The other that D' mode is seen only in defected samples, while 2D' can be observed even in high quality samples due to emission of two phonons with opposite momenta. Those similarities come from the fact that the activation mechanism for those phonons is the same as for D and 2D bands, namely the DR condition. The differences come from the fact that now phonons selected in DR process must have rather small wavevector to allow scattering inside a single Dirac cone. Thus they come from the vicinity of Γ point. However since electron-phonon coupling is not the same for phonons from the vicinity of Γ and K point, the relative intensities of 2D and 2D' peaks is not the same. In fact experimentally determined ratio of the areas below those peaks $A(2D)/A(2D')$, which is proportional to the scattering probability ratio is about 25-30. Those probabilities can be calculated theoretically [63], which yields:

$$\frac{A(2D)}{A(2D')} = 2\left(\frac{\lambda_K}{\lambda_\Gamma}\right)^2$$

where λ_Γ and λ_K are the dimensionless electron-phonon coupling constants, as defined in Chapter 3, for phonons from the Γ and K points respectively. This expression shows that, apart from the factor of two, the main cause of the observed difference in the inter- and intra-valley scattering process lies in the largely higher value of el.-phon. coupling constant at K point.

2.3 Number of layers

One of the biggest advantages of using Raman spectroscopy in the studies of graphene based materials is that it allows a quick determination of the number of graphene layers. *Ferrari et al.* [69] have shown that there is a huge change in the shape of 2D band when going from bulk graphite to monolayer graphene. In Bernal stacked bulk graphite it is G peak at ∼1580 cm^{-1} that is the most intense Raman feature, followed by 2D band, composed of two components: $2D_1$ and $2D_2$. Their height being approximately $1/4$ and $1/2$ of the G peak intensity, respectively. For monolayer graphene however the situation is different, 2D band is single peaked and few times higher than G peak (Fig. 2.5left). This difference in shape and relative intensity of the 2D band is so pronounced that it serves now as a quick tool for distinguishing monolayer graphene from Bernal stacked bulk graphite. In fact for each few-layer Bernal stacked graphene 2D band has a characteristic well defined shape. Fig. 2.5 right) shows how it changes from single component peak for a monolayer, through four component peak for bi-layer, and evolving toward two component peak for bulk graphite. In practice the shape of 2D band can be used for a determination of the number of layers for multi-layer graphene systems up to the thickness of 3-4 monolayers.

For thicker samples it is difficult to distinguish their response from that of a bulk graphite. This strong dependence of 2D band shape on the number of atomic layers is closely related to the origin of 2D band as doubly resonant scattering process, which links the phonon dispersion with the electronic bandstructure. The latter one changing significantly when the number of layers increases in multi-layer graphene.

As we recall adding one more layer to the multi-layer graphene structure results in adding one more conduction and one more valence band to the already existing one [37].

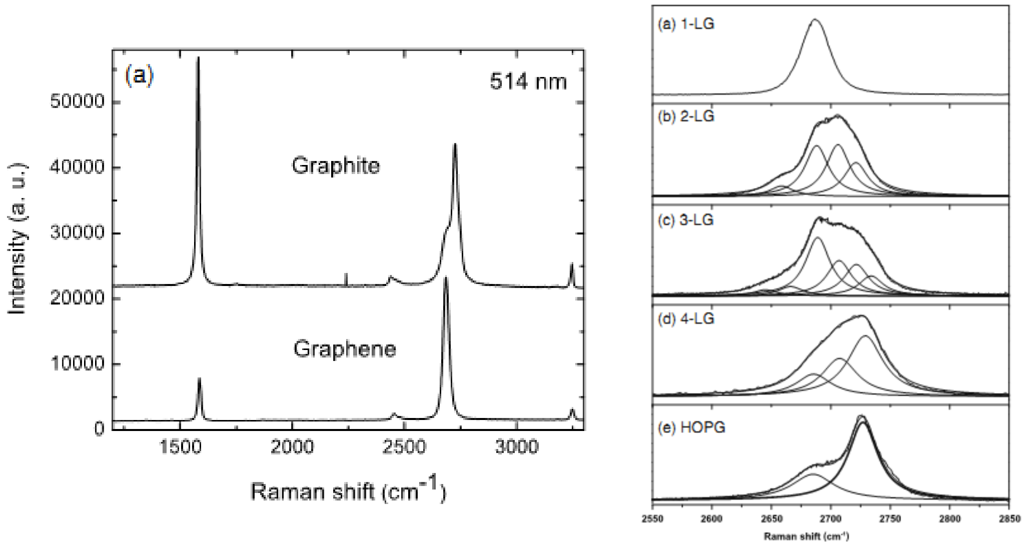

Figure 2.5: Left: Raman spectra of graphite and graphene deposited on Si/SiO_2. They are rescaled to have similar intensities of 2D peaks at ∼2700cm^{-1}. From ref. [69]. Right: Raman spectra of HOPG graphite and a set of few-layer graphenes varying in thickness, deposited on Si/SiO_2. Black solid lines show Lorentzian fits to the measured data. From ref. [70].

This increases the number of possible scattering events. It is illustrated in Fig. 2.6b), where scattering between two different initial and two final states can occur in a bi-layer graphene. In contrast with the case of mono-layer graphene where only one initial and final state is allowed by a DR condition. Or to be more precise just one set of scattering processes in full two-dimensional picture, as opposed to four different sets of allowed scattering processes in bi-layer. Of course not all of those scattering events have the same probability which is reflected in different areas of those peaks. For instance in bi-layer graphene two components of the 2D band Raman peak are much more intense than the other two [69]. However all of them occurs in an energy range which is comparable with twice the linewidth of a single component. Which results in merging of those peaks as their number increases with the growing thickness of the sample. Already for multi-layer graphene samples composed of 10 atomic layers, the Raman signature of 2D band is closely resembles that of a bulk graphite [23].

2.4 Stacking order and twisted multi-layers

The DR nature of the 2D band makes it a sensitive tool for studying changes in the electronic bandstructure. This is because even small changes in the carrier dispersion alter the resonance condition and thus select phonons with a slightly different energy, what is reflected in the shape and position of the 2D Raman peak. There is a class of multilayer graphene systems, often referred to as turbostratic graphene, where the consecutive layers orientation differ from the Bernal (AB) or rombohedral (ABC) stacking, in fact the direction of their in-plane lattice vectors can be misaligned by an arbitrary twist angle. Theoretical calculations of electronic bandstructure of such non-ideal multilayer graphene have shown that even small twist angle between adjacent layers significantly reduce the interlayer coupling [71, 72].

This has a paramount effect on the electronic dispersion, and for instance twisted graphene bilayer shows two Dirac cones instead of two parabolic conduction bands for the Bernal stacked bilayer (Fig. 2.7). This change is seen both in electrical [73, 74] and optical [75] experiments. This necessarily affects the DR conditions and as a result 2D band in turbostratic bilayer graphene shows a single component Lorentzian shape [76, 77]. Its peak is broader, having FWHM=45-60 cm^{-1} as compared to FWHM≈15 cm^{-1} of monolayer graphene. Also the relative intensity of the 2D peak to that of the G-band I_{2D}/I_G is much smaller for

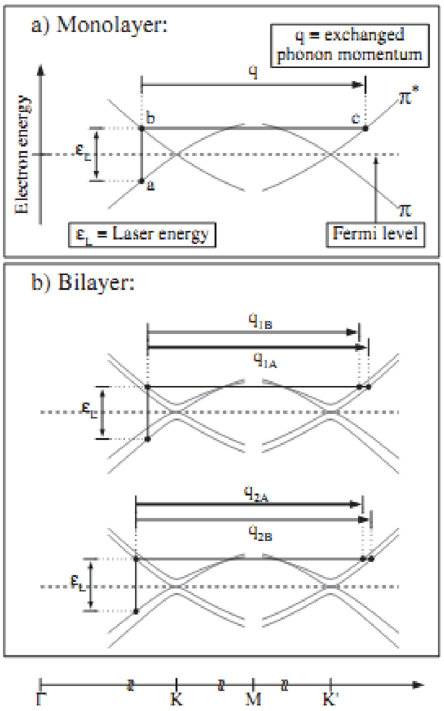

Figure 2.6: Double resonance scattering process with phonons having momentum q close to K. a) for a monolayer graphene, b) for a bilayer graphene. From ref. [69]

turbostratic graphene and its position is shifted toward higher energy from that of monolayer graphene.

In fact even graphite or multi-layer graphene with a regular stacking order which differs from the most common (AB...) Bernal stacking shows much different electronic dispersion spectrum [78, 79]. Examples of such ordering include simple hexagonal (AAA...), rombohedral (ABC...) and (ABA...) stacked graphene multi-layers. This obviously affects Raman spectra, making it more difficult to establish unambiguously number of atomic layers in the sample by looking on the shape and position of 2D band alone.

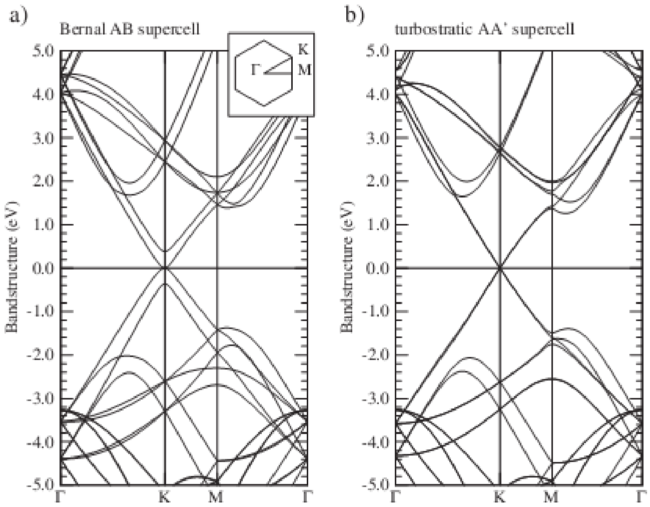

Figure 2.7: Electronic bandstructure of a) Bernal (AB) and b) turbostratic AA' stacked bilayer graphene. From ref. [71]

2.5 Strain

One of the intense research topic in the field of graphene is related to understanding how does the strain affect its properties. This aspect is particularly important for the optical properties of graphene, because it is expected that applying external stress may open an electronic gap in monolayer samples. Since for many applications in semiconductor industry existence of energy gap is essential, the gap-less bandstructure of graphene is a serious factor limiting its possible applications. Calculations show that monolayer graphene is quite robust against applying an uniaxial strain. It would require a deformation exceeding 20% to open energy gap [80], which is close to the limit of elastic deformation [81] that it can still sustain without breaking. However it was calculated [82] that for a specifically designed type of stress with a triangular symmetry it is possible to open a gap as large as 0.1 eV for stress less than 10%. Another interesting result of applying strain is that it shifts Dirac cones at K and K' points into opposite direction. This is analogous to the effect induced on charge carriers by external magnetic field $\mathbf{B}$ applied perpendicular to the graphene plane. Therefore applying a strain to graphene has he same effect as if there would be a built-in pseudo-magnetic field $\mathbf{B}_S$. This pseudo-magnetic field however, has a highly anisotropic distribution over the hexagonal lattice of graphene. So the resulting field averages over macroscopic distances, but gives non-zero contribution on sub-micron scale. *Guinea et al.* [83] have calculated that strain caused by height fluctuations (ripples) of graphene is large enough to induce such pseudo-magnetic field. This tends for instance to broaden the observed Landau levels in the real magnetic field **B**.

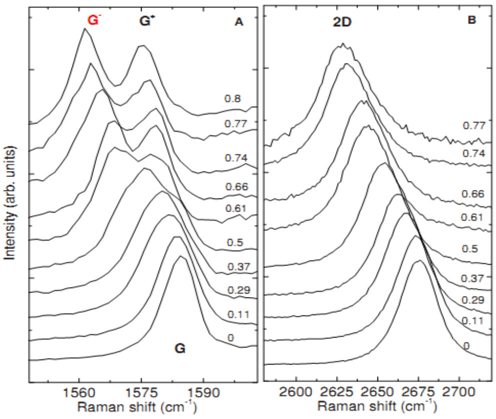

Figure 2.8: Raman features: a) G band and b) 2D band of monolayer graphene as a function of applied uniaxial strain. Laser excitation wavelength λ =514 nm. Incident light is polarized along the strain direction, scattered light collected with no analyzer. Applied strain is indicated on the right hand side of the spectra. From ref. [84]

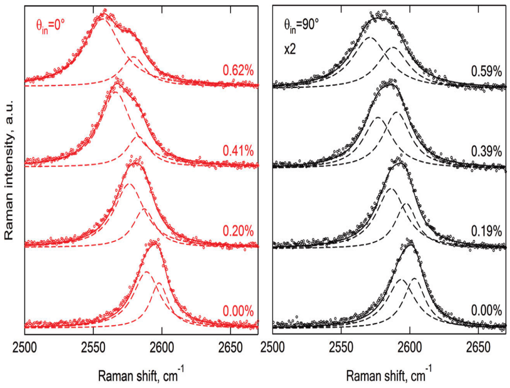

Figure 2.9: Polarization resolved 2D band Raman spectra of monolayer graphene as a function of applied uniaxial strain. Laser excitation wavelength λ =785 nm. The spectra in the left and right panels were acquired with laser polarization parallel (θ_{in} = 0°) and perpendicular (θ_{in} = 90°), respectively, with respect to the strain axis. From ref. [85]

Another consequence of applying strain to the graphene sheet is shifting and splitting of the G and 2D bands. Fig. 2.8a shows how a doubly degenerated phonon with E_{2g} symmetry shifts towards lower energies and splits into two components G^- and G^+. This splitting being a reminiscent of what is observed in carbon nanotubes, where curvature induced strain also lifts the double degeneracy of E_{2g} phonon. *Mohiuddin et al.* have performed Raman scattering experiment on uniaxially strained graphene sample, using λ=514 nm laser source. They reported shifts of G^-, G^+ and 2D peaks being $\frac{\partial \omega_{G+}}{\partial \epsilon} \approx -10.8\,\mathrm{cm}^{-1}$, $\frac{\partial \omega_{G-}}{\partial \epsilon} \approx -31.7\,\mathrm{cm}^{-1}$ and $\frac{\partial \omega_{2D}}{\partial \epsilon} \approx -64\,\mathrm{cm}^{-1}$ respectively. In their experiment there is no evident signature of 2D band splitting, except for small asymmetry in the shape of 2D band, which seems to grow with applied stress (Fig. 2.8b). Contrary to that *Frank et al.* [85] have reported a significant splitting of the 2D band (Fig. 2.9) when using red illumination λ=785 nm. Both components having nearly linear strain dependence, with slope of -46.8 cm^{-1} and -23.6 cm^{-1} for the low and high energy peak, respectively. Interestingly, they also showed that 2D band subpeaks intensities exhibit a strong dependence on the incident and scattered light polarization. The different behavior of 2D band under red and green light illumination is explained in terms of contribution of two groups of phonons to the 2D peak. Both of them being from the vicinity of K point, but one laying on the $\Gamma - K$ line, and the other along the $K - M$ direction. Because effects of trigonal warping of Dirac cones increase with increasing energy, when high energy laser source is used, like for instance λ=514 nm, those effects effectively select one of those

phonons over the other, leading to a single component 2D peak formation.
Those results show clearly that strain in graphene can significantly change shape and position of the 2D band, thus again obscuring the simple picture where it could be used to unambiguously determine number of atomic layers in multilayer graphene.

2.6 Doping

One of the problems which is haunting research of exfoliated graphene is the unintentional doping. The most commonly used substrate for graphene is monocrystalline silicon covered with a thin (90-300nm) layer of silicon dioxide. Its surface however is neither atomically flat nor electrically neutral. The main sources of charges are impurity atoms adsorbed on the rough silicon surface, as well as dangling bonds at silicon surface. When exfoliated graphene is being deposited on top of them, they become a source of doping. Therefore, it is prudent to briefly comment how doping can affect Raman spectra of graphene.
An experiment performed by *Das et al.*, in which the Fermi level in a monolayer graphene was controlled by application of bias voltage, allowed to monitor how charge doping affects the Raman spectra [86]. Their work showed that both G-band and 2D band shapes and positions depends on the doping level, however changes were much more pronounced for G-band (Fig. 2.10). It was found that doping can shift G-band towards higher energy even by 20 cm^{-1}, independently on the sign of charge carriers. This high sensitivity of Γ point phonon to the Fermi level position is a direct effect of non-adiabatic lifting of the Kohn anomaly at the Γ point. This is discussed in Chapter 3, devoted to electron-phonon

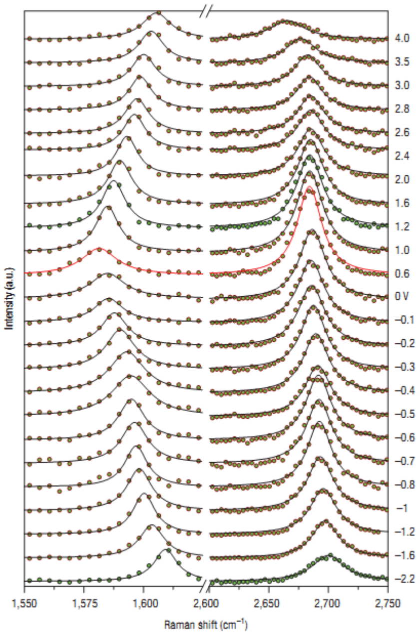

Figure 2.10: Raman spectra of graphite and graphene as a function of gate voltage. Dots are the experimental points, solid lines are the Lorentzian fits. Red curve corresponds to Dirac point. Positive (negative) gate voltage corresponds to electron (hole) doping. From ref. [86]

interaction in graphene.

On the other hand the evolution of the 2D band is less pronounced. For hole doping it slightly shifts toward higher energy, but for electron doping it stays constant up to the doping level of about $\sim 3 \times 10^{13}$ cm^{-1} and then rapidly shifts toward lower energy. In both cases loosing much of its intensity. Thus for large doping levels it shape and position can be used to deduce the sign of charge dopants.

In principle, the doping dependence of phonon frequencies in graphene is a result of two effects: (i) a change of the equilibrium lattice parameter, which stiffens/softens phonon frequency (ii) effects beyond the adiabatic Born-Oppenheimer approximation which affects phonon dispersion close to the Kohn anomalies. Although for G band the latter is a dominant factor influencing its doping dependence, for 2D band it is the opposite. When Raman scattering experiments are performed with a laser wavelength $\lambda = 514$ nm, which corresponds to photon energy of $\hbar\omega_l = 2.5$ eV, then DR condition of 2D band scattering selects phonons laying along $\Gamma - K$ direction with wavevector $|\vec{q}| = 0.844$ in $2\pi/a_0$ units. This means that involved phonons are too far away from the K point to be influenced by the Kohn anomaly. In this case the lattice expansion/contraction effects prevails.

In summary we would like to note that the position and the shape of G and 2D peaks observed in graphite, graphene and multilayer graphene carry plenty of information about the number of atomic layers, structural ordering, strain and doping present in the system. Although a single Lorentzian shape of 2D peak is nowadays commonly accepted as a signature of monolayer graphene, its worth to remember that it is in fact a signature of very weak interlayer coupling or even absence of that coupling. So under specific conditions some multi-layer graphene systems may give a Raman response very similar to that of a true monolayer graphene. Therefore identification of graphene monolayers based on their Raman spectrum can be applied only to the systems which we know that are Bernal stacked, without significant strain or doping.

Chapter 3

Electron-phonon interaction

Studies of effects related to electron-phonon interaction form a very important branch of research on graphene properties. Plenty of physical phenomena observed in graphene and closely-related carbon nanotubes depend on the electron-phonon coupling (EPC), some of them include: ballistic transport, superconductivity, excited state dynamics, Raman spectra and phonon dispersions. In nanotubes, the optical phonons EPC are very important since electron scattering by optical phonons sets the ultimate limit to the charge mobility [87, 88, 89, 90, 91], which determines whether ballistic transport regime can be obtained or not. Up to now the key factors limiting the carriers mobility is scattering of charge carriers due to the presence of impurities atoms and structural defects in the sample, as well as nanometer-scale roughness of the sample substrate and the electric field potential of unsaturated dangling bonds from the substrate – usually crystalline Si covered with few hundreds nm thick SiO_2 layer. As the quality of graphene samples improves with the progress in manufacturing techniques, and new types of substrates are investigated (suspended samples [92], hBN [93, 94, 95], bulk graphite [96, 13, 44]), the role of the before-mentioned factors will slowly diminish. On the other hand, scattering of carriers due to electron-phonon interactions is an intrinsic property, that will remain to limit the maximum possible charge mobility even in the case of a perfect crystal. Therefore, the proper understanding of the existing coupling mechanism between electronic and vibrational subsystems is of paramount importance if some predictions about the limits of the future applications of graphene are to be made.

3.1 Phonon dispersion in graphene

At every finite temperature, the position of the atoms in the crystal is not fixed but instead they oscillate slightly around their equilibrium positions. This quite complex collective vibrations of the atoms can be easily described by decomposing it into few elementary vibrations propagating through the crystal. Each of those vibrational modes is characterized by a particular relative movement of the atoms in the crystal unit cell and by a wave-vector describing its direction of propagation. In the quantum mechanical formalism, the energy of these vibrational normal modes becomes a quantized, and the single quantum of such vibration is known as a phonon. Each one is described by its wavevector $\mathbf{k}$ (which is proportional to its pseudo momentum $\hbar\mathbf{k}$) and also by its transformations symmetries (which determines to which phonon branch it belongs). In every crystal with N atoms in the unit cell there is a maximum of 3N different phonon modes, three of them are acoustic (A) modes and $3(N-1)$ are optical (O) modes. Those phonons can be further divided into longitudinal (L) and transverse (T) modes depending whether atoms displacement is in the same or in a perpendicular direction with respect to the direction of propagation, respectively. One can also distinguish between transverse modes which oscillate in the graphene plane(i-) or in the direction pointing out-of plane(o-).

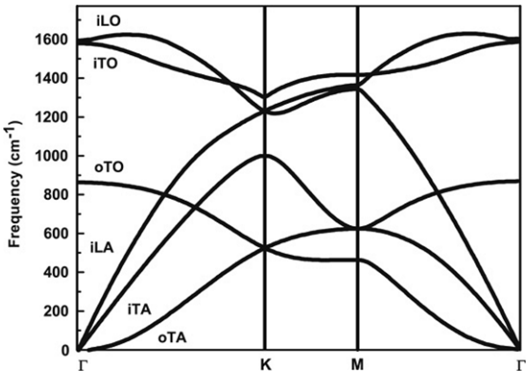

Figure 3.1: Phonon dispersion in graphene. From ref. [70] after [97]

The two atoms in the graphene unit cell give rise to the three acoustic and three optical branches in phonon dispersion relations. *Lazzeri et al.* have calculated the dispersion of these modes [97] using DFT technique, which is shown in Fig. 3.1. At high symmetry points phonons can be classified according to their transformation symmetries. From the viewpoint of Raman spectroscopy the most important points in the Brillouin zone are Γ and K points, because phonons from the vicinity of those points form the most prominent Raman peaks both in graphene and graphite. At the Γ point phonons transform accordingly to the representations of the D_{6h} point group. Since two phonon modes are there doubly degenerated it leaves just four distinct phonon modes with the symmetries $A_{2u} + B_{2g} + E_{1u} + E_{2g}$ [68]. There is one doubly degenerate in-plane optical mode – E_{2g} at $\sim$ 1580 cm^{-1}, and one out-of-plane optical mode B_{2g} at $\sim$ 850 cm^{-1}. Only the E_{2g} phonons are Raman active, while the B_{2g} optical phonon is neither Raman nor infrared active [98].

The phonon modes around the K point are also very important, since the D band and 2D band are related to phonon modes in the vicinity of the K point. At the K point phonon modes belong to one of the irreducible representations of the D_{3h} point group. The phonon which comes from the iTO branch is non-degenerate, belongs to the A_1' irreducible representation and has an energy of about $\sim$ 1350cm^{-1}. The LO and LA phonon branches meet each other at the K point, which gives rise to a doubly degenerate phonon, with E' symmetry [99].

Phonon dispersions in bi-layer graphene and graphite are qualitatively similar to that of monolayer graphene. The main difference stems from the fact that, in the former case, there are four atoms in the unit cell. This doubles the number of optical modes, and is responsible for the infrared activity of graphite [98]. In graphite all the optical modes

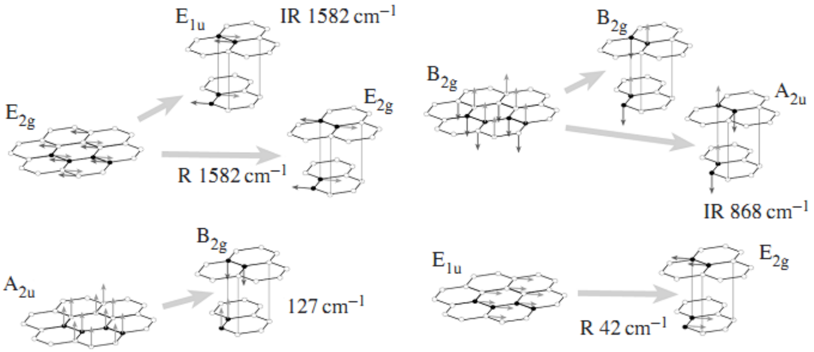

Figure 3.2: Displacement of atoms in graphene and graphite for the phonons from the Γ point. Every phonon eigenvector of graphene gives transforms into two distinct vibrations in graphite. Next to the graphite modes is indicated whether they are Raman (R) or infrared (IR) active and the experimentally observed phonon frequencies. From ref. [68].

become Davydov-doublets, which is shown in Fig. 3.2. For instance, the E_{2g} phonon in graphene splits into an infrared-active E_{1u} phonon and a Raman-active E_{2g} phonons in graphite, the B_{2g} optical phonon goes into an infrared-active A_{2u} phonon and an inactive B_{2g} phonon. Additionally, antisymmetric combinations of the acoustic modes becomes the optically inactive B_{2g} phonons and the low-frequency Raman active E_{2g} modes. The symmetric combinations of the acoustic modes remain A_{2u} and E_{1u} [98]. Therefore in graphite at the Γ point phonons belong to one of the following irreducible representations: $\Gamma = 2(A_{2u} + B_{2g} + E_{1u} + E_{2g})$ [59, 70].

The main difficulty in the calculations of the phonon dispersion in graphene and graphite lies in the correct treatment of the Kohn anomalies that occur at Γ and K points. For a long time the various proposed models [67, 100, 101, 99, 102] were not able to correctly describe the linear phonon dispersion around Γ and K points until *Piscanec et al.* included the Kohn anomaly in their DFT calculations [103]. This anomaly leads to a renormalization of phonon energies due to processes when phonon excites virtual electron-hole pairs. To correctly understand the origin of these processes one has to go beyond the framework of the usually employed Born-Oppenheimer approximation and include the electron-phonon coupling mechanisms.

3.2 Electron-phonon coupling constant

Generally, one can distinguish two main mechanisms responsible for the electron-phonon interaction in a crystal: the Frölich interaction and the deformation potential interaction. The former one is only present in polar crystals, which can exhibit a macroscopic electric field generated by long-wavelength optical phonons. Graphene however, as well as other materials derived from graphite, is a non-polar material, so it is the deformation potential that is responsible for the electron-phonon coupling. In this mechanism the coupling between electronic subsystem and lattice vibrations occurs due to small changes in the potential energy ΔV felt by electrons due to distortion of atoms from their equilibrium positions [104]. The electron-phonon coupling matrix element describes the scattering probability of an electron in band i and with momentum $\mathbf{k}$ to the empty state in band j with momentum $\mathbf{k}+\mathbf{q}$ due to interaction with a phonon with wavevector $\mathbf{q}$ [105, 103]:

$$D_{(\mathbf{k}+\mathbf{q})j,\mathbf{k}i} = \langle \mathbf{k}+\mathbf{q}, j|\Delta V_{\mathbf{q}}|\mathbf{k}, i\rangle \tag{3.1}$$

Where the $\Delta V_{\mathbf{q}}$ is the change in the periodic potential induced by a phonon with wavevector $\mathbf{q}$. Although EPC matrix elements are defined for each electron and phonon separately like above, the only quantities which are observable experimentally are the averages over the Fermi surfaces (denoted as $\langle ...\rangle_F$) of the squares of matrix elements. Due to symmetry reasons, most of the scattering events occur with phonons from the high symmetry lines in Brillouin zone. It turns out that the only non-zero EPC constants are those which describe scattering by phonons from the doubly degenerated highest optical mode at the Γ point, and by phonons from transverse optical (TO) branch at K point [105, 103]:

$$\langle D_\Gamma^2\rangle_F = \sum_{i,j} \frac{1}{4}|D_{\mathbf{K}j,\mathbf{K}i}|^2 \qquad \text{and} \qquad \langle D_K^2\rangle_F = \sum_{i,j} \frac{1}{4}|D_{\mathbf{K}'j,\mathbf{K}i}|^2 \tag{3.2}$$

EPC can be also defined in other ways the one most commonly used is the dimensionless EPC constant λ, which is defined for phonons from the Γ and K points as:

$$\lambda_{\Gamma,K} = \frac{F_{\Gamma,K}^2 A_{u.c}}{2M\omega_{\Gamma,K} v_F} \tag{3.3}$$

Where $\omega_\Gamma(\omega_K)$ is the energy of phonons from the $\Gamma(K)$ point respectively, M is the mass of the carbon atom, $A_{u.c.}$ the unit cell area, while $F_\Gamma(F_K)$ is the proportionality coefficient between the change in the effective Hamiltonian and the lattice displacement along the corresponding phonon mode. There is a close correspondence between those two definitions, which comes from the following relations [63]:

$$F_\Gamma^2 = 4\langle D_\Gamma^2\rangle_F = 8M\omega_\Gamma\langle g_\Gamma^2\rangle_F \tag{3.4}$$
$$F_K^2 = 2\langle D_K^2\rangle_F = 4M\omega_K\langle g_K^2\rangle_F \tag{3.5}$$

There are also other definitions of the EPC constant in use and the choice is usually determined by the method used to extract this parameter. When calculations are made using the density functional theory (DFT), EPC is usually defined as the matrix element of the Kohn-Sham potential, differentiated with respect to phonon displacement, like in Eq. 3.2 [107, 103, 97, 115]. In ARPES experiments EPC is extracted from the differences in the slope of the electron dispersion around energies corresponding to the two phonons [114]. In the Raman scattering experiments, where the Fermi energy ϵ_F is tuned by the gate voltage, the EPC leads to a dependence of the G-band energy on the ϵ_F. The corresponding shifts in the G-band energy can also be used to extract information about EPC constant [107, 106, 116, 117]. One of the simplest ways to estimate the EPC value is to measure the linewidth of the Raman scattering features associated with a given phonon. In graphene there is only one peak in the Raman scattering spectrum originating from a first order scattering process with a phonon – the G-band. Therefore EPC coupling can be estimated for the E_{2g} phonon branch at Γ point. In a crystal without any defects, the

$\lambda[\times 10^{-2}]$	System	Method	Source
Γ point phonon			
2.8	monolayer graphene	DFT calculations	[103]
3.4	exfoliated graphene on SiO_2	G-band linewidth	[106]
2.6	exfoliated graphene on SiO_2	G-band energy shift	[106]
2.7	exfoliated graphene on SiO_2	G-band linewidth	[107]
4.5	multilayer epitaxial graphene	Fit to MPR	[108]
2.6	graphite	X-ray diffraction	[105] based on [99]
3.1	graphite	G-band linewidth	[105]
6.4	graphene flakes on graphite	Fit to MPR	[109]
3.2	graphite	Fit to MPR	[45]
4.4	graphene flakes on graphite	Fit to MPR	[32]
K point phonon			
3.4	monolayer graphene	DFT calculations	[103]
6.0-12.0	mono- and bilayer exfoliated graphene	Fits done by *Basko et al.* to the experimental G and 2D peaks area ratio	[63] based on [86, 110, 69, 92, 111]
5.4	monolayer graphene	GW calculations	[63] based on [97, 112]
4.4	graphite	phonon dispersion slope at K point measured in inelastic x-ray scattering	[63] based on [113, 114]

Table 3.1: Values of EPC constants in graphene based materials as obtained by different groups.

linewidth γ of a phonon is determined by its interaction with other elementary excitations. Usually $\gamma = \gamma^{e-h} + \gamma^{an}$, where γ^{an} is a broadening due to the interaction with other phonons and γ^{e-h} with electron-hole pairs. γ^{an} is determined by anharmonic terms in the interatomic potential and is always there. γ^{e-h} is determined by the EPC and is present only if the electronic gap is zero. If the anharmonic contribution γ^{an} is negligible or otherwise known, measuring the linewidth is a simple way to determine the EPC. A broadening due to phonon from branch η and with wavevector $\mathbf{q}$ interacting with an electron-hole pairs is given by the Fermi golden rule [105]:

$$\gamma^{e-h}_{\mathbf{q}\eta} = \frac{4\pi}{N_k} \sum_{\mathbf{k},i,j} |g_{(\mathbf{k}+\mathbf{q})j,\mathbf{k}i}|^2 \left[f_{\mathbf{k}i} - f_{(\mathbf{k}+\mathbf{q})j}\right] \delta\left[\epsilon_{\mathbf{k}i} - \epsilon_{(\mathbf{k}+\mathbf{q})j} + \hbar\omega_{\mathbf{q}\eta}\right] \tag{3.6}$$

where the sum is over the electrons with wavevectors $\mathbf{k}$ and bands i and j, N_k is the number of $\mathbf{k}$ vectors, $f_{\mathbf{k}i}$ is the occupation of the electron state $|k, i\rangle$, with energy $\epsilon_{\mathbf{k}i}$, δ is the Dirac distribution and $g_{(\mathbf{k}+\mathbf{q})j,\mathbf{k}i}$ is the EPC constant as defined in Eq. 3.5. For phonons from the Γ point which give rise to the G band, calculating the above sum yields:

$$\gamma^{e-h}_{\mathbf{\Gamma}} = \frac{\sqrt{3}a_0^2\hbar^2}{4M(v_F\hbar)^2}\langle D^2_\Gamma\rangle_F \tag{3.7}$$

By measuring the G band linewidth and treating the anharmonic term γ^{an} as small campared with broadening induced by EPC the above expression allows to estimate the EPC constant.

The diverse definitions of EPC constant brought the need to relate them to each other in order to be able to compare results obtained using different methods. This was done by *Basko et al.* [63] and allowed to get an overall estimation of the EPC constants for phonons from the Γ and K points and the accuracy up to which they are currently known, which is summarized in Table 3.1.

As it is seen from the table, there is still some uncertainty about the exact values of the EPC constants, however for the Γ point phonon it can be quite reliably assumed to fall into the range $3 \times 10^{-2} < \lambda < 4.5 \times 10^{-2}$. On the other hand there are fewer measurements of the EPC for the K point phonons, but both theoretical calculations and experimental results shows that its value is higher than for Γ point phonons.

3.3 Kohn anomalies

The characteristic feature of graphene is its zero gap band structure, which causes graphene to behave like a semimetal. In general, the atomic vibrations are partially screened by electrons. In metals and semimetals this screening can change rapidly for vibrations associated with certain wavevectors $\mathbf{q}$ in the Brillouin zone, which are determined by the shape of the Fermi surface. This leads to the renormalization of phonon energies at these particular points in the Brillouin zone. The resulting anomalous behavior of the phonon dispersion is called Kohn anomaly [118]. The Kohn anomalies may occur only for phonons with such a wavevector $\mathbf{q}$ and energy $\hbar\omega(q)$ that there are two electronic states $\mathbf{k_1}$ and $\mathbf{k_2}$ on the Fermi surface ϵ_F that can be connected by a scattering with this phonon:

$$\mathbf{k_2} = \mathbf{k_1} \pm \mathbf{q} \tag{3.8}$$

In graphene, the electronic gap is zero only at the two inequivalent points in Brillouin zone: K and K'. Therefore, scattering of carriers from the Fermi surface can only occur either in an intra-valley scattering process, i.e. when both initial and final electronic state lies in the vicinity of the same valley (at K or K' point) or it can also occur in the inter-valley scattering process, i.e. when carrier is scattered from the vicinity of the $K(K')$ point to the proximity of the $K'(K)$ point. In the intravalley scattering process, only phonons with a very small wavevector $\mathbf{q}$ can participate, i.e. those from the vicinity of Γ point. On the other hand for an intervalley scattering phonons with a large wavevector are needed: $\mathbf{K'} \pm \mathbf{K} = \mathbf{K}$. Thus, Kohn anomalies can be found in the phonon dispersion relations only at the Γ and K points in the Brillouin zone.

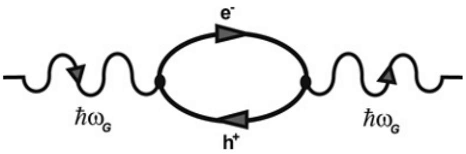

Figure 3.3: Feynman diagram for the second-order scattering process that renormalizes the phonon energy. The first node shows the decay of a phonon into an electron-hole pair, and the second node shows the recombination of the electron and hole resulting in the emission of a phonon. From ref. [70]

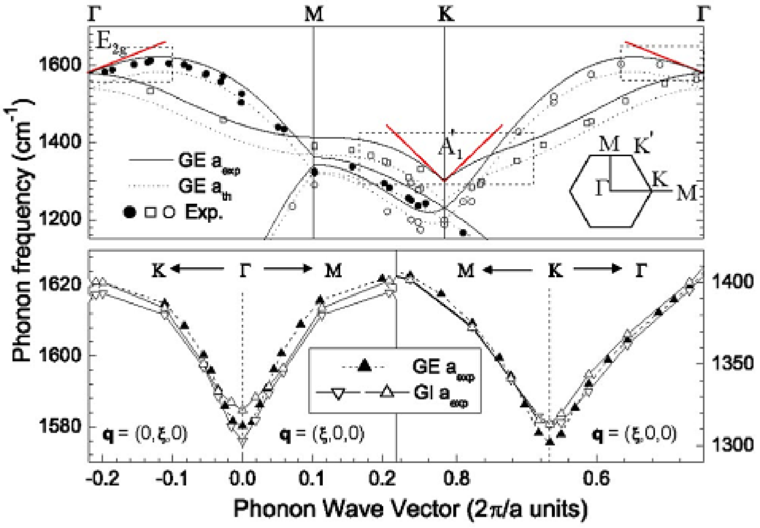

Figure 3.4: Phonon dispersion in graphene. Energies of the highest optical branches at Γ and K points are renormalized due to Kohn anomalies. From ref. [103]

This scattering of carriers from the Fermi surface by phonons, can also be seen as a process in which an electron in the valence band is first excited to the conduction band by absorbing a phonon, thus creating an electron-hole pair. The electron and hole then recombine and emit a phonon. Both the frequency and lifetime of the phonon are significantly affected by this second-order process [105, 117]. The renormalization of the phonon energy can be described by time dependent second-order perturbation theory. In this formalism the contribution to the energy of the electron-hole bubble process shown in Fig. 3.3 is negative, which causes the lowering of the phonon energy by about 5% with respect to the unperturbed phonon energy.

The effect of this link between phonons and electron-hole excitations, not only lowers the phonon energy at Γ and K points, but also makes the phonon dispersion around those points linear (see red tangent lines in Fig. 3.4). In graphene, this coupling is seen only for phonons from the highest optical branches at those two points, i.e. for the LO phonon(E_{2g} mode)at Γ point and for the TO phonon(A_1' mode) at K point. The non-zero EPC matrix elements for phonons at those points lead to discontinuity in the derivative of the phonon energy dispersion relation. The linear slope $\alpha_{\Gamma(K)}^{E_{2g}(A_1')}$ of a phonon energy dispersion

$$E_{\Gamma(K)}^{ph}(q) = \hbar\omega_{\Gamma(K)} + \alpha_{\Gamma(K)}^{E_{2g}(A_1')}|q| \tag{3.9}$$

in the vicinity of $\Gamma(K)$ points is entirely determined by the EPC between phonon and electron-hole excitations, which tends to lower the phonon energy $\hbar\omega_{\Gamma(K)}$ at those points. The slope of phonon dispersion close to Γ or K point is given by:

$$\alpha_{\Gamma(K)}^{E_{2g}(A_1')} = \frac{\sqrt{3}\hbar a_0 \langle D_{\Gamma(K)}^2 \rangle_F}{8M\hbar\omega_{E_{2g}(A_1')}^{\Gamma(K)} v_F} \tag{3.10}$$

where a_0 is the graphene lattice constant, M carbon mass, $\hbar\omega_{E_{2g}(A_1')}^{\Gamma(K)}$ energy of the E_{2g} or A_1' phonon and $\langle D_{\Gamma(K)}^2 \rangle_F$ is the averaged over the Fermi surface square of the EPC

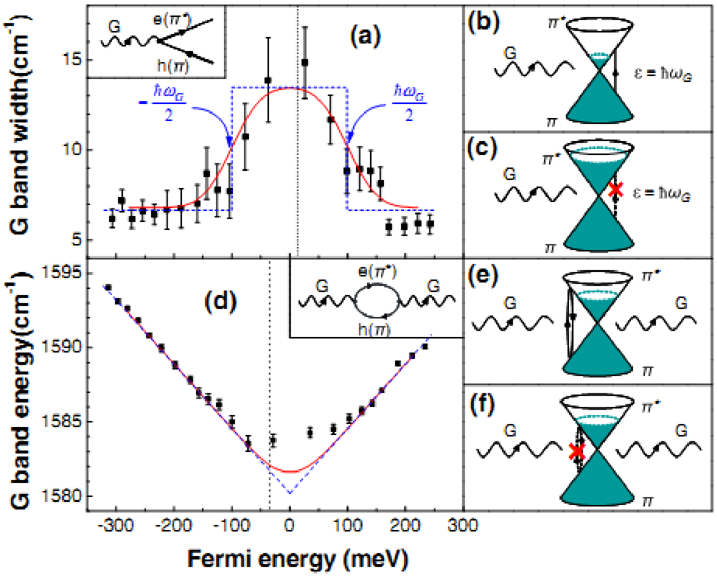

Figure 3.5: a) Linewidth and d) energy of the G band in monolayer graphene as a function of Fermi energy position (charge doping). Black dots – experimental points, blue lines – theoretical fits for the ideal graphene, red lines – theoretical fits for the nonuniform graphene. b) G band broadening of the due to decay into electron-hole pair. c) Decay into electron-hole particles is forbidden due to Pauli blocking when $2|\epsilon_F| > \hbar\omega_G$ e) Γ point phonon energy renormalized through interaction with virtual electron-hole pairs. f) electron-hole pairs creation is suppressed for energies smaller than $2\epsilon_F$ From ref. [106]

constant as defined in Eq. 3.1 and 3.2. This relation gives a possibility to experimentally measure the EPC constants by measuring the phonon dispersion around the Γ and K points. It was done by a variety of experimental methods such as: neutron scattering [119], electron energy-loss spectroscopy [120, 121, 122], angle-resolved photoemission spectroscopy (ARPES) [114], inelastic x-ray scattering [113, 99, 123], and double resonance Raman scattering [64, 101]. The EPC constants extracted from some of those measurements were presented in Table 3.1.

3.4 Γ phonon energy tuning with ϵ_F

Energy tuning The EPC in graphene makes it possible to tune the energy of the Γ point phonon by changing the level of the Fermi energy. *Yan et al.* have shown that both the energy and the linewidth of the G band peak in Raman scattering experiment strongly depend on the position of the Fermi energy ϵ_F (Fig. 3.5). First it was demonstrated in a single layer graphene where the Fermi energy was varied either by chemical doping [124] or by electric field gate effect [107, 106, 86] and then it was also observed in bi-layer graphene [110]. These works have shown that Γ phonon frequency has the lowest value when ϵ_F is at the charge neutrality point and it increases with both electron or hole doping. The linewidth on the other hand has the largest value (~ 15 cm^{-1}) at the charge neutrality point and decreases to the lowest value of about ~ 7 cm^{-1} at high electron or

hole doping level. The onset of this decrease is close to Fermi energy being equal to half the energy of Γ point phonon $\epsilon_F = \pm\frac{\hbar\omega_\Gamma}{2}$. In fact, for clean enough systems, a logarithmic divergence in the energy of the Γ phonon, and a steep change between broadened and narrow FWHM of this phonon, are expected to occur at $E_F = \pm\frac{\hbar\omega_\Gamma}{2}$. However, those subtle details were always smeared out by a disorder in all the systems that were studied up to now.
The Kohn anomaly at Γ point is at the very center of this effect. As the ϵ_F moves away from the charge neutrality point more and more virtual electron-hole pairs that previously participated in the renormalization of the phonon energy (Fig. 3.5e) are now blocked due to Pauli exclusion principle (Fig. 3.5f). The renormalization of phonon energy leads to lowering its value in graphene, now in a doped graphene the renormalization effect is weaker, which pushes the phonon energy up, towards its non-renormalized value.

The described above G band energy dependence on the ϵ_F is an interesting example of a phenomena in graphene that cannot be theoretically described without abandoning the usually employed adiabatic Born-Oppenheimer approximation (ABO) [107]. The ABO approximation is a textbook solution frequently used to describe many solid state systems. It assumes that because of the big difference between electron and nuclei masses (1:2000), their motion can be treated separately. It means that when calculating the energy dispersion of vibrational modes of the lattice (phonons) an assumption is made that lighter electrons adjust adiabatically to the motion of heavier nuclei, remaining at all times in their ground state. Thus giving no contribution to the energy of phonons. This approach gives good results in the case of insulating and semiconducting materials where electronic energy gap is much larger than the energy of the vibrational excitations. In metallic systems however where the electronic energy gap is zero this approximation is questionable. In spite of that, for some metallic systems, the ABO proved to be still effective and helped to accurately determine chemical reactions [125], molecular dynamics [126, 127] and phonon energies [128, 129, 130]. However, in other metallic systems, like e.g. osmium, it fails [131, 132].
Works of *Lazzeri and Mauri* [116], *Pisana et al.* [107] and *Yan et al.* [106] have shown that graphene is one of the systems where the adiabatic Born-Oppenheimer approximation fails and the time-dependent perturbation theory must be used to correctly describe behavior of the Γ point phonon.

Linewidth tuning A similar dependence on the ϵ_F position is seen in the Γ phonon linewidth (Fig. 3.5a). Here, the G peak linewidth decreases almost by half, when the Fermi energy ϵ_F is higher (lower) than half of the Γ phonon energy. This change of linewidth can be understood in the following way. First, we have to recall that the linewidth of a phonon is inversely proportional to its lifetime τ. The lifetime is determined by the rate of intrinsic phonon decay processes $\frac{1}{\tau_{an}}$ due to anharmonic terms in the phonon Hamiltonian and due to phonon interaction with other excitations in the systems. In case of graphene it is the phonon decay into electron-hole pair (Fig. 3.5b) which play the major role as extrinsic source of phonon decay processes, adding additional rate $\frac{1}{\tau_{e-h}}$. So we can write the phonon lifetime as a sum: $\frac{1}{\tau} = \frac{1}{\tau_{an}} + \frac{1}{\tau_{e-h}}$. It follows straightforwardly from this expression, that phonon lifetime should increase if the additional channel of phonon decay into electron-hole pairs could be somehow blocked. In fact this blocking occurs in graphene due to the Pauli exclusion principle when $\epsilon_F > \frac{\hbar\omega_\Gamma}{2}$ i.e. when all potential final states in the conduction band are already occupied (Fig. 3.5c). For the hole doping, the situation is analogous and the blocking occurs when $\epsilon_F < -\frac{\hbar\omega_\Gamma}{2}$ i.e. when all potential initial states are empty. This effect creates an opportunity to investigate the role of electron-phonon interaction on the properties of phonon by switching on and off the electron-phonon interaction just by controlling the gate voltage applied to the graphene sample. Results of such experiment performed in a high magnetic field on a monolayer graphene, grown by a chemical vapour deposition (CVD) technique, will be presented in Chapter 9.

3.5 K point phonons coupling effects

Up to now the EPC effects related to K point phonons were observed mainly in the renormalization of the electron bands dispersion as it is evidenced by the angle resolved photoemission spectroscopy (ARPES) experiment in epitaxial graphene [114] and in intercalated graphite compounds [133]. Moreover phonon dispersions in the vicinity of the K point was also probed through the double resonance Raman processes in graphitic materials [100].

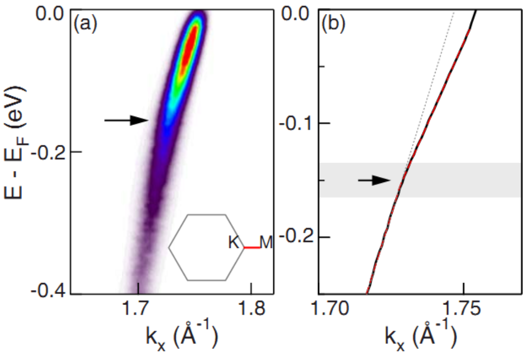

Figure 3.6: a) ARPES data taken along KM direction. b) Dispersion (black curve) extracted by fitting the raw data. The dashed line is the fit using two straight lines with different slopes. Kink in the phonon dispersion marks the energy of a K point phonon. From ref. [114]

ARPES measurements allows to measure electronic dispersions, renormalized by interactions in given material. *Zhou et al.* have performed such experiment on a sample of epitaxial graphene [114]. A characteristic for graphene linear band dispersion was observed, with a few distinct deviations from the linearity. Usually when a sudden kink in the electron band dispersion is observed it can be related to interaction with phonons having the same energy. In their experiment three kinks were observed: two very weak ones around 60 ± 15 meV and 200 ± 15 meV, and a pronounced one at 150 ± 15 meV. Those peaks can be easily identified as corresponding to: (i) low energy out-of-plane phonon from the K point, (ii) E_{2g} phonon from Γ point and (iii) A'_1 phonon from the highest optical branch at K point. It is possible to obtain a value of the EPC constant by comparing the slopes of the measured electron dispersion in energy-momentum space. In this case the dimensionless EPC constant λ is defined as: $\lambda = v_b/v_F - 1$. Where v_b is the bare band velocity (above the kink), and v_F is the renormalized Fermi velocity (below the kink). Values of EPC obtained in this way confirmed previous theoretical calculations [103, 115] predicting that A'_1 phonon has the largest value of EPC constant among all phonons in graphene. However, both the ratio of λ_K/λ_Γ and magnitude of λ_K were surprisingly high. Previously calculated ratio was expected to be $\lambda_K/\lambda_\Gamma = 2$ [103], while this experiment shows that the difference is by at least an order of magnitude bigger. In addition to that, the measured $\lambda_K = 0.14$ has a much higher value than expected $\lambda_{K-theory} = 0.02$ [115]. To explain these discrepancies, an interplay between electron-phonon and electron-electron interactions was proposed, which would enhance the EPC [115, 134]. ARPES measurements on doped graphene done by *Siegel et al* showed that the observed kink, in the range of energies $150 - 200$ meV, is more pronounced for doped graphene as compared to neutral graphene [135]. Another experiment performed by *Bostwick et al.* [136] have revealed yet another small kink, very close to the Dirac energy E_D (crossing of conduction and valence band), which causes that extrapolation of valence band does not pass through conduction band. Its origin is explained again in terms of many-body electron-electron interactions which modify electronic band dispersion. It was proposed that, since K point phonons are already affected by charge carriers in graphene (Kohn anomaly), it is possible that electron-electron interactions are responsible for the unexpectedly high electron-phonon coupling value for this phonon [136].

3.6 Magneto-phonon resonance

Applying a magnetic field to graphene, offers a unique possibility to study the EPC effects via oscillations in the Γ point phonon energy [117, 137, 138]. This effect, usually referred to as magneto-phonon resonance (MPR) or magneto-phonon effect, is a direct consequence of a coupling between Γ phonon with some of the inter-band inter-Landau level electron-hole excitations. This coupling leads to the formation of hybridized phonon-magneto-exciton modes which show a distinct avoided crossings in clean enough samples [108, 109, 44, 32] (graphene inclusions on the surface of graphite) or merely small oscillations in samples of lower quality or doped [139] (exfoliated graphene deposited on SiO_2). So far magneto-phonon resonance has been also observed in multilayer graphene specimens [140] and in bulk graphite for both H and K point carriers [45, 46] and is now used as a tool to study the electron-phonon interaction and also to perform the Landau level spectroscopy of unknown systems.

Magnetic field applied in the direction perpendicular to the graphene surface induces Landau quantization for clean enough electronic systems and changes the continuous interband electronic excitation spectrum at $B = 0$T into a discrete excitation spectrum among Landau levels of index n with an energy that increases with magnetic field as:

$$E_n = sign(n) v_F \sqrt{2e\hbar B}\sqrt{|n|} \tag{3.11}$$

The relevant electronic excitations $L_{n,m}$ between Landau levels of index n and m, for the electron-phonon interaction are those fulfilling the optical selection rule $\Delta|n| = |n| - |m| = \pm 1$. When these specific excitations are tuned to the phonon energy by increasing the strength of the magnetic field, the electron-phonon interaction induces a coherent mixing of these modes. It manifests itself through the magneto-phonon resonance – a series of avoided crossings between the phonon mode and the electronic excitation spectrum each time one $\Delta|n| = \pm 1$ inter-Landau level excitation is tuned to the phonon energy [108, 109, 44, 32, 139, 141].

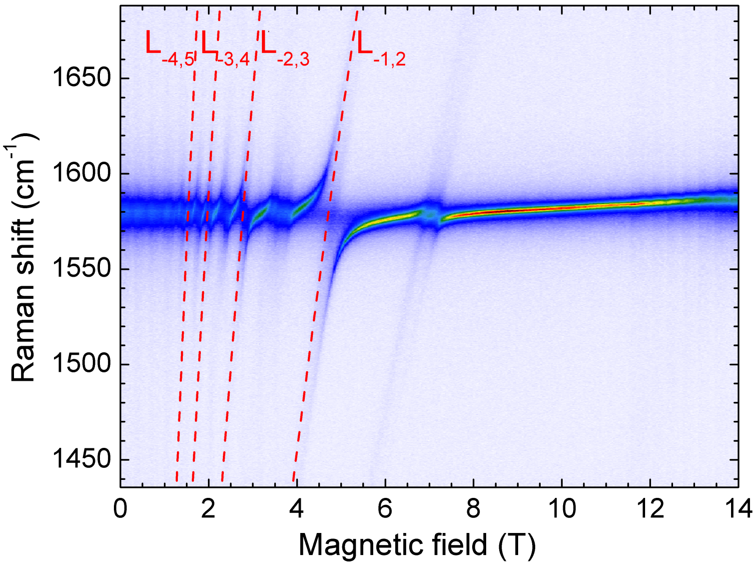

Figure 3.7: Magneto-phonon resonance in graphene inclusion on the surface of graphite, as seen through magneto-Raman scattering. Intensity of the G band at 1580 cm^{-1} is shown in the false color scale. Dashed red lines show the energies of first few electronic excitations which are expected to hybridize with Γ phonon. The phonon energy oscillations at B = 4.7T, 2.7T, 1.9T, 1.6T,... are the hallmark of the magneto-phonon resonance. $\lambda_{exc.} = 720$ nm, cross-circular polarization.

Theory describing MPR developped by *Ando* [117, 137, 142] and *Goerbig* [138] allows to reproduce energy and linewidth of the interacting Γ point phonon. In this approach, the energy of non-interacting relativistic Dirac electrons is described by a Hamiltonian:

$$\mathcal{H}_0 = \gamma \begin{pmatrix} 0 & \hat{k}_x - i\hat{k}_y \\ \hat{k}_x + i\hat{k}_y & 0 \end{pmatrix} = \gamma(\boldsymbol{\sigma} \cdot \boldsymbol{k}) \tag{3.12}$$

where γ is the band parameter proportional to the nearest neighbour hopping integral γ_0:

$$\gamma = \frac{\sqrt{3}a}{2}\gamma_0 \tag{3.13}$$

$a = 0.142$nm is the nearest neighbour inter-atomic distance, $\boldsymbol{\sigma} = (\sigma_x, \sigma_y)$ stands for the Pauli spin matrix, while $\hat{\mathbf{k}} = (\hat{k}_x, \hat{k}_y) = -i\nabla + e\mathbf{A}/(\hbar c)$ is a wave-vector operator with the vector potential $\mathbf{A} = (Bx, 0)$ in magnetic field B perpendicular to the system. Then, optical phonons are described by a vector $\mathbf{u}(\mathbf{r})$ representing the relative displacement of the two sub-lattice atoms A and B:

$$\mathbf{u}(\mathbf{r}) = \sum_{\mathbf{q}} \sqrt{\frac{\hbar}{2NM\omega_0}}(b_{\mathbf{q}} + b^{\dagger}_{-\mathbf{q}})\hat{\mathbf{e}}(\mathbf{q})e^{i\mathbf{q}\cdot\mathbf{r}} \tag{3.14}$$

where N is the number of unit cells, M is the mass of a carbon atom, ω_0 is the optical phonon frequency at Γ point, $\hat{\mathbf{e}}$ is the direction of the atom displacement, $\mathbf{q} = (q_x, q_y)$ is the phonon wavevector, while $b^{\dagger}_{\mathbf{q}}$ and $b_{\mathbf{q}}$ are the creation and annihilation operators, respectively. The optical phonon temporarily distorts the distance between neighbouring carbon atoms, which modifies the band structure through the change in the overlap integral γ between carbon atoms. The resulting change in the electron Hamiltonian describes the electron-phonon interaction which, in the case of graphene, is given by:

$$\mathcal{H}^K_{int} = -\sqrt{2}\frac{\beta\gamma}{b^2}\boldsymbol{\sigma} \times \mathbf{u}(\mathbf{r}) \tag{3.15}$$

where the vector product for vectors $\mathbf{a} = (a_x, a_y)$ and $\mathbf{b} = (b_x, b_y)$ in two dimension is defined by $\mathbf{a} \times \mathbf{b} = a_x b_x - a_y b_x$, and $b = a/\sqrt{3}$ is the equilibrium bond length. The dimensionless parameter β describes the change in the wavefunction overlap integral between electrons localized on the two nearest neighbour atoms, with respect to the change in inter-atomic distance:

$$\beta = -\frac{dln\gamma_0}{dlnb} \tag{3.16}$$

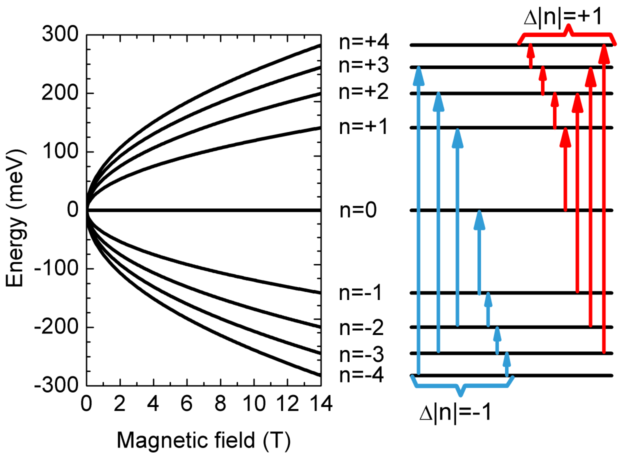

Figure 3.8: Left: Tuning LLs energy by applying a magnetic field. Right: electronic excitations that participate to the renormalization of the Γ phonon energy through a magneto-phonon resonance. If small electron-hole asymmetry is neglected, the $L_{-n,n+1}$ and $L_{-n-1,n}$ excitations are degenerated, but are active in two different light polarizations $\sigma-$ and $\sigma+$ respectively.

The energy and linewidth of the phonon, can be calculated from the poles of the phonon Green's function, which describes the phonon dressed by interactions with electron-hole pairs:

$$D(\mathbf{q}, \omega) = \frac{2\hbar\omega_0}{(\hbar\omega)^2 - (\hbar\omega_0)^2 - 2\hbar\omega_0 \Pi(\mathbf{q}, \omega)} \tag{3.17}$$

Where ω_0 is the unperturbed frequency of the Γ phonon, while ω is the energy of a hybridized phonon-magneto-exciton due to interactions with interband inter-LL excitations with $\Delta|n| = \pm 1$ and with intra-band inter-LL excitations with $\Delta|n| = \pm 1$(cyclotron resonance). This interaction is described by the phonon self-energy $\Pi(\mathbf{q}, \omega)$:

$$\begin{aligned}\Pi(\mathbf{q}, \omega) = -\frac{1}{4}\lambda(v_F\sqrt{2\hbar eB})^2 \sum_{s,s'=\pm 1}\sum_{n=0}^{\infty} \Bigg(&[f(s\epsilon_n) - f(s'\epsilon_{n+1})] \\ \times \frac{2(s\epsilon_n - s'\epsilon_{n+1})}{(\hbar\omega + i\delta)^2 - (s\epsilon_n - s'\epsilon_{n+1})^2} &- \frac{1 - ss'}{\epsilon_{n+1} + \epsilon_n}\Bigg)\end{aligned} \tag{3.18}$$

In these expressions $f(s\epsilon_n)$ is an occupation factor of nth Landau level with energy ϵ_n in a conduction ($s = +1$) or valence ($s = -1$) band. It is given by a Fermi-Dirac distribution function:

$$f(\epsilon) = \frac{1}{e^{(\epsilon-\xi)/(k_B T)} + 1} \tag{3.19}$$

The energy of the Fermi level decides which excitations have non-zero oscillator strength and participates in the phonon's energy renormalization. Whenever some initial electron state is completely empty, or when the final state is fully occupied, such excitations cannot take place, which is usually referred to as Pauli blocking. λ in the expression 3.18 is the dimensionless EPC constant, that was defined in Eq. 3.3, and δ is a phenomenological broadening parameter due to scattering of an electrons by disorder or acoustic phonons.

Equations 3.17 and 3.18 are then used to solve in a self-consistent manner for the renormalized phonon energy:

$$(\hbar\omega)^2 = (\hbar\omega_0)^2 + 2(\hbar\omega_0)^2 \text{ Re } \Pi(\mathbf{q}, \omega) \tag{3.20}$$

and its linewidth:

$$\Gamma = -\frac{2}{\hbar} \text{ Im } \Pi(\mathbf{q}, \omega) \tag{3.21}$$

Alternatively one can also calculate the phonon spectral function:

$$\rho(\mathbf{k}, \omega) = -\frac{1}{\pi} \text{ Im } D(\mathbf{q}, \omega) \tag{3.22}$$

which, at a given magnetic field B gives the phonon spectral density at each value of energy $\hbar\omega$. This quantity can be then directly compared with the intensity of the Raman scattering at the same energy $\hbar\omega$.

3.7 K point phonons in magneto-absorption

The ARPES measurements have shown that the coupling between electron-hole pairs and phonons in graphene is not restricted to phonons from the Γ point only [114, 133]. By using magnetic field this interaction can be also conveniently studied in the magneto-absorption experiment, as was done by *Orlita et al.* [143]. When the multilayer epitaxial graphene grown on the surface of SiC is placed in the magnetic field, a series of absorption dips emerge that evolve in magnetic like $\sim \sqrt{B}$ [40]. They correspond to inter-LL transitions $L_{n,m}$, which obey the $\Delta|n| = \pm 1$ selection rule for the infrared active excitations. *Orlita et al.* have observed that in addition to the well known dips from inter-LLs excitations, and additional feature can be also observed. In a range of magnetic field from 17 to 20T the lowest absorption dip $L_{0,1}$ develops a shoulder at the energy of 150 meV (Fig. 3.9a). It is even better visible when results are plotted as a false color map showing the energy evolution of $L_{0,1}$ absorption peak against applied magnetic field (Fig. 3.9b). Again, around 150 meV, a significant deviation from the simple $\sqrt{B}$ evolution is observed. This energy corresponds to the highest optical branch of K point phonon in graphene [103].

To explain this splitting, a coupling between two types of excitations was proposed. These two excitations are: a doubly degenerate optical excitation $L_{0,1}$ or $L_{-1,0}$, and a combined

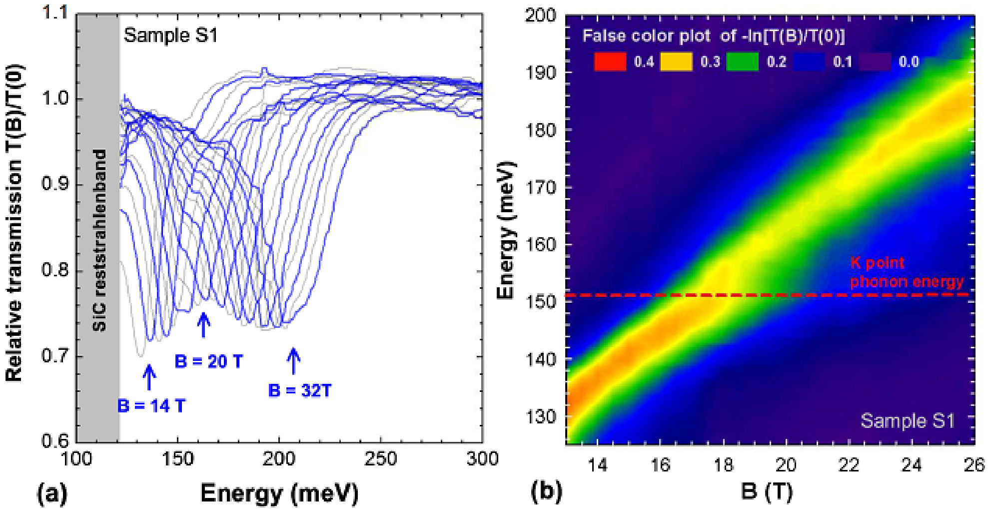

Figure 3.9: a) Relative transmission spectra (T(B)/T(0)) of multilayer epitaxial graphene. b) The same data presented in a form of false color map, red dotted line marks the energy of K point phonon. From ref. [143]

excitation composed of a K-point phonon and a zero-energy inter-valley electron-hole pair. This second one can be created in a process where first a usual optical excitation $L_{0,1}$ is created and then, the electron from the $n = 1$ LL in K valley is scattered to the $n = 0$ LL in K' valley, gaining quasi-momentum $k = \vec{K}$, and the simultaneous emission of K point phonon having momentum $q = -\vec{K}$. Process for the $L_{-1,0}$ excitation is analogous, but then it is a hole from the $n = -1$ LL which is scattered to $n = 0$ LL in the K' valley. In both cases, the final state consists of a phonon with momentum $|q| = K$ and of an electron and a hole at $n = 0$ LL, but one is located at K point while the other at K' point. Importantly the quasi-momentum is conserved in the whole process. This process is resonant in magnetic field in the sense that by tuning the energy separation between the $n = 0$ LL and the $n = +1$ ($n = -1$) LL by increasing the magnetic field, a resonance with the energy of the K point phonon can be achieved. Under such conditions the scattering event with emission of K point phonon can satisfy both the energy and the momentum conservation laws. This additional relaxation channel for the $L_{0,1}$ or $L_{-1,0}$ excitation leads to the observed splitting.

Chapter 4

Raman scattering due to electronic excitations

The gapless graphene bandstructure makes it easy to excite low energy inter-band electron-hole pairs, often referred to as electronic excitations. They have been observed through various experimental methods, either though indirect effects in angle-resolved photoemission spectroscopy [144] or magneto-absorption in monolayers [40, 28] and bilayers [145, 146, 147, 148], and finally by a direct observation in magnetic field through Raman scattering in monolayer graphene [44, 32] as well as in bulk graphite [45, 46]. The theoretical calculations of their corresponding Raman features intensity has been done for monolayer [31] and bilayer [149] graphene and then was summarized in an broad review article [150].

These electronic excitations can be created in the system regardless of the presence of an external magnetic field. However in the absence of magnetic field, their excitation spectrum is a continuous band at energies higher than twice the Fermi energy E_F, which form a linearly increasing background in Raman scattering spectra (see dotted line in Fig. 4.1) and makes it difficult to selectively address and study excitations of different symmetry properties. On the other hand, when a magnetic field is applied in the direction perpendicular to the surface of graphene, the continuous linear dispersion of electronic bands is quantized into a set of discrete Landau levels (LLs) and the continuum of electronic excitations energy is transformed into a discrete set of excitations. Some of them can be seen in the magneto-absorption process and some in magneto-Raman scattering. A set of selection rules derived from the symmetry properties of the lattice predicts which types of excitations can be seen in which experiment, while detailed calculation of the scattered intensity based on the electrons Green function gives more insight into the relative scattering amplitudes of different types of electron-hole excitations. Since Raman scattering under Landau quantization is a well established measurement technique that has been used intensively in the past for studies of bulk materials [151, 152, 153] and semiconductor heterostructures [154, 155, 156, 157], it is now successfully employed to unravel a rich physics in atomically-thin graphene [44, 32].

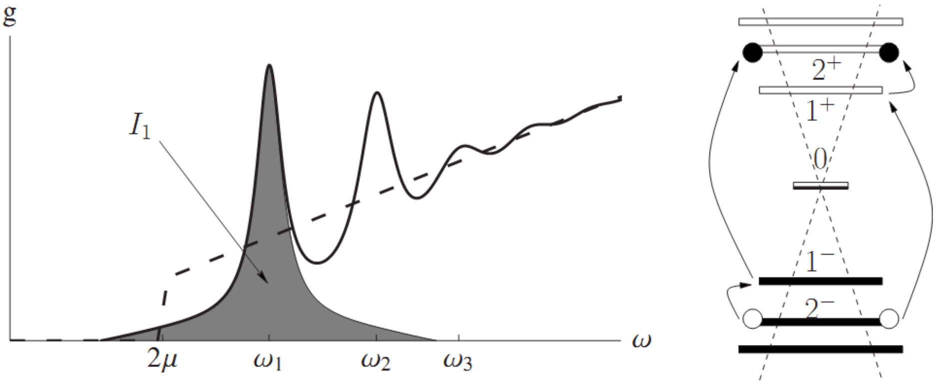

Figure 4.1: Spectral density g(ω) of light inelastically scatterred from electronic excitations in graphene at quantizing magnetic fields (solid line) and at B=0 (dashed line). Here $\omega \ll \Omega$ is the Raman shift. Sketch illustrates intermediate and final states of the dominant Raman process. From ref. [31]

4.1 Electronic excitations in the absence of magnetic field

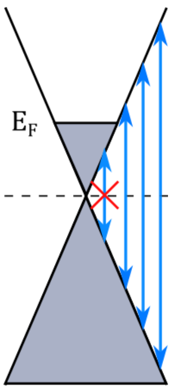

Figure 4.2: Electron-hole excitations in graphene in the absence of magnetic field. Excitations with energy lower than $2E_F$ are not allowed due to Pauli blocking.

When photons with energy Ω smaller than the graphene bandwidth are scattered from graphene they can create inter-band electron-hole pairs (electronic excitations). Because incident photons have very small momentum as compared with the size of the Brillouin zone all these excitations have virtually zero total momentum ($k_e + k_h = 0$). Their energy is determined by the momentum of one of the excited quasi-particle $E = 2\hbar|k_e(h)|$. Its upper bounds are limited only by the graphene bandwidth ($E_{max} \approx 3\ eV$), while the lower by the position of the Fermi energy ($E_{min} = 2\hbar|k_F|$). A thorough description of such excitations has been published by *Kashuba&Fal'ko* [31, 150] who divided the possible excitations according to their transformation symmetries and polarization configurations in which they are visible. The Raman scattering intensity can be derived from the electron Green function, which in turn requires knowledge of the Hamiltonian describing graphene interacting with electro-magnetic radiation. It turns out that inclusion of trigonal warping term in the non-interacting Hamiltonian is necessary if all experimentally observed excitations are to be reproduced by this model. Thus, the Hamiltonian of non-interacting monolayer graphene can be written as:

$$\hat{H} = \xi v \boldsymbol{\sigma} \cdot \boldsymbol{p} - \frac{v^2}{6\gamma_0}(\sigma^x(p_x^2 - p_y^2) - 2\sigma^y p_x p_y) \tag{4.1}$$

Where $\boldsymbol{\sigma} = (\sigma^x, \sigma^y)$ are the Pauli matrices acting on the two components of the electronic wavefunction, corresponding to states localized in one of the two sublattices of graphene hexagonal lattice. The in-plane momentum is denoted by $\mathbf{p}$ and counted from the corner of the Brillouin zone (K or K' point), $\gamma_0 \approx 3$ eV is the nearest-neighbour hopping integral, which also determines the value of the Fermi velocity $v_F \approx 10^6$ m/s. Then to include the interaction of electrons in graphene with photons, the Peierls substitution is employed, which substitute electron momentum $\mathbf{p}$ with canonical momentum $p - \frac{e}{c}\mathbf{A}$. Where the vector potential:

$$\mathbf{A} = \sum_{l,\mathbf{q},q_z} \frac{\hbar c}{\sqrt{2\Omega}} \left(\mathbf{l} e^{i(\mathbf{q}\cdot\mathbf{r} - \Omega t)/\hbar} b_{l,\mathbf{q},q_z} + h.c. \right) \tag{4.2}$$

describes an incoming a photon with polarization $\mathbf{l}$, in-plane momentum $\mathbf{q}$, energy Ω and out-of plane momentum $q_z = \sqrt{\Omega^2/c^2 - \mathbf{q}^2}$. Expanding the Hamiltonian up to the second order in the vector potential $\mathbf{A}$ yields the interaction Hamiltonian:

$$H_{int} = -\frac{e v_F}{c} \mathbf{J} \cdot \mathbf{A} + \frac{e^2}{2c^2} \sum_{i,j} A_i A_j \tag{4.3}$$

where $(e v_F/c) J_i = (e/c)\partial_{p_i} \hat{H}$ is the current vertex and $e^2/(2c^2)\partial^2_{p_i,p_j} H$ is the two-photon contact interaction tensor. These two terms lead to two terms in the Raman scattering amplitude $R = R_D + R_w$, which describes the scattering of incident photon, with energy Ω, momentum $\mathbf{q}$ and polarization $\mathbf{l}$, on electrons. The scattered photon has changed energy $\tilde{\Omega} = \Omega - \omega$ ($\omega = \epsilon_f - \epsilon_i$ is the energy of created excitation – Raman shift), momentum $\tilde{\mathbf{q}}$ and polarization $\tilde{\mathbf{l}}$. The two leading terms of the scattering amplitude are shown in Fig. 4.3 using Feynman diagrams. The R_w term describes a one-step scattering process which is mediated by a contact interaction between electron and two photons. Although for non-relativistic particles contact interaction is important, it is absent in the case of Dirac fermions. Here it reappears, only after breaking the rotational symmetry of the system through trigonal warping term in Hamiltonian (Eq. 4.1). Then it leads to the creation of electronic excitations which have the symmetry of E_2 representation of the C_{6v} point group.

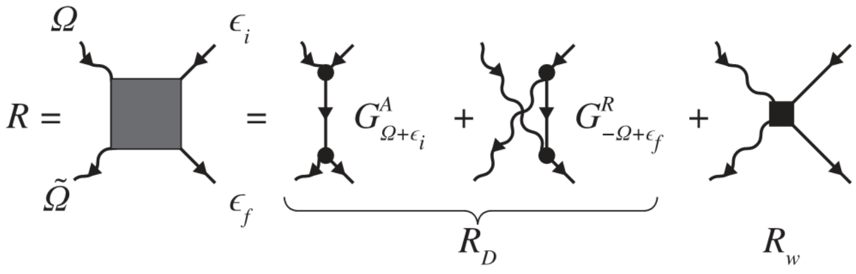

Figure 4.3: Feynman diagrams for the Raman scattering amplitude R from the ground state to the final state with electron-hole excitation. From ref. [150]

On the other hand the R_D term in the Raman scattering amplitude is responsible for a two-step scattering process, which involves an intermediate virtual state. The excitation process may proceed in two ways both of which consist of the same steps, but in a reversed time order. In the first process, the absorption of a photon with energy Ω transfers an electron from an occupied state in the valence band and energy ϵ_i into a virtual state in the conduction band, which is followed by the emission of the second photon with energy $\tilde{\Omega} = \Omega - \omega$, and leaves an electron in a real state with energy $\epsilon_f = \epsilon_i + \omega$. In the second process, a photon with energy $\tilde{\Omega} = \Omega - \omega$ is first emitted, leading to the virtual electron state with a large deficit of energy. Then, a photon with energy Ω is absorbed, which brings the electron to the same excited state ϵ_f as discussed above. The net amplitude of the whole scattering process is determined by the sum of the partial amplitudes of the two opposite processes.

In monolayer graphene, the two-step scattering process via the virtual state and the contact interaction process have different properties and polarization selection rules. This reflects their relation to the different irreducible representations of the symmetry group of the crystal. Generally, the components of the scattering amplitude R realize a representation of the lattice symmetry group C_{6v}. Since the polarization vectors of the incoming and scattered photons, $\mathbf{l}$ and $\tilde{\mathbf{l}}$ respectively, belong to the E_1 representation, the R representation can be expanded into irreducible ones:

$$E_1 \otimes E_1 = A_1 \oplus A_2 \oplus E_2 \tag{4.4}$$

Therefore the scattering probability w can be written in a general form:

$$w = w_{A_1}\Xi_{A_1} + w_{A_2}\Xi_{A_2} + w_{E_2}\Xi_{E_2} \tag{4.5}$$

As a sum of the partial scattering probabilities w_i in a process where polarization vectors transform accordingly to a given representation. The weights Ξ_i are given by the polarizations of the incoming and scattered photons [150]:

$$\begin{aligned} \Xi_{A_1} &= |l \cdot \tilde{l}^*|^2 \\ \Xi_{A_2} &= |l \times \tilde{l}^*|^2 \\ \Xi_{E_2} &= |\mathbf{d}|^2 = 1 + (l \times l^*)(\tilde{l} \times \tilde{l}^*) \\ \text{where } \mathbf{d} &= (l_x\tilde{l_y}^* + l_y\tilde{l_x}^*, l_x\tilde{l_x}^* + l_y\tilde{l_y}^*) \end{aligned} \tag{4.6}$$

Which means that excitations with A_1 and A_2 symmetries can be created and detected in a co-circular configuration, while excitations with E_2 symmetry should be visible in cross-circular configuration.

4.2 Electronic excitations in magnetic fields

4.2.1 Monolayer graphene

Applying a magnetic field in the direction perpendicular to the graphene plane causes the quantization of energy states into highly degenerate LLs described by a quantum number n. The incoming electro-magnetic wave can perturb electrons in those states, which results in the formation of inter-LLs electron-hole pairs. Such electronic excitations are usually denoted by symbol $L_{-n,m}$, where n stands for the initial electron state and m for the final electron state after excitation. The energy of these excitations is equal to $L_{-n,m} = \epsilon_m - \epsilon_n$. Neglecting the very small asymmetry between conduction and valence

C_{6v} rep.	$\Delta\|n\|$	Transition	Intensity	Observable in
A_2	0	$-n \to n$	Dominant in Raman	Raman $\sigma\pm \to \sigma\pm$
E_2	± 1	$-n \to n+1$ $-(n+1) \to n$	Weak in Raman, strong in magneto-phonon resonance, active through trigonal warping	Raman $\sigma\pm \to \sigma\mp$
A_1	$\pm$ 2	$-(n-1) \to n+1$ $-(n+1) \to n-1$	Weak in Raman	Raman $\sigma\pm \to \sigma\mp$
E_1	± 1	$-n \to n+1$ $-(n+1) \to n$	Not seen in Raman	Infrared active

Table 4.1: Selection rules of inter-LLs excitations in graphene

bands, this expression can be written as:

$$L_{-n,m} = v_F\sqrt{2e\hbar Bm} + v_F\sqrt{2e\hbar Bn} = \\ = v_F\sqrt{2e\hbar B}(\sqrt{n}+\sqrt{m}) \tag{4.7}$$

Electronic excitations can be classified accordingly to their symmetry properties and to the change in the LL index n which is proportional to the change of angular momentum of the carriers $\Delta m = \hbar\Delta|n|$. Each class of transitions have symmetry properties that make it either active in Raman scattering or in far infrared absorption or not active at all. Additionally, Raman active excitations can be further divided into two groups: these that can be observed in the co-circular configuration (circular polarization of scattered photons is the same as polarization of incoming ones), and those that can be seen in cross-circular configuration (circular polarization of scattered photons is opposite to the polarization of incoming ones). All excitations active in either Raman scattering or far-infrared absorption, together with selection rules are presented in Table 4.1.

The selection rules can be derived directly from the electron Green function, which yields the expressions for the intensities of Raman scattering for each class of excitations. It turns out that the dominant Raman active excitations are the $\Delta|n| = 0$ which are visible in co-circular configuration. The amplitude of the Raman scattering process from those excitations is given by [31, 150]:

$$R_{-n\to n} = \frac{1}{4}\frac{(ev\hbar)^2}{c^2\Omega}\sum_{\alpha=\pm}\left[\frac{(\mathbf{l}\mathbf{e}_+)(\tilde{\mathbf{l}}^*\mathbf{e}_-)}{\Omega-\epsilon_n-\alpha\epsilon_{n+1}} - \frac{(\mathbf{l}\mathbf{e}_+)(\tilde{\mathbf{l}}^*\mathbf{e}_-)}{\epsilon_n-\Omega-\alpha\epsilon_{n-1}} - \frac{(\mathbf{l}\mathbf{e}_-)(\tilde{\mathbf{l}}^*\mathbf{e}_+)}{\Omega-\epsilon_n-\alpha\epsilon_{n+1}} + \right. \\ \left. + \frac{(\mathbf{l}\mathbf{e}_-)(\tilde{\mathbf{l}}^*\mathbf{e}_+)}{\epsilon_n-\Omega-\alpha\epsilon_{n-1}}\right] \tag{4.8}$$

Where the $\mathbf{le}_\pm$ vector describes the circular polarization of the incoming photon, while the $\tilde{\mathbf{l}}^*\mathbf{e}_\pm$ describes polarization of the scattered one, ϵ_n stands for energy of the intermediate LLs involved in the scattering process, while Ω stands for the energy of the incoming photon. $L_{-n,n}$ excitations have the symmetry of A_2 representation of the C_{6v} point group and incoming and scattered photons have the same circular polarization.

Therefore, there is no net transfer of angular momentum to/from the lattice. Since $L_{-n,n}$ excitations give the major contribution to the total Raman signal from electronic excitations, the spectral density of the angle-integrated Raman signal can be obtained from Eq. 4.8 by integrating over all directions of propagation of the scattered photons [31, 150]:

$$g_{n^- \to n^+} \approx \Xi_s \left(\frac{v^2}{c^2} \frac{e^2/\lambda_B}{\pi\Omega} \right)^2 \sum_{n \geq 1} \gamma_n(\omega - \omega_n) \tag{4.9}$$

Where $\gamma_n(x) = \pi^{-1}\Gamma_n / \left[x^2 + \Gamma_n^2\right]$ is a normalized Lorentzian function, and Γ_n stands for inelastic LL broadening that increases with the LL number. According to this model Raman signal should decrease like $1/\Omega^2$ with the frequency Ω of incoming photon. Therefore, in order to maximize Raman signal from electronic excitations, laser sources with longer wavelengths should be used. Another result of this model is the notion that the scattering cross-section for each inter-LL excitation is the same regardless of the LL index – n. However, experimentally measured intensity of excitation lines decreases with n due to two reasons. Firstly, because linewidth of $L_{-n,n}$ excitations increases with n, which for the same area of peaks results in their lower heights. Secondly, at a given magnetic field B, the peak separation decreases as $\sqrt{n+1} - \sqrt{n}$. At some point tails of two neighbouring peaks start to overlap which is seen as an increase in the background level, while peaks apparent height decreases.

There are two types of $\Delta|n| = \pm 1$ excitations which belong to two different representations of the C_{6v} point group. The one with E_1 symmetry are infrared active and are responsible for the 'optical-like' series of $L_{-n,n+1}$ and $L_{-(n+1),n}$ excitations. The wavefunction describing such excitations is composed of a symmetric combination of electron wave functions at K and K' points, thus it is also said to be 'valley-symmetric'. There is also another set of excitations following the same selection rules $\Delta|n| = \pm 1$, but these excitations have the symmetry of the E_2 representation. They are formed by the antisymmetric combination of electron wavefunctions at the two inequivalent valleys. Since these excitations have the same symmetry as the Γ point optical phonon, these two can couple and give rise to the magneto-phonon resonance, which is seen as a series of oscillations of G-band energy in magnetic fields. These excitations can be created in graphene due to the R_w term in the electron Green function, which gives much smaller amplitude than the dominant term $R_{-n \to n}$. Therefore, the intensity of the Raman scattering peaks corresponding to $L_{-n,n+1}(L_{-(n+1),n})$ excitations are weaker than the dominant $L_{-n,n}$. Even though cross-circular configuration in Raman scattering implies a net change in the photon angular momentum $\Delta m = \pm 2$, it is still possible to observe $\Delta|n| = \pm 1$ excitations in this configuration. This is made possible by the fact that R_w term in Green function originates from the trigonal warping term in the graphene Hamiltonian. This breaking of the full rotational symmetry makes it possible to transfer $m = \pm 3$ angular momentum from electrons to the lattice, which makes it feasible to create/annihilate $\Delta|n| = \pm 1$ excitations.

The last set of Raman active electronic excitations is formed by $\Delta|n| = \pm 2$ transitions.

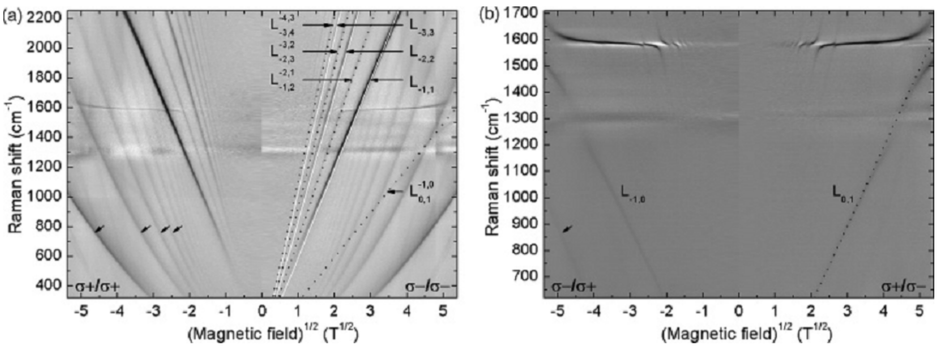

Figure 4.4: Magneto-Raman-scattering response of graphene on natural graphite measured in (a) co-circular configuration and (b) crossed-circular configuration. Raman scattering intensities are plotted in the form of color plots. Black (white) corresponds to high (low) intensity. From ref. [32]

The amplitude of the Raman scattering from those excitations is given by [31, 150]:

$$R_{-(n\mp1)\to(n\pm1)} = \mp\frac{1}{4}\frac{(ev\hbar)^2}{c^2\Omega}(\mathbf{l}\mathbf{e}_\pm)(\tilde{\mathbf{l}}^*\mathbf{e}_\pm)\sum_{\alpha=\pm}\left[\frac{\alpha}{\Omega-\epsilon_{n+1}-\alpha\epsilon_n}+\frac{\alpha}{\epsilon_{n-1}-\Omega-\alpha\epsilon_n}\right] \tag{4.10}$$

It turns out that the scattering amplitudes of $L_{-(n\mp1),n\pm1}$ excitations are much lower than those of the dominant $L_{-n,n}$. Even though these excitations are supposed to be active in the cross-circular configuration, so far they have not yet been observed experimentally. Signatures, of the $L_{0,2}(L_{-2,0})$ excitation, which may be responsible for the small kink in the G-band evolution in magnetic field, at $B\sim 14$T have been observed [32].

The selection rules obtained above have been experimentally verified by measuring the Raman scattering signal in magnetic fields in two different polarization configurations by *Kühne et al.* [32]. These results are shown in Fig. 4.4. In co-circular polarization, strong lines evolving like $\sqrt{B}$ were observed, and they correspond to $L_{-n,n}$ excitations. Surprisingly, also weaker $L_{-n,n+1}(L_{-(n+1),n})$ excitations were present in this polarization configuration, which is at odds with their selection rules. However since they do not interact with the Γ point phonon it was suggested that they may originate from the infrared active modes which have the E_1 symmetry and, through some unidentified selection rule breaking process, become Raman active. The same measurement, performed in a cross-circular configuration, gave a completely different result, showing only $L_{-n,n+1}(L_{-(n+1),n})$ excitations that have the same symmetry E_2 as the optical phonon and resulting in a pronounced magneto-phonon resonance Fig. 4.4b).

From the experimental point of view, the biggest challenge to observe electronic excitations in monolayer graphene lies in providing a clean enough system, with a Fermi energy close to the charge neutrality point, and with Landau levels sharp enough to do not overlap each other. Depositing graphene on a substrate has usually a deteriorating effect on its properties. In the case of commonly used Si/SiO$_2$ substrates, the trapped charges, unsaturated dangling bonds of Si and surface corrugations, cause global and local charge doping and a general deterioration of its electronic properties, which manifest through relatively low charge mobilities $\mu < 10^4$ cm^2/(V·s). Therefore up to now electronic excitations has been only observed in graphene inclusions that can be found on the surface of bulk graphite [44, 32] which are characterized by an exceptional electronic quality (see Chapters 5.1 and 7 for more details about this system) that can yield charge mobilities $\mu > 10^7$ cm^2/(V·s) [13]. However other systems where the interaction of graphene with the substrate has been either completely removed (suspended graphene flakes) or its negative effects largely reduced (graphene on hexagonal BN) gives hope to be able to observe electronic excitations also in those systems. In fact in Chapter 8 we report an observation of the most intense $L_{-n,n}$ excitation in graphene sample deposited on thin layer of atomically flat h-BN.

4.2.2 Graphite

Similarly to graphene, electronic excitations have been also observed in bulk graphite [158, 45, 46]. When graphite is placed in an external magnetic field, charge motion in the plane perpendicular to the applied field is quantized. However, in the direction parallel to the field, carriers can still move freely. For that reason quantized energy states of quasi-particles form Landau bands with a k_z dispersion, instead of discrete levels like in monolayer graphene [51]. The other difference between these two systems stems from the fact that character of the carriers dispersion change qualitatively along k_z as is decribed by the Slonczewski-Weiss-McClure bandstructure model [3, 2]. At the K point, bands have a usual parabolic in-plane dispersion, which leads to equally spaced and linear in magnetic field B Landau levels. On the other hand as one moves towards H point, carriers in-plane dispersion becomes linear, characteristic for massless Dirac particles, which leads to the formation of non-equally spaced, evolving like $\sqrt{B}$ Landau levels. In magnetic field electron-hole excitations between those Landau bands can occur, which are subject to the same selection rules as in the case of graphene.

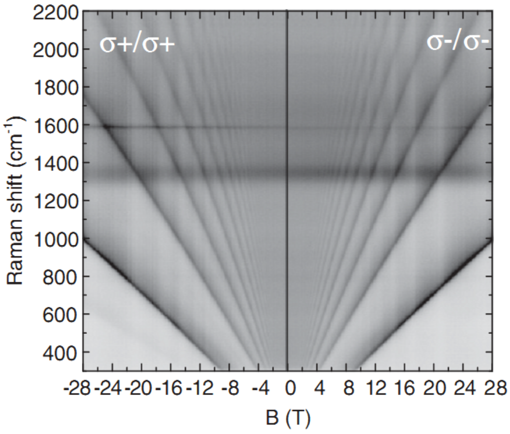

Figure 4.5: False-color map of the Raman scattering intensity at T =4.2 K from bulk graphite, as a function of the magnetic field in the two co-circular configurations. Electronic excitations energies evolve like $\sim B$. From ref. [69]

In the magneto-Raman scattering experiments, the created electronic excitations have many different momenta in the k_z direction. However, due to the singularities in the joint density of states, mainly massive carriers from the vicinity of K points are probed in the experiment. This is seen in the Raman scattering spectra (Fig. 4.5) since only excitations which energies evolve linearly in magnetic field are observed, which is a hallmark of usual massive quasi-particles. Instead of using the full Slonczewski-Weiss-McClure model to derive expressions for LL evolution in magnetic field, the in plane dispersion of these electronic states can be well approximated by the one of the effective bilayer graphene. The only difference is that the interlayer coupling must be enhanced by a factor of 2 with respect to a true bilayer graphene [36, 159, 53]. This model gives a relatively simple expression for the energies of Landau levels in graphite:

$$E_n^{Gr} = sgn(n)\frac{1}{\sqrt{2}}\left[(2\gamma_1)^2 + (2n+1)E_1^2 - \sqrt{(2\gamma_1)^4 + 2(2n+1)(2\gamma_1)^2E_1^2 + E_1^4}\right]^{1/2} \tag{4.11}$$

Where $E_1 = v_F\sqrt{2e\hbar B}$, v_F is the Fermi velocity and $\gamma_1 \approx 400$ meV is the nearest neighbour inter-layer hopping integral in graphite. So energies of the Raman active electronic excitations in bulk graphite $L_{-n,n}^{Gr}$ are equal to $2E_n^{Gr}$.

Chapter 5

Graphene systems studied

5.1 Graphene flakes on the surface of graphite

Physical properties of solids have been investigated since centuries. However for most part of the history those studies were focusing on the bulk properties. It was not until the beginning of 20th century when importance of the surface effects was realized [160]. But a really rapid progress was made possible thanks to the development, in the second half of the 20th century, the surface selective experimental techniques like: X-ray photoemission spectroscopy(XPS), Auger electron spectroscopy, low energy electron diffraction (LEED), ion scattering spectroscopy, atomic force microscopy (AFM), scanning tuneling microscopy (STM), Dual polarization interferometry (DPI) or surface-enhanced Raman scattering (SERS). Years of experiments showed us that properties of surface can be drastically different than those of the bulk [161]. Adsorption of chemical molecules, surface lattice relaxation [162], surface phonons [163, 164] and plasmons [165, 166] are just a few phenomena that are specific to the surface. Not to mention the recent active research in the field of topological insulators [167].
Graphite is not exempt from that rule. Quite recently if was found that physical properties of its surface are not uniform. Both Raman scattering [168] and scanning tunneling microscopy [96] have shown that some regions on the surface of graphite give a response characteristic of rather a monolayer graphene than of a bulk graphite. Those regions are usually described as either graphene-like inclusions or graphene flakes on the surface of graphite. It seems that they originate from the structural defects (e.g. ridge-like defect [96]) in one of the atomic layers closest to the graphite surface. Those defects may lead to increased inter-plane atomic distance, which decouples the electronic states in the topmost layer from those of the graphite substrate below. Such decoupled flake can then behave like usual mono-layer exfoliated graphene, but showing much higher charge mobility [13] and low concentration of charge doping. This is mainly caused by the fact that graphite constitutes an ideal substrate for graphene due to the same crystal symmetry on the surface and the same lattice constant. Moreover, since those graphene inclusions are not being transfered from one substrate to another, the graphene-graphite interface is never exposed to the environment which could pollute the system.

Below we would like to present the major points about the current state of knowledge about this system, as evidenced by different groups and by various experimental techniques.

5.1.1 STM

Graphene flakes on the surface of graphite were studied in a STM measurement by *Li et al.* [96]. Their work showed that a ridge like defect can electronically decouple graphene layer from the underlying graphite (Fig. 5.1). To prove that properties of decoupled layer are indeed different from the surrounding bulk graphite several independent measurements were performed. In first of them a detailed topography of the graphite surface near the ridge-like defect was done using STM technique. It showed that there are two distinct regions separated by the ridge. One (region B) showed a triangular surface structure as expected from Bernal-stacked graphite. The other (region A) showed a hexagonal structure, as expected from decoupled graphene flake. Then a step height between those regions and an atomic layer below was measured. It showed an increased interlayer separation distance - 0.44 nm for the decoupled flake as compared with the 0.34 nm distance for the coupled region(Fig. 5.1c) and d)).

In the third experiment a tunneling conductance was measured as a function of bias voltage. Obtained quantity is proportional to the local density of states DOS, and it shows a clear change from the linear dependence, which goes to zero at the Dirac point in the decoupled region to the more complex behavior which always shows a finite DOS in the other.

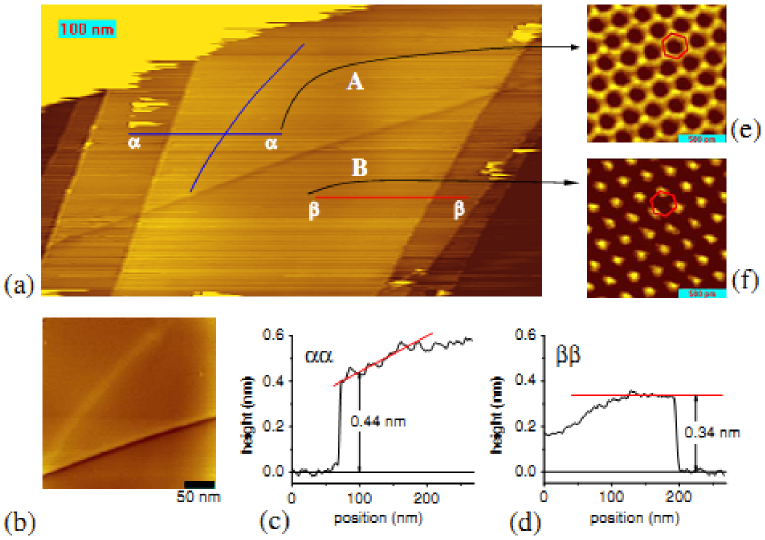

Figure 5.1: a) Topography of graphene layer in the vicinity of two ridge-like defects on the surface of graphite. More pronounced ridge-like defect is the diagonal dark line separating region (A) with a honeycomb structure (panel e)) and region (B) with a triangular structure (panel f)). The fainter one intersecting line $\alpha\alpha$ is shown in b). Panel c) shows a height cross-section along line $\alpha\alpha$. Separation between atomic planes is larger (0.44 nm) near the fainter ridge than the equilibrium value of 0.34 nm measured far away from any ridges- along line$\beta\beta$ in panel d). From ref. [96]

In the fourth experiment a magnetic field up to 10 T was used to induce Landau quantization of the electronic levels which is seen as an appearance of sharp peaks in the measured tunneling conductance. The energy evolution of those peaks followed a characteristic for massless Fermions $E_n = sgn(n)v_F\sqrt{2e\hbar|n|B}$ dependence.
Those measurements show that structural defects, can lead to increased interlayer distance, and electronically decouple the topmost atomic layer on the surface of bulk graphite.

5.1.2 EPR-like technique

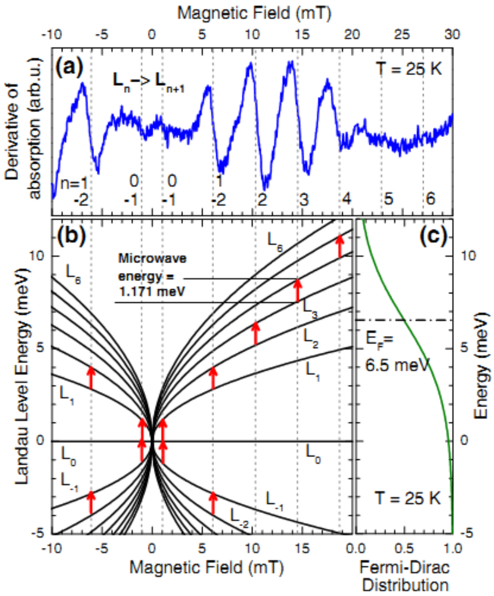

Figure 5.2: a) Magneto-absorption spectrum measured at 25 T and microwave energy $\hbar\omega = 1.171$ meV. b) Landau levels fan chart. Dashed lines mark the magnetic fields where energy levels separation is equal to the energy of microwave radiation (red arrows) c) Fermi-Dirac distribution of carriers for sample with doping level equal to $E_F = 6.5meV$. From ref. [13]

Electron paramagnetic resonance (EPR) known also as an electron spin resonance(ESR) is an experimental technique which is used to study materials which exhibit Zeeman effect. Usually sample is exposed to fixed frequency of microwave radiation in varying magnetic field. When magnetic field dependent energy of Zeeman splitting comes into resonance with applied microwave radiation, electron can be excited between those split energy levels. This is seen as an increase in microwave absorption. The same principle can be applied to low dimensional systems which energy bands become quantized into discrete Landau levels, and excitations between them can be detected. It was used by *Neugebauer et al.* to study graphene inclusions on the surface of bulk graphite [13]. In Fig. 5.2a) result of their magneto-absorption experiment is shown. A set of absorption resonances was observed. Each of them occurring at a magnetic field value corresponding to optically active $L_{n,n+1}$ transitions, for LLs which evolve according to $E_n = sign(n)v_F\sqrt{2e\hbar B|n|}$ rule, which revealed a presence of the relativistic Dirac carriers in the system. This experiment was also performed at higher temperatures which demonstrated that those absorption resonances proved to be persistent up to 50K and showed no sign of broadening. This behaviour is exactly what could be expected from the two-dimensional graphene but not from the three dimensional graphite. Since the energy of used microwave radiation is on the order of $\sim$ 1meV, very low magnetic fields are needed to observe those transitions. Moreover, the lowest magnetic field at which $L_{0,1}$ transition is observed is at $B = 1$ mT, which allows to estimate carrier mobility $\mu > 10^7$ cm^2/(V·s). This value is almost two orders of magnitude lager than in suspended [169, 170] or epitaxial graphene [171]. The high electronic quality of that system is further confirmed by evaluating peak's broadening parameter γ. It's very small value $\gamma = 35\mu eV$ sets limits on both: carrier scattering time $\tau = 20ps$ and mobility

$\mu = 3 \times 10^7$ cm^2/(V·s).
Fitting those measurements to a model allowed to estimate Fermi energy to be $E_F = 6 - 7$ meV, which means that charge doping is lower than $n_0 = 3 \times 10^9$ cm^{-2}.
In summary, EPR-like experiment of *Neugebauer et al.* showed that the electronic quality of graphene inclusions on the surface of bulk graphite surpasses by orders of magnitude other graphene-based systems. In addition to that, very low charge doping make those samples quasi-neutral which is important for instance for the observation of inter-Landau levels, interband excitations in magneto-Raman scattering experiment. Finally the same lattice constant of graphene allows to work with a strain-free system.

5.1.3 Raman spectroscopy

In the same time as the STM measurements gave an evidence of possible existence of graphene like domains on the surface of graphite, a supporting result was obtained using the Raman spectroscopy. *Luk'yanchuk et al.* were measuring the Raman spectra from the different locations on the surface of highly oriented pyrolitic graphite (HOPG) [168]. They observed that the shape of the 2D band is not uniform across the sample but sometimes its lower energy component significantly increases with respect to the high energy side of 2D band. This low energy component is seen at the same energy as single component 2D Raman peak observed in monolayer-graphene (see Fig. 5.3). They have concluded that those changes result from the superposition of Raman signals from graphite substrate mixed with monolayer graphene-like domains. The subsequent magneto-micro-Raman measurements showed that charge carriers in that domains exhibit Landau levels (LL) spectrum that increases with a square-root of magnetic field $\sim \sqrt{B}$ and a square-root of LL index $\sim n$, which is a fingerprint of the Dirac fermions. In that experiments firstly a magneto-phonon resonance (MPR) was observed [109], and then first direct observation of purely electronic, symmetric $L_{-n,n}$ inter-LL excitations in graphene followed [44]. Those excitations proved to be very efficient way to identify those domains since it was shown that they can be observed even at the room temperature [32]. In parallel studies of the magneto-Raman scattering response from bulk graphite were progressing [158, 45]. Raman spectra of graphite also showed peaks corresponding to inter-band LL excitations, but their energy increased linearly with magnetic field which is characteristic for massive fermions. Although linear band dispersion also exist in graphite at the H point of the Brillouin zone, the observed Dirac-like behaviour of carriers is unlikely to come from those carriers, mainly because that particular graphene-like response is not observed on the whole graphite surface. Instead it was always registered on a continuous, well defined and finite region of the graphite surface. The characteristic length of those locations can be as large as $\sim 100\mu$m, but usually smaller flakes are found. They are rather scarce on the surface and not easily observed since they do not give any optical contrast under the microscope. Thus methods based on the analysis of the 2D band lineshape must be used, or if magnetic field is available on observation of inter-LL excitations. Those methods are described in more details in Chapter 7.2.1. Unfortunately, even knowing the method to identify those flakes doesn't guarantee the success, since there may not exist even single one on a surface as large as 3x3 mm. In that case peeling the upper layers with a sticky tape may either expose those graphene domains which lay lower in the bulk, or create them on the surface.

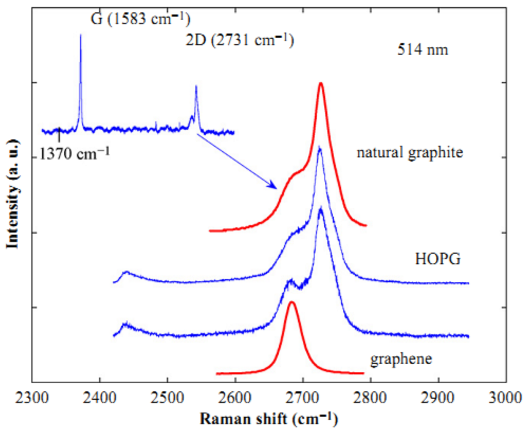

Figure 5.3: The double resonance, 2D micro-Raman band of HOPG graphite (two blue plots in the middle) demonstrates the superposition of the features typical for bulk natural graphite (upper plot with left-shoulder profile) and for the monolayer graphene (lower single-peak plot). The relative weight of these features depends on the position of the laser spot on the surface of HOPG. The typical Raman spectrum of graphite is shown in the upper-left corner. From ref. [168]

The major difficulty in working with graphene flakes found on graphite surface is that they form a system, that is not very well defined. Most notably the degree of coupling graphene flake to the substrate below is not a simply binary state: coupled/decoupled but rather a plethora of intermediate states which depend on the orientation of graphene lattice with respect to graphite below. Various twist angles as well as various lattice defects may lead to many different levels of coupling. This is evidenced by the Raman scattering spectra measured in magnetic field, which sometimes show features corresponding to just a monolayer graphene, other times it also shows weaker features characteristic for graphite. So far it is also not clear if bi-, tri- and multi layers of graphene can be also decoupled in this way. Because the most often used method of analyzing the 2D band shape can hardly be relied on in this particular situation, due to recording a superposition of Raman signals coming from the flake and a bulk below.
In this work we do not aim to answer all these questions. We rather focus on methods how to search and identify these locations using Raman spectroscopy, both with and without magnetic field. In addition to that we report on the observed interaction between inter-LL excitations and phonons present in graphene. Which so far could be only observed in only this type of graphene system, due to its excellent electronic quality.

5.2 Graphene on BN

Extraordinary properties of graphene stem from its peculiar, linear dispersion of electronic bands and its two dimensional nature. The fact that a stable 2D crystal can exist in nature [5] was a great discovery which renewed interest in the research in the area of layered materials. This group includes materials which properties range from metallic ($NbSe_2$), through semimetallic (graphite), semiconducting (MoS_2) and topological insulator (Bi_2Se_3) to insulating (BN). All of them however, share a similar crystal structure, where atoms are tightly bound in-plane by strong covalent bonds while being only weakly coupled to other layers by van der Waals forces. Due to a large anisotropy of physical properties of those materials they were intensively studied in the past in the form of bulk [172, 173, 174, 175], thin crystals (few dozens atomic layers) [176, 177, 178] and intercalated compounds [179]. Up to now, a great progress has been made in the fabrication methods of single atomic layers of those materials. They can be obtained by either micro-mechanical cleaving [5], chemical exfoliation with the help of solvents [180], selective thinning of few-layer sheets by high-energy electron beam [181], graphene growth on the surface of SiC [182, 183] or CVD growth [184, 185] to just name the few most popular methods. This progress in 2D crystals fabrication techniques allowed envisaging production of completely new complex materials. They can be created on demand by intentionally stacking a sequence of layered materials which results in a new structure possessing the desired optical, mechanical and electronic properties [186]. The resulting heterostructures (Fig. 5.4) would exhibit properties of all its constituents which could be employed to create:

- ultra-strong nano-composite materials
- electro-mechanical devices for ultra-fast electronics
- materials with predetermined band-gap and work functions for next generation photovoltaic (solar-cells) applications
- very efficient tunneling field-effect transistors [95, 187, 188]

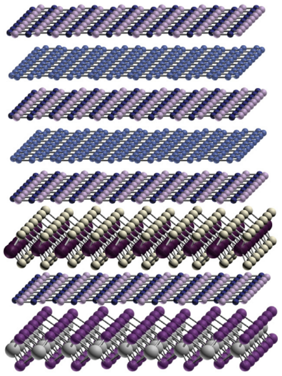

Figure 5.4: Hypothetical example of a 2D-crystals based heterostructure. From ref. [186]

However, although this kind of nano-engineering can be used to create structures with predefined properties, new effects can also emerge due to a weak inter-layer interaction [95, 93]. Currently the widest research in this domain is done on structures made of graphene layers separated by layers of hexagonal boron nitride (hBN). The hBN is especially useful in all applications where an insulating layer is needed due to its wide bandgap 5.97 eV [189]. In addition to that, hBN is structurally isomorphic to graphite, where boron and nitrogen atoms occupy two inequivalent A and B sub-lattice sites in the Bernal stacked structure. The same crystal lattice and similar size of boron and nitrogen atoms to that of carbon leads to a very small (1.7%) lattice mismatch between graphite and hBN [93]. Due to strong, in-plane, ionic bonding of the hexagonal lattice structure, hBN is relatively inert and has much less dangling bonds or surface charge traps as compared with other materials commonly used as a dielectric substrate for graphene. Moreover, the atomically flat surface form an excellent substrate for graphene, which on more uneven surface tends to exhibit ripples. Also dielectric properties of hBN ($\epsilon = 3-4$ and $V_{breakdown}$=0.7 V nm^{-1}) are better than those of SiO_2. In addition to that surface optical phonon modes of hBN have energies two times larger than corresponding modes in SiO_2 which is promising for the performances of hBN/graphene based devices operating at high-temperatures. All those factors speak in favor of replacing the commonly used insulating layer of SiO_2 on top of Si wafer with an atomically flat layer of hBN. Already the first attempts of depositing graphene on $\sim$ 14 nm thick BN flake showed that graphene surface corrugation is reduced three-fold as compared to graphene resting directly on Si/SiO$_2$ [190]. The extreme flatness of the surface and reduced number of dangling bonds results in much smaller disorder-induced carrier density fluctuation. Obtained values $\delta n \sim 10^9$cm-2 [95] are about two orders of magnitude lower than in graphene samples on SiO$_2$, while being only one order of magnitude higher than values measured for a suspended graphene samples [169]. In the same time density-independent mobility μ_C was observed to be more than three times higher ($\mu_C = 60000$ cm^2 V^{-1}s^{-1}) than typical values obtained at SiO$_2$ substrate [191].

All those results show that depositing graphene on an atomically flat hBN surface offers many advantages as compared to other types of graphene-based systems. The most straightforward one is the possibility to study properties of graphene in a quasi-neutral doping regime and low defect density environment. Although the achieved electron mobilities in hBN-graphene structures are not yet as high as the record values observed in graphene flakes floating on the surface of bulk graphite [13], they can be matched only by the values seen in suspended graphene samples. Yet BN-graphene system has a significant advantage over the other two mentioned graphene-based systems [169]. The former one is not a well defined system. It is difficult to exclude *a priori* layers stacking effects and interaction of detached flake with bulk graphite below. The latter one suffers from the need of complicated substrate etching process in order to be able to suspend a graphene flake over a small trench or hole in the substrate. Even after a successful deposition of exfoliated flake over such hole, those samples are known for its fragility due to lack of mechanical support below. Also a small bending of such flake due to the gravitational force adds effects of strain. Graphene deposited on hBN is free of such problems. Contrary to the case of graphene on graphite (Sec. 5.1) exfoliated graphene is a very well defined system. The exact number of layers in the flake can be cross-checked using a number of techniques (e.g. Raman, AFM) before transferring it to the hBN substrate, and in case of few-layer graphene samples, also their stacking order can be determined. On the other hand, since graphene on hBN is laying on a solid substrate it is mechanically stable, and strain-free. Additional caping layer of hBN can provide an extra protection against environmental contamination, thus reducing the effect of aging.

Unfortunately, production of such stacked structures is extremely difficult and at the moment only few groups in the world are able to make them. The production process involves several exfoliation steps, followed by transferring flakes one on top of the other. This transfer process is done nowadays manually, and therefore requires much skill and experience to produce good quality samples. This technique naturally limits the size and scalability of the obtained structures. So there is a great need to research new techniques, based probably on variations of CVD or MBE processes, that would allow to implement those structures, in the future, on the industrial scale.

The extraordinary properties of graphene flakes deposited on hBN surface has incited quickly growing interest in studying properties of that system. It has already resulted in first reports about its transport properties [190, 95, 192, 193, 94], however there are still just few about its optical properties [193, 194, 195], and basically none about magneto-optical. We hope to contribute to the great effort of scientific community aiming into unraveling those properties by presenting our results of a magneto-Raman scattering experiments performed on graphene-BN composite system in Chapter 8.

5.3 CVD grown graphene

The outstanding mechanical, electronic and optical properties of graphene make it a promising material for many future applications. It has been demonstrated that the performance of field-effect transistors, where silicon is replaced by a monolayer graphene, greatly benefits from the exceptionally high mobility of carriers in graphene [196, 197]. Using graphene as a transparent conductive electrodes is yet another example of its possible application. The currently used materials like e.g. indium tin oxide (ITO) or fluorine tin oxide (FTO) suffer from: i) the scarcity of some of the elements (like indium) in the Earth crust, ii) their instability in the presence of acid or alkali ii) their susceptibility to ion diffusion into polymer layers and iv) their limited transparency in the near-infrared region [198]. These problems can be overcome by substituting the currently used materials with a monolayer graphene [199, 198]. This is possible due to the abundance of carbon in the nature, the high chemical stability of graphene, its impregnability to the gases, and a flat absorption in the very wide spectral range [200].

However for all these applications the large area graphene sheets are required, often much lager than 1 cm^2 in area. The historically first method of graphene production – the mechanical exfoliation doesn't yield flakes larger than about tens of micrometers across. Therefore, it cannot be used for the industrial scale processes. Nevertheless, there are other methods of producing monolayer graphene that can be easily scaled up. Among them the chemical vapor deposition (CVD) is probably the most promising one. In this method a gaseous precursor, like e.g. methane, is supplied over a flat metallic surface. The high temperature, on the order of 1000 °C, causes decomposition of the precursor, and the metallic surface acts like a catalyst on which a thin layer of carbon atoms deposits. Mostly, polycrystalline nickel (Ni) [201, 184, 202] or copper (Cu) [203, 188, 204] foils are used as a substrate. In the last step, the graphene sheet is transfered to the desired substrate, usually insulating, after etching away the metallic foil.

This relatively simple and low-cost method has been successfully applied to produce graphene that can reach impressive sizes. Rectangular, graphene sheets as large as 30

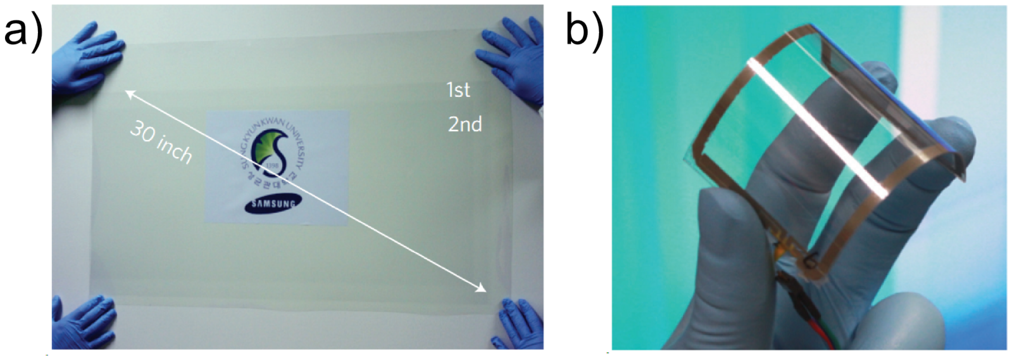

Figure 5.5: Photographs of the graphene sheets produced in a CVD process. a) a transparent, large-area graphene film transferred on a 35-inch polymer (PET) sheet. b) an assembled graphene/PET touch panel showing outstanding flexibility. From ref. [205]

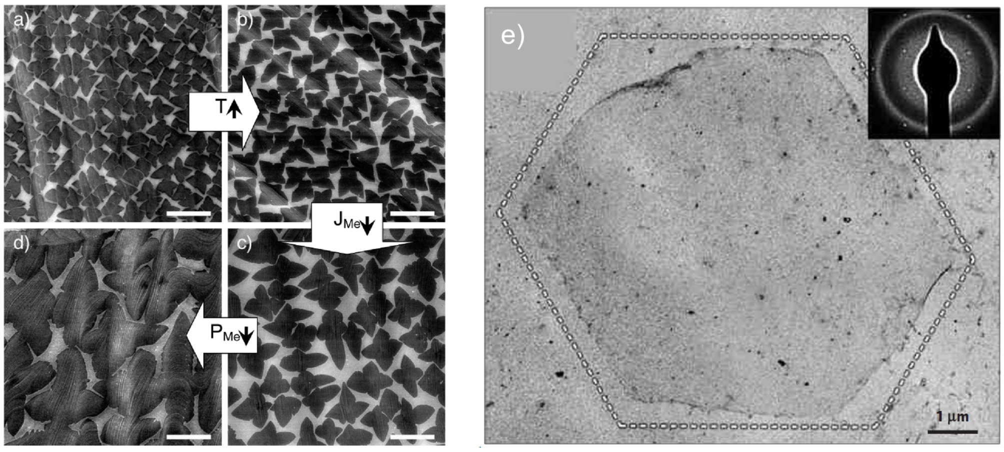

Figure 5.6: a)-d) Scanning electron microscope picture of the CVD grown graphene partially covering the copper substrate. The leaf-like shaped graphene grains have sizes that changes with the growth parameters: temperature (T), methane flow rate (J_{Me}) and methane pressure (P_{Me}). From ref. [206]. e) Transmission electron microscope picture of the CVD grown graphene with a hexagonal grain shape. From ref. [210].

inches across have been obtained and transferred to another substrates (see Fig. 5.5a). Electronic quality of such CVD grown graphene is high enough to make a working, flexible transparent electrode (Fig. 5.5b). However, the large-scale synthetic graphene films, produced so far, are typically polycrystalline [203, 206]. They consist of many single-crystalline grains separated by grain boundaries [207, 208]. The location of those grains is largely random and uncontrolled during the growth. As the growth of these grains proceeds, they coalesce and eventually form an interconnected polycrystalline film. The grain boundaries largely degrade the electrical [206, 209, 210] and mechanical [211] properties of the resulting films. The carrier scattering on the graphene boundaries leads, for example, to lower carrier mobilities than those found in the monocystaline exfoliated graphene. This problem may be partially overcome by stopping the growth process at a stage when graphene grains are still smaller than the average distance between these grains. This results in substrate surface being only partially covered with graphene. Each graphene grain is monocrystaline, but their sizes usually do not exceed $\sim 10\mu m$ [206] in diameter. By controlling the growth parameters, such as the temperature, the precursor gas pressure and the flow rate, it is possible to change the size distribution and even the shape of the monocrystalline graphene grains. The shape of these grains reflects the sixfold rotational symmetry of the graphene lattice, and the grains usually take form of either hexagons or more irregular, leaf-like shape (see Fig. 5.6).

The monoclystalline graphene grains have higher carrier mobility than the larger polycrystalline graphene sheets. However their mobility μ usually strongly varies from one grain to another and does not exceed few thousands $\mathrm{cm}^2\mathrm{V}^{-1}\mathrm{s}^{-1}$. With the exception of one report about CVD graphene flake with $\mu = 16000$ $\mathrm{cm}^2\mathrm{V}^{-1}\mathrm{s}^{-1}$ [206], most of the groups are able to obtain now CVD grown samples which mobilities vary in the range $\mu = 800 - 6000$ $\mathrm{cm}^2\mathrm{V}^{-1}\mathrm{s}^{-1}$ [210, 203, 184, 212]. The main sources of the carrier scattering, which limits the mobility, are the grain boundaries and defects that are created during the fast cooling [203] and transferring the sample from one substrate to another.

The other factor that deteriorates the properties of CVD grown graphene is the occurrence of bilayer inclusions around the nucleation centers. Carbon atoms have a tendency to accumulate faster around those nucleation centers than at the edges of the graphene grain. This frequently results in forming an additional layer of graphene, somewhere in the center of the grain, that can typically cover up to $\sim 10\%$ of the underlying graphene layer. However, by using the alternating pulses of hydrogen gas and precursor/hydrogen gas mixture it is possible to obtain monolayer graphene grains without this second layer [212].

Chapter 6

Experimental setup

6.1 General description

All experiments which are presented in this work are based on an inelastic light scattering technique (the Raman scattering), mostly in the presence of an intense external magnetic field. Optical experiments which are performed at high magnetic fields require a specially designed optical setup due to very limited space inside magnet coils. Fig. 6.1 shows the

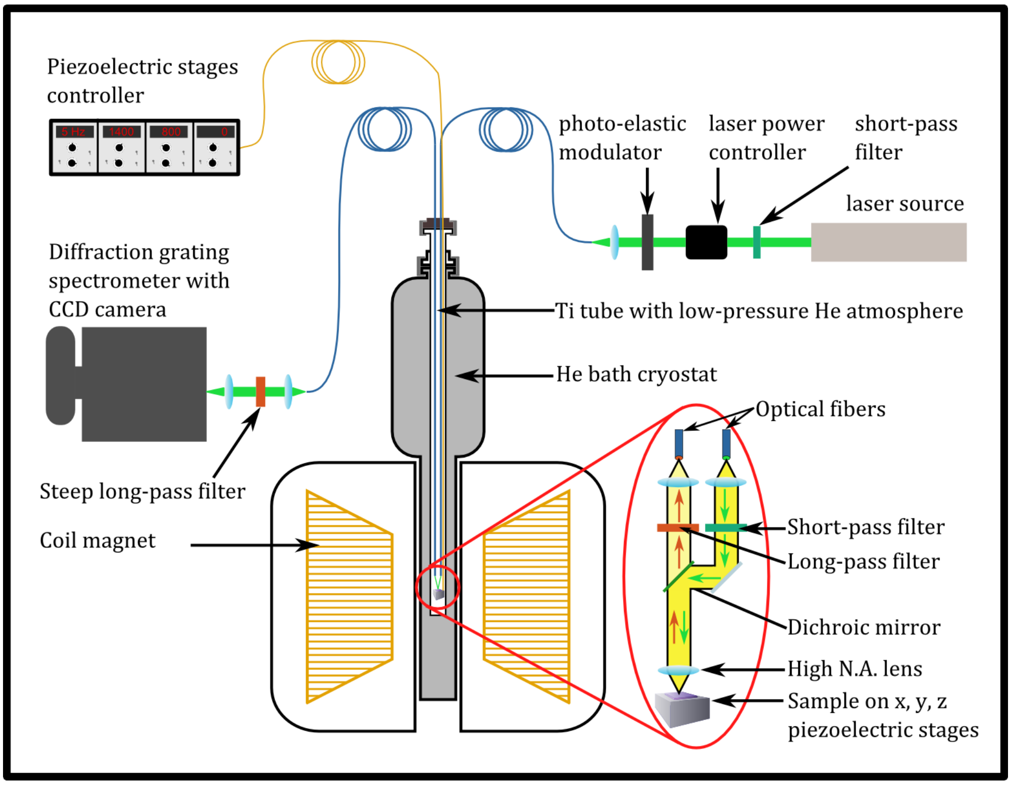

Figure 6.1: Experimental setup used in micro-magneto-Raman scattering experiments in non-polarization resolved configuration.

experimental setup used in our experiments. It consists of four major parts: the excitation light source, the micro-Raman probe which contain the investigated sample, the detection part and the magnet coil with cryostat.

Excitation

Since, the intensity of the Raman scattering signal is proportional to the excitation power and is generally six orders of magnitude lower than that of the elastically scattered light, a strong source of monochromatic radiation is needed in the experiment. For that reason we used a laser radiation as the excitation source. Two types of lasers were used in our experiments: an argon-ion laser which have a very intense laser line at $\lambda = 514.5$nm and that was used for most experiments. In few experiments a tunable Ti:sapphire laser was used instead. It was working in the continuous wave(CW) mode of operation and was pumped by a semiconductor diode laser (Millenia) using a second harmonic line at $\lambda = 532$nm. In principle Ti:sapphire laser could be used at any chosen wavelength in its operating range ($\lambda = 650 - 1100$nm) but the need to use dichroic mirror and a set of low-pass and high-pass filters inside the micro-Raman probe limited our choice to wavelengths for which we possessed a full set of optical filters, namely $\lambda = 720$ nm and $\lambda = 785$ nm. In order to obtain spectrally clean laser beam, either a laser-line dielectric filter or a small prism based on a monochromator was used. For controlling the laser power a Laser Power Controller (Brockton Electro-Optics Corp.) was used. It uses the fact that laser beam is linearly polarized to dynamically attenuate the laser beam due to Pockels effect in liquid crystals. This not only allows us to vary the excitation power, but also stabilizes it against time variations. Next optical element that is used in our setup is the photo-elastic modulator PEM-90 (Eqipments scientifique). It is operating on a principle of photo-elastic effect, in which a mechanically stressed sample (transducer) exhibits a birefringence proportional to the resulting strain, which oscillates with the frequency of 50kHz. When the crystal axis is set at the angle of 45° to the linearly polarized laser beam one component of the propagating light is retarded with respect to the other. The retardation amplitude is time-dependent and follows the sinusoidal modulating signal of the strain applied to the transducer. When the maximum amplitude is chosen appropriately to the wavelength of the incoming light, photo-elastic modulator acts as a quarter-waveplate when the retardation amplitude is at its maximum. It results in modulating the laser beam polarization in time. It oscillates between linear, through elliptical to right- and left-circular polarization at high frequency of the modulating signal. Those temporal variations in the beam polarization can be viewed as using a non-polarized light, since the shortest acquisition times in our experiments are on the timescale of seconds, which effectively averages over many different light polarizations. This laser beam depolarization was needed due to large Faraday effect exhibited by optical fibers in the micro-Raman probe for a linearly polarized light. This resulted in a large modulation of excitation power, in magnetic fields, and in consequence in the modulation of the intensity of scattered light.

Micro-Raman probe

The micro-Raman probe or insert is the central part of our experimental setup. It is essentially a frame on which a miniaturized optical table has been build, that can be easily manipulated and inserted into a cryostat inside the magnet coil. The whole probe is protected by an additional vacuum-tight tube and filled with He gas at pressure $p = 150 - 250$ mbar which acts as an exchange gas to provide a thermal conductivity between the sample and the environment (in most cases the cryostat at temperature $T = 4.2$ K). Due to the large magnetic fields used in our experiments and the need for high rigidity and low thermal conductivity of the probe, a titanium was chosen as the main material used in its construction. Partially, because it is paramagnetic, have low thermal conductivity and very high tensile strength, and partially because the piezo-electric stages, that are used for positioning the sample in the probe, are made of titanium. Since the probe has been always aligned at the room temperature and then, during the experiments, cooled down to 4.2 K, it was important to use the same materials for the whole probe to avoid misalignment due different thermal expansion of each part.

The light is injected and collected from the bottom part of the probe by two optical fibers which provide a convenient way to couple the optical elements of the probe with excitation and detection part of experimental setup. Inset on the right hand side in Fig. 6.1 shows the scheme of the bottom part of the probe. The light is injected by a mono-mode optical fiber with 5 μm core. Then is collimated by a lens and passes through low-pass filter which is chosen appropriately to the used laser wavelength. The high intensity of the laser light induces a luminescence in the optical fiber which overlaps later with the Raman signal if the low-pass filter is not used. Then the laser beam is reflected from one silver and one dichroic mirror. The dichroic mirror allows us to reflect the full intensity of the laser beam, while it transmits all scattered light at the higher wavelengths. Then the laser beam is focused on the $\sim 1\mu$m spot on a sample by a high numerical aperture (N.A.) lens. The backscattered light is then collected by the same lens.

Using a high N.A. lens improves the intensity of the collected signal due to large collection angle, but it also leads to working effectively in a quasi-backscattering geometry where not only strictly back-scattered light is collected but also light scattered at slightly higher angles. This may lead to the observation of Raman features that would be normally inactive due to selection rules which are mostly derived for a strictly back-scattering geometry. The collected light passes then through a dichroic mirror and sharp edge high-pass filter which reduces intensity of the elastically backscattered laser light. But in the same time also blocks the scattered light at energies close to the laser, which set a limit on the possibility to observe low energy excitations. In our case the cut-off energy was at ~ 100 cm^{-1}. Finally, the light is collected by a multi-mode fiber with 50 μm core. The small diameter of the collection fiber acts as a pinhole in a confocal microscope setup, which improves our axial resolution.

The sample is mounted on a set of the piezo-electric stages (Attocube), which can move it in three different directions with a ~ 0.5 μm step accuracy. Two of them allow moving in a plane perpendicular to the laser beam and are equipped with encoders that enable to record the position where the measurement was performed. It was essential for doing the spatial maps of the Raman scattering from the sample. The third stage moving in the direction parallel to the light propagation (and the magnetic field) was used for fine-

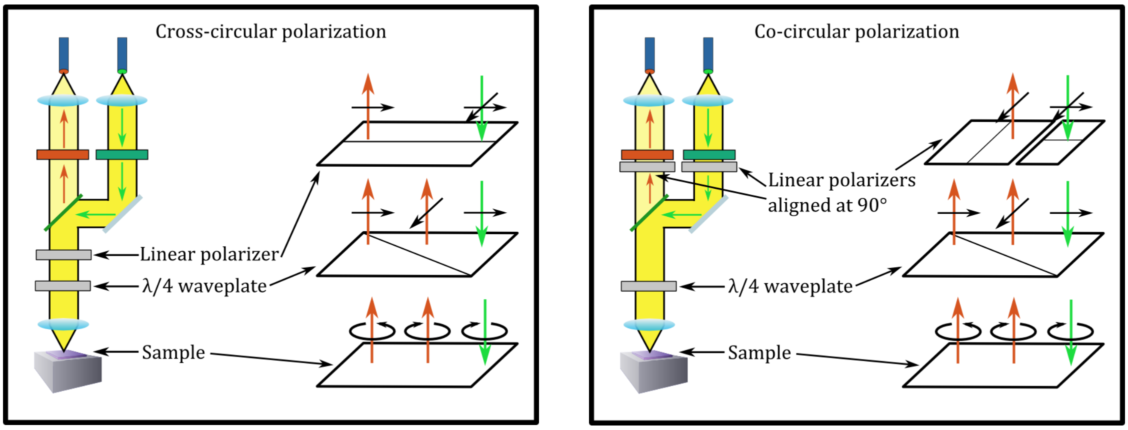

Figure 6.2: Micro-probe configurations for polarization resolved experiments. Left: for cross-circular configuration, Right: for co-circular configuration.

focusing the laser light on the sample surface.

Detection

In the detecting part of our setup, the light from the fiber is first collected by a lens, then goes through another sharp edge high-pass filter to further reduce the scattered laser light intensity. It is then focused on the spectrometer entrance slit. For light dispersion we used one of the two the same Acton SP2500 spectrometers (Princeton Instruments) with 0.5 m long optical path and four different gratings with either 300, 600, 1800 or 2400 groves per mm. A back-illuminated, cooled with liquid nitrogen CCD camera was used. Detector based on Si provided a good quantum efficiency in all the visible and near infrared range of energy, up to $\sim 950-1000$nm.

Polarization configurations

When information about the circular polarization of scattered light is needed, micro-Raman probe can be modified to excite the sample with circularly polarized light and to collect only this light that have the same or opposite circular polarization. In magnetic field instead of speaking about left- and right-circular polarization which is defined with respect to the direction of propagation of light, the $\sigma+$ ($\sigma-$) notation is used, which defines the circular polarization of light with respect to the direction of external magnetic field. Fig. 6.2: Left shows a setup configuration that is used in cross-circular polarization, i.e. when the scattered light has the opposite circular polarization than the incoming laser light. Or in other words when scattering process involves transfer of $\pm 2\hbar$ quantum of angular momentum to/from the sample. For that purpose a single set of linear polarizer and a quarter-waveplate set at 45° angle to each other, are used to circularly polarize the incoming laser beam and to analyze the scattered light. This configuration is later on often referred to as $\sigma+/\sigma-$ configuration, where the first term describes the polarization of the incoming beam while the second of the scattered beam. Since $\sigma+/\sigma-$ polarization are defined with respect to the external magnetic field direction, it is enough to simply reverse the magnetic field direction to switch to the $\sigma-/\sigma+$ polarization configuration.

It is particularly useful since it does not require removing the probe from the cryostat and can be achieved by changing the direction of the current flow in the magnet coil. When the scattered light is expected to have the same circular polarization as the incoming beam, the co-circular configuration is used, often denoted as $\sigma + /\sigma +$. In this configuration there is no net angular momentum transfer. Fig. 6.2: Right shows the configuration of a micro-Raman probe for doing this type of experiment. Two linear polarizers twisted at 90° angle to each other, are used in this configuration, both of them set at 45° to the axis of the quarter-waveplate. Here again changing the direction of the magnetic field allows to switch between working in the $\sigma + /\sigma +$ and $\sigma - /\sigma -$ configurations.

Magnets

High magnetic field used in our experiment was provided by two types of magnets: superconducting and resistive ones.

The superconductive magnet was based on a Nb_3Sn superconducting solenoid that can achieve fields up to 14T. Due to its critical temperature $T_c = 18.3$ K it has to be kept at low temperature by liquid He bath($T = 4.2$ K), which is further isolated from the environment by an additional outer jacket containing liquid nitrogen ($T = 77$ K). The biggest advantage of superconducting magnets is no need for expensive cooling during the operation, due to the fact that high current flowing through the superconducting wires does not dissipates in the form of Joule heating. It can be used in two operating modes. In first of them the magnetic field is slowly swept between two chosen values (in the range 0-14 T) by changing the current flowing through the magnet coil. In this process the energy is consumed for energizing/de-energizing the solenoid. On the other hand, a constant value of the magnetic field can be maintained for a long time when the superconducting coil is short circuited. In this persistent mode of operation no energy is needed to sustain the high current flowing through superconducting coil, which permits to perform long measurements at high and very stable magnetic fields. The main advantages of the superconducting magnets over the resistive ones are:

- smaller amount of electrical power needed to deliver high magnetic fields
- possibility to work in persistent mode, when no power is consumed to sustain a high magnetic field
- magnet cooling is needed just to keep the wires in a superconducting state (new types of magnets can achieve it even without the need of cryogenic liquids)

The main limitation for this type of magnets is the maximum magnetic field (H_c) they can sustain. At a critical value of magnetic field the coil goes out of the superconducting state into a normal resistive faze, which limits the highest magnetic fields that can be achieved by those magnets. Up to now fields as high as 22T can be achieved by this method, and the further progress depends very much on the progress in the research of new superconducting materials with higher critical field H_c.

The highest magnetic field (B=30 T) we were able to obtain by using a resistive magnet. In this type of magnet, the solenoid is made out of normal resistive metal (copper), that can sustain a very high current and which generates large amount of heat. The main limitations for this kind of magnet are set only by the amount of heat that can be evacuated by the use of high-debit water cooling system and by its mechanical resistance to the large stresses due to Lorentz forces. The resistive coil used mainly in this work consists of two outer Bitter coils (inner diameter 400 mm) with a polyhelix insert. The Bitter coils are made of thin circular metallic sheets separated by insulating layers and stacked in a helical pattern. The resistive polyhelix insert consists of a set of concentric coils, each constructed by cutting a helicoidal line into a copper tube. The geometry of this insert is then optimized in such a way that it allows producing very high continuous magnetic fields.

Chapter 7

Results: graphene on graphite

7.1 Introduction

Motivation and content

Graphene flakes that can be found on the surface of graphite exhibit unprecedented electronic quality and low charge doping [13]. This enables a direct observation of inter-Landau levels (LL) electronic excitations [44, 32], which is so far not possible in the most commonly studied exfoliated mono-layer graphene flakes deposited on Si/SiO$_2$ substrate. In the latter case the high doping due to charges trapped in between graphene flake and substrate, as well as due to dangling bonds of Si atoms severely obscures the magneto-phonon resonance and makes direct observation of inter-LL excitations in Raman spectra unfeasible.

In this chapter we present results of a series of magneto-Raman scattering experiments performed on graphene flakes found on the surface of natural graphite. We start by presenting the representative spectra of graphene inclusions and of the majority of graphite surface at a chosen value of the magnetic field. Based on them a set of criteria is proposed, which can be employed when searching for those flakes in two situations: when a source of strong, constant, magnetic field is available or not (Sec. 7.2.1). Then we present magnetic field evolution of inter-Landau levels(LL) excitations that can be usually observed in that system (Sec. 7.2.2), and which confirm the linear dispersion relation of carriers in studied flakes. Afterward we discuss the characteristic features of those inter-LL magneto-excitons. First, Raman spectra measured at room temperature (RT) are compared with those measured at liquid helium temperature (4.2 K) (Sec. 7.3.1). Then we explore how their intensity depends on laser excitation energy and compare it with existing theoretical predictions (Sec. 7.3.2). Then their lineshape variation (Sec. 7.3.3) and coupling of $L_{-1,1}$ mode to Γ phonon (Sec. 7.3.4) are discussed. In the next section (Sec. 7.4.2) we report a clear observation of $L_{0,1}/L_{-1,0}$ finestructure at high magnetic fields and discuss its possible origin. Finally, the most significant result of this chapter is presented in section 7.5, where we report a first observation of resonant effects between inter-LL electronic excitations and other excitations, which we identify as K point and near Γ point phonons. The specific values of magnetic field strength and inter-LL excitation energies at which the resonances are observed can be understood in the framework of two models: general one based on opening a new relaxation channel (Sec. 7.5.2) and more detailed one based on resonant coupling of two or three different excitation modes (Sec. 7.5.3).

Experimental details

Magneto-Raman experiments presented in this chapter, were performed on few different graphene flakes which we found on the surface of natural graphite crystal. Before each experiment, the topmost graphite layers were peeled off using a weakly adhesive tape, in order to remove those layers which were exposed for a long time to the atmosphere and possible contaminants. This allowed us to study the clean, freshly made graphite surface. From the experimental point of view we used the custom made micro-Raman insert, that can be used for studies in magnetic field, as described in Chapter 6. All experiments were performed at a liquid helium temperature (4.2 K), except those discussed in section 7.3.1 which compares results measured at ambient temperature ($\sim 290K$) with low temperatures (4.2 K). Similarly, for excitation a 514.53 nm line of the argon ion laser was generally used, except for the section 7.3.2 which compares Raman spectra measured using 720 nm line from a tunable Ti:Sapphire laser with those obtained under 514.53 nm excitation. In every experiment similar laser power was used – 5 ± 1 mW, as measured on the sample. It was high enough to provide a reasonable number of scattered phonons, and thus high quality spectrum could be obtained on a timescale of ~ 2 min., yet at the same time it was low enough to do not induce any thermal effects. Unless stated otherwise for a given experiment, usually a non-polarised detection configuration was used. In the same time much care was taken to depolarize the exciting laser beam before light entered the optical fibers, by the use of photoelastic modulator (see Chapter 6). Nevertheless, the remaining small variation in the excitation power in changing magnetic field due to Fraday effect in optical fibers had to be compensated in recorded Raman spectra. It was done by normalizing the intensity of the whole spectrum with respect to intensity of spectral features that were supposed to be constant in magnetic field. Although those intensity variations can reach even up to 30% of the background level, they occurred at much larger magnetic field scale than the reported resonant inter-LL broadening and affected intensity of the whole spectrum, instead of just the inter-LL Raman peaks for the discussed effects. Therefore those two effects – Faraday effect in optical fibers and actual variation in intensity and linewidth of inter-LL excitations could be easily distinguished and separated. As a result, the obtained Raman spectra were not sensitive to any given light polarization, enabling us to observe at the same time $\Delta|n| = 1$ and $\Delta|n| = 0$ excitations, at the expense of loosing information whether they were $\Delta n = +1$ or $\Delta n = -1$ transitions.

7.2 Identification of the graphene inclusions on the surface of graphite

The exfoliated monolayer graphene flakes can be observed under an optical microscope due to light interferences in graphene and thin layer of SiO_2 below. Optical contrast can be maximized by the appropriate choice of SiO_2 layer thickness and illumination wavelength [213]. Thus providing a fast and easy method for finding small graphene flakes. Unfortunately, this approach is difficult to use to find graphene flakes on the surface of graphite, since the refractive index of graphene and graphite substrate are essentially the same. Therefore other methods have to be employed to localize those flakes. In the following part of this section we describe a method based on differences in spectroscopic features of Raman scattering signal obtained on graphite and on graphene. Thus by scanning the graphite surface and recording the Raman scattering response it is possible to identify regions where monolayer graphene inclusions exist. We start by presenting results of such scanning or mapping procedure at constant magnetic field $B = 10$ T. At this value of magnetic field a strong Raman peak corresponding to $L_{-1,1}$ magneto-exciton is expected to be seen in the spectral range between G-band and 2D band. Therefore it can be used for identification of graphene flakes when magnetic field is available. Once a flake has been found we turn to analysis of 2D band lineshape, which is very weakly dependent on the magnetic field B. The found differences in its lineshape measured on graphene flake and on pure graphite substrate can be later used as a criterion for finding graphene flakes on the surface of graphite when no source of strong magnetic field is available for the experimentalist.

7.2.1 Spatial mapping at constant magnetic field

In order to find graphene-like inclusions a spatial mapping of Raman scattering response form graphite surface was performed. This is a relatively slow but reliable method to find graphene flakes. It is based on acquisition of Raman scattering spectra from each point of a regular array of them. Naturally sample area that can be scanned using this method depends on the acquisition time at each point, total number of points where measurement is performed and a distance between them. In practice a 10 hour experiment allows to scan a a region of 1.5 mm × 1.5mm with a distance between points $\sim 30\mu$m and acquisition time ~ 20 s. Such spacing of measurement points allows us to detect the largest flakes, which characteristic length often exceed 50μm. This procedure can be also sped up by scanning and recording Raman spectra in a real time with $1 - 2$ s refresh rate which is enough to see a weak trace of $L_{-1,1}$ excitation at magnetic field $B = 10$ T. Here we used a combination of those two methods to find a $70 \times 70\mu$m area which have shown an additional Raman peak in the spectral range between G-band and 2D band at $B = 10$ T. To illustrate the differences in Raman spectra characteristic for the overwhelming majority of the graphite surface with those measured on a very specific small area, their representative spectra are compared in Fig. 7.1. The black curve is a Raman spectrum of a graphite surface, while the red one is a spectrum of graphene flake of a regular shape, being roughly 70μm long in diameter. In order to facilitate comparison of relative magnitudes of Raman features, red curve has been rescaled to

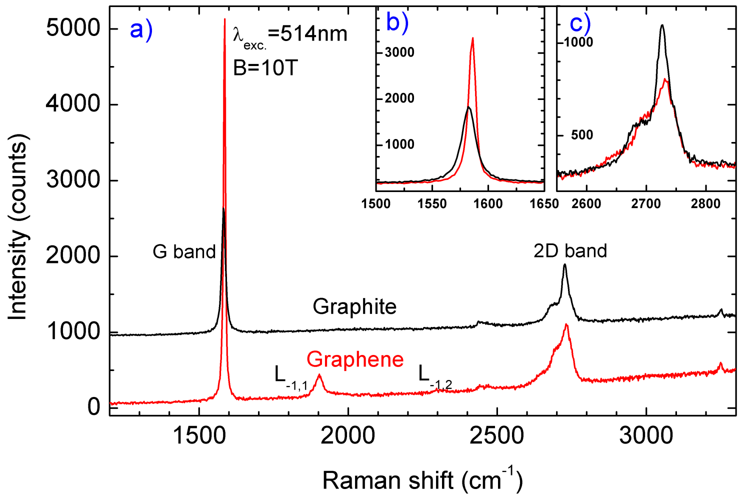

Figure 7.1: a) Spectra of two locations on the surface of bulk graphite. Upper characteristic for most of the surface area, the lower one from a graphene-like inclusion having an irregular shape with dimensions of roughly $70x70\mu$m. Lower spectrum was rescaled to have the same 2D band height as the upper one. b) G band and c) 2D band for not rescaled spectra. Measurement done in non-polarized configuration, using $\lambda_{exc} = 514$ nm and at magnetic field B=10T. Should be compared with Fig. 2.5left).

have the same intensity of 2D band as in case of graphite. Although they share many similarities like two most pronounced Raman peaks- G-band at ~ 1580 cm^{-1} and 2D band at ~ 2700 cm^{-1}, there are also some differences. The most striking one is an appearance of two additional Raman peaks in graphene as compared with graphite. First pronounced one is seen at 1904 cm^{-1} while the other, much smaller, at 2300 cm^{-1}. Which is where we would expect to see $L_{-1,1}$ and doubly degenerate $L_{-1,2}/L_{-2,1}$ electronic excitations in monolayer graphene. Since the energy of those interband excitations:

$$E_{n,m} = v_F\sqrt{2e\hbar B}(\sqrt{n} + \sqrt{m}) \text{ , for } n \cdot m < 0$$

depend only on one parameter v_F, we can extract it from position of the observed peaks. It turned out to be $v_F = 1.029 \times 10^6$ m/s which agrees up to few percent with previously reported v_F values on such graphene inclusions [96, 13].

There are however also other important differences between those two Raman scattering spectra. It was early reported by *Ferrari et al.* [69] that contrary to graphite where the G band is the most pronounced Raman feature – dominating over the 2D band, in graphene it is much less intense. Thus G and 2D bands intensity ratio $I(G)/I(2D)$ change from ~ 2 in graphite to $\sim 1/4$ in graphene.

In our case G band is not only all the time the most intense Raman feature, but it becomes even more intense at graphene-like inclusion, with the ratio reaching $I(G)/I(2D) \approx 6$. Insets in Fig. 7.1 present the same spectra but before any rescaling. It shows that G band is not only relatively more intense for graphene inclusion but it is also more intense in absolute values. However, we have performed the sample mapping at magnetic field $B = 10$ T, so the $I(G)/I(2D)$ ratio had been seriously distorted by the magneto-phonon resonance, therefore its absolute values shouldn't be compared directly with the ones

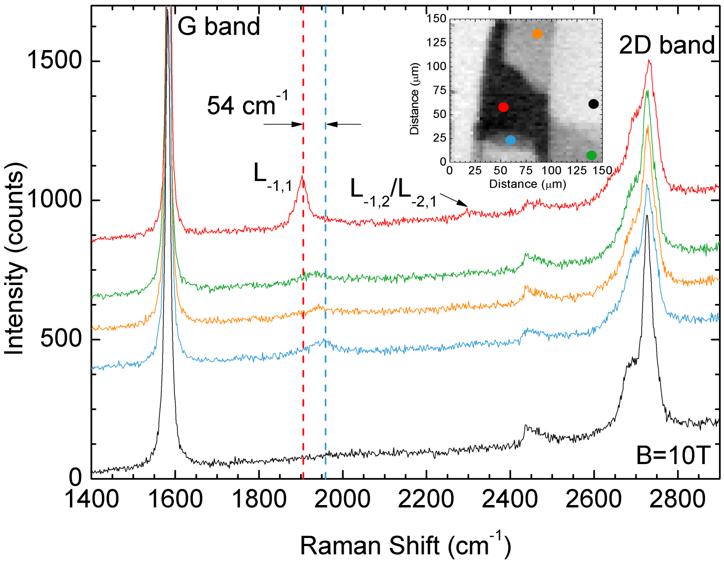

Figure 7.2: Raman spectra of chosen points on the surface of graphite obtained at magnetic field B=10T, $\lambda_{exc.}$=514.53nm and T=4.2K. Inset shows spatial distribution of $L_{-1,1}$ excitation intensity, where black(white) colour indicates high(low) intensity. Three distinct regions can be seen: light gray-graphite substrate, black-graphene-like inclusion, dark gray-intermediate layer. Each point in the inset corresponds to a curve with the same colour, indicating position where measurement was performed. Acquisition time 15s.

given by *Ferrari et al.*. The ~ 3 cm^{-1} up-shift of the G band in graphene, as compared with graphite, is yet another sign of the magneto-phonon resonance in monolayer graphene. It is caused by the interaction between E_{2g} phonon and $L_{0,1}$ excitation leads to an anti-crossing at $B \sim 25$ T. The effect of this interaction can already be seen at $B = 10$ T as a few cm^{-1} up-shift of phonon frequency. Those changes in the G band position and intensity confirm that the investigated flake behaves like a graphene monolayer and not like graphite.

Finally, the third striking difference between a graphene inclusion and an exfoliated graphene flake is the shape of the 2D band. The latter one has a characteristic single component Lorentzian shape which distinguishes it from bulk graphite [69]. The former one has a three components shape, with two major components at positions close to that of graphite 2D band, plus an additional small shoulder on the low energy side. This is most probably a result of superposition of Raman spectra from the graphene flake on the surface and Raman spectra from the bulk graphite below.

In order to verify spatial homogeneity of the flake we have made a detailed mapping of that area at magnetic field $B = 10$ T, with a spatial resolution of 3μm, and compared spectra from the map. Then it turned out that not two but three distinct classes of spectra can be found in these area. They are presented in Fig. 7.2, where the topmost curve corresponds of graphene monolayer, the lowest lying one to graphite substrate, while the three middle ones to three points on an area around the main flake, which we believe correspond to another layer of partially decoupled graphene flake.

The most pronounced difference between those curves is the intensity of scattered light at the energy of $L_{-1,1}$ excitation peak in graphene (1870-1930 cm^{-1} at B=10 T). It can be used to visualize those different regions by plotting in the form of gray scale intensity map the spatial distribution $L_{-1,1}$ excitation intensity, which is shown in the inset of Fig. 7.2. There, black(white) colour denotes a high(low) $L_{-1,1}$ intensity. The graphite substrate is seen as a light gray area around the flake, where no sign of $L_{-1,1}$ excitation is present (black curve in the graph). The flake itself is seen as a black region in the center of the map, which exhibits strong Raman peak at $\sim$ 1900 cm^{-1} and a small shoulder at $\sim$ 1960 cm^{-1} (red curve in the graph). Finally there is also another L-shaped region, seen as dark gray area where $L_{-1,1}$ Raman peak is also seen, but it is much less intense, broader and up-shifted to $\sim$ 1960 cm^{-1}. Locations in this region show some variation in the intensity and energy of the $L_{-1,1}$ peak, as well as in the shape of 2D band which is illustrated by the three middle curves in Fig. 7.2. Since all those measurements were performed in the same conditions, we propose to use the intensity of the $L_{-1,1}$ peak as an indirect measure of the amount of monolayer graphene response in the scattered Raman signal. For each spectrum, an amplitude of the $L_{-1,1}$ peak was measured and normalized with respect to its maximum value, found in the black region. Now we focus on the lineshape analysis of 2D band. In the first approximation it consist of two peaks: smaller one, at lower energy value ($\sim$ 2680 cm^{-1}) and larger at higher energy ($\sim$ 2730 cm^{-1}). We noticed that the energy position, the full width at half maximum (FWHM) and the area of the two of them are strongly correlated with the $L_{-1,1}$ peak intensity (Fig. 7.3). As the $L_{-1,1}$ intensity increases, the 2D band higher wavelength component up-shifts by about 5 cm^{-1} with an almost constant linewidth of 34±3 cm^{-1} and a small decrease of its area. Changes for the lower energy component of the 2D band are much more pronounced: it

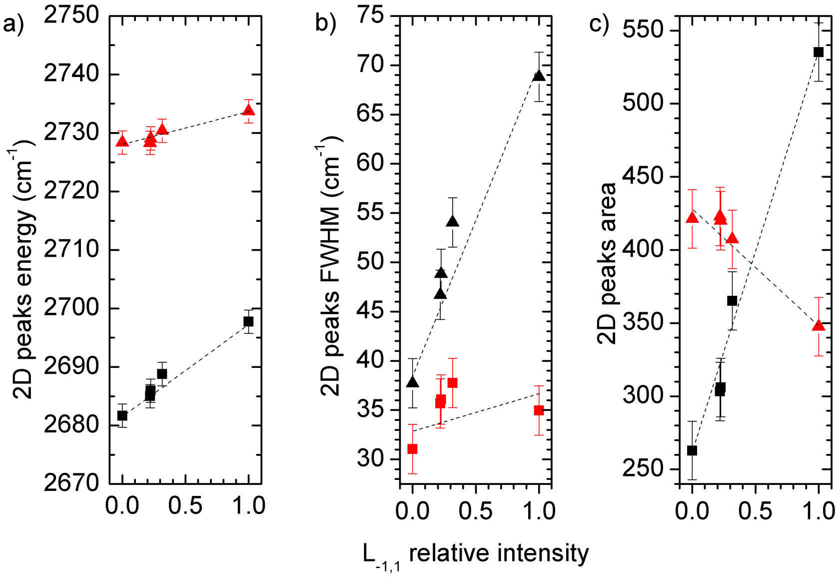

Figure 7.3: a) Energy, b) FWHM and c) area of the two component Lorentzian fit to the 2D band as a function of 'graphene-likeness' measured by $L_{-1,1}$ peak intensity. Black lines indicate energetically lower component while red the upper.

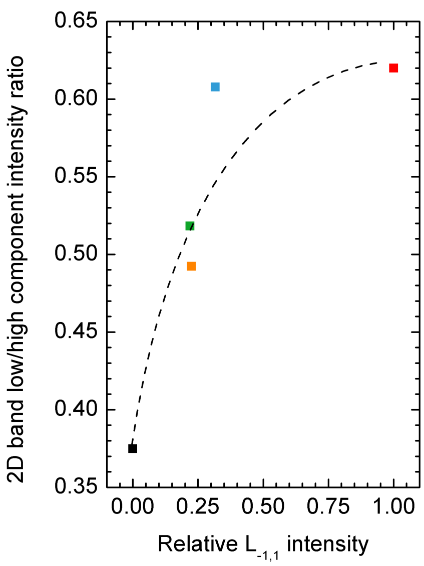

Figure 7.4: Low to high energy component of 2D band intensity ratio as a function of normalized L$_{-1,1}$ peak intensity for different locations on the sample. Colour of each point corresponds to the point and a curve of the same colour in Fig. 7.2. Dashed line is a guide for the eye only.

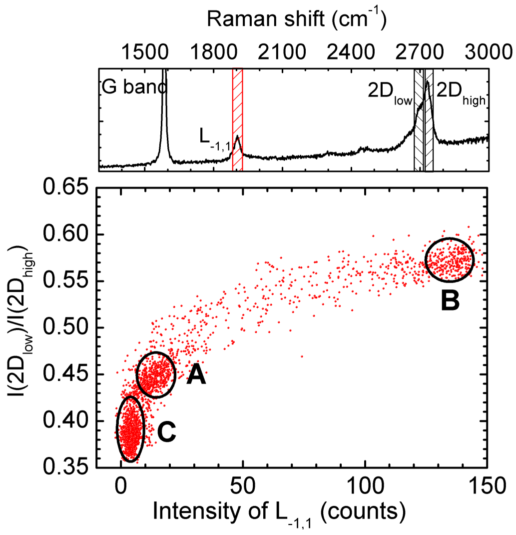

Figure 7.5: Relation between electronic excitation $L_{-1,1}$ intensity and 2D band components intensity ratio extracted for every point every 3 μm in a 150μm ×150μm area. Left panel shows 2D band component ratio as a function of low energy side of $L_{-1,1}$ peak, while right panel as a function of higher energy side of $L_{-1,1}$ peak. Upper panel shows spectrum ranges used for both plots. Red and black circles show three ranges of I(2D-low)/I(2D-high) with much higher than average points density.

up-shifts by 16 cm^{-1}, doubles its linewidth to FWHM=70 cm^{-1} and doubles the area. The overall result of those changes is a significant increase of the intensity ratio I_{low}/I_{high} of 2D band components. Fig. 7.4 shows that it changes value from about 1/3 for bulk graphite, through 1/2 for intermediate layer to 2/3 for graphene-like inclusion.

To check if the chosen Raman scattering spectra and the associated I_{low}/I_{high} ratios, are representative for those three regions (graphite, graphene and intermediate graphene layer) in our sample, we extracted I_{low}/I_{high} values for every point in the mapped area. That gave us a statistic which is shown in Fig. 7.5. We see a continuous distribution of $L_{-1,1}$ peak intensity $I(L_{-1,1})$. However, most of the points fall into three regions marked in this graph by black circles. They show once again that one can distinguish three distinct regions (labeled A, B and C) in the scanned area characterized by well defined and rather uniform properties. In region C, the $L_{-1,1}$ feature is absent – its intensity is not exactly but close to zero. The small offset on the order of 5 counts is caused by the visible background, and may be considered as a measure of the error when measuring the height of $L_{-1,1}$ Raman peak. Region C corresponds to the bulk graphite substrate, where we do not expect to see any sign of monolayer graphene response. In this region the ratio of the 2D band components intensities is in the range of $I_{low}/I_{high} = 0.39 \pm 0.03$.

In region A, a small $L_{-1,1}$ peak intensity, on the order of 10-20 counts is observed. Although it has a mall intensity, it is large enough to be able to distinguish it from the

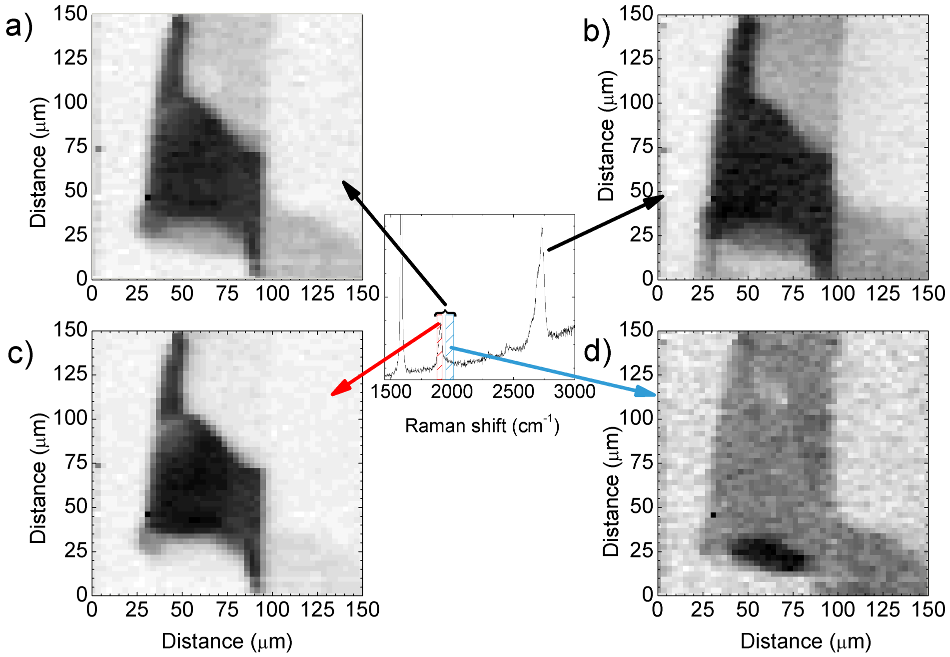

Figure 7.6: False colour intensity maps of: a) $L_{-1,1}$ peak measured in a broad range from 1875 to 2010 cm^{-1}, b) ratio od 2D band components I_{low}/I_{high}, c) low energy, high intensity $L_{-1,1}$ peak component - from 1875 to 1920 cm^{-1}, d) high energy, low intensity $L_{-1,1}$ peak component - from 1875 to 2010 cm^{-1}. In the center a spectrum measured on the decoupled layer region (central, black area in a)) with marked spectral ranges used to construct maps a)-d). λ_{exc}=514.35 nm, T=4.2K

background signal. It shows a response characteristic for monolayer graphene though quite weak. So we will call this area flake A. Meanwhile the characteristic 2D band shape changes in this region and is characterized by the ratio $I_{low}/I_{high} = 0.45 \pm 0.02$. Then we observe some points scattered between the second and the third area which could correspond to the points on the map localized along the edges of decoupled flakes. Since the size of our laser spot is on the order of 1μm, spectra measured on the edge of the graphene flake are a convolution of both the response from the graphene flake and that from bulk graphite. In fact because those points form broad, but well defined bands between previously mentioned three circled areas, it supports our conclusion that they come from spectra being merely a superposition of graphite and graphene optical response along the decoupled flake edge.

Finally region B marks points measured on top of graphene flake which gives a strong Raman scattered $L_{-1,1}$ peak. Here the peak intensity is on the order of 9.3 counts/s. It also shows a significantly different 2D band components ratio $I_{low}/I_{high} = 0.57 \pm 0.02$ which clearly distinguishes it from flake A, and for that reason we are going to call that area flake B.

By counting the number of points inside each circle and between them one can estimate portion of the scanned area corresponding to bulk graphite, the first decoupled layer (flake A), the second decoupled layer (flake B) and the edges of flakes. It turned out that about 44% of the mapped sample area displays the graphite-like behaviour. Flake A occupies about 21% of the mapped surface, while flake B about 11%. Points which do not belong to any of the black circles in Fig. 7.5 constitute about 24% of the surface. Regions A and B not only differ in the intensity of the observed $L_{-1,1}$ feature, but also in the energy at which this peak is observed (see in Fig. 7.2). This could be used to visualize their spatial positions. A gray scale map showing the intensity distribution of $L_{-1,1}$ measured in a broad energy range from 1875 to 2010 cm^{-1} is presented in Fig. 7.6a). Three different regions can be distinguish on the sample. However we can also plot the intensity of the smaller subrange: from 1875 to 1920 cm^{-1} to visualize only the flake B (Fig. 7.6c). Similarly if we focus on the high energy side of this range we can see the flake A (Fig. 7.6d). As is seen from those maps flake A is much larger than flake B and it is seen not only around but also below the second one.

Finally, since it was shown before that the shape of 2D band is basically magnetic field independent in the range from 0 to 10 T [214], those results can be extrapolated to measurements in the absence of external magnetic field. This offers a new criterion, based on the intensity ratio of low to high energy components of 2D band I_{low}/I_{high}, that can be used to locate decoupled graphene flakes. Its major advantage being that, contrary to often used AFM and STM techniques, this one is based on Raman scattering spectroscopy that offers a higher throughput of the scanned area.

7.2.2 Evolution of electronic excitations in magnetic field

In order to check if a smaller $L_{-1,1}$ peak seen on flake A is not some spurious background feature which almost coincide with true $L_{-1,1}$ excitation peak at B=10 T, we have measured Raman scattering response while slowly sweeping magnetic field from B=0 to B=14 T on the two distinct locations on this sample. The first sweep in field was done over the flake B location while the other over flake A. In Fig. 7.7 we present results of the first measurement where the intensity of the Raman signal at a given energy, at given magnetic field is colour coded into the shades of gray scale. The darker the colour the more intense the Raman signal is. The features which are of our interest are those which show a strong evolution in magnetic field. We observe basically two types of magnetic field dependence: excitations with an energy evolving like $\sim \sqrt{B}$ and much weaker ones which follow a quasi-linear magnetic field dependence $\sim B$. The former ones are characteristic for monolayer graphene and their magnetic field evolution is described by Eq. 1.23, with only one free parameter – Fermi velocity v_F. The latter ones are observed in bulk graphite, and to describe their evolution properly, in the simplest model (Eq. 1.26) one needs one more adjustable parameter – γ_1. In Fig. 7.7 we compared the magnetic field evolution of electronic excitation energies measured experimentally with theoretical curves based on those expressions. We have found a general agreement between them, which allowed us to identify the origin of each of the lines. The few energetically lowest are labeled on the right side of the figure. For the monolayer graphene-like excitations we were able to observe both allowed $\Delta|n| = 0$ and weakly allowed due to trigonal warping effects $\Delta|n| = \pm 1$ transitions [45, 58]. Those with no net angular momentum transfer $\Delta|n| = 0$ are the most pronounced ones, similarly to what was theoretically predicted [31] and experimentally reported [32].

As we see those models are able to reproduce the general evolution of electronic excitations in magnetic field, allowing us to extract the values of $v_F = 1.04 \pm 0.02 \times 10^6$ m/s and $\gamma = 415 \pm 1$ meV. However there are also some important differences. Most notably

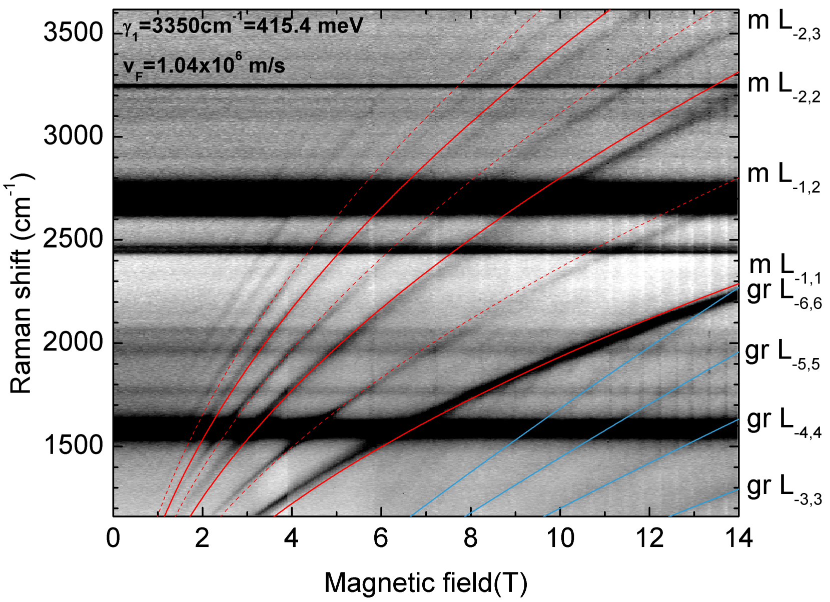

Figure 7.7: False intensity map of Raman spectra measured on the decoupled flake of graphene on the surface of bulk graphite plotted as a function of magnetic field. Black colour indicates high signal. Red (blue) solid lines are the theoretical curves for interband LL electronic excitations in graphene (graphite). Landau levels involved in first few of those excitations are noted on the right, with gr-denoting bulk graphite and m - monolayer graphene. Magnetic field resolution ΔB=35 mT, spectral resolution $\Delta\lambda \approx 2$ cm^{-1}. λ_{exc}=514.35 nm, T=4.2 K

graphene-like energy levels clearly deviate from the theoretical $\sim \sqrt{nB}$ behavior. Fermi velocity in Fig. 7.7 was chosen to provide a good match between measured and calculated $L_{1,1}$ excitation peak energy at magnetic field B=10 T. As we change magnetic field and go along excitations with given LL index-n, an increasing discrepancy between the model and experiment is seen, clearly violating the $\sim \sqrt{B}$ dependence. Similar deviation is observed for excitations with higher n at constant magnetic field, which violates the $\sqrt{n}$ evolution. The origin of this deviation is still uncertain, but non-zero interaction between decoupled flake and the underlaying graphite substrate remains a likely cause of this anomaly. Finally we would like to comment about the intensity of weakly seen electronic excitations of graphite. First of all, their intensity is much weaker than that of graphene monolayer. This is partially caused by the fact that at this range of magnetic field we were able to observe excitations involving LLs with relatively high index ($n \geq 3$). Since the quantum efficiency of scattering process decrease with increasing n observed lines are rather weak. Secondly the intensity of Raman scattered signal from those excitations varies significantly among each decoupled flake. There also exist flakes which do not show any sign of electronic LLs excitation originating from graphite substrate below. This points to the conclusion that electronic decoupling of a graphene flake from the graphitic substrate is not a discrete function – coupled/decoupled, but rather a continuous process, with many intermediate states.

7.3 Characterization of inter-LL electronic excitations

In this section we would like to give a short overview of properties of $L_{-n,m}$ electronic excitations in graphene from the experimental point of view. For that reason we compare the Raman scattering response of such flakes measured at different temperatures (Sec. 7.3.1) or using different excitation wavelengths(Sec. 7.3.2). Then we also present variations in the $L_{-n,m}$ lineshape that can be found among an assemble of graphene-like inclusions (Sec. 7.3.3) and the unexpected weak coupling of $L_(- n, n)$ symmetric modes to Γ phonon (Sec. 7.3.4). Finally, we introduce resonant effects that affect $L_{-n,m}$ excitations lines which is seen in the first approximation as broadening of those lines at chosen values of magnetic field (Sec. 7.3.5).

7.3.1 Low (4.2K) and high (RT) temperature measurements

In order to check how temperature affects intensity and energy position of $L_{-n,m}$ excitations we repeated magneto-Raman measurements at room temperature (RT) $\sim$ 290 K on the same graphene flake that was described in the previous section (Sec.7.2). Firstly, a probe with the sample inside was slowly warmed up from 4.2 K to RT on a timescale of one day. Then a repeated mapping procedure revealed that we were still focused on the same graphene flake. Afterward a Raman scattering spectrum was measured using the same excitation wavelength $\lambda_{exc} = 514.53$ nm and power $\sim$ 5 mW as in previous experiment at low temperatures.

A Raman scattering spectrum was chosen that is representative for the whole mapped graphene flake. It is compared in Fig. 7.8 with previously measured spectrum at liquid helium temperature T=4.2 K. For better clarity from spectrum measured at low temperature a background had to be removed. It originates from the spurious luminescence of optical fibers used in our experimental setup, which is always more pronounced at low temperature. Although attention was paid to use the same excitation power as before, variation on the order of several percent are unavoidable in the setup with optical fibers which randomly bend axis of polarization of incoming linearly polarized light. To get rid of this effect both spectra have been normalized to have the same intensity of the G band. The first observed difference is a small shift of G band frequency toward lower energy at RT. Observed shift is on order of 2 cm^{-1}, which is clearly seen in the spectra but it is too close to the spectral resolution of our setup to measure it more precisely. This is in line with the previous

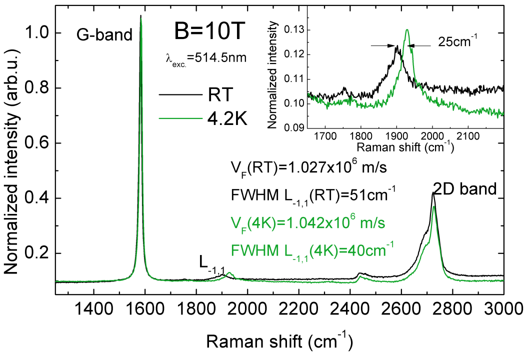

Figure 7.8: Raman spectra of a decoupled graphene flake on the surface of graphite measured at T=4 K and at room temperature (RT). They are rescaled to have the same intensities of G peaks at $\sim$1580cm^{-1}. Inset shows a magnification of $L_{-1,1}$ excitation peak.

Raman scattering observations, that demonstrated a shift in the G band energy with temperature at the rate of -0.016 cm^{-1}/K [215].

The electronic transition $L_{-1,1}$, however, shows much more pronounced changes. This peak shifts by 25 cm^{-1} toward lower energy, loses about 1/3 of its intensity and broadens by 1/4 from 40 to 51 cm^{-1} at RT. This shift expressed in terms of Fermi velocity means its decrease by 1.5%, from $v_F = 1.042 \times 10^6$ m/s at 4.2 K to $v_F = 1.027 \times 10^6$ m/s at RT. This effect cannot be explained by a thermal expansion of the crystal lattice. Graphene has a negative thermal expansion coefficient α, which in the temperature range 0-300 K is on the order of $\alpha = 1 \times 10^{-6}$ K^{-1}. The relation between Fermi velocity and the lattice coefficient a_0 is given by [24, 25]:

$$v_F = \frac{3}{2\hbar} a_0 \gamma_0$$

So, as γ_0 decreases with temperature, v_F should decrease as well, but the amplitude of that decrease is about two orders of magnitude smaller from the experimentally observed one. The exact mechanism responsible for the decrease of Fermi velocity with temperature is still unclear for us.

Despite these effects interband LLs excitations give rise to pronounced Raman features which persist up to RT and may be used to detect decoupled graphene flakes also at the ambient conditions, provided that a source of strong magnetic field is available.

7.3.2 Excitation wavelength dependence

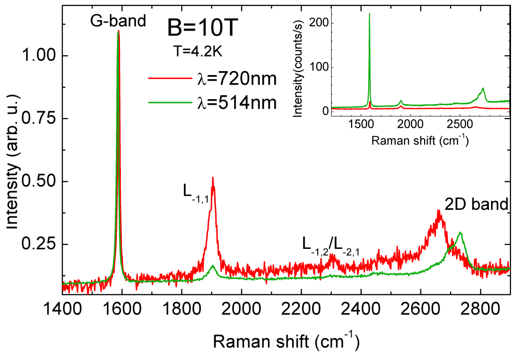

Figure 7.9: Raman spectra of a decoupled graphene flake on the surface of graphite measured at T=4 K using two different excitation laser wavelengths $\lambda_1 = 514.5$ nm and $\lambda_2 = 720$ nm. They are rescaled to have the same intensities of G peaks at ~1580 cm^{-1}. Inset shows the same spectra but not rescaled with intensities as measured.

In order to check how our results depend on the laser wavelength used to probe graphene properties, another set of magneto-Raman scattering experiments was performed on the same piece of natural graphite using 720 nm (1.72 eV) line from a tunable Ti:Sapphire laser. By repeating the mapping procedure we were able to locate and recognize exactly the same flake which was studied before with $\lambda_{exc} = 514.53$ nm (2.41 eV).

Raman spectrum measured at B=10 T with λ_{exc} = 720nm and laser power P = 3 mW on the sample is compared in Fig. 7.9 with previously obtained spectrum measured with argon laser $\lambda = 514.53$ nm line and the same power. In order to better visualize the differences both spectra have been normalized to have the same intensity of G band. Inset of this figure show the same spectra before normalization procedure with intensity scale expressed in counts per second. The first observation is that Raman scattered signal obtained using red laser light ($\lambda_{exc} = 720$ nm) was about

5 times less intense, for the same power applied, than the one obtained using green light excitation ($\lambda_{exc} = 514.53$ nm). Some part of this difference can be attributed to worse quantum efficiency of CCD camera in the near-infrared spectral region. The other significant difference is the observed 2D band shift with laser wavelength, which is a characteristic feature of 2D band in graphite and graphene [65, 66, 67]. The observed 68±5 cm^{-1} upshift of 2D band for the 514 nm excitation with respect to its energy measured at 720 nm excitation gives us a dispersion rate of 98 cm^{-1}/eV, which is in a very good agreement with previously reported values.

Finally, using the red light illumination, the intensity of $L_{-1,1}$ excitation is much stronger as compared with the intensities of the two phonon features. While in the case of green light illumination, intensity of the electronic Raman signal was only 5% of the G peak intensity, for the red light illumination it raised up to 35%. In the same time FWHM of $L_{-1,1}$ peak didn't change preserving its value of 40 cm^{-1}. The difference is even more pronounced when we compare areas under Raman peaks which are proportional to the quantum efficiencies (QE) of the scattering processes. Though, there are too many factors involved during the experiment (like CCD wavelength dependent sensitivity) to be able to directly compare absolute areas of $L_{-1,1}$ peak as it is seen when using $\lambda = 514$ nm or $\lambda = 720$ nm laser lines. So instead, we are going to compare the ratio of $L_{-1,1}$ peak area A(L) to the G-band peak area A(G). Raman peaks of G-band and $L_{-1,1}$ excitation seen in Fig. 7.9 were fitted with a single Lorentzian function and the obtained area under the curve gave us the relative QE of $L_{-1,1}$ transition scattering process with respect to the QE of scattering by a G-band:

$$I_{\lambda=514} = \frac{A(L)_{514}}{A(G)_{514}} = 0.234$$

$$I_{\lambda=720} = \frac{A(L)_{720}}{A(G)_{720}} = 1.309$$

As we see when the $\lambda = 720$ nm laser line is used the relative QE of scattering process by a $L_{-1,1}$ excitation is $I_{720}/I_{514} = 5.6$ times larger than for $\lambda = 514.53$ nm. This value can be compared with theoretical predictions for both the G-band [216] and inter-LLs excitations [31] in graphene. For the $L_{-1,1}$ excitation the QE dependence on Ω is:

$$QE_L(\Omega) = \left(\frac{v_F^2 e^2}{c^2 \pi \lambda_B \Omega}\right)^2 \sim \frac{1}{\Omega^2} \tag{7.1}$$

Where the magnetic length λ_B is defined as $\lambda_B = \sqrt{\hbar c/eB}$. For the G-band it is:

$$QE_G(\Omega) = \frac{2\pi\lambda_\Gamma}{3}\left(\frac{e^2}{c}\right)^2\left(\frac{\Omega a}{c}\right)^2 f\left(\frac{\Omega}{t_0}\right) \sim (\Omega)^2 f\left(\frac{\Omega}{t_0}\right) \tag{7.2}$$

Where $a = 1.42$ Å is the inter-atomic distance in graphene, $t_0 \approx 3$ eV a nearest-neighbour hopping integral, λ_Γ a dimensionless electron-phonon coupling constant and $f\left(\frac{\Omega}{t_0}\right)$ a function which is described in more detail in ref. [216]. Although above expressions could be evaluated directly, it is much simpler when only a ratio of those quantities evaluated at $\Omega_{514} = 2.41$ eV ($\lambda = 514.53$ nm) and at $\Omega_{720} = 1.72$ eV ($\lambda = 720$ nm) is taken:

$$\frac{QE_L(720\ nm)}{QE_G(720\ nm)} / \frac{QE_L(514\ nm)}{QE_G(514\ nm)} =$$
$$= \left\{ \left(\frac{1}{\Omega_{720}}\right)^2 \frac{1}{(\Omega_{720})^2 f(\Omega_{720}/t_0)} \right\} / \left\{ \left(\frac{1}{\Omega_{514}}\right)^2 \frac{1}{(\Omega_{514})^2 f(\Omega_{514}/t_0)} \right\} =$$
$$= \frac{(\Omega_{514})^4 f(\Omega_{514}/t_0)}{(\Omega_{720})^4 f(\Omega_{720}/t_0)} = 4.6$$

So according to existing theoretical models $L_{-1,1}$ excitation should be approximately 4.6 times more intense when using $\lambda = 720$ nm illumination source as compared to its intensity measured with $\lambda = 514.53$ nm laser. Although this is just a rough estimation it is in a good agreement with experimentally obtained enhancement factor $I_{720}/I_{514} = 5.6$.

7.3.3 $L_{-n,m}$ excitations lineshape variation

Lineshape analysis of the most pronounced electronic excitation $L_{-1,1}$ peak given above is representative for many of the flakes which can be found on the surface of bulk graphite. However there are also flakes which Raman scattering response reveal some internal structure of the $L_{-n,n}$ and $L_{-n,n+1}$ excitations. Fig. 7.10 present $L_{-1,1}$ peaks measured in magneto-Raman scattering experiments each performed on a different specimen of decoupled graphene flake, using different experimental conditions which are indicated in the figure for each spectrum but at the same value of magnetic field B=10 T. First of all we see a variation of the position of $L_{-1,1}$ peak. The most pronounced difference in energy of the peak is seen again between spectra measured using green illumination ($\lambda = 514.53$ nm)

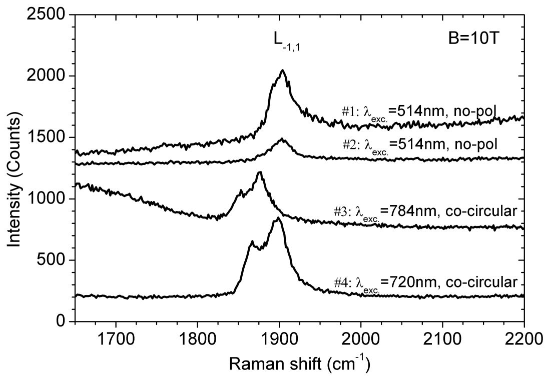

Figure 7.10: Raman spectra of four different graphene flakes found on the surface of graphite measured in either co-circular polarization or non-polarization resolved experiments, using different excitation wavelengths. Spectra have been vertically shifted for better clarity. Magnetic field B=10T.

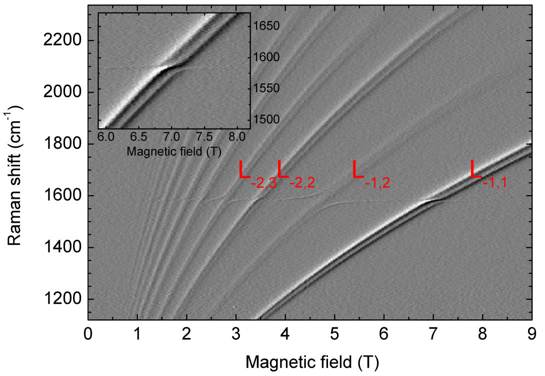

Figure 7.11: False intensity plot of differentiated Raman spectra measured on graphene flake exhibiting significant splitting of electronic excitations peaks and magneto-phonon resonance. Spectra were differentiated to obtain better contrast. Inset shows datails of $L_{-1,1}$ excitation passing through Γ point phonon energy. $\lambda_{exc} = 720$ nm, co-circular polarization.

or one of the Ti:sapphire laser lines in the red part of the spectrum ($\lambda = 720$ nm and $\lambda = 784$ nm). Those four distinct flakes exhibit yet another variation-in the lineshape of the electronic excitation peaks. Some of them are clearly split into two components, some are only asymmetric while other have a symmetric single Lorentzian shape. The flake measured using $\lambda_{exc} = 720nm$ laser line shows a large $L_{-1,1}$ mode splitting which at B=10 T reach 29 cm^{-1}. In Fig. 7.11 we present results of Raman scattering measurement performed in co-circular polarization on this flake in the range of magnetic field from 0 to 14 T. In order to enhance contrast spectra were differentiated along magnetic field axis. It is clearly seen that mentioned splitting is a common property of both doubly degenerated, non-symmetric $L_{-n,n+1}/L_{-n-1,n}$ excitations and non-degenerated, symmetric modes $L_{-n,n}$. One could suspect that breaking electron-hole symmetry would result in slightly different energies of $L_{-n,n+1}$ and $L_{-n-1,n}$. Which would be seen as a splitting of $L_{-n,n+1}/L_{-n-1,n}$ in non-polarization resolved experiment. However since $L_{-n,n}$ are not degenerated, even presence of electron-hole asymmetry would not lead to double-splitting of that line. Nevertheless, this splitting is experimentally observed. Therefore another mechanism had to be invoked for explanation of this effect, one that is not based on the electron-hole degeneracy.

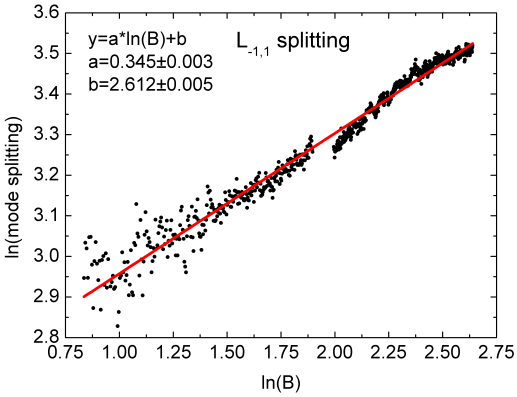

Figure 7.12: $Ln(\Delta x)$ of $L_{-1,1}$ peak as a function of $ln(B)$.

In addition to that it is also observed that for each electronic excitation line, splitting – Δx increases with magnetic field. To check if value of splitting follows some simple power law for each electronic excitation peak we have extracted positions of each component of a two component Lorentzian fit to the data. Then we plotted $ln(\Delta x)$ as a function of ln(B). Since, if Δx follows some simple relation:

$$\Delta x = a \cdot B^{\alpha},$$

where a is some proportionality constant and B-magnetic field, then by taking logarithm

$$ln(\Delta x) = \alpha ln(B) + ln(a)$$

we would obtain a linear relation between $ln(\Delta x)$ and $ln(B)$, with α being the slope. Fig. 7.12 presents such plot done for the splitting of $L_{-1,1}$ peak. It clearly follows a linear dependence, except for a small divergence at a value of magnetic field when it crosses the G peak energy, and exhibit very weak anti-crossing. Red line is a linear regression line of the measured data. It gives a slope $\alpha = 0.35$. This procedure was repeated for next few excitation lines involving higher LLs indices. It turned out that the splitting for all the symmetric excitations $L_{-n,n}$ follows similar dependence with $\alpha = 0.35 \pm 0.02$, while the splitting of the non-symmetric excitations increases generally faster. Intensity of those lines is weaker in co-circular polarization which was used in experiment. It leads to more scattered results of fitting procedure, but clearly centered around $\alpha = 0.5 \pm 0.1$.

The origin of the splitting is still unclear for us. One of the likely explanations may be that degree of coupling between topmost graphene layer and graphite below may be different for each flake. When it is very weak a single Lorentzian shape of electronic excitations is observed. When it is stronger, it may lead to formation of a bilayer with a random twist angle. As mentioned in Chapter 2.4, bandstructure in the vicinity of Fermi energy of such bilayer consist of two Dirac cones with slightly different Fermi velocities [75]. This would result in the observation of two sets of Raman peaks each of them originating from different Dirac cone. However in that case value of the splitting would increase as $\sim \sqrt{B}$, so $\alpha = 0.5$. This would explain only half of the observed cases–for non-symmetric $L_{-n,n+1}$ transitions. Further theoretical works about bandstructure and Landau levels in twisted graphene multi-layers and non-Bernal stacked graphene can bring more insight into this debate.

7.3.4 Coupling with Γ point phonon

Co-circular polarization is expected to be selective to electronic transitions with no net angular momentum transfer $\Delta|n| = 0$. Nevertheless in Fig. 7.11 two types of electronic excitations are visible: symmetric across the Dirac point $\Delta|n| = 0$ and optical-like with $\Delta|n| = \pm 1$. In addition to that, optical-like excitations show a complex structure of the MPR. Traces of them show one component which interacts with Γ point phonon at $\sim$ 1580 cm^{-1} and results in a pronounced anti-crossing of those two lines. However the second component of optical-like excitation passes through the phonon peak almost unaffected. This is an experimental illustration of what was predicted by *Goerbig et al.* [138]. Since optical excitations in graphene can be expressed using wavefunctions $\Psi_{\circlearrowleft}(n, K_\pm)$ which describes an electron promoted to the n^{th} LL in conduction band and a hole left at $n+1$ LL in a valence band, both of them in the same one of the two valleys $K_\pm$. Similarly $\Psi_{\circlearrowright}(n, K_\pm)$ stands for an electron at $n+1$ LL in a conduction band and a hole left at n^{th} LL in the valence band. In ideal graphene the real excitations induced by laser light must not distinguish between carriers located at K_+ or K_- point, so they always form a coherent superposition of wavefunctions. They can form a valley-symmetric mode:

$$\Psi_{\circlearrowleft,s} = [\Psi_{\circlearrowleft}(n, K_+) + \Psi_{\circlearrowleft}(n, K_-)]/\sqrt{2}$$

which couples to photons through a dipolar interaction and is seen in the infrared absorption experiments. Alternatively they form a valley-antisymmetric mode:

$$\Psi_{\circlearrowleft,s} = [\Psi_{\circlearrowleft}(n, K_+) - \Psi_{\circlearrowleft}(n, K_-)]/\sqrt{2}$$

which through electron-phonon interaction couples to phonons. The valley-antisymmetric mode is responsible for characteristic anti-crossings of the MPR [44, 32, 137], while the valley-symmetric mode is seen as a non-interacting line, passing straight through Γ point phonon energy. Although the valley-symmetric mode is not supposed to be Raman active, selection rules breaking may be responsible for observation of these modes.

On the other hand at least one symmetric across Dirac point excitations $\Delta|n| = 0$ which is not supposed to exhibit any sign of a MPR, show a weak signature of interaction with Γ point phonon. Inset in Fig. 7.11 shows how $L_{-1,1}$ excitation passes through the Γ point phonon energy and anti-crosses with that line. This effect is much weaker than for excitations with $\Delta|n| = \pm 1$, however still clearly observable. A mechanism similar to that described above may lead to the observation of normally Raman inactive mode, that weakly interacts with the Γ phonon.

7.3.5 Resonant broadening of inter-LL excitation lines

Extending our measurements of electronic excitations lines to energies above 2000 cm^{-1} reveals additional effects. Fig. 7.13 presents a false intensity map obtained by measuring the Raman scattering signal from exactly the same flake as discussed above(Sec. 7.2). But now, measured range of energies extends up to $\sim$ 3500 cm^{-1} and magnetic field up to B = 10 T. In order to enhance the signal to noise ratio, a measurement was done in a co-circular polarisation configuration. It allowed us to observe a new process which leads to broadening of some magneto-excitonic lines at selected values of magnetic field. The effect is most strongly seen for the $L_{-2,2}$ transition line. The well defined magneto-excitonic line suddenly broadens and looses intensity around $B = 9$ T. At the same value of magnetic field two other lines are also affected : $L_{-1,2}/L_{-2,1}$ and $L_{-2,3}/L_{-3,2}$. The only common factor for those excitation lines is that at least one of the initial or final states is the $n = 2$ LL. A similar effect is observed at $B \approx 6.1$ T, and again three lines are affected. This time however those are: $L_{-2,3}/L_{-3,2}$, $L_{-3,3}$ and $L_{-3,4}/L_{-4,3}$, in other words excitations which involve transition from/to LL with index $n = 3$. The same effect

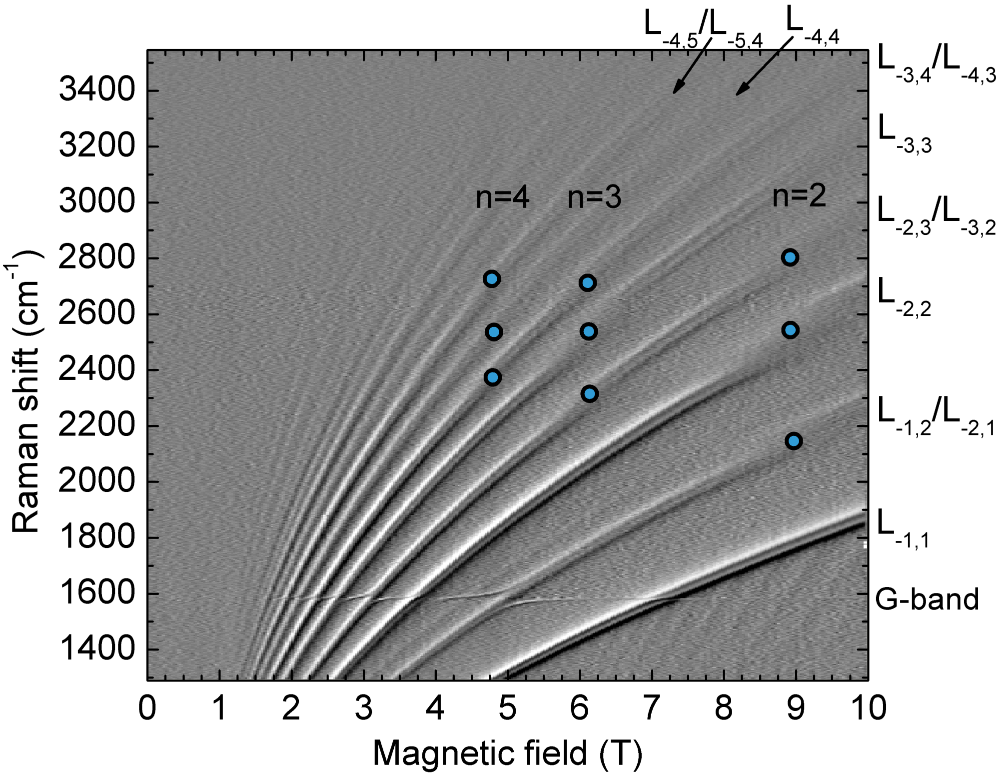

Figure 7.13: False intensity map of differentiated Raman spectra measured on graphene flake on the surface of graphite. Markers indicate locations where excitonic lines undergo broadening process. Above each triplet of affected lines their common index is shown. $\lambda_{exc} = 720$ nm, co-circular polarization, magnetic field resolution $\Delta B = 28$ mT.

is seen for three excitation lines which involve LL with index $n = 4$ at magnetic field $B \approx 4.8$ T.

Since a broadening of magneto-exciton line implies a shortening of their lifetime, it is usually interpreted as a sign of interaction with another system. It is important to note that this effect is different from the well known MPR, where the hybridization of vibrational and electronic excitation modes occurs when the energy of magneto-exciton comes into resonance with the energy of Γ point phonons. It is seen as an anti-crossing of their corresponding Raman peaks, and occurs for all $\Delta|n| = \pm 1$ electronic excitations at the same energy – the one of the Γ point phonon. Here however the observed broadening doesn't occur at the same energy for all lines. Instead, the broadening is observed simultaneously for few excitations, that have different energies, at a given value of magnetic field.

Since the magnitude of the observed broadening decreases with increasing LL index n, it can be expected to be even more pronounced for magneto-excitons which involve transition from/to LL with $n = 1$. However high magnetic fields are needed in order to tune $L_{-1,1}$ excitation in the ~ 2600 cm^{-1} energy range. The section 7.5 is devoted to measurements performed in high magnetic field and with a broad spectral window in order to observe all possible instances where magneto-exciton lines show signatures of interaction with another system.

7.4 $L_{0,1}/L_{-1,0}$ excitation fine-structure

In this section we would like to present results of magneto-Raman measurements performed over a graphene-like inclusion found on the surface of graphite in high magnetic fields. In the center of our interest was the evolution of inter-LL excitations in the low energy (< 2000 cm^{-1}) regime, and particularly the details of a magneto-phonon resonance (MPR) at $B \sim 27$ T. The magneto-phonon resonance effect involving Γ point phonon in graphene has been already intensively studied both theoretically [117, 137, 21, 15] and experimentally [109, 108, 44]. However, a clear observation of this effect requires working with a high quality and low doping level system. Since most of exfoliated graphene flakes suffer from the extrinsic charge doping, some of the details of MPR has eluded experimentalist for a long time. Only recently traces of a theoretically predicted fine-structure of MPR [138] has been observed in a CVD grown graphene [141]. Here we present spectroscopic data which clearly demonstrate this effect for the $L_{-1,0}(L_{0,1})$ magneto-exciton. Since graphene flakes on graphite exhibit much higher electronic quality and charge neutrality than other graphene systems [13] we were able to observe this fine-structure with much more details. This in turn allowed us to draw some conclusions on the possible origin of this splitting.

7.4.1 Flake identification

We have started our measurements by finding a graphene flake on the surface of graphite. For that purpose spatial mapping of the Raman scattering response from thee graphite surface was performed and then methods described earlier in section 7.2 were employed to find such flake. Fig. 7.14(left panel) shows the obtained map using the false colour

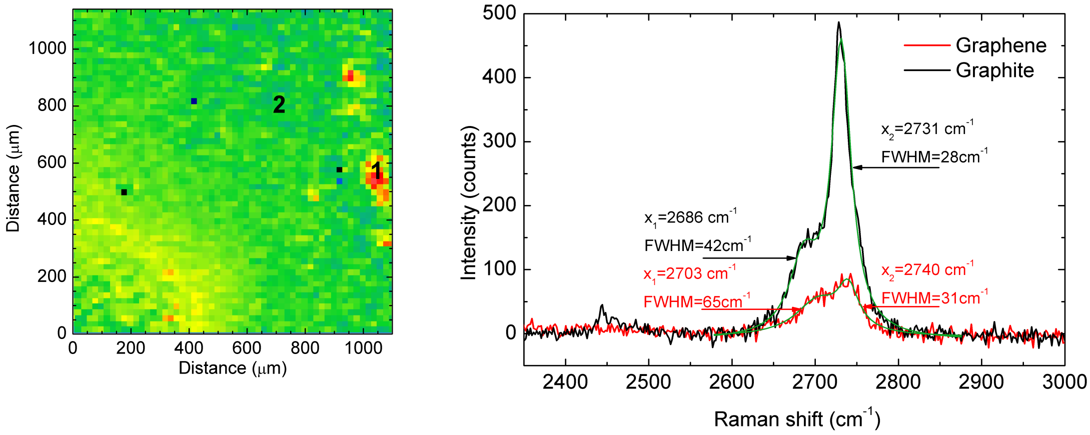

Figure 7.14: Left: A map of the I_{low}/I_{high} ratio of 2D band components of the surface of graphite. Number '1' shows a location of a monolayer graphene. Right: Raman spectra of 2D band taken at two locations on the map: '1'-graphene flake, red curve and '2'- bulk graphite substrate, black curve. B=0T

scale where the green/yellow colour of the background corresponds to the ratio of 2D band components $I_{low}/I_{high} = 0.35 - 0.40$. Close to the right edge of the map a well defined region is seen, marked with number '1', which has dimensions of 70×150 μm. It exhibits a much higher low to high energy 2D band components ratio of $I_{low}/I_{high} = 0.5$. According to our previous studies (see Sec. 7.2.1) this should correspond to a monolayer graphene inclusion. In the right panel of the same figure, two Raman spectra of 2D band are compared together with a two components Lorentzian fits. One spectrum was measured at the flake location (red curve) and the other was measured on the graphite substrate (black curve). First of all, the intensity of the 2D band of the graphene flake is no more than 20% of the intensity of signal from graphite. Then, a huge difference in the shape of the 2D band is seen. In addition to the already mentioned higher I_{low}/I_{high} ratio, also linewidths of both components change for those two locations. The FWHM of lower energy component increases significantly from 42 cm^{-1} for bulk graphite to 65 cm^{-1} for graphene inclusion. At the same time the FWHM of the higher energy component changes only weakly - 28 cm^{-1} for graphite and 31 cm^{-1} for graphene. Those values agree very well with our previous measurements done on another graphene flake in magnetic field (see Fig. 7.3) and allowed us to identify this region as a monolayer-like graphene inclusion.

7.4.2 High magnetic field $L_{0,1}/L_{-1,0}$ excitation evolution

Fig. 7.15 shows the result of a Raman scattering experiment in magnetic field up to 30 T performed with a 600 grooves/mm grating, which gives a spectral resolution of about $\sim$ 2 cm^{-1}. Since this measurement was performed in non-polarisation resolved configuration two main classes of features dominate the spectrum: inter-LL electronic excitations and the E_{2g} phonon mode showing very clear magneto-phonon resonance down to magnetic field as small as $B = 1.3$ T. This is a sign of a very low doping level in this sample and of a high quality. In addition to that, electronic excitations are characterized by a

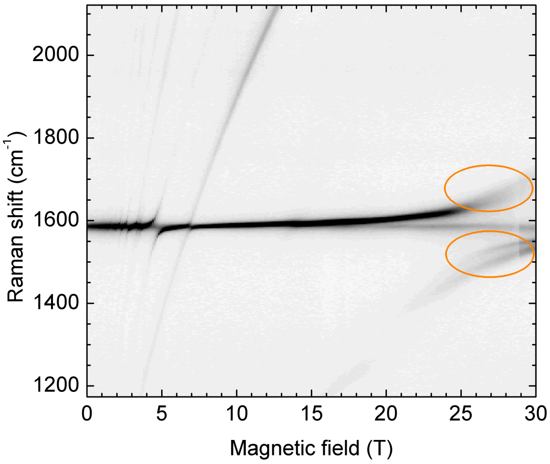

Figure 7.15: Gray scale false intensity map of a Raman scattering signal from a graphene domain in magnetic field. Orange circles shows where each branch of the hybridized phonon-magneto-exciton mode is split into two components.

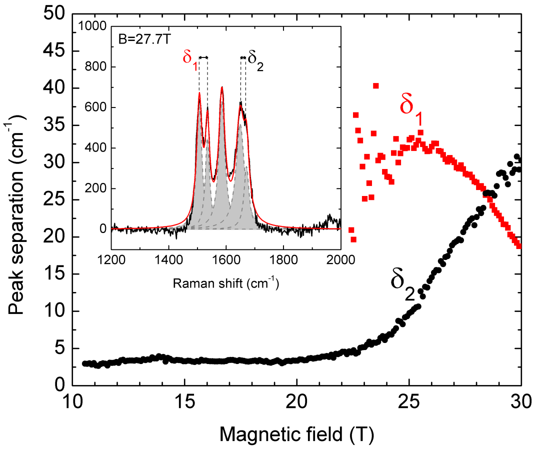

Figure 7.16: Magnetic field evolution of the hybridized phonon-magneto-exciton modes energy splitting. The inset shows a Raman spectrum at magnetic field $B = 27.7$ T which consist of 5 modes: non-interacting E_2g phonon at 1588 cm^{-1}, two split modes below and two split modes above that energy.

single Lorentzian shape and there are no signs of electronic excitations evolving linearly in B, which could come from the graphite substrate below. It makes this particular flake exceptional as compared with other similar flakes studied and presented before. Assuming that the two component electronic excitations observed on some graphene-like flakes comes from two monolayer graphene flakes stacked on top of each other, the single component shape is a signature of a true monolayer graphene. This validates our description of this system as an isolated monolayer graphene in the following part of this chapter.

Although MPR was already measured on a variety of graphene-based systems, usually at $B \sim 27$ T only a simple anti-crossing between E_{2g} phonon and $L_{0,1}/L_{-1,0}$ excitations was observed. Here however, at the resonance, five distinct components are observed. One has the energy of non-interacting E_{2g} phonon, while the other four form two sets of avoided crossings with different coupling strength. At $B \sim 27$ T each branch of the hybridized phonon-magneto-exciton mode is split into two twin peaks. The splitting of these peaks is as large as $25 - 30$ cm^{-1}. It makes each component to be clearly distinguishable from its twin counterpart (see inset of Fig. 7.16). As it is presented in Fig. 7.16, the energy splitting changes with the magnetic field. It increases with field for the two modes which have an energy above the energy of E_{2g} phonon while it decreases with field for the two modes with lower energy. In other words, the further away from the resonance at $B \sim 27$ T one is, the more pronounced splitting is observed.

7.4.3 Discussion

The origin of this splitting lies in the double degeneracy of $L_{0,1}/L_{-1,0}$ inter-LL excitation, which hybridize with E_{2g} phonon. Once this degeneracy is lifted we should expect to see two sets of avoided crossings at slightly different energies. Then, since in our experiment we were not selective towards any given light polarization the resulting spectrum consist of those two sets of avoided crossings superimposed on each other and seen as 4 distinct peaks. There are two main causes that may lead to the lifting of this degeneracy:

- charge doping
- conduction and valence bands asymmetry - caused by trigonal warping

Doping

The fine-structure of the magneto-phonon resonance clearly depends on the charge doping [138], since the magnitude of the splitting depends on the effective coupling strength λ^{eff} of those modes. The lower the value of this parameter, the less pronounced is the anti-crossing between phonon and electronic excitations. On the other hand when this parameter increases, the mode splitting becomes larger. The effective coupling strength λ^{eff} is in fact nothing else than the dimensionless electron-phonon coupling constant λ multiplied by the number of filled/empty states in the initial/final LL:

$$\lambda^{eff} = \lambda f_i(1 - f_f)$$

Where $f_{i(f)}$ denotes the partial filling factor of the initial (final) LL of the excitation. In the following we use a convention in which a neutral graphene system corresponds to half filled ($f_0 = 0.5$) $n = 0$ LL. Then completely filling ($f_0 = 1$) or emptying ($f_0 = 0$) this LL means doping with $\rho = 1.31 \times 10^{12}\mathrm{cm}^{-2}$ electrons or holes respectively. Any value of the filling factor between $0.5 < f_0 < 1$ increases the effective coupling strength for the $L_{0,1}$ excitation, while decreasing the effective coupling strength for $L_{-1,0}$ transition, eventually blocking $L_{-1,0}$ excitation for $f_0 = 1$, when all possible final states are fully occupied. Similarly for hole doped system, when $0 < f_0 < 0.5$ it is the $L_{-1,0}$ transition which has larger effective coupling strength than $L_{0,1}$. Finally, when $n = 0$ LL becomes completely empty, the $L_{0,1}$ transition is blocked. Extreme case of this effect, when the $n = 0$ LL was completely empty was observed by *Kossacki et al.* in a polarization-resolved magneto Raman experiment measured on the exfoliated graphene on Si/Si0$_2$. In their experiment the E_{2g} phonon showed a clear anti-crossing with the $L_{-1,0}$ electronic excitation in one polarization, while it didn't interact at all with $L_{0,1}$ excitation in the other polarization. On the other hand, *Neugebauer et al.* have shown that Fermi energy in graphene flakes on graphite is closer than 6 meV away from the charge neutrality point [13]. Therefore, we expect that any doping of our sample would not be large enough to shift the Fermi level away from the $n = 0$ LL.

In order to estimate how large a doping should be to explain an observable fine-structure of MPR at $B = 27T$ we used a simplified model based on the one proposed by *Ando* [137]. The energies of the hybridized electron-phonon excitations can be found by searching for zeros of the phonon's Green function. Lets consider one polarization of light in which $L_{-n,n+1}$ excitations are active and assign it with mark $\circlearrowleft$. Then in order to find the energies of hybridized modes ϵ we need to solve this expression:

$$\epsilon_{\circlearrowleft}^2 - \epsilon_0^2 = 4\epsilon_0\lambda E_1^2 \sum_{k=0}^{\infty} \left\{ f_{-k}(1 - f_{k+1}) \frac{L_{-k,k+1}}{(\epsilon_{\circlearrowleft} + i\delta)^2 - L_{-k,k+1}^2} + \frac{1}{L_{-k,k+1}} \right\}$$

Where $L_{-k,k+1} = E_{k+1} - E_{-k}$ is the energy of the electronic transition from initial k LL to the final $k+1$ LL. Since anti-crossing between E_{2g} phonon peak and $L_{0,1}$ or $L_{-1,0}$ occurs at much higher magnetic field than anti-crossings with all other electronic excitations, we can very well describe MPR around $B = 27$ T in this polarization by considering only the interaction with $L_{0,1}$ excitation and neglecting all the others. Then above equation simplifies considerably into:

$$\epsilon_{\circlearrowleft}^2 - \epsilon_0^2 = 4\epsilon_0 \lambda E_1^2 f_0(1-f_1)\frac{L_{0,1}}{\epsilon_{\circlearrowleft}^2 - L_{0,1}^2}$$

which gives:

$$(\epsilon_{\circlearrowleft}^2 - \epsilon_0^2)(\epsilon_{\circlearrowleft}^2 - L_{0,1}^2) = 4\epsilon_0 \lambda E_1^2 f_0(1-f_1)L_{0,1}$$

Solving this doubly quadratic equation for $\epsilon_{\circlearrowleft}$, gives us two solutions which give:

$$\epsilon_{\circlearrowleft}^{\pm} = \sqrt{\frac{\epsilon_0^2 + L_{0,1}^2}{2} \pm \frac{1}{2}\sqrt{(\epsilon_0^2 - L_{0,1}^2)^2 + 16 f_0(1-f_1)\epsilon_0 \lambda E_1^2 L_{0,1}}} \tag{7.3}$$

Following the similar procedure for the other polarization $\circlearrowright$, when only $L_{-1,0}$ excitation is considered, we obtain:

$$\epsilon_{\circlearrowright}^{\pm} = \sqrt{\frac{\epsilon_0^2 + L_{-1,0}^2}{2} \pm \frac{1}{2}\sqrt{(\epsilon_0^2 - L_{-1,0}^2)^2 + 16 f_{-1}(1-f_0)\epsilon_0 \lambda E_1^2 L_{-1,0}}} \tag{7.4}$$

These expressions allow us to plot the energies of the hybridized magneto-exciton-phonon modes and to visualize what is the effect of doping on those modes as seen in the two

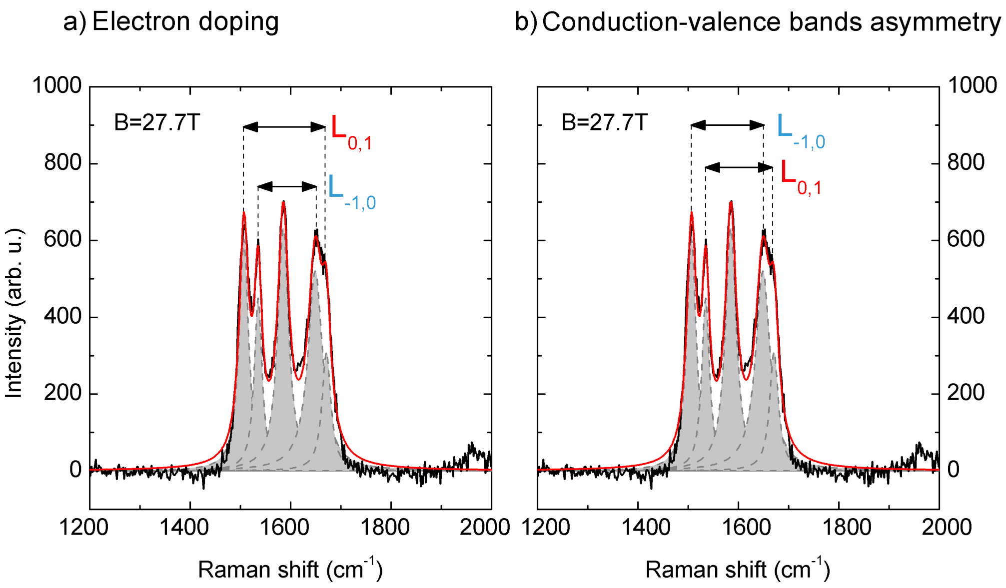

Figure 7.17: Identification of the fine-structure peaks of MPR in graphene at $B = 27.7$ T caused by different strength of effective electron-phonon coupling between E_{2g} phonon and with either $L_{-1,0}$ or $L_{0,1}$ excitation, which originates from: a) electron doping (for hole doping labeling of peaks is reversed) b) conduction-valence bands asymmetry.

different polarizations. In Fig. 7.18(upper row) we present the extracted positions of the experimentally measured Raman features (black dots) and the calculated energies of the hybridized modes (solid lines) for different doping levels. Since our measurements were done without resolving polarization, we observe the effect of E_{2g} phonon coupling to $L_{-1,0}$ mode (blue lines) and $L_{1,0}$ mode (red lines) simultaneously. In charge neutral graphene, the energies of the hybridized phonon-magneto-exciton modes at each magnetic field are the same for $L_{-1,0}$ and $L_{0,1}$ magneto-excitons. However, a finite doping modifies size of the anti-crossing gap and has an opposite effect for the effective strength of E_{2g} phonon interaction with two excitations: $L_{-1,0}$ and $L_{0,1}$. This is seen as two pairs of avoided crossings formed by two external and two inner pairs of Raman peaks occurring at the same value of magnetic field (see Fig. 7.17a)). We simulated the effect of doping on the

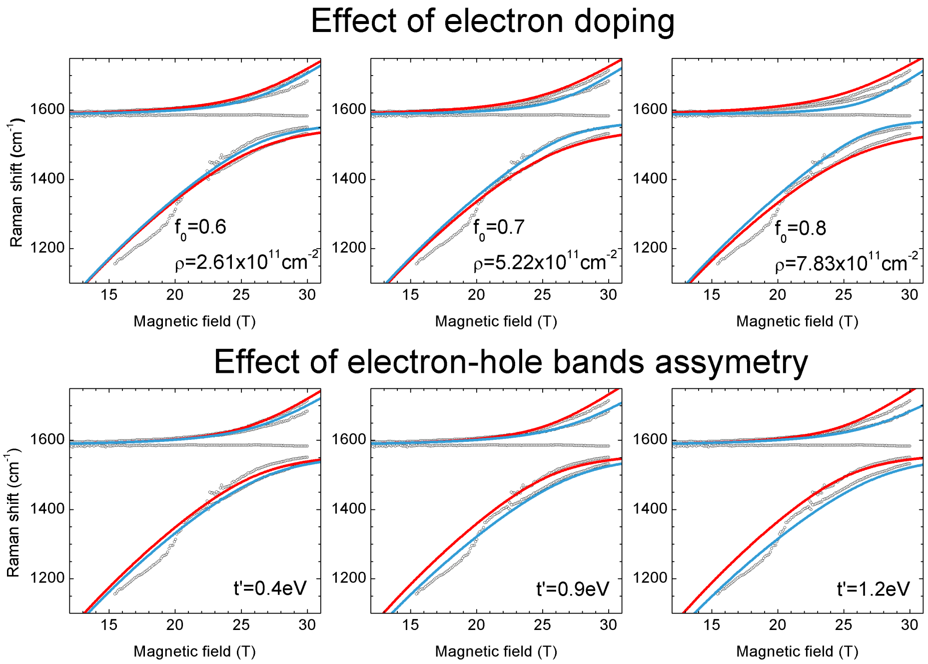
Effect of electron doping

Effect of electron-hole bands assymetry

Figure 7.18: Experimental results of magnetophonon effect in graphene (black dots) and calculations (solid lines) which take into account only doping of the sample (upper row) or only effect of conduction-valence bands asymmetry(lower row). Blue and red lines correspond to coupling of E_{2g} phonon with either $L_{-1,0}$ or $L_{0,1}$ excitations.

MPR in graphene for few values of doping level, while assuming a conduction-valence bands symmetry and setting $v_F = 1.04 \times 10^6$ m/s. Results of such calculations are shown in the upper row of Fig. 7.18. They show that for a doping level which sets the $n = 0$ LL filing factor around $f = 0.7$ we can get a reasonably good match between experimental data and our simulations. According to our estimations best fit to the data should fall in the range of filling factor between $f = 0.65$ and $f = 0.75$ which corresponds to charge density $\rho = 5.2 \pm 1.3 \times 10^{11}$ cm^{-2}. Since we assumed a complete conduction and valence bands symmetry, equations 7.3 and 7.4 are also symmetric with respect to exchanging $L_{-1,0}$ with $L_{0,1}$ excitation and simultaneously changing the type of carriers.

Electron-hole asymmetry

Another possible explanation for the observed MPR fine-structure is an asymmetry in conduction and valence bands dispersion relations. Although close to a K point in the first Brillouin zone, the dispersion is very well approximated by a relation $E(\vec{k}) = \pm\hbar v_F|\vec{k}|$ it is still an approximation. This particular expression shows up naturally when a nearest neighbour tight-binding method is used to calculate the dispersion relation. In this approximation only interaction with the nearest neighbouring atom is included in the Hamiltonian of the system. The strength of this interaction is described by the so called nearest-neighbour hopping term t, which is proportional to the Fermi velocity $v_F = \frac{3a}{2\hbar}t$ (where a is the graphene lattice constant $a = 0.14$ nm) and is the only parameter needed to describe the electronic dispersion around the K point. Then, when a magnetic field is applied to the system described by such a dispersion relation, Landau quantization leads to the formation of LLs with energies evolving like $\sqrt{B}$, and are symmetric with respect to reflection across the Dirac point:

$$E_{\pm,n} = \pm v_F\sqrt{2\hbar eBn}$$

However, the model describing the electronic dispersion can be further refined by including one more hopping term t' in the tight binding Hamiltonian, which describes interaction of a given carbon atom with its next-nearest neighbour in the same graphene sheet. This leads to breaking of conduction and valence band symmetry but also reduces the full rotational symmetry of those bands around K point to 3-fold rotational symmetry. This is seen as a warping of the Dirac cones surfaces and is also known as the trigonal warping. The detailed calculation of the LLs evolution in magnetic fields in graphene which includes this term was presented by *Plochocka et al.* [29] and here, we will give only the final result:

$$E_{\pm,n} = \pm v_F\sqrt{2\hbar eBn} + \frac{9}{2}\frac{a^2e}{\hbar}t'Bn \tag{7.5}$$

This expression shows that the $L_{0,1}$ excitation always has an energy higher than that of $L_{-1,0}$, and this energy difference is increasing linearly with magnetic field like:

$$\Delta E = L_{0,1} - L_{-1,0} = 9\frac{a^2e}{\hbar}t'Bn \tag{7.6}$$

The lower row of Fig. 7.18 presents results of calculations based on Eq. 7.3, 7.3 where evolution of LLs is described by the above expression Eq. 7.5 which includes the next-nearest neighbour term responsible for conduction-valence band asymmetry. The three graphs show how the splitting of the hybridized modes increases with increasing the value of the t' hopping integral. The leftmost graph presents calculations based on the assumption that $t' = 0.4$ eV, which is the most commonly reported value of that constant in the literature. However, in order to obtain a reasonably good match between the calculated curves and the experimentally measured points a larger value of t' has to be used, namely $t' = 0.9$ eV. There is an important difference between modes splitting caused by a charge doping and by bands asymmetry. In the case of doping, one from the two transitions $L_{-1,0}$(blue lines) and $L_{0,1}$(red lines) always form two external Raman peaks, while the other transition form the two internal ones, as is seen in Fig. 7.17a. In the case of electron-hole asymmetry, the Raman peaks corresponding to the $L_{-1,0}$

transitions always have lower energy than those stemming from $L_{0,1}$ (Fig. 7.17b). So if the observed MPR fine-structure originated from the combination of those two effects if would lead to an inevitable crossing between two branches of the anti-crossing modes (blue with red lines in Fig. 7.18). Our measurement however shows very clearly that there is not any crossing of the split bands anywhere in between 15 and 30 T. Since bands asymmetry is an inherent attribute of a graphene monolayer which we cannot neglect, the conclusion is that bands asymmetry must be the factor responsible for observed MPR fine-structure. This conclusion is in line with reported observation of circular dichroism in MPR on the same kind of graphene system by *Kühne et al.* [32]. Their measurements showed that two components of split phonon-excition mode at 27 T are shifted in energy in the same direction for one polarization with respect to the same peaks seen in the other polarization, which is exactly what we would expect to see when an asymmetry is considered. Thus following the assumption presented above, we can determine the t' nearest-neighbour hopping integral from an experiment. Then, by slightly varying the doping level around the charge neutrality point we can find a maximum doping level that still wouldn't change too much the calculated curves. Using this approach we were able to determine the next-nearest neighbour hopping integral $t' = 0.9 \pm 0.2$ eV, which is about two times larger than its usually reported value. Obtained filling factor falls in the range $0.48 < f < 0.52$, which means that carrier (either electrons or holes) concentration due to doping is lower than $\rho = 5.2 \times 10^{10}$ cm^{-2}. Since much of our conclusions depends on the validity of an assumption that charge doping is the main factor responsible for the observed mode-splitting, it would be reasonable to check it in the polarization-resolved experiment. This would help to assign each branch of the observed magneto-phonon resonance to one of the two possible excitations $L_{-1,0}$ or to $L_{0,1}$.

7.5 Resonant electron-phonon interaction effects

In this section we present a more detailed study of the resonant effects affecting inter-LL excitations in graphene that were outlined in section 7.3.5. We found that those resonances can be grouped into two series: a first one that encompasses resonances whose energies converges to the energy of K-point phonons and a second one for resonances which energies are centered around the energy of optical phonons from the vicinity of Γ point. Then we present two phenomenological models that can qualitatively explain the observed resonances.

7.5.1 Observed inter-LL excitations resonances

The measurements were performed on the same graphene flake on the surface of graphite that we described in section 7.4. This time however a broader spectral window was used in the range from 900 to 5400 cm^{-1}. Experiments were done at liquid helium temperature, using 514.53nm line from argon-ion laser and a home-made custom micro-Raman setup. Laser power was set to 5mW and no polarizers were used. Fig. 7.19 shows a gray scale intensity map of Raman spectra obtained during a magnetic field sweep up to $B = 30$ T. The most prominent features in the figure are the G-band at energy of 1580 cm^{-1} and the electronic excitations, with energies evolving as $\sqrt{B}$. In order to en-

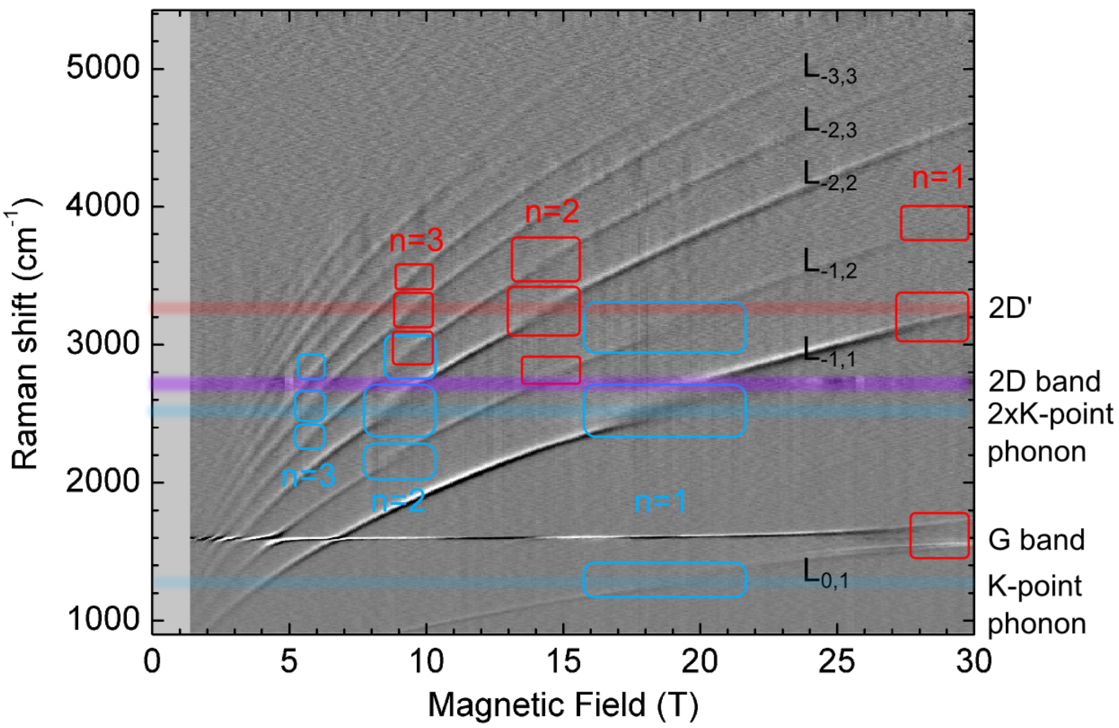

Figure 7.19: False intensity map of differentiated Raman spectra measured on graphene flake on the surface of graphite. Rectangles indicate locations where excitonic lines undergo broadening process. Above each triplet of affected lines their common index is shown. Violet horizontal line marks the energy of 2D band, which was removed from the spectra. Blue horizontal lines indicates the energies of K-point phonon and 2× K-point phonon. While red line of $2D'$ phonon mode. $\lambda_{exc} = 514.53$ nm, no polarization selected, magnetic field resolution $\Delta B = 75$ mT.

hance small changes in the evolution of electronic excitations, care was taken to remove artificial background originating from the luminescence of optical fibers in the experimental setup. Since the 2D band changes very weakly in magnetic field it has vanished from the spectra. To further improve the signal to noise ratio, spectra were differentiated in magnetic field. Compared with previous measurements of electronic excitations [44, 32] the most pronounced difference is seen in the appearance of significant deviations from simple $\sqrt{B}$ evolution at some specific values of magnetic fields. These deviations take the form of either as a sudden broadening of the line, or for those which are the most intense, of a clear splitting of the line into two or three anti-crossing modes. Such behaviour is often a signature of two excitations which energies come into a resonance with each other. Since we do not know *a priori* what is the origin of the second excitation nor the exact resonance mechanisms it is useful to observe patterns of instances when those resonant processes occur.

In order to better visualize electronic excitation evolution anomalies, each peak was fitted with a single Lorentzian function. Their linewidth evolution against magnetic field and against peak's energy are shown in Fig. 7.20 and Fig. 7.21 respectively. Since a single Lorentzian function is used in the fitting procedure, the FWHM is strongly overestimated in the range of magnetic fields where a clear anti-crossing is observed e.g. $L_{-1,1}$ at $B = 19$ T. The true linewidth of each single component is significantly smaller. However it is still a useful method to obtain information about the value of magnetic field or about the energy at which the peak is influenced by interaction with some other excitation. As it is seen from the general map (Fig. 7.19) where the rectangles mark the areas where the lines broaden and from the plot of FWHM versus energy (Fig. 7.21), broadening/anti-crossing does not always occur at the same energy. This means that the energy of the whole excitation process $E_n - E_m$ is not the main factor responsible for the resonance to occur. There are however some characteristic patterns: first of all, each time an excitation with $\Delta|n| = 0$ undergoes a broadening/anti-crossing two neighbouring lines show the same effect at the same value of magnetic field (Fig. 7.20). It means that only one of the initial or final states is involved in the resonance effect. So it is the energy separation between the 0 LL and n LL that matters. Assuming that each interband electronic excitation may be divided into two steps, first from $-m$ LL to the 0 LL, which doesn't have to be in resonance with any other excitation, and then in the next step, from 0 LL to n LL which is in resonance with some other excitation, we could understand this simultaneous broadening of the three lines.

We see immediately that the $\Delta|n| = 0$ excitations are somehow special, because energy difference between $-n$ LL and 0 LL is exactly the same as the energy difference between 0 LL and n LL. So, when the resonance which causes broadening/anti-crossing of $L_{-n,n}$ electronic excitation occurs, it happens at an energy which is twice the energy of the other so-far unknown excitation.

Fig. 7.21 reveals that, although excitations with $\Delta|n| = \pm 1$ show a broadening at many different energy values, the $\Delta|n| = 0$ excitations broaden at only one of the two possible values, either $E_a = 2560 \pm 60$ cm^{-1} or $E_b = 3230 \pm 50$ cm^{-1}. This allows us to group the instances when line broadens/shows anti-crossing into two categories marked in Fig. 7.19 with either blue or red rectangles. We conclude that there are two different excitations which have to be identified, each of them responsible for one set of instances when electronic excitations broaden/show anti-crossing.

The most likely candidates for those excitations in graphene are phonons and their energy should be equal to half the energy of E_a and E_b. Thus $\frac{E_a}{2} \approx 1280$ cm^{-1} and $\frac{E_a}{2} \approx 1615$ cm^{-1}. The first value corresponds to the energy of K-point phonons (compare with Fig. 3.1). The second one is close to the energy of Γ point phonons.

7.5.2 Discussion: new relaxation channel model

Phenomenologically, the observed broadening of the electronic excitation Raman peaks can be understood in terms of shortening of the quasi-particle lifetime caused by the opening of a new relaxation channel. Below, we present a model based on that principle, which is a simple generalization of a model proposed by *Orlita et al.* [143], now extended to the whole family of excitations observable in Raman scattering. Fig. 7.23 presents a scheme illustrating two cases: when the energy difference between 0 LL and 1 LL or between 0 LL and 2 LL comes into a resonance with K point phonon energy. At $B \approx 18$ T, $L_{0,1}$ approaches the energy of K point phonons $E_K \approx 1300$ cm^{-1}. Among all electronic excitations which are visible in our experiment only three of them have

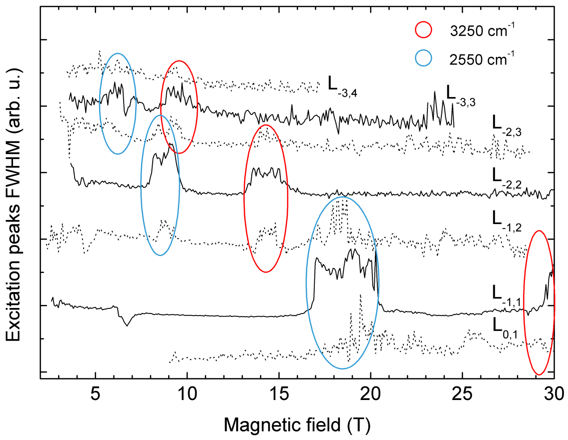

Figure 7.20: FWHM of a single Lorentzian fit of the excitation peaks as a function of the magnetic field. Blue and red ellipses show ranges of magnetic field for which $\Delta|n| = 0$ electronic excitations are in resonance with 2× K-phonon energy (at 2550 cm^{-1}) or with $2 \times \Gamma$ point phonons (at 3250 cm^{-1}).

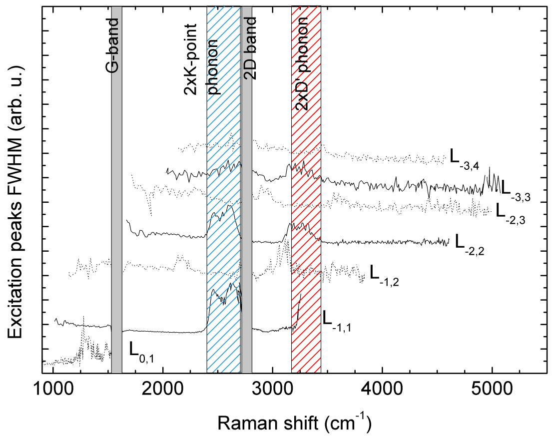

Figure 7.21: FWHM of a single Lorentzian fit to excitation peaks as a function of energy. Blue and red dashed rectangles shows the range of energies when $\Delta|n| = 0$ transitions broaden simultaneously.

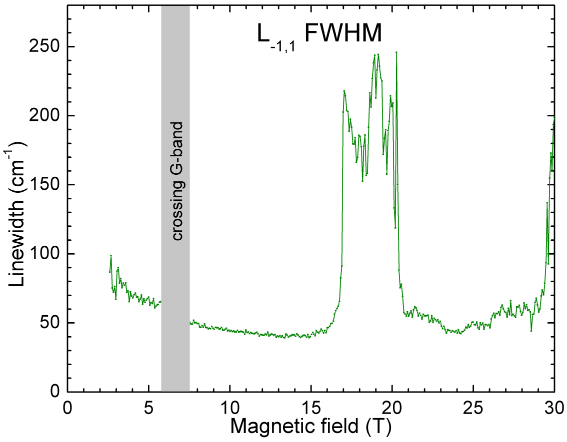

Figure 7.22: FWHM of a single Lorentzian fit to $L_{-1,1}$ electronic transition as a function of magnetic field.

the 1 LL as a final state. Those are $L_{0,1}$, $L_{-1,1}$ and $L_{-2,1}$ electronic transitions. Once a magneto exciton is created it has finite intrinsic lifetime, which is determined by averaged interactions with its environment which eventually leads to carrier relaxation into the ground state. For undoped graphene in magnetic field it will be the 0 LL. This finite lifetime is reflected by the finite linewidth of the corresponding Raman peak. However, when the energy of the final state is in resonance with K point phonon a new relaxation channel opens. It allows to scatter a carrier to the 0 LL with simultaneous emission of phonon. Since in undoped graphene 0 LL is partially empty, there are always empty states into which a carrier can relax. This new relaxation channel reduces the lifetime of a carrier in the excited state which manifests itself as a broadening of the Raman peak. One complication which arises from the fact that K-point phonons carry a considerable momentum, is the need to propose an intervalley scattering. In that case, a carrier excited to the n LL in the K(K') valley can relax to the 0 LL in the K'(K) valley. As the magnetic field decreases, the energy of LLs decreases as well, so LLs with higher indices will come into resonance with the energy of the phonon. This is illustrated in the right panel of Fig. 7.23, where at $B \approx 9$ T the 2 LL is in resonance with E_K and the same broadening of the Raman peaks is observed. However this time the affected lines are those which have the 2 LL as a final state, like $L_{-1,2}$, $L_{-2,2}$ and $L_{-3,2}$. Those diagrams shows processes where an electron is scattered by the phonon, however the process is analogous when a hole scatters. The only difference is that the effect is now observed for electronic excitations which share the common initial state, like $L_{-1,0}$, $L_{-1,1}$ and $L_{-1,2}$ at $B \approx 18T$ or $L_{-2,1}$, $L_{-2,2}$ and $L_{-2,3}$ at $B \approx 9T$.

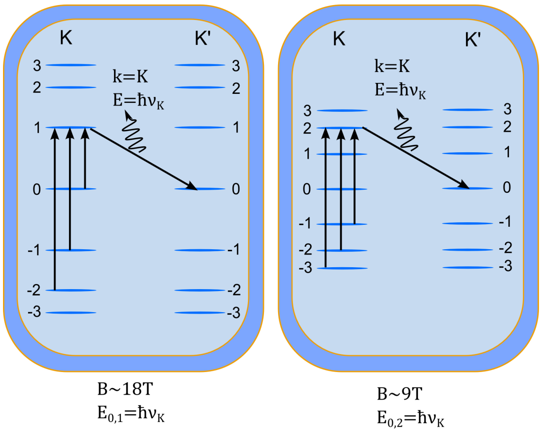

B~18T
$E_{0,1}=\hbar\nu_K$

B~9T
$E_{0,2}=\hbar\nu_K$

Figure 7.23: Illustration of a resonant scattering of an electron by K-point phonon

In the case of resonance with the Γ point phonons, the effect is almost the same. Here however phonons involved in the scattering process come from the vicinity of the Γ point so their momentum is negligible. Consequently, all the scattering events occur in the same valley.

7.5.3 Discussion: multiple excitations interaction model

Beyond simple broadening

When the lineshape of the electronic excitation is examined closely, it becomes apparent that the observed anomalies are not simply broadened lines but that they have an internal fine-structure. Fig. 7.24 presents a gray scale intensity map of the measured Raman spectra together with the positions of Lorentzian fits to the first three excitations. In order to obtain a good fit to the experimental data, multiple Lorenzian functions had to be used. In Fig. 7.25, a spectrum of the $L_{-1,1}$ excitation peak at $B = 18.4$ T is shown. It

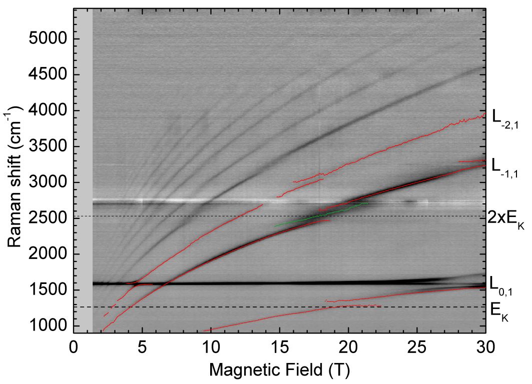

Figure 7.24: False colour intensity map of Raman spectra of graphene together with position of multiple component Lorentzian fits to the electronic excitation peaks. λ_{exc}=514.5 nm

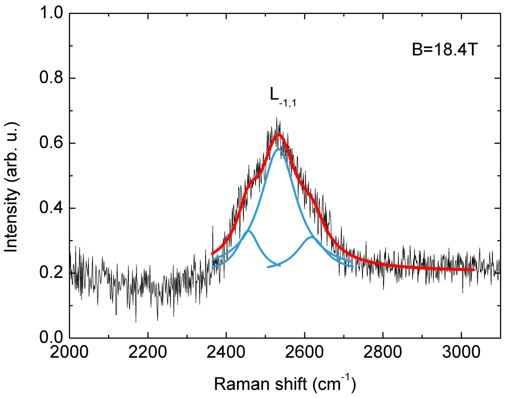

Figure 7.25: $L{-1,1}$ excitation peak at B=18.4 T. Three component Lorentzian fit to the curve is shown tohether with its components.λ_{exc}=783 nm

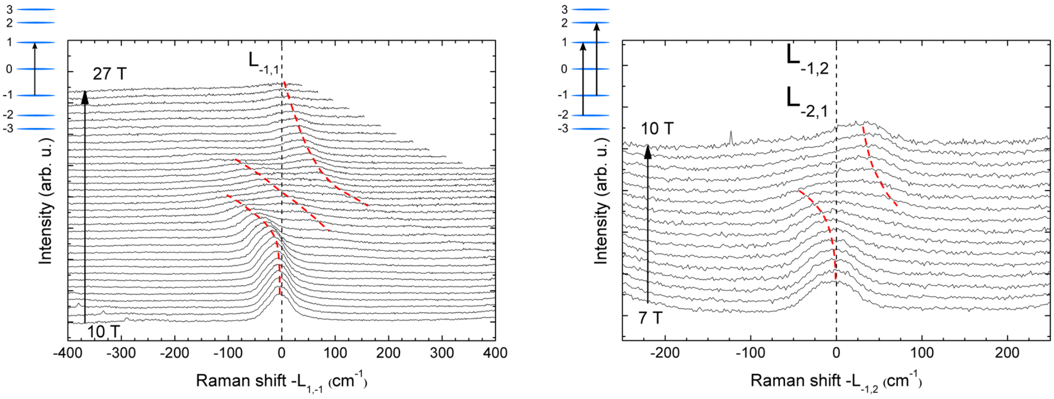

Figure 7.26: Raman scattering spectra of electronic excitation peaks $L_{n,m}$ in the anomalies region shifted in energy according to their theoretical evolution $\sim \sqrt{B}(\sqrt{n}+\sqrt{m})$. Left: for the $L_{-1,1}$ excitation(λ_{exc}=783 nm) and right: for the $L_{-1,2}/L_{-2,1}$ excitation(λ_{exc}=720 nm). To obtain a higher signal to noise ratio spectra were averaged across magnetic field range ΔB=0.2 T, which obscures the double component shape of each Raman peak

clearly consists of three peaks with linewidths varying in the range $70-110$ cm^{-1}. Since the number of components into which a given line splits due to the interaction closely matches the number of interacting modes, this means that at $B \approx 18$ T in addition to the purely electronic $L_{-1,1}$ excitation, there also exist two other excitations which have exactly the same energy and which couple to the $L_{-1,1}$ mode. This coupling leads to the formation of new hybridized modes which show an avoided crossing. A similar three component splitting is seen for $L_{-2,2}$ peak at $B \approx 9$ T. However for $\Delta|n| = \pm 1$ transitions another behaviour is found. Those magneto-exciton lines split into two components only, which is shown for $L_{0,1}$ and $L_{-1,2}$ peaks at $B \approx 18$ T in Fig. 7.24. To clearly illustrate this difference, Fig. 7.26 presents Raman scattering spectra obtained at selected values of magnetic field, which were shifted in energy in order to compensate the expected

evolution of electronic excitation energy in magnetic field. If the energy of that peak evolved according to simple $\sim \sqrt{B}$ model they would be seen all aligned at 0 on the x-scale. However clear avoided crossings are observed. In the left panel for the $L_{-1,1}$ excitation line three modes are seen, while in the right panel for $L_{-1,2}/L_{-2,1}$ only two modes appear.
The difference in the number of interacting modes for the $\Delta|n| = 0$ and $\Delta|n| = \pm 1$ electronic excitations can be understood once we propose a model that can explain which excitations take part in the different interactions.

Model

In the following discussion, for the sake of simplicity, we will focus on the case when the energy of the first LL is in resonance with K-point phonons at $B \approx 18$ T. The generalization for other cases is straightforward and done by substituting $1 \rightarrow n$ and $2 \rightarrow n+1$. Also the case of interaction with Γ point phonons is almost completely analogous, the only difference being that the Γ point phonons carry a momentum that is close to 0, so all electronic excitations and scattering events occur in the same valley.

In a solid state system many possible excitations have been observed and reported. Some are observed in every crystal- like quanta of atomic vibrations - phonons. Others require specific properties of a material to create excitations like e.g. a hole, exciton, polariton, polaron, plasmon, magnon, etc... Yet others are formed only when an external magnetic field is applied to the sample, like magneto-excitons. This classification of excitations is based on an assumption that one could separate the whole crystal into a set of independent subsystems: nuclei, core electrons, valence and conduction band electrons, nuclear and electron spin etc. However at some point those subsystems are not independent anymore. For instance, the motion of nuclei changes the instantaneous electric field felt by the electrons and thus affects their behaviour. This is known as the electron-phonon interaction, and may lead to formation of the hybridized modes that involve both phonons and excitons. In graphene, the MPR is probably the best known example of such hybridization. Here we employ the same concept of hybridization of already existing excitations in the system, to explain the observed anti-crossings at energies above $\sim 2000 cm^{-1}$.
When the magnetic field is set to $B = 18$ T, a resonance occurs between $L_{0,1}$ electronic excitation and the K-point phonons ($E_K \approx 1300$ cm^{-1} Fig. 3.1). This is seen directly in the splitting of $L_{0,1}/L_{-1,0}$ excitations, as well as in $L_{-1,2}/L_{-2,1}$ mode, together with the triple splitting of the $L_{-1,1}$ for the same value of the magnetic field. However, no signs of splitting is seen at the same energy (1300 cm^{-1}) for excitations other than $L_{0,1}$ at lower magnetic field (Fig. 7.19), which makes it qualitatively different from the MPR. $L_{0,1}$ appears as a special case that will be discussed at the end of this chapter. Now, we will focus on $L_{-1,1}$ excitation as representative for all $L_{-n,n}$ transitions.

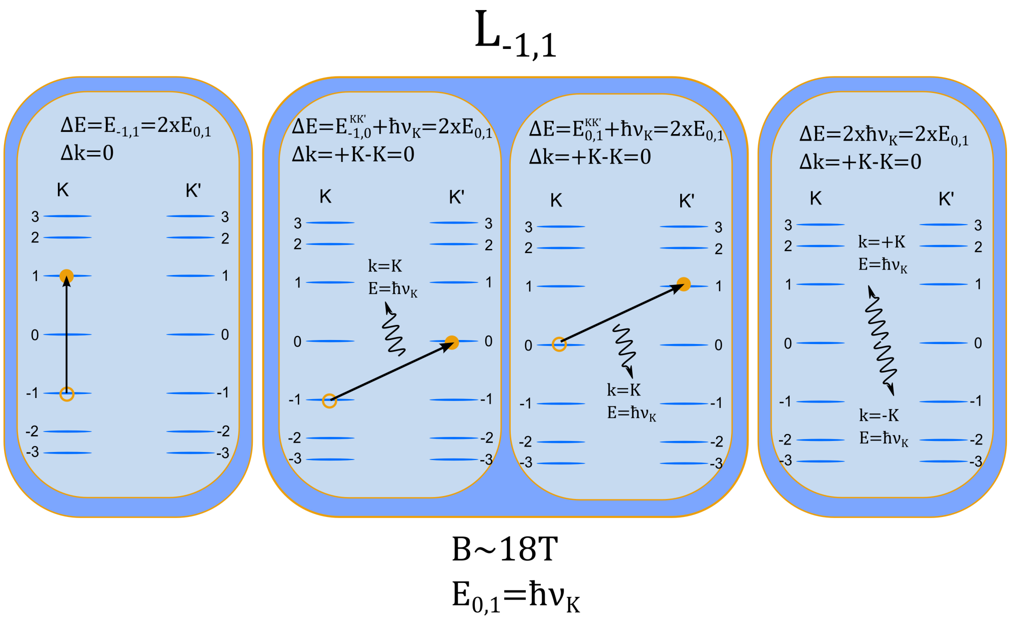

Figure 7.27: Three classes of excitations with degenerate energies in graphene at magnetic field value $B = 18$ T. Left: purely electronic $L_{-1,1}$ magneto-exciton. Middle: doubly degenerated mixed mode consisting of a sum of K-point phonon and intervalley $E^{K,K'}_{-1,0}$ (or $E^{K,K'}_{0,1}$) exciton. Right: purely vibrational, two K-point phonons with opposite K vectors. Filled circles denote electrons, empty – holes. Solid lines represent scattering/excitation of an electron, wavy lines – emission of a K point phonon. In each case the wavevector k is conserved in the whole process ($\Delta k = 0$).

$\Delta|n| = 0$ excitations

Fig. 7.27 presents three kinds of excitations which are in resonance at $B \approx 18$ T. In the first case (Fig. 7.27: Left) it is a simple interband magneto-exciton $L_{-1,1}$ with an energy $L_{-1,1} \approx 2600$ cm^{-1}. In the second case (Fig. 7.27 right) it is a process which results in the emission of two K-point phonons with opposite wavevectors $k_1 = +\vec{K}$ and $k_2 = -\vec{K}$. Therefore, the momentum is conserved in the whole process. In principle, those two phonons could be created via direct interaction with light of the illuminating laser. However direct interaction of light with phonons is rather weak and the resulting scattering cross-section is small. In theory of Raman scattering the much higher contribution to the scattering cross-section is given by a higher order process [55] which involve first the interaction of light with electrons which leads to the creation of a virtual electron-hole pair, and then emission of phonons due to electron-hole pairs decay. Since at $B = 18$ T, the energy of this virtual electron-hole pair would be in resonance with real electronic states, the probability of such processes could be resonantly enhanced. In the middle panel of Fig. 7.27 a third kind of excitation is shown, for which the final state consists of a coherent superpositon of one K-point phonon and an intervalley $L^{K,K'}_{-1,0}$ (or $L^{K,K'}_{0,1}$) magneto-exciton. In order to conserve momentum in the excitation process, wavevectors of the K-point phonon and the inter-valley scattered quasi-particle must cancel each other. As long as we consider valence and conduction bands dispersion to be symmetric, energies of mixed phonon-magneto-exciton modes are going to be doubly degenerated,

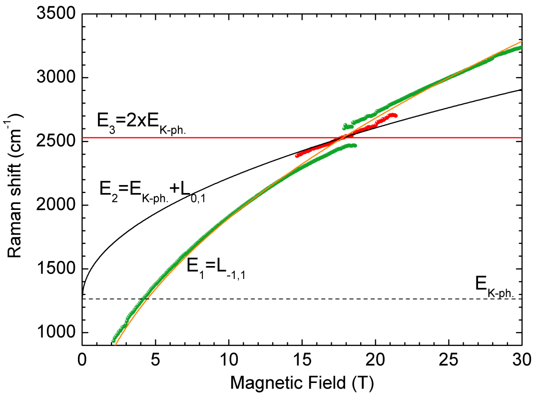

Figure 7.28: $L_{-1,1}$ excitation energy as extracted from magneto-Raman scattering experiment(dots). Lines-theoretical magnetic field evolution of three excitation modes energies: E_1-non-interacting $L_{-1,1}$ magneto-exciton, E_2-mixed mode consisting of K-point phonon and inter-valley $L_{0,1}^{K,K'}$ magneto-exciton, E_3-two K-point phonons.

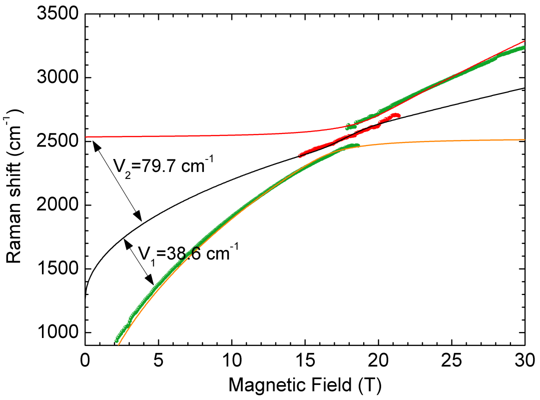

Figure 7.29: $L_{-1,1}$ excitation energy as extracted from magneto-Raman scattering experiment(dots). Lines- fitted to experimental data magnetic field evolution of three coupled excitation modes energies as in Fig. 7.28.

because $L_{-1,0}^{K,K'}$ and $L_{0,1}^{K,K'}$ magneto-excitons have the same energy. A peculiar feature of this mixed mode is the formation of an intervalley magneto-exciton.

Those three classes or modes of excitation can exist in graphene at all values of magnetic field B. However their energy evolves differently in B what is shown in Fig. 7.28. The energy of K-point phonons is independent of the magnetic field, and thus $E_3 = 2 \times E_K$ is constant. For the latter calculations we used the value extracted from Fig. 7.28, at the center of observed anti-crossing – $2E_K = 2530 \pm 20$ cm^{-1}, resulting in a K-point phonon energy value $E_K = 1265 \pm 10$ cm^{-1}. On the other hand the purely electronic mode E_1 increases like $L_{-1,1} \sim \sqrt{B}$, while energy of mixed mode E_2 evolves like $L_{0,1} \sim \sqrt{B}$ shifted by E_K value. Thus it is not a coincidence that energies of all three of those modes cross each other exactly at the same value of B. In fact for any $L_{-n,n}$ we have:

$$\begin{aligned}
&E_1 = v_F\sqrt{2e\hbar}\sqrt{B}(\sqrt{|-n|}+\sqrt{|n|}) = 2v_F\sqrt{2e\hbar}\sqrt{B}\sqrt{|n|}\\
&E_2 = E_K + v_F\sqrt{2e\hbar}\sqrt{B}(\sqrt{|0|}+\sqrt{|n|}) = E_K + v_F\sqrt{2e\hbar}\sqrt{B}\sqrt{|n|}\\
&E_3 = 2E_K
\end{aligned}$$

So at the magnetic field B_0 when E_1 crosses E_3, we calculate the energy of the E_2 mode:

$$\begin{aligned}
E_1 &= E_3 \\
2E_K &= 2v_F\sqrt{2e\hbar}\sqrt{B_0}\sqrt{|n|} \\
v_F\sqrt{2e\hbar}\sqrt{B_0} &= \frac{E_K}{\sqrt{|n|}} \\
E_2 &= E_K + v_F\sqrt{2e\hbar}\sqrt{B_0}\sqrt{|n|} = E_K + \frac{E_K}{\sqrt{|n|}}\sqrt{|n|} = E_K + E_K = 2E_K
\end{aligned}$$

Thus, at B_0, these three excitations are degenerated in energy and, as is shown by our Raman scattering experiments, are subject to hybridization.

In order to qualitatively reproduce the effect of modes hybridization on their respective energies, we used a simple phenomenological approach in which modes are coupled using a 3×3 Hamiltonian:

$$\hat{H}_{int} = \begin{pmatrix} E_1 & V_1 & 0 \\ V_1 & E_2 & V_2 \\ 0 & V_2 & E_3 \end{pmatrix} \tag{7.7}$$

Diagonal elements are the magnetic field dependent energies of each non-hybridized mode, defined as previously. The off-diagonal elements V_1 and V_2 are responsible for coupling the 0-phonon mode E_1 with 1-phonon mode E_2, and 1-phonon mode E_2 with 2-phonon mode E_3 respectively. Those coupling constants are expressed in the same units as the diagonal elements i.e. in units of energy, here cm^{-1}. At each value of the magnetic field B, the energies of the non-interacting modes E_1, E_2 and E_3 can be explicitly calculated. Thus, assuming some values for the coupling constants V_1 and V_2, the Hamiltonian (Eq. 7.7) can be numerically diagonalized, to find its eigenvalues $E{*}_1$, $E{*}_2$, $E{*}_3$ and eigenvectors. We have performed such diagonalization using the standard LAPACK procedures and for each value of the magnetic field $B \leq 30T$ we have calculated the energies of the three coupled modes. These energies were then compared with the experimentally determined energies of split Raman active $L_{-1,1}$ mode. By using least-square method the optimum values of coupling constants V_1 and V_2 were found.

Solid lines in Fig. 7.29 present the results of such calculations, showing a very good agreement with experimental points, denoted by green and red dots. This shows that even a simple model like this is able to reproduce the most important effects of modes hybridization. The obtained values of $V_1 = 38.6$ cm^{-1} and $V_2 = 79.7$ cm^{-1} reveal a significant asymmetry in the strength of coupling between the mixed mode and purely vibrational or purely electronic modes respectively.

Those off-diagonal terms in the Hamiltonian matrix can be related to the dimensionless electron-phonon coupling constant λ_K which is defined as in ref. [63]:

$$\lambda_K = \frac{F_K^2 A_{u.c.}}{2M\omega_K v_F^2} \tag{7.8}$$

Where, $\omega_K = 1210\ \mathrm{cm}^{-1} = 0.150\mathrm{eV}$, $M = 2.88 \times 10^3$ (eV Å^2)$^{-1}$ is the mass of the carbon atom and $A_{u.c.}$=5.24 Å^2 is the area of the graphene unit cell. While F_K is a proportionality coefficient, which has the dimension of a force. With such coupling constant, the relation to the phenomenological V_1 and V_2 is the following:

$$V_1 = v_F \sqrt{\frac{\lambda_K e B \hbar}{4\pi}} \tag{7.9}$$

$$V_2 = V_1 \sqrt{\frac{3}{2} - \frac{1}{e}} \approx 1.064 V_1 \tag{7.10}$$

Using the above expressions one can estimate the dimensionless coupling constant between K-point phonons and electrons to be: $\lambda_K = 0.023$ which is about one third lower from the value obtained in the DFT calculations $\lambda_K^{DFT} = 0.034$ [103]. The above model correctly predicts that the coupling between 2-phonon excitation and 1-phonon excitation should be larger than the coupling between 1-phonon mode and 0-phonon mode. However the expected asymmetry of the order of 6% largely underestimates the experimentally found two-fold increase in the strength of the coupling for the latter pair of excitation modes.

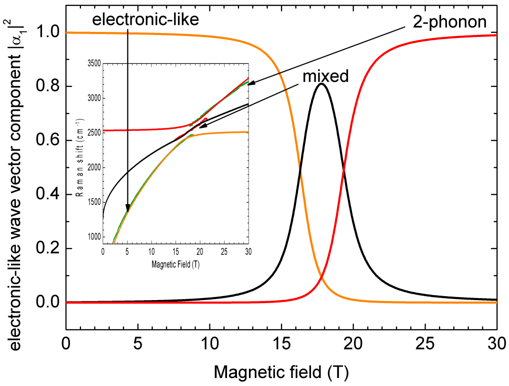

Figure 7.30: Amount of Raman active wavefunction component $|\alpha_1|^2$ in each of the interacting, coupled modes.

It is important to note, that out of 3 excitation modes presented above only one – the purely $L_{-1,1}$ excitation is Raman active. Therefore only this mode can be observed in our Raman scattering experiment in whole range of magnetic field. The two other modes: two K-point phonon emission $2 \times E_K$ and a mixed mode of phonon plus inter-valley magneto-exciton cannot be directly observed in whole range of magnetic field in our experiment. However, when those modes hybridize their wavefunctions $\Psi{*}_n$ become a coherent superposition of the non-interacting modes wavefunctions Ψ_n:

$$\Psi_n^* = \frac{1}{\sqrt{3}}(\alpha_{1n}\Psi_1 + \alpha_{2n}\Psi_2 + \alpha_{3n}\Psi_3)s \tag{7.11}$$

Thus, some part of Raman active $L_{-1,1}$ mode wavefunction is mixed with the two other modes. This enables them to gain some oscillator strength which makes them visible in the experiment. This process of transferring Raman active component α_{1n} of the wavefunction between those modes can be visualized by plotting the amount of modulus square of it for each hybridized mode as a function of magnetic field (Fig. 7.30).

As is expected, at low values of magnetic field the vast majority of $|\alpha_1|^2$ component belongs to the mode originating from the purely electronic excitation. Then, between 14 and 18 T it looses most of it in favor of the mixed- phonon plus $L_{0,1}$ excitation which becomes Raman active in a narrow range of magnetic field between 16 and 20 T. This is also the only range where all of the three modes have non-negligible amount of $|\alpha_1|^2$ component and thus can be observed in the experiment simultaneously. And finally the whole Raman active $|\alpha_1|^2$ component is transfered to the excitation mode which originated from the two-phonon emission process.

$\Delta|n| = \pm 1$ excitations

After explaining the hybridization of different excitation modes for $\Delta|n| = 0$ transitions, we turn back to $\Delta|n| = \pm 1$ transitions which split into two modes only. This different behaviour can be analyzed by considering the doubly degenerated $L_{-1,2}/L_{-2,1}$ excitations. As in the case discussed above $L_{-1,2}/L_{-2,1}$ shows anti-crossing at magnetic field $B \approx$ 18 T when $L_{0,1}$ excitation is in resonance with K-point phonons. So in addition to purely electronic excitations $L_{-1,2}/L_{-2,1}$ it is also possible to create in the system an excitation which is a superposition of one K-point phonon and an intervalley-magneto-exciton $L_{0,2}^{K,K'}$. Again, to compensate momentum of the particle which is scattered into another valley $\vec{k} = -\vec{K}$, the emitted phonon must have exactly opposite wavevector $\vec{k} = \vec{K}$. In this case however, the energy of the two phonon emission process is too small to be in resonance with those excitations. So in the end there are only two modes of excitation which can have the same energy and therefore hybridize with each other. This should be reflected in the Raman spectra by a two component splitting of $L_{-1,2}/L_{-2,1}$ or in general $L_{-n,n+1}/L_{-n-1,n}$ magneto-excitons at selected magnetic field values. Which is exactly what was found in the experiment.

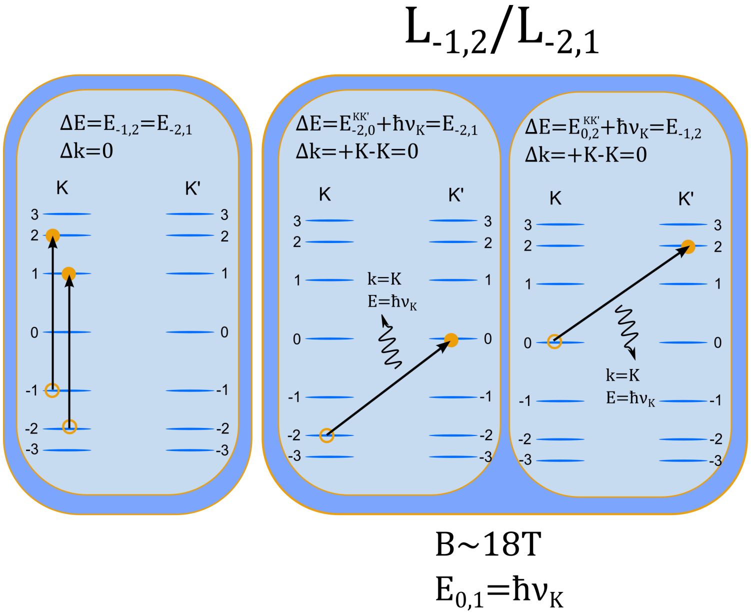

Figure 7.31: Two classes of excitations with degenerate energies in graphene at magnetic field value $B = 18T$. Each class of transitions is doubly degenerated due to electron-hole symmetry. Left: purely electronic $L_{-2,1}$ (or $L_{-1,2}$)magneto-exciton. Right: mixed mode of a sum of K-point phonon and intervalley $E_{-2,0}^{K,K'}$ (or $E_{0,2}^{K,K'}$) exciton. Filled circles denote electrons, empty – holes. Solid lines represent scattering/excitation of an electron, wavy lines – emission of a K point phonon. In each case wavevector k is conserved in the whole process – $\Delta k = 0$.

From all $\Delta|n| = \pm 1$ magneto-excitons there is one pair that is slightly different. These are the $L_{-1,0}$ and $L_{0,1}$ excitations. In all the so far discussed cases, the mixed mode consisted of a K-point phonon plus an inter-valley, inter-band magneto-exciton. For the $L_{-1,0}$ and $L_{0,1}$ excitations, however the mixed mode is composed of a K-point phonon plus zero-energy, inter-valley exciton. Due to electron and hole being both at the 0 LL, but one in the K valley while the other in the K'. Excitation mixing for $\Delta|n| = \pm 1$ can be described analogously as for the $\Delta|n| = 0$ magneto-excitons, the only difference being the size of the interaction Hamiltonian matrix - 2×2. Fig. 7.32 shows the extracted from experiment Raman peaks energies together with energy of $L_{0,1}$ excitation (E_1), of K-point phonon (E_2) and Γ point E_{2g} phonon. Due to large MPR of $L_{0,1}$ excitation it was necessary to include Γ point phonon in the calculation in order to obtain good fit to the experimental data. So we again used a 3×3 matrix for the interaction Hamiltonian:

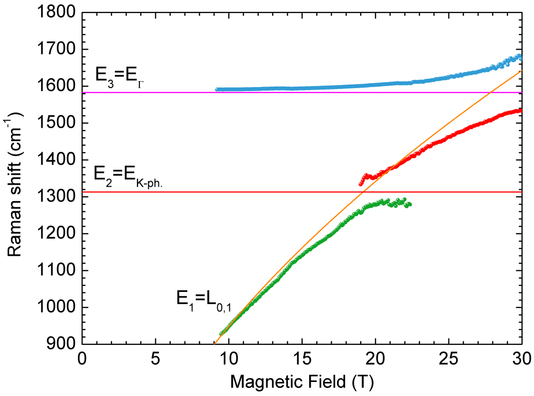

Figure 7.32: $L_{0,1}$ excitation energy as extracted from magneto-Raman scattering experiment(dots). Lines-theoretical magnetic field evolution of three excitation modes energies: E_1 – non-interacting $L_{0,1}$ magneto-exciton, E_2 – mixed mode consisting of K-point phonon and zero energy inter-valley $L_{0,0}^{K,K'}$ magneto-exciton, E_3 – Γ point phonons.

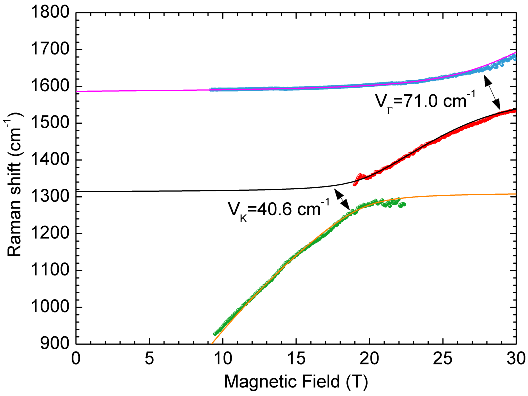

Figure 7.33: $L_{-1,1}$ excitation energy as extracted from magneto-Raman scattering experiment(dots). Lines – fitted to experimental data magnetic field evolution of three coupled excitation modes energies as in Fig. 7.32.

$$\hat{H}_{int} = \begin{pmatrix} E_\Gamma & V_\Gamma & 0 \\ V_\Gamma & E_{0,1} & V_K \\ 0 & V_K & E_K \end{pmatrix} \tag{7.12}$$

Where $E_\Gamma = 1580\text{cm}^{-1}$ is the energy of Γ point phonon, $E_K = 1310\ \text{cm}^{-1}$ energy of the K-point phonon [103] and $E_{0,1}$ energy of non-interacting $L_{0,1}$ excitation. While V_Γ and V_K are off diagonal matrix elements that couple $L_{0,1}$ excitation to Γ and K point phonons, respectively. Following the same Hamiltonian diagonalisation procedure and least-square fitting as before, a result shown in Fig. 7.33 was obtained. It shows a good agreement with the data, however, a higher value for the K-point phonon energy had to be used. One that matched the energy of anti-crossing of $L_{0,1}$ excitation with K phonon observed at ~ 18 T. This value $E_K = 1310 \pm 5\ \text{cm}^{-1}$, is about $50\ \text{cm}^{-1}$ larger than the one estimated from the anti-crossings involving $L{-n,n}$ excitations. Reason of this discrepancy is still unclear for us.

Γ point phonon

Finally we have repeated the same analysis for $L_{-2,2}$ magneto-exciton when it couples to a phonon at 3250cm^{-1}. We identify it as an overtone of phonons from the vicinity of the Γ point [63]. Anti-crossings produced by the interaction of $L_{n,m}$ excitations with this phonon form essentially the same set of resonances as in case of K point phonons, but they are centered at higher energy (see Fig. 7.19). This process is very similar to the one described previously with K point phonons, but in this case the emitted phonons carry momentum close to zero. This implies that all the scattering events occur in the same valley. Since Γ phonons have higher energy than those from K point, the respective resonances are observed at higher magnetic fields. The most pronounced ones involving the $n = 1$LL should occur in magnetic field just above $B = 30$T. Thus in our experiment we were able to observe just a beginning of those processes. For that reason in our analysis we used the second most pronounced anti-crossing involving the $L_{-2,2}$ excitation. Following the same procedure as before of coupling two-phonon emission process, with a mixed mode consisting of $L_{0,2}$ excitation with emission of K phonon and coupling this mode to the $L_{-2,2}$ excitation we managed to extract the coupling constants. It gave very similar results to those obtained for $\Delta|n| = 0$ excitations interacting with K-point phonons. It gave values of $V_1 = 31.0$ cm^{-1} for coupling between $L_{-2,2}$ excitation and mixed mode, while $V_2 = 73.4$ cm^{-1} being the coupling constant between two Γ point phonon emission process and a mixed mode. This confirms the asymmetry of the coupling constants V_1 and V_2, which are in this case lower by 8% and 20% than those found for K-point phonon. This is in qualitative agreement with theory predicting that K-point phonon should couple twice as strongly to electrons as Γ point phonon [103].

7.6 Conclusions

To conclude, we have presented in this chapter the current state of knowledge about graphene-like domains that can be found on the surface of bulk graphite. We have presented results of a series of magneto-Raman scattering experiments which reveal existence of the relativistic Dirac particles in those domains and confirms the unprecedented electronic quality and low doping level of this system. A method was presented, based on the analysis of 2D band shape, which allows for identification of those flakes even in the absence of the external magnetic field. Most importantly, we reported a new manifestation of the electron-phonon interaction in graphene flakes, which is entirely different from the well known magneto-phonon resonance. Finally we have identified phonons responsible for the observed electronic excitation peak splittings, as the K-point phonon and optical phonons from the vicinity of Γ point. We have proposed a simple, phenomenological model that allowed us to explain the difference in the number of interacting modes for $\Delta|n| = 0$ and $\Delta|n| = \pm 1$ excitations, reproduce energies of the hybridized modes and evaluate value of the electron-K-point phonon coupling constant.

Chapter 8

Results: graphene on BN

In this chapter we are going to present and discuss the results of Raman scattering experiments performed on the single-layer graphene flake encapsulated by two thin hexagonal boron nitride (hBN) flakes. Those experiments were performed at liquid helium temperature (4.2 K) and using the micro-Raman setup described in Chapter 6. For the excitation, we used 514.53 nm line of the argon laser and about 4-5 mW power on the sample. In order to maximize the scattered signal intensity we didn't use any polarizes in the presented experiments. So we were not sensitive to the polarization of the incoming nor outgoing light.

8.1 Sample description and characterization

The structures studied in these experiments has been kindly provided to us by the research group from the University of Manchester. In order to obtain a graphene sample encapsulated between two layers of hBN, an exfoliation technique was used, followed by a precise positioning of flakes, one on top of the other. In the first place, flakes of hBN were prepared on oxidized silicon surface by micro-mechanical exfoliation technique. Then, using an optical microscope, two flakes were selected, which exhibited an optical contrast characteristic for flakes having thickness $\sim$ 30 nm. Since inter-plane lattice distance in hBN is equal to 0.666 nm [217], these flakes were composed of $\sim$ 45 atomic layers, which is a number large enough to separate the upper surface from the roughness of the Si/SiO$_2$ substrate. In the next step, graphene flakes were prepared on another substrate and then one was transferred on top of hBN flake, using dry transfer technique (Fig. 8.1a). Then, the sample was annealed at 300°C in an Ar-H$_2$ atmosphere. Finally, the second flake of hBN was used to encapsulate the graphene-hBN structure (Fig. 8.1b). The complete structure has roughly triangular shape, being 150μm long and 100μm wide in the central part. Fig. 8.1c) shows details of the shapes of particular flakes building the structure. Since they do not overlap completely, one can find regions where graphene flake:

- is located directly on Si/SiO$_2$ substrate,
- lies on one hBN flake, but is not covered by the other hBN layer,

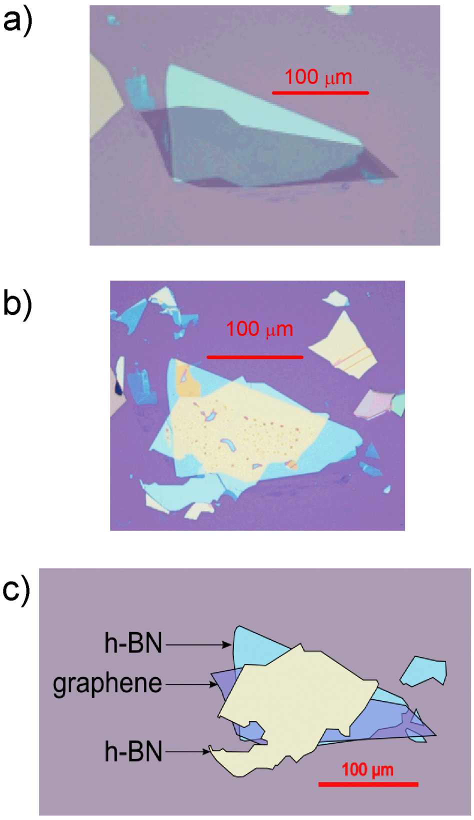

Figure 8.1: a) Optical microscope image of a graphene flake deposited on hBN flake. b) Image of a flakes shown in a) after covering the structure with a second hBN flake. c) Schematic picture highlighting shapes of each particular flake.

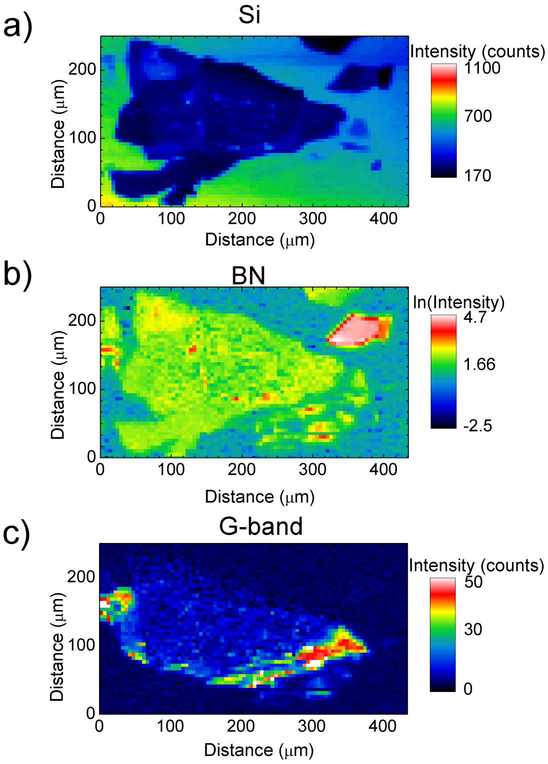

Figure 8.2: Reconstructed maps of Raman scattering intensity of hBN-graphene-hBN sample when plotting the intensity of Raman signal at the energy of phonons in: a) Si-peak at $\sim$ 520 cm^{-1}, b) hBN-peak at 1368 cm^{-1}, c) graphene G-band at $\sim$ 1590 cm^{-1}. Magnetic field B=0T, acquisition time for each point: 2s.

- is fully encapsulated in between two hBN flakes.

Since a color of the flake, as it is seen under the optical microscope, is determined by the white light interference condition in the thin film, one can estimate the thickness of each part of the flake by comparing their colors. The blue areas in Fig. 8.1b) show parts of the hBN flake which are approximately 30 nm thick, while yellow ones correspond to the places where the upper and lower flake overlap each other and the structure is $\sim$ 60 nm thick.

Due to using optical fibers in our experimental setup (Chapter 6) for measurements in magnetic fields, we couldn't directly image the surface of the sample as it is done under an optical microscope. Thus, in order to find and characterize the sample, a mapping of the surface was performed by measuring the Raman scattering signal from a regular array of points. Then, plotting the Raman signal intensity at a given energy (Raman shift) allowed us to selectively image the different components of sample's structure. Fig. 8.2

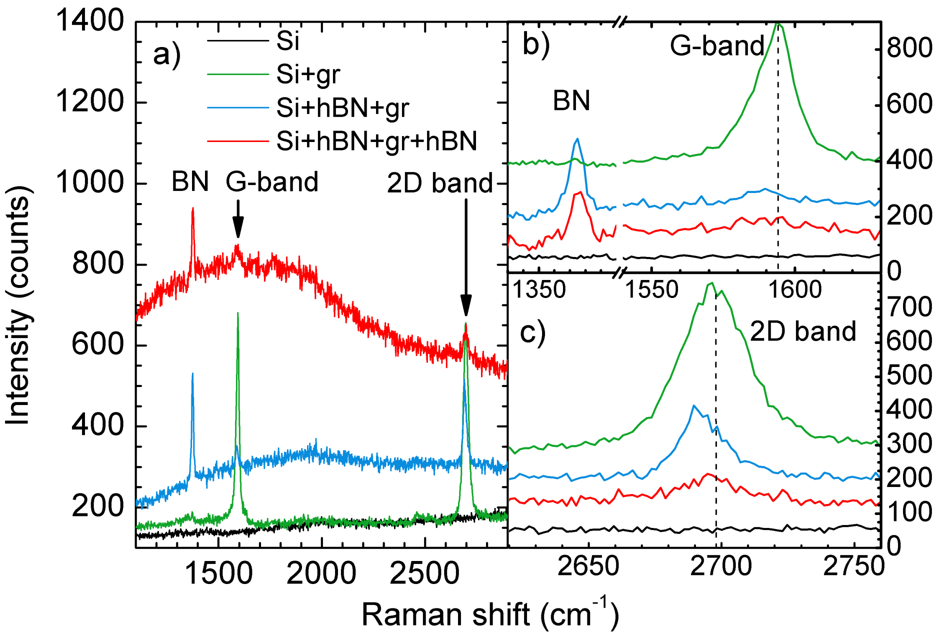

Figure 8.3: Raman spectra measured at different locations of the exfoliated graphene sample: green curve-graphene deposited directly on Si/SiO$_2$ substrate, blue curve- graphene deposited on hBN flake, red curve- graphene deposited on and covered by hBN flakes, black curve- Si/SiO$_2$ substrate response.

shows such maps measured at 4K and without any external magnetic field ($B = 0$ T), while more detailed maps showing only a part of the studied flake measured at magnetic field $B = 10$ T are shown in Fig. 8.4. Maps reconstructed at the energy of Si peak (520 cm^{-1}), show how strongly the Raman signal from the substrate is attenuated by different flakes lying on the surface. Since ~ 30 nm – thick BN flakes are much thicker than a single layer graphene, these are mainly BN flakes that are visualized with a Raman response from the Si substrate (Fig. 8.2a). In the detailed map in Fig. 8.4a one can clearly distinguish two regions of BN with either one hBN flake (dark blue) or two flakes stacked on top of each other (black).

Similarly a map of Raman scattering intensity at the energy of one of the main hBN phonons, at 1368 cm^{-1} reveals the locations of hBN flakes. However, this time not only the thick flakes are visible, but also the thiner and smaller ones, as seen below the main triangular flake in the Fig. 8.2b. The detailed map in Fig. 8.4b shows a clear difference between two parts of BN flakes: the bottom one as well as the upper one, used to cover the graphene flake.

G-band Repeating the procedure at the energy of G-band (~ 1590 cm^{-1}) one can also visualize the position of the graphene flake even if it is additionally covered by hBN. It is shown in Fig. 8.2c, where a lighter shade of blue marks the area on the hBN flake which is covered with graphene, while the extremely intense G-band is seen close to boundaries of hBN flake, where graphene lies directly on Si/SiO$_2$ substrate. This strong dependence of G-band intensity of graphene on the substrate and/or it's capping is even better seen in the raw Raman scattering spectra as shown in Fig. 8.3a,b. For each region of graphene sample, a single representative spectrum was selected and shown. Considering the G-band, it clearly shows that it is the most intense on the parts of graphene lying directly on Si/SiO$_2$ substrate(Si-gr). However, on those locations the G-band also exhibits very high variations in the intensity as compared to other Raman peaks like the 2D band or Si peak. Nevertheless, taking the spectrum shown in Fig. 8.3 as the average one, we clearly see the decrease in the G-band intensity on the areas resting on the hBN flake. In fact, in the locations where graphene was deposited on top of hBN flake but not covered with another flake (Si-hBN-gr) the G-band intensity decreased 10-fold. On the other hand, in the areas where it was encapsulated from both sides by hBN (Si-hBN-gr-hBN) it was 15-times less intense.

The observed decrease in G-band intensity was a surprise, since depositing the exfoliated graphene on hBN was expected to improve the system's quality. However, an assumption of improved cleanliness may not be fully valid in this case since at the same time we observed an enormous increase in the amount of dispersed light leading to much higher background. As seen in panel a) of Fig. 8.3, at the locations where graphene was lying on top of hBN the background rose to about twice higher level as compared to the graphene resting on Si/SiO$_2$. This effect is even more pronounced on the places where graphene was encapsulated by hBN, which show from two to five times higher background, depending on the energy of scattered light. This higher background originates from the contamination which remains after each step of flake transferring process, when the PMMA compound is used. These contaminants tend to group together and form bubbles, most of which have a sub-micron size. The largest of them are seen as the darker spots in the central part of the flake (seen in Fig. 8.1b), but they also occur on parts of graphene on hBN which are not covered by the second flake. They can be seen in dark field image under the optical microscope and in transmission electron microscope (TEM). The first measurements made on those bubble revealed the presence of hydrocarbons which is what we would expect to see in the response of the PMMA residue. These contaminations contribute to the higher dispersed light background. Yet, as we are going to present it in the later part of this chapter, we were able to observe the effects on this sample which are very sensitive to the electronic quality of graphene or to charge doping. Therefore we were still able to observe them, the presence of those hydrocarbons bubbles couldn't have a major detrimental effect on the system's quality.

Charge doping level can be estimated from the energy position of the G-band in the absence of the external magnetic field. In the case of the parts of graphene flake lying directly on the Si/SiO$_2$ we found that G-band energy varied in the range from 1593 to 1595 cm^{-1}. The fragments which were either lying on hBN or were completely encapsulated showed a higher variation of the position of G-band, but generally at a lower energy – from 1583 to 1591 cm^{-1}. This seems to confirm the fact that depositing graphene on hBN flake reduces unintentional doping of the sample. However due to the presence of hydrocarbons bubbles the doping profile is rather non-uniform across the sample. Based on the works of *Yan et al.* [106] we can make a rough estimation that in the least doped areas charge density in our sample is close to 1×10^{12} cm^{-2}.

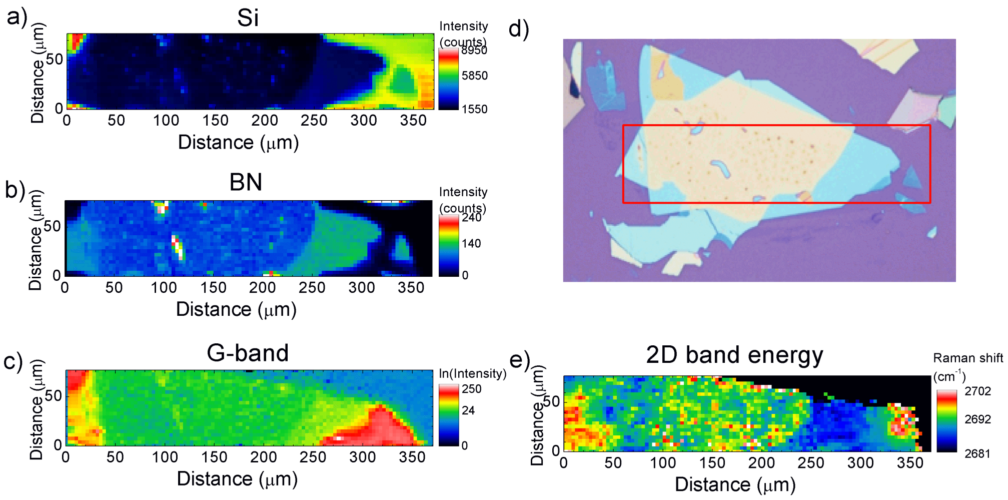

Figure 8.4: a)-c)Reconstructed maps of Raman scattering intensity of a region of hBN-graphene-hBN sample shown inside red rectangle in panel d). Intensity of Raman signal was plotted at the energy of phonons in: a) Si-peak at $\sim$ 520 cm^{-1}, b) hBN-peak at 1368 cm^{-1}, c) graphene G-band at $\sim$ 1590 cm^{-1}. e) Map of the energy position of 2D band. Magnetic field B=10 T, acquisition time for each point 20s.

2D band Considering the 2D band, its intensity exhibits a similar behavior to that of the G-band, being the most intense on graphene on Si/SiO$_2$, decreasing 2.5 times for graphene on hBN and being 6 times lower for graphene in between two hBN layers. The overall tendency to lower the intensity of the 2D band peak is the same as for the G-band, but the rates at which it occurs are slightly different. This leads to the change in the relative intensity of the G-band to the 2D band. At the locations of graphene resting directly on Si/SiO$_2$ due to large variations of G-band intensity, it is either higher or comparable in height with the 2D band. However, on graphene resting on or sandwiched between hBN flakes the G-band is about 2-4 times smaller than the 2D band. This better resembles a commonly reported Raman spectrum of exfoliated monolayer graphene [69]. Interestingly, the energy at which the 2D band is observed depends very clearly whether graphene lies on the Si/SiO$_2$ substrate, on an hBN or it is surrounded by hBN from both sides. The map shown in Fig. 8.4 and spectra in Fig. 8.3 reveal that the 2D band measured on graphene on Si/SiO$_2$ is seen at the energy 2697 cm^{-1} while on hBN flake it clearly downshifts by 6 cm^{-1} toward 2691 cm^{-1}. The latter value is pretty much uniform across the sample. However, at locations where graphene is encapsulated by hBN from both sides, the 2D band energy rises again to $\sim$ 2696 cm^{-1}. The same value of 6 cm^{-1} downshift was observed when mapping the surface of the sample regardless whether external magnetic field was applied or not. Since the origin of the 2D band comes from a double resonant scattering process, the observation of the 2D band at different energy means that phonons of different energies and k-vectors were selected in the scattering process. As we will argue later on, this downshift of the 2D band on hBN flake can be understood in terms of a double resonant scattering process and a Fermi velocity which varies depending on the substrate.

Effects which were mentioned above showed that changing substrate from Si/SiO$_2$ to hBN does indeed have an effect on the electronic properties of graphene. This is reflected in the change in recorded Raman spectra. However, to better understand origin of this change, we needed an insight into the changes of the electronic bandstructure of graphene once that it is deposited on top of hBN. Fortunately, magneto-Raman spectroscopy provides us with tools which can be used to deduce such changes. By analyzing the details of the magneto-phonon resonance(MPR) and inter-Landau level electronic excitations, some information about the electron bandstructure can be extracted. Results of experiments focusing on those effects are presented below.

8.2 Magneto-phonon resonance

So far, the magneto-phonon resonance in graphene has been observed only on those types of systems which are characterized by an exceptionally good electronic quality and very low charge doping level. Those systems include: epitaxial graphene grown on SiC surface [108], graphene inclusions on the surface on graphite [109, 44, 32], bulk graphite [45, 46]. On the other hand, an exfoliated graphene deposited on the surface of Si/SiO$_2$ is usually too much doped to show any sign of MPR other than with the most pronounced resonance with $L_{-1,0}/L_{0,1}$ excitation at high magnetic fields $\sim$ 24 T [139]. In order to check if depositing exfoliated graphene on top of hBN flake can reduce charge doping to such a low level that MPR can be observed we measured Raman spectra of graphene while sweeping magnetic field up to $B = 30$ T.

8.2.1 hBN-graphene

First, we chose such a location where the graphene flake was lying on top of hBN flake but not covered with another one. It is marked by a red dot on the optical microscope picture of the sample in the inset of Fig. 8.5Right). Then, we measured Raman spectra, focusing on the energy of the G-band (~ 1590 cm^{-1}) while sweeping the magnetic field at rate of 87 mT per spectrum. Results of such experiments are shown in the form of a false color intensity map in Fig. 8.5: Left. This figure clearly shows that the energy at which Γ point phonon (G-band) is seen exhibits clear oscillations in magnetic field, which is a hallmark of the magneto-phonon resonance. To better see those oscillations, we have fitted the G-band peak at each single spectrum with a single component Lorentzian curve. Then, the position of the center of each peak was plotted in Fig. 8.5: Right. At least three resonances at which the G-band energy deviates strongly from its zero-magnetic field value are clearly observed. Positions of those resonance are marked with red, dashed lines and correspond to the values of magnetic field at which the optical-like inter-Landau levels excitations are crossing the zero-magnetic field G-band energy. At magnetic field $B = 22\pm1$ T a resonance with $L_{0,1}$ and $L_{-1,0}$ excitations is seen. Similarly, we observe resonances at $B = 3.31 \pm 0.1$ T for $L_{-1,2}$ and $L_{-2,1}$ excitations, as well as at $B = 1.74 \pm 0.08$ T for the $L_{-2,3}$ and $L_{-3,2}$.

Usually, the experimentally obtained MPR can be satisfactorily fit by calculating the poles of the phonon Green function which take into account the renormalization of phonon energy due to optical-like inter-LL excitations. This is equivalent to searching for zeros of the function defined by Eq. 3.17, where only $\Delta|n| = \pm1$ transitions are taken into ac-

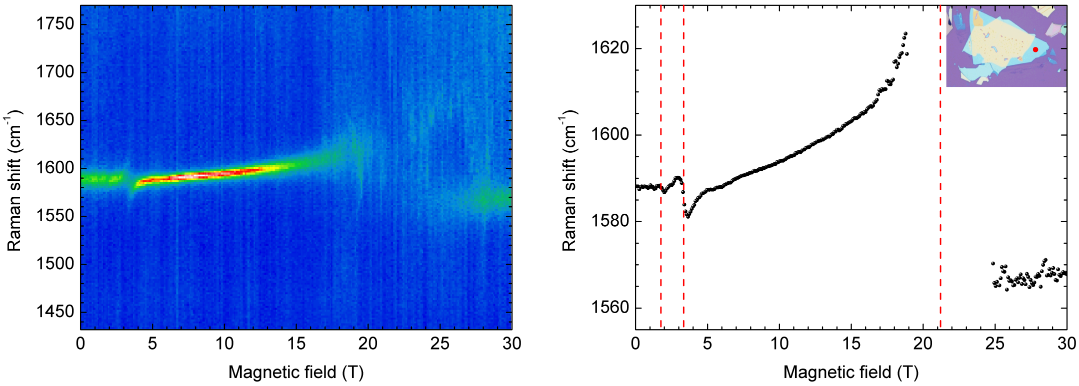

Figure 8.5: MPR measured on a quasi-neutral exfoliated graphene sample, deposited on a hBN flake. Left: a false color intensity map of Raman scattering intensity measured up to 30 T. Right: the extracted energy position of the G-band exhibiting a MPR. Red dot in the inset shows the position on the flake where the measurements were performed.

count. Since calculations are done in the complex plane, the real part of the root of that equation corresponds to the renormalized energy of Γ point phonon, while the imaginary part gives the contribution δ_{e-ph} of electron-phonon interaction to the phonon linewidth δ. There are, however, also other factors responsible for a finite Γ phonon linewidth δ_0, which are always present, even in the absence of electron-phonon interaction. Since analytical model proposed by *Ando* [137] does not take δ_0 into account, the phonon linewidth obtained in the calculations has to be adjusted to the experimentally measured value by adding that constant $\delta = \delta_{e-ph} + \delta_0$.

We used the same procedure to model MPR measured on graphene on hBN, assuming the same value of electron-phonon coupling constant as reported before [108, 32] $\lambda = 4.5 \times 10^{-3}$, thus the only free fitting parameter being Fermi velocity v_F. The calculated value of G-band linewidth had to be increased by a constant factor $\delta_0 = 4$ cm^{-1}, which describes a contribution to phonon linewidth from other factors than electron-phonon interaction effects.

However, it turned out that it was not possible to fit all three observable resonances with a single value of v_F. To illustrate this we compared in Fig. 8.6 the experimental results (black dots) with three sets of calculated (red lines) energies and linewidths of Γ phonon. In each set a different value of v_F was used to provide a good match between simulation and experiment close to a given resonance. In addition, a $\sqrt{B}$ scale on horizontal axis was used since this is the scale of electronic excitations energy evolution and it helps to observe all the resonances on the same graph. Panels a) and d) show that a good fit to experimental data in the vicinity of a resonance at $B = 22 \pm 1.5$ T is obtained when Fermi velocity is set to $v_F = 1.15 \times 10^6$ m/s. However with this value of v_F all resonances visible at lower energy are not well described by the calculated curve. Similarly, using a higher value of Fermi velocity $v_F = 1.24 \times 10^6$ m/s we can obtain a good match between calculated and measured values for a resonance at $B = 3.3 \pm 0.1$ T. And again quality of the match diverges when going away from the resonance. For the next resonance at lower magnetic field $B = 1.74 \pm 0.08$ T even higher Fermi velocity is needed $v_F = 1.28 \times 10^6$ m/s. Additionally, a weak sign of interaction between $L_{-1,1}$ excitation

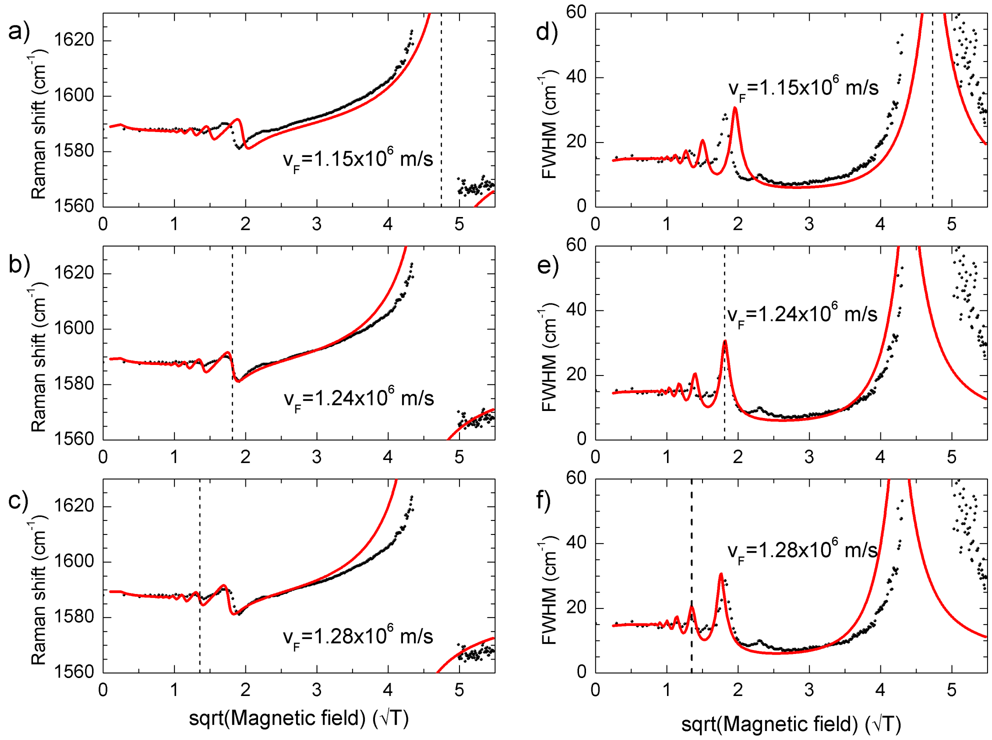

Figure 8.6: Experimentally determined energy and linewidth of Γ point phonon (black dots) and result of calculations which assumed different values of Fermi velocity.

with Γ-phonon is seen as a small broadening of phonon linewidth at $B = 5.30 \pm 0.15$ T. Theoretically, the $L_{-1,1}$ excitation does not have the proper symmetry to couple to the Γ phonon, but a weak sign of coupling of this excitation to the phonon has already been observed in graphene flake on the surface of graphite. Altogether, the following relations between Fermi velocity and LL index of participating excitations has been observed:

excitation	resonance field (T)	Fermi velocity($\times 10^6$ m/s)
$L_{0,1}/L_{-1,0}$	22.0± 1.5	1.15
$L_{-1,1}$	5.30± 0.15	1.18
$L_{-1,2}/L_{-2,1}$	3.3± 0.1	1.24
$L_{-2,3}/L_{-3,2}$	1.74± 0.08	1.28

The above results show that in graphene deposited on hBN, the Fermi velocity v_F is not a constant parameter, but it either decreases with magnetic field B or it increases with LL index n. Moreover, the fact that the $L_{-2,3}/L_{-3,2}$ excitation is observed allows us to set an upper limit for the charge doping $\rho_{max} < \frac{eB}{h}\nu_{max}$. Considering the most doped system for which at least one of those transition would be still possible, we obtain a condition that filling factor ν must be lower than ν_{max} corresponding to the fully occupied $n = 3$ LL. Inserting the value of the magnetic field, at which the resonance is observed $B = 1.74$ T and $\nu_{max} = 14$ we obtain the limiting value for charge doping $\rho_{max} < 7.35 \times 10^{11}$ cm^{-2}.

8.2.2 hBN-graphene-hBN

In order to check if covering a graphene flake deposited on hBN surface with another hBN flake does have any effect on it's properties an analogous experiment was performed on the location marked with a red dot in Fig. 8.7. In general due to about twice lower signal to noise ratio on that location as compared to hBN-graphene spot the measured MPR was not as well resolved as for the previous spot. Moreover, an additional component of the G-band appeared that remained constant in magnetic field. This double structure of the G-band is known to be seen in doped graphene samples. In the case of doped graphene, the MPR would be seen just in one polarization of the light, depending on the sign of doping, while it would be blocked in the other light polarization. Since we were performing measurements without resolving the incoming nor outgoing light polarization, we would have observed a spectrum which consists of a G-band that has two components: one constant in B and one showing a MPR. This is exactly what was observed in the experiment.

Fig. 8.7 shows the energy position (upper panel) and the linewidth (lower panel) of the G-band, as extracted from the Raman spectra using a one component Lorentzian fit to the G-band peak. Red lines mark the magnetic field values, where MPR resonances occur. As compared to the measurements on the uncapped hBN-graphene region, now the resonances are seen at slightly higher magnetic fields. Again, we can extract v_F parameter from the value of magnetic field at the resonance for different excitations, obtaining:

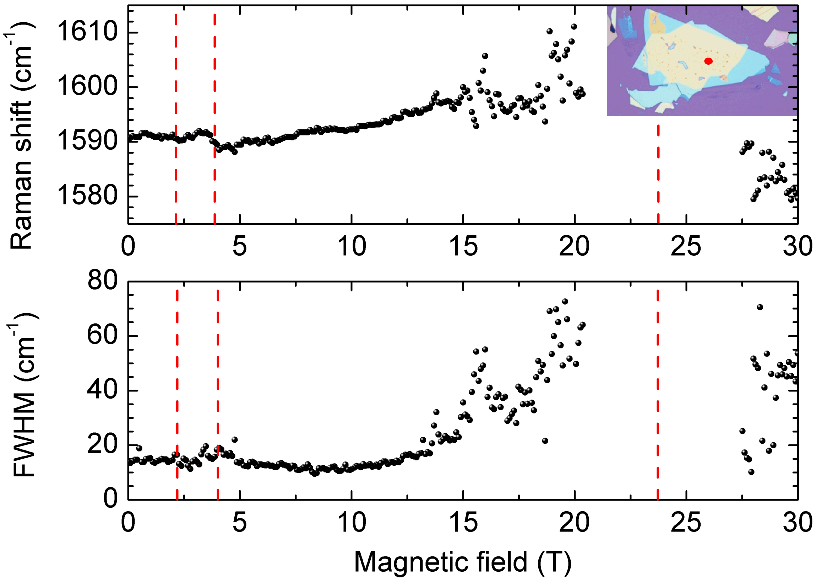

Figure 8.7: Energy position (upper) and linewidth (lower) of the one-component Lorentzian fit to the Raman scattering spectra measured on the encapsulated graphene sample (hBN-graphene-hBN).

excitation	resonance field (T)	Fermi velocity($\times 10^6$ m/s)
$L_{0,1}/L_{-1,0}$	23.50± 1.50	1.12
$L_{-1,2}/L_{-2,1}$	3.80± 0.20	1.15
$L_{-2,3}/L_{-3,2}$	2.17± 0.13	1.17

Those results also allow us to fix a limit on the charge doping level. Repeating the same procedure as in the section 8.2.1, we obtain an estimation for $\rho_{max} < 5.9 \times 10^{11}$ cm^{-2}, which is about 20% lower than the value obtained on the part of graphene on hBN that was not covered. Both of those values being approximately half of the charge density usually reported for exfoliated graphene flakes deposited directly on Si/SiO$_2$-$\rho \sim 2 \times 10^{12}$ cm^{-2} [139].

The presented above results of Raman scattering in graphene deposited on hBN and in graphene encapsulated by hBN showed few main effects. First, they demonstrated that it is possible to obtain an exfoliated graphene sample with a charge doping density below 7.35×10^{11} cm^{-2}. This is sufficiently low to see at least three first resonances in MPR. Thus, this proved a usefulness of employing high quality hBN flakes to reduce the effect of substrate on charge doping in graphene. Second, the experiments showed that the value of Fermi velocity in graphene deposited on hBN is higher than in other types of graphene-based systems. For instance in graphene flakes on the surface of graphite [44] and in the multilayer epitaxial graphene [108] it is usually reported to be $v_F = 1.02 \pm 3 \times 10^6$ m/s. It also turned out that Fermi velocity is higher for a system where graphene flake is deposited on top of hBN but not covered, as compared with the case where it is fully encapsulated. Finally, we note that v_F cannot be described with a single parameter, since it changes either with LL index or with the strength of the magnetic field. Those two cases can be distinguished if one could measure v_F for a single $L_{-n,n}$ electronic excitation at some range of magnetic fields and check if it is changing with the field or not. However, so far the electronic excitations have been observed only in the highest quality graphene system – graphene flakes on graphite [44, 32], as well as in bulk graphite [45]. But they have not been seen in any kind of exfoliated graphene sample, yet.

8.3 $L_{-1,1}$ electronic excitation in graphene on hBN

To detect the presence of electronic excitations in our system we have measured Raman scattering spectra in a wide range of energy (1300 – 3500 cm^{-1}) and in magnetic fields up to 24 T. Usually, the intensity of Raman signal coming from electronic excitations in graphene is lower than the intensity of phonon-related features. Thus, for those graphene systems where it is difficult to clearly observe the G-band and the 2D band, it is very unlikely that one could observe clear electronic excitations. For that reason when we measured the Raman scattering signal on a hBN-graphene-hBN spot we couldn't observe any other feature than two main phonons. However the same experiment performed over a spot, where graphene was just deposited on top of hBN but was not covered, revealed an additional feature.

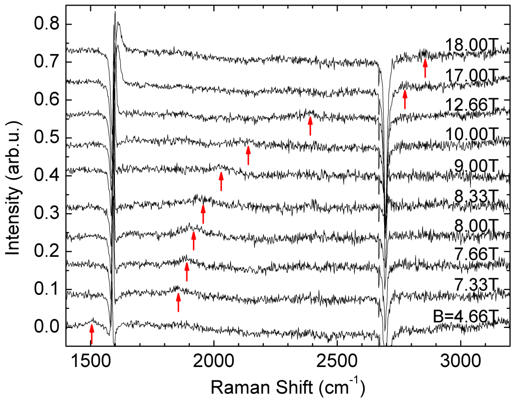

Figure 8.8: The Raman spectra of graphene deposited on hBN at chosen magnetic fields, normalized by a zero-field spectrum. Red arrows shows the position of a $L_{-1,1}$ Raman peak. Acquisition time for each spectrum: $t = 5$ min. Laser wavelength $\lambda = 514.53$ nm. Laser power on the sample $P = 4 - 5$ mW.

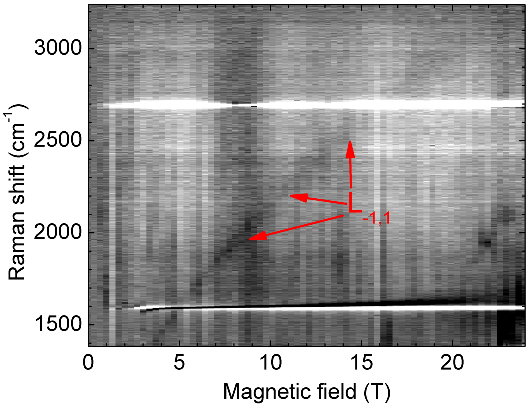

Figure 8.9: False color intensity map of Raman scattering from graphene deposited on hBN. The darker the color the more intense the signal is. Red arrows point to the $L_{-1,1}$ electronic excitation.

Raman spectra A few Raman spectra measured at chosen values of magnetic field are shown in Fig. 8.8. To enhance those features which were changing with the field, the zero-field spectrum was subtracted from each spectrum. Red arrows in the figure mark the positions of a Raman peak which energy is clearly increasing with the field. Despite low intensity of this feature, which is only about 4% of the intensity of the G-band, it can be clearly observed in the spectra. The character of it's evolution in the magnetic field can be more easily observed when a series of Raman spectra measured every 0.33 T from 0T to 24 T is gathered together and plotted in the form of a false color intensity map (Fig. 8.9). Due to low intensity of the dispersive mode seen in the spectra, each spectrum was acquired for 5 min to obtain sufficiently high intensity of the signal. The map shows that there are three prominent features visible in the spectra. The first one is the G-band at $\sim$ 1590 cm^{-1}, which energy slightly oscillates in magnetic field due to MPR. The second feature is the 2D band at $\sim$ 2680 cm^{-1}, which does not vary with magnetic field. Finally, the third line is observed which energy increases in magnetic field as a $\sqrt{B}$. This latter feature, which is marked with red arrows in Fig. 8.9, we identified with an $L_{-1,1}$ electronic excitation in graphene.

Both theoretical [31] and experimental [32] works, showed that observed intensity of electronic excitations decreases with LL index n. Also our measurements on graphene flakes on surface of graphite showed that $L_{-1,1}$ electronic excitation is the most intense one. Therefore it is not surprising that $L_{-1,1}$ excitation is the only one which we were able to observe on hBN-graphene, considering the large level of background seen in the spectra.

$L_{-1,1}$ energy & linewidth From the spectra presented in Fig. 8.8 one can extract linewidths (FWHM) of $L_{-1,1}$ excitations. Those results are shown in Fig. 8.11. Apart from few

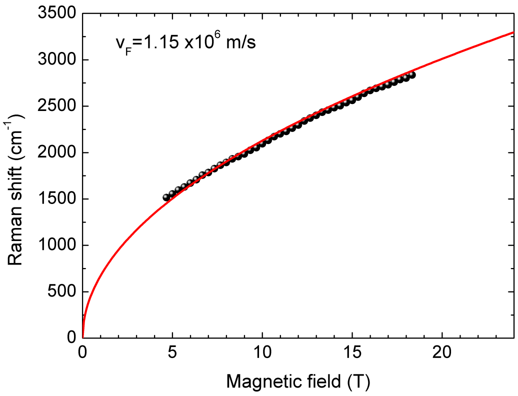

Figure 8.10: Black dots – energy of $L_{-1,1}$ excitation as seen in Fig. 8.9. Red line – energy of $L_{-1,1}$ excitation in graphene calculated for $v_F = 1.15 \times 10^6$ m/s.

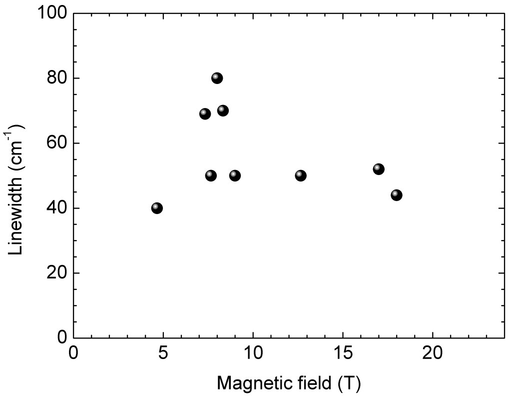

Figure 8.11: $L_{-1,1}$ electronic excitation linewidth.

points, a majority of the results are grouped around $FWHM = 50 \pm 5$ cm^{-1}. This is about 15 cm^{-1} higher than the linewidths of electronic excitations seen in graphene flakes on the surface of graphite, measured in the similar magnetic field range – up to 18T. In the latter case, however, the FWHM had a tendency to increase in fields higher than $\sim$ 18 T. We couldn't check if the same trend is seen in our hBN-graphene structure since the intensity of $L_{-1,1}$ line decreased significantly in fields higher than $\sim$ 18 T. On the other hand, if $L_{-1,1}$ linewidth would have increased in higher fields proportionally to how it increased in graphene on graphite samples, then the peak would be so broad and low that we couldn't observe it anymore on top of the high and changing background.

In the next step, by following the black trace visible in the map (Fig. 8.9), we extracted the positions of the center of the $L_{-1,1}$ Raman peak at each value of the magnetic field in the range from 4 T to 18 T. We used this approximative method to find the energy of the $L_{-1,1}$ Raman peak due to low intensity of the signal, as compared to the background level and noise. Generally, for the data with high noise to signal ratio, instead of trying to fit the weak signal with some peak function, it is easier to follow evolution of the line plotted on the map. The result of our procedure is shown in Fig. 8.10, which compares the measured values (black dots) of $L_{-1,1}$ excitation with a theoretical (red line) evolution:

$$L_{-1,1} = v_F\sqrt{2e\hbar}\sqrt{B}(\sqrt{1}+\sqrt{1}) = 2v_F\sqrt{2e\hbar}\sqrt{B} \tag{8.1}$$

The best match was obtained using the Fermi velocity value $v_F = 1.15 \times 10^6$ m/s. This is in good agreement with v_F values estimated for $L_{-1,0}/L_{0,1}$ and $L_{-1,1}$ excitations being in resonance with Γ phonon, as seen before in MPR.

However, a closer examination of Fig. 8.10 reveals that the calculated energy of $L_{-1,1}$ excitation is underestimated as compared with experimental points measured in the low magnetic field limit ($B < 10$ T). To further check, if experimentally measured evolution of $L_{-1,1}$ energy can be described by Eq. 8.1, we transformed this equation to express v_F as a function of the magnetic field B, and $L_{-1,1}$ energy:

$$v_F = \frac{L_{-1,1}}{2\sqrt{2e\hbar}\sqrt{B}} \tag{8.2}$$

Then, we used the $L_{-1,1}$ energy values extracted from Fig. 8.9 to plot v_F as a function of the magnetic field. The result is shown with blue dots in Fig. 8.12, together with v_F values extracted from MPR on hBN-graphene location (orange points) and encapsulated hBN-graphene-hBN location (red points). Those results clearly show that Fermi velocity decreases with magnetic field. Moreover, a scale of those changes agrees well with the few v_F extracted before from the MPR. Since now we could observe the continuous change in the v_F for a single excitation involving just one pair of LLs, we can exclude the hypothesis that v_F depends on the LL index. Those results show instead that it is the value of magnetic field that leads to the observed decrease in v_F. The range of that change is large since for hBN-graphene location v_F dropped down from 1.29×10^6 m/s at $B = 1.83$ T to $\sim 1.14 \times 10^6$ m/s at $B = 22$ T which is a 12% decrease. Similarly for hBN-graphene-hBN location the observed decline in the v_F from $\sim 1.17 \times 10^6$ m/s at $B = 2.18$ T to $\sim 1.12 \times 10^6$ m/s at $B = 23.5$ T makes for over 4% downturn. By making a very crude linear extrapolation of the measured v_F values down to $B = 0$ T we would obtain:
$v_F(B = 0)_{hBN-gr} \approx 1.34 \times 10^6$ m/s at hBN-graphene and,
$v_F(B = 0)_{hBN-gr-hBN} \approx 1.20 \times 10^6$ m/s at hBN-graphene-hBN.
This would yield 15% and 7% decrease at high field limit in the former and latter case, respectively.
This decrease in the v_F value with the magnetic field was already observed in the case of graphene flakes on the surface of graphite(see Chapter 7). However, the degree of this decline was observed on much smaller scale. The black points in Fig. 8.12 show v_F extracted from the energy of many different inter-LL excitations observed in graphene on graphite using the same approach as described above. Since the electronic quality of this system, evaluated for instance by carrier mobility, is orders of magnitude higher than for our hBN-graphene sample, many more electronic excitations were seen there, exhibiting much subtler effects, which adds to the spread of that points. Although the v_F is lower in the whole magnetic field range from the values observed in hBN-graphene, the main tendency is the same – v_F decreases with magnetic field.

8.4 Substrate dependent Fermi velocity

In addition to establishing a magnetic field dependence of Fermi velocity the above results show that v_F depends also on the substrate or more generally the closest environment of the graphene flake. Recently *Hwang et al.* have shown in an ARPES experiment that, depending on the substrate, Fermi velocity in graphene can change from 1.15×10^6 m/s for graphene on SiC, to 2.49×10^6 m/s for graphene on crystalline quartz [218]. They proposed that the factor responsible for the changes in the v_F is the screening of electron-electron interaction due to the immediate environment of graphene. Our results are in line with that theory, adding examples of few more systems where the same relation holds between the Fermi velocity of graphene flake and the effective dielectric constant $\epsilon_{eff.}$ of its environment. This relation can be understood in a following manner. In the tight binding method of calculating the electronic bandstructure and the nearest-neighbour approximation, the only free parameter is the hopping integral γ_0, which is proportional to v_F. One can compute the value of this constant from the first principles using for

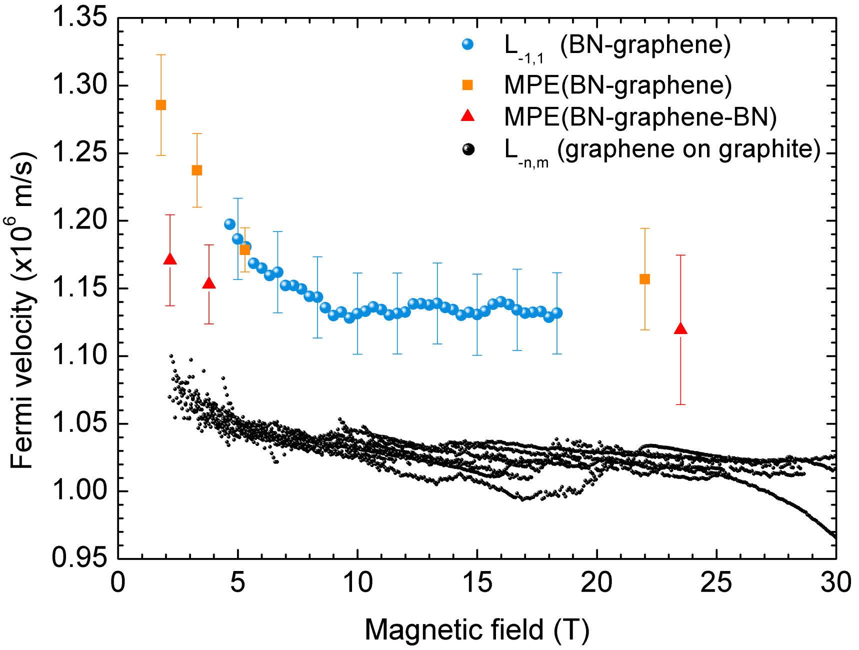

Figure 8.12: Fermi velocity of graphene as extracted from: i) MPR on hbN-graphene sample (orange points), ii) $L_{-1,1}$ electronic excitation on hbN-graphene sample (blue points), iii) MPR on hbN-graphene-hBN sample (red points), iv) $L_{-n,m}$ electronic excitations on graphene falke on the surface of graphite (black points).

instance Density Functional Theory (DFT) in the simplest Local Density Approximation (DFT-LDA) method. These calculations regularly yield Fermi velocity values on the order of $v_F = 0.85 \times 10^6$ m/s [115, 219], which is about 10-20% lower than the lowest experimentally reported values. This difference comes from the electron-electron interaction which renormalize the electronic bandstructure. Peculiarly for graphene, those interactions tend to increase the v_F. This is a direct consequence of the linear dispersion of bands in graphene. Since close to the Fermi energy the low energy electronic excitations are described by an effective field theory that is Lorentz invariant [220]. This implies that graphene behaves differently than more traditional systems with parabolic band dispersion that are described by theories which are invariant under Galilean transformation – like Fermi liquid model. Unlike the systems with band dispersion described by an effective mass, in graphene an increase of electron-electron interactions induces an increase of the Fermi velocity.

If we could modify the strength of el.-el. interaction in graphene, we could also change its v_F. This can be achieved by few methods: by changing the curvature of the graphene sheet, by applying external periodic potential [221, 222] or by modifying the dielectric screening [135, 223]. The last one is probably the simplest method to realize experimentally, since it requires only to deposit or cover graphene flake with different materials. The dielectric constant ϵ of the medium below/above graphene sheet screens to some extent the strength of the el.-el. interaction, and the higher the ϵ is the more el.-el. interaction is screened, while the correction that it ads to the renormalized Fermi velocity becomes smaller.

Ideally screened graphene (LDA calculations)	Graphene on graphite	hBN – graphene – hBN	hBN – graphene	Suspended graphene
$\epsilon_{eff} = \infty$	$\epsilon_{eff} = 7.5$	$\epsilon_{eff} = 5$	$\epsilon_{eff} = 3$	$\epsilon_{eff} = 1$
	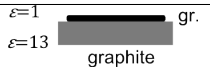			
v_F 0.85×10^6 m/s [115, 219]	v_F 1.05×10^6 m/s	v_F 1.20×10^6 m/s	v_F 1.34×10^6 m/s	v_F $(1.4 - 3) \times 10^6$ m/s [170]
E_{2Dband} ——	E_{2Dband} 2701 cm^{-1}	E_{2Dband} 2696 cm^{-1}	E_{2Dband} 2691 cm^{-1}	E_{2Dband} ——

Figure 8.13: Comparison of different graphene based systems, which differ in the dielectric constant of the surrounding medium. For calculations of the effective dielectric constant $\epsilon_{eff.}$ we used: $\epsilon_{air} = 1$, $\epsilon_{hBN} = 3$, $\epsilon_{graphite} = 1$, $\epsilon_{ideal-screening} = \infty$.

This tendency is shown in Fig. 8.13 where we summarized the values of v_F that we obtained on three different structures: on graphene flakes on the surface of graphite, on graphene deposited on atomically flat surface of hBN and on graphene deposited and covered by hBN. In addition to that we included information about free-standing graphene and graphene in LDA calculations, since they form two limiting cases: without any screening (strong el.-el interactions) and with completely screened interactions, respectively. For each structure we have made a rough estimation of the effective dielectric constant of the graphene's environment by taking the mean value of the dielectric constant of the medium above and below graphene flake. We observe that the DFT calculations predict the lowest Fermi velocity value $v_F = 0.85 \times 10^6$ m/s for a system which is equivalent to graphene flake surrounded by a perfect dielectric medium ($\epsilon = \infty$). Then we see that the Fermi velocity monotonically increases as the effective dielectric constant ϵ_{eff} decreases. Finally, v_F reaches its highest value for a freely suspended graphene, that is surrounded only by air/vacuum, when the el-el. interactions are screened the least ($\epsilon_{air} = 1$).

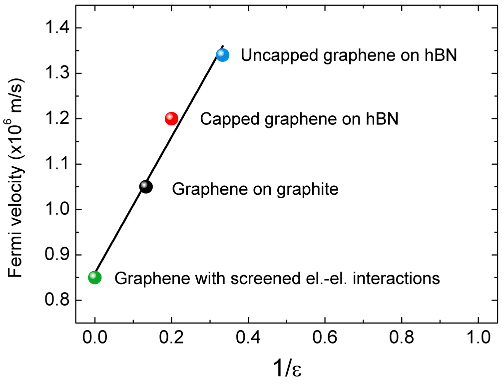

Figure 8.14: Fermi velocity at $B = 0$ T on graphene flakes deposited on different types of substrate, as a function of the inverse of effective dielectric constant of the medium.

It turned out that the correlation between v_F and ϵ_{eff} closely follows the $v_F \sim 1/\epsilon_{eff}$, which is predicted by the Random Phase Approximation (RPA) calculations [218, 170]. Fig. 8.14 presents v_F values extrapolated to $B = 0$ T that we obtained in magneto-Raman experiments on graphene flakes on graphite and two locations of graphene flake deposited on top of hBN flake – one covered with another hBn flake the other not. In addition, we used the literature data for v_F values calculated using LDA method [115, 219] and an experimental data for suspended graphene sample [170]. This plot confirms a good agreement of experimental data with the theoretical prediction of v_F being proportional to $1/\epsilon_{eff}$. Those points were fitted using the $v_F = \alpha\frac{1}{\epsilon} + \beta$ function, and we obtained fitting coefficients $\alpha = 1.652 \times 10^6$ m/s and $\beta = 0.837 \times 10^6$ m/s. This power law can be used for engineering v_F value by an adequate choice of dielectric substrate.

Dispersive 2D band Once we have established how the Fermi velocity changes depending on the substrate dielectric constant, we can explain why the energy of the 2D band also depends on the graphene's substrate (see Sec. 8.1). The origin of the 2D peak in graphene, similarly like in graphite lies in the fully resonant scattering process [62, 68]. In this process, after exciting electron-hole pair, all states into which an electron or hole is being scattered are the real electronic states. Since scattering occurs between two valleys – K and K', the change in the momentum of the carrier is compensated by the emission of phonon. This phonon has a large wavevector and comes from the highest optical phonon branch in the $\Gamma - K$ direction. Fig. 8.15 shows one of the possible scattering steps that leads to emission of two phonons with $|k| \sim K$. The other possible process include the same type of scattering events in which either electron or hole are being scattered in all possible permutations of time order. Close to the Dirac point electronic bands dispersion is described by:

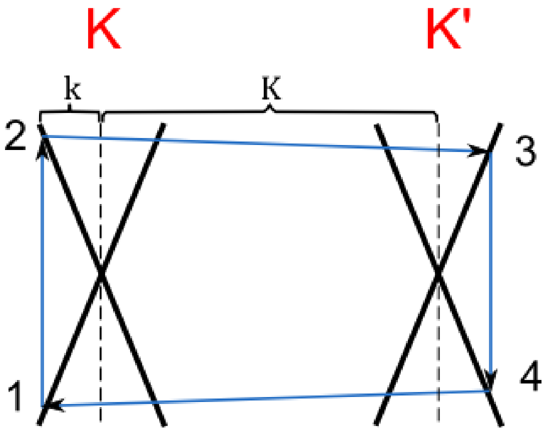

Figure 8.15: Fully resonant scattering process behind the 2D peak in graphene. 1 → 2 el.-h. pair creation. 2 → 3 electron scattering with emission of phonon with $k \sim +K$. 3 → 4 el.-hole recombination. 4 → 1 electron scattering with emission of phonon with $k \sim -K$.

$$E = \pm v_F \hbar k$$

where plus sign is for conduction band and minus for valence band. For a given energy of the incoming laser radiation E_{laser} we create an el.-h. pair with wavevector:

$$E_{laser} = 2 v_F \hbar k \tag{8.3}$$

$$k = \frac{E_{laser}}{2 v_F \hbar} \tag{8.4}$$

During the inter-valley scattering process, the carrier change its momentum by nearly:

$$\Delta k = K + 2k$$

This change in the carrier's momentum is compensated by emission of phonon with opposite momentum:

$$q_{ph} = -K - 2k \tag{8.5}$$

$$q_{ph} + K = -2\frac{E_{laser}}{2v_F\hbar} \tag{8.6}$$

$$|q_{ph} + K| = \frac{E_{laser}}{v_F\hbar} \tag{8.7}$$

$$\tag{8.8}$$

As we see from this expression, the wavevectors of phonons which are emitted during the 2D band scattering process is determined by the incoming laser radiation energy and the value of Fermi velocity. More specifically, as Fermi velocity increases the emitted phonon wavevector, as counted from the K point, decreases. Since the highest optical branch has a positive dispersion close to K point, the emitted phonons from points closer and closer to the K point, have higher and higher energies. Thus, from this model we would expect to see the 2D band shifting towards lower energy as the graphene v_F increases. This agrees well with the observed 2D peak positions measured on three samples with different v_F as it is presented in Fig. 8.13.

8.5 Conclusions

To summarize, our magneto-Raman experiments showed how powerful technique it is for quick characterization and also detailed analysis of complex layered structures. In our case, this experimental technique was used to study a graphene flake deposited on top of atomically flat surface of hBN, and partially covered with another hBN flake. Mapping the surface of such structure enabled us to selectively image different layers of the structure and also observe how the properties of graphene changes depending on its immediate environment. The analysis of the G-band energy showed a large distribution in the range from 1583 to 1591 cm^{-1}. Those values are however lower than the G-band energy observed on the same graphene flake, but on a part which was deposited directly on Si/SiO$_2$. It means that, the use of hBN substrate does indeed help to reduce the effect of external charge doping. However the broad distribution of the G-band energy position and the high background observed on the hBN-graphene and hBN-graphene-hBN locations are a direct result of the unwanted hydrocarbon residue which was deposited on the flakes during the transferring procedure. This points to the need to improve sample fabrication techniques to be able to obtain purer systems.

Considering experiments in magnetic fields, hBN-graphene and hBN-graphene-hBN locations on the sample turned out to be the first quasi-neutral exfoliated graphene samples, which didn't require application of any bias voltage to observe higher resonances of MPR. In addition, the electronic quality of hBN-graphene sample was so high that we were able to observe the $L_{-1,1}$ excitation evolving continuously in the magnetic field from 4 T to 18 T. These measurements revealed that v_F is not constant but it decreases with magnetic field. Moreover, together with our magneto-Raman measurements of graphene flakes found on the surface of graphite we observed that v_F is substrate dependent. In fact, our results are in line with models predicting v_F being inversely proportional to the average dielectric constant of the surrounding medium. Finally, we showed that the changing value of the Fermi velocity can explain the difference in observed positions of the 2D band in graphene deposited on different types of substrates.

Chapter 9

Results: gated CVD graphene

In this chapter we present results of tuning with electric field the coupling between optical Γ point phonon and low energy electronic excitations in graphene. The most pronounced effect of this coupling and the possibility to tune it is seen in the details of a magneto-phonon resonance (MPR) at $\sim 27B$. The observed strength of MPR is directly related to the effective strength of electron-phonon coupling which can be switched on and off by tuning the position of the Fermi level. In the first section (Sec. 9.1) we present the idea of tuning the strength of electron-phonon interaction by changing the Fermi energy by applying a gate voltage. Then details of sample production process and magneto-Raman scattering experiment are presented (Sec. 9.2). Results showing how Γ phonon energy changes depending on the applied gate voltage follows in section (Sec. 9.3) for measurements without any external magnetic field applied and in section (Sec. 9.4) where measurement were done at magnetic field values: below, above and at the fundamental MPR resonance.

9.1 Tuning electron-phonon interaction

Because graphene is a gapless material, low energy interband electronic excitations with zero momentum, often referred to as 'direct' or 'optical-like' excitations, exist and the electronic excitation spectrum can be easily modified by external means. It can be achieved for instance by tuning the position of the Fermi level with an electrostatic gate [224] or by applying an intense magnetic field perpendicular to the plane of the graphene crystal [40, 28]. Effects related to electron-phonon interaction in graphene are very sensitive to those 'direct' electronic excitations. As a result, those effects can be tuned by modifying the 'direct' electronic excitations spectrum. Here we use one of such effects – the magneto-phonon resonance (MPR) to monitor how switching on and off the electronic excitations affects the renormalized Γ phonon energy.

The energy of optical phonons at the Γ and K points in graphene is determined up to 5% of their energies, by the electron-phonon interaction. This is caused by the two Kohn anomalies in the phonon energy dispersion at those points [103]. As a result, the phonon energy as well as its linewidth, as seen through Raman scattering experiment, can be tuned externally by modifying the electronic excitation spectrum, for instance, by changing the position of the Fermi level [107, 106], or by applying a strong magnetic field [137, 138].

The magneto-phonon resonance, described in more details in Chapter 3, occurs when the energy of one of the 'optical-like' $\Delta|n| = \pm 1$ electronic excitations matches the energy of Γ point phonons. In such case the electron-phonon interaction leads to the hybridization of vibrational and electronic excitations, which manifest itself by a clear anti-crossing of those two modes. At the resonance, the splitting energy depends on the applied magnetic field and on the strength of the electronic excitation. The latter one is determined by the occupancy of the initial and final LLs implied in the excitation. Up to now, all experiments were performed on graphene specimens with a fixed carrier density. Here, we demonstrate experimentally that by changing the position of the Fermi level among the LLs by electrostatic gating, it is possible in graphene in a magnetic field , to externally switch on and off the resonant electron-phonon interaction.

Above $B \sim 5$ T, all inter-LLs excitations have an energy higher than that of the optical phonon, except for the $L_{-1,0}$ and $L_{0,1}$ excitations, whose energies increase like $T_0 = v_F\sqrt{2e\hbar B}$, where v_F is the Fermi velocity, and which go into a resonance with the phonon at much higher magnetic field at $B \sim 25$ T. When such a high magnetic field is applied, all $\Delta|n| = \pm 1$ electronic excitations have an energy much higher than the phonon energy except for the $L_{-1,0}/L_{0,1}$. These high energy electronic excitations contribute to the phonon energy renormalization, by slightly lowering its value. This effect is analogous to the lowering of the phonon energy, in the absence of a magnetic field, by virtual creation and annihilation of electron-hole pairs due to the Kohn anomaly at the Γ point. Without magnetic field, by changing the Fermi energy one can change the number of possible electron-hole pairs contributing to the phonon energy renormalization. When high magnetic field ($B > 5$ T) is applied to the sample, the inter-LL excitations $L_{n,m}$, with $n, m > 1$, have much larger energy than the Γ phonon and are possibly overlapping at high energy. In such case creation of the inter-LL excitations with $n, m > 1$ also leads to lowering of the Γ phonon energy. The effect of $L_{-1,0}/L_{0,1}$ excitations on the phonon energy at high magnetic fields is seen through a resonant coupling, which manifest itself as a pronounced anti-crossing of those modes. Strength of that coupling can be tuned by varying the filling factor. In fact, when the number of occupied Landau levels at a fixed magnetic field changes in between $\nu = +6$ and $\nu = -6$ the resonant coupling between Γ phonon and $L_{-1,0}/L_{0,1}$ excitations can be switched on and off. This effect can be traced by performing a polarization resolved magneto-Raman scattering experiments and by simultaneously tuning the Fermi energy, by applying a gate voltage to the sample.

9.2 Sample & experimental details

In the experiment the graphene grains obtained in a chemical vapor deposition(CVD) process were studied. The graphene single grains were grown on the Cu substrate at the temperature kept at 1000°C, while partial pressures for hydrogen and methane were 25 mbar and 50 mbar, respectively. The growth was stopped at 5 min, before graphene grains merge into a continuous layer. The graphene grains are then transferred onto 285 nm SiO/Si wafer with the PMMA-assisted method [203]. Those randomly scattered

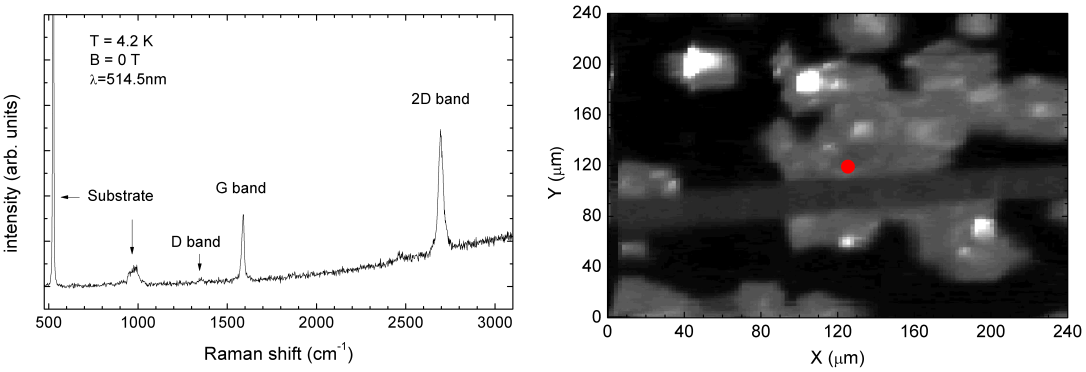

Figure 9.1: Left: Typical Raman scattering spectrum of the sample measured at T=4.2 K using $\lambda = 514.5\ nm$ excitation. Right: Gray scale map of the G band feature intensity (black and white stand for low and high intensity respectively). The metallic gate electrode is visible in the middle of the flake, and the red dot is the location at which the measurements have been performed.

graphene grains on SiO_2 were finally contacted with arrays of long metallic leads (50nm Au/ 5nm Ti), each serving as an individual ground when performing Raman scattering measurements. When patterned into a hall bar geometry, such samples show an electronic mobility of $\sim 4000\text{cm}^2/(\text{V}\cdot\text{s})$. Polarization resolved Raman scattering measurements have been performed with a home made miniaturized optical bench, which is described in more details in Chapter 6. As an excitation source, we used the 514.5 nm line from argon-ion laser, with the power set to 4 mW, focused on a 1μm diameter spot. By using a set of polarizers and a quarter-waveplate, a cross-circular polarization configuration $\sigma \pm /\sigma \mp$ (excitation polarization/collection polarization) was probed in the experiment. This polarization configuration selects the $\Delta|n| = \pm 1$ electronic excitations and optical phonons at the Γ point (G band) [45, 31] in graphene. With the use of this setup, experiments at liquid helium temperature and in magnetic fields up to 28 T were carried out. They have been performed either at a fixed gate voltage while sweeping the magnetic field, or at constant magnetic field while sweeping the gate voltage.

Fig. 9.1Left) shows a typical Raman scattering spectrum of the graphene flake which has been further investigated in magnetic fields. The 2D band has a single Lorentzian shape, characteristic of graphene monolayer [69, 59]. Fig. 9.1Right) shows a spatial map of the G band intensity and helps to visualize the shape of the flake together with the electrode. The bright spots appearing in this figure correspond to bilayer graphene with a non-Bernal stacking, which are typical for CVD grown graphene. They are characterized by an enhanced G band intensity, a single Lorentzian shaped 2D band feature slightly shifted towards higher energies, and by a presence of an additional feature, the R band, observed in the present case at 1490 cm^{-1} [225, 226]. Measurements were performed at the location indicated by the red dot in Fig. 9.1Right), close to the electrode.

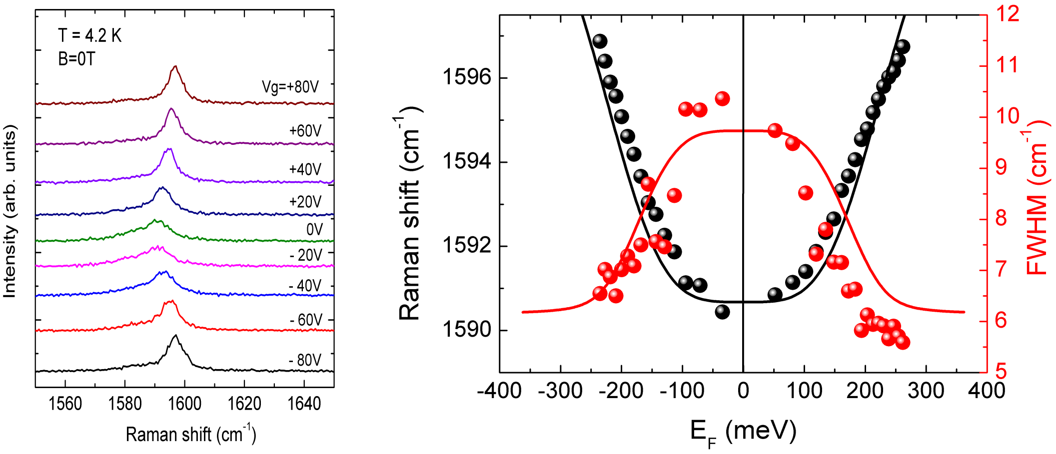

Figure 9.2: Left: typical spectra at B=0 T for different values of the gate voltage. Right: evolution of the phonon energy(black points) and FWHM(red points) as a function of the Fermi level.

9.3 Electric field tuning of Γ phonon energy at B=0 T

Even in the absence of external magnetic field, tuning the position of the Fermi energy at low temperature leads to a renormalization of the phonon energy and full width at half maximum (FWHM) [107, 106] as a result of a gradual quenching of electronic excitations due to Pauli blocking. Typical Raman scattering spectra for different values of the gate voltage are presented in Fig. 9.2Left). The evolution of the phonon energy and FWHM as a function of the Fermi energy, together with the calculations of this effect using a phonon energy $\epsilon_0 = 1588.7$ cm^{-1}, a dimensionless electron-phonon coupling constant $\lambda = 4.0 \times 10^{-3}$, a Fermi velocity $v_F = 1.08 \times 10^6$ m/s and carrier density fluctuations of $\sim 1.2 \times 10^{11}$ cm^{-2} are shown in Fig. 9.2Right). This value for the Fermi velocity is determined by the observation of the resonant coupling of the $L_{0,1}$ inter-LL excitation with the optical phonon at B $\sim$ 25 T. The Fermi energy was deduced from the applied gate voltage using the relation $n_s = \alpha V_G$, where n_s is the electron sheet density, $\alpha = 7.56 \times 10^{10}$ cm^{-2}V^{-1} is the capacitance per unit area (expressed in elementary charge units) of a 285nm thick SiO$_2$ layer and $E_F = \hbar v_F \sqrt{\pi n_s}$.

9.4 Electric field tuning of Γ phonon energy at high magnetic field

9.4.1 Tuning the Gamma phonon energy – model

The magneto-phonon resonance in graphene described in more details in Chapter 3, is observed as oscillations in Γ point optical phonon energy, at magnetic fields when energies of some of the inter-LL excitations come into a resonance with the zero-field phonon energy. The relevant inter-LL excitations are those inter-band ones which change the LL index by one ($\Delta|n| = \pm 1$), and one or two (depending on the exact value of the filling factor) intra-band electronic excitations which also change the LL index by one (cyclotron resonance).

In this chapter, to calculate the energies and spectral functions of the hybridized phonon-magneto-exciton modes, we use a model that is based on the one proposed by *Ando* [117, 137] and *Goerbig* [138] (see Sec. 3.6). However, the model used below allows to properly calculate the phonon's energies in a polarization resolved experiment.

The Raman spectrum is assumed to be proportional to the phonon spectral function

$$A = -(1/\pi) Im D_{\pm}(\omega) \tag{9.1}$$

, which is determined by the retarded phonon propagator,

$$D_{\pm}(\omega) = \frac{2\omega_0}{\omega^2 - \omega_0^2 - 2\lambda\omega_0\,\Pi_{\pm}(\omega)}. \tag{9.2}$$

Here $\Pi_{\pm}(\omega)$ is the retarded polarization operator which is diagonal in the circular basis, the two circular polarizations being denoted by $\pm$. The polarization operator can be straightforwardly evaluated, at an arbitrary filling factor ν, following the procedure described in ref. [137, 138]. Keeping all the non-resonant terms (some of which were omitted in refs. [137, 138], we obtain:

$$\Pi_{\pm}(\omega) = \sum_{n=n_F}^{\infty} \frac{\omega(\omega+i\gamma)T_0^2/T_n}{(\omega+i\gamma)^2 - T_n^2} + \sum_{n=0}^{n_F-1} \frac{T_0^2}{T_n} + W_{\nu}, \tag{9.3}$$

$$\begin{aligned} W_{\nu>2} = {} & \frac{T_0^2}{2}\left(\frac{f}{T_{n_F}} - \frac{1-f}{T_{n_F-1}} - \frac{1-f}{\omega_c^-} - \frac{f}{\omega_c^+}\right) + \\ & + \frac{\omega T_0^2}{2}\left[-\frac{f/T_{n_F}}{\omega+i\gamma \pm T_{n_F}} + \frac{(1-f)/T_{n_F-1}}{\omega+i\gamma \mp T_{n_F-1}}\right] + \\ & + \frac{\omega T_0^2}{2}\left[\frac{(1-f)/\omega_c^-}{\omega+i\gamma \mp \omega_c^-} + \frac{f/\omega_c^+}{\omega+i\gamma \mp \omega_c^+}\right], \end{aligned} \tag{9.4}$$

$$W_{-2<\nu<2} = \pm\frac{\omega T_0^2\,(2f-1)}{(\omega+i\gamma)^2 - T_0^2}, \tag{9.5}$$

$$\begin{aligned} W_{\nu<-2} = {} & \frac{T_0^2}{2}\left(\frac{1-f}{T_{n_F}} - \frac{f}{T_{n_F-1}} - \frac{f}{\omega_c^-} - \frac{1-f}{\omega_c^+}\right) + \\ & + \frac{\omega T_0^2}{2}\left[-\frac{(1-f)/T_{n_F}}{\omega+i\gamma \mp T_{n_F}} + \frac{f/T_{n_F-1}}{\omega+i\gamma \pm T_{n_F-1}}\right] + \\ & + \frac{\omega T_0^2}{2}\left[\frac{f/\omega_c^-}{\omega+i\gamma \pm \omega_c^-} + \frac{(1-f)/\omega_c^+}{\omega+i\gamma \pm \omega_c^+}\right]. \end{aligned} \tag{9.6}$$

Here we denoted by $n_F \geq 0$ the (non-negative) index of the Landau level which is partially filled (the integer part of $|\nu|/4 + 1/2$), and by f the average electronic occupation of this partially filled level ($0 \leq f < 1$). We also introduced the interband transition frequency $T_n = (\sqrt{n} + \sqrt{n+1})T_0$ and the two intraband frequencies corresponding to the cyclotron resonance, $\omega_c^+ = (\sqrt{n_F+1} - \sqrt{n_F})T_0$ and $\omega_c^- = (\sqrt{n_F} - \sqrt{n_F-1})T_0$. The electronic damping γ is introduced phenomenologically, keeping in mind that $\Pi_{\pm}(\omega)$ should satisfy the general condition $sign(Im\Pi_{\pm}(\omega)) = -sign(\omega)$ and be continuous upon the change of the filling factor when $n_F \to n_F + 1$.

Since effective oscillator strength, in above equations, for both inter- and intraband excitations depends on the filling factor ν they can be switched off and on by varying

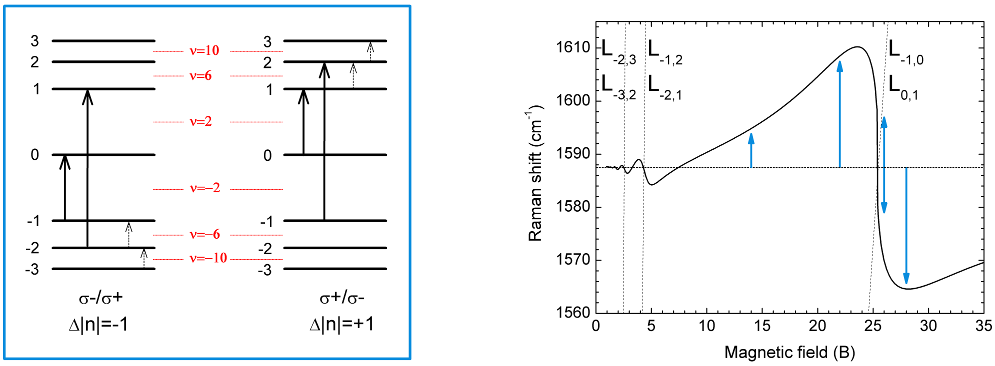

Figure 9.3: Left: Schematic of the LL structure in grphene at finite magnetic field, with relevant interband (solid arrows) and intraband (dotted arrows) excitations in both polarization configuration. Right: Calculated evolution of the Γ point phonon energy as a function of the magnetic field for neutral graphene. Blue arrows indicate the magnetic fields at which the filling factor has been varied. The horizontal line indicates the phonon energy in the absence of magnetic field.

the Fermi energy. This is illustrated in Fig. 9.3: Left which shows a schematic of the 4-fold degenerate LLs in graphene with an applied magnetic field together with the interband (solid arrows) and intraband (dashed arrows) excitations which are active in the two cross-circular configurations $\sigma\pm/\sigma\mp$ and that can be probed selectively with polarization resolved Raman scattering techniques. Particular values of the filling factor $\nu = (n_s\hbar)/(eB)$, where n_s is the carrier sheet density, are indicated. The intraband contribution is only active in the $\sigma-/\sigma+$ configuration for $\nu > +2$ and in the $\sigma+/\sigma-$ configuration for $\nu < -2$. Depending on the value of the filling factor, both intraband and interband excitations can be allowed or quenched due to Pauli blocking. For instance, the $L_{0,1}$ excitation is allowed for $-2 < \nu < +6$ and has maximal oscillator strength at $\nu = +2$, while the $L_{-1,0}$ excitation is allowed for $-6 < \nu < +2$ and its oscillator strength reaches maximum value at $\nu = -2$. Concerning the intraband excitations, similar conditions on the filling factor can be derived and for instance, the $L_{1,2}$ excitation is allowed for $+2 < \nu < +10$ and is the most intense at $\nu = +6$, when the first LL is completely occupied and the second LL is completely depleted.

Fig. 9.3Right) shows our calculation of Γ phonon energy as a function of magnetic field, obtained by solving the Eq. 3.17. The phonon energy shows clear oscillations representative of the magneto-phonon resonance, when the interband excitations are tuned, one after another, in resonance with the phonon energy. The magnitude of the change in the phonon energy from the zero field value, depends on the magnetic field strength (compare different arrows in Fig. 9.3) and on the Fermi energy position. The former dependence simply states that the most pronounced differences in the G band energy from the zero field value are observed at magnetic field when one of the $L_{-n,n+1}$ or $L_{-n-1,n}$ excitations energy comes into resonance with Γ point phonon energy. This is particularly well seen for the resonance at $B \sim 25$ T, when all excitations with $n > 0$ have much higher energy than that of Γ phonons and the interacting phonon energy is mainly determined by only $L_{0,1}$ and $L_{-1,0}$ excitations. These excitations tend to increase phonon energy at magnetic field below the resonance at $B = 25$ T and decrease it at fields above the resonance. Understandably, the closer to the resonant field, the larger is the observed phonon energy shift.

The phonon energy dependence on the filling factor is shown in Fig. 9.4. It presents energy of the G band phonon mode at few chosen values of magnetic field as the filling factor changes from $\nu = -12$ (E$_F$ at n=-3 LL, which is halfway occupied) to $\nu = +12$ (E$_F$ at n=+3 LL, which is halfway occupied). Calculations were done for the $\sigma+/\sigma-$ configuration, or in other words when only excitations with $\Delta|n| = +1$ were allowed. It shows that when the filling factor is outside the $-2 < \nu < +6$ range (regions 1 and 3 in Fig. 9.4), the G band energy steadily increases as the Fermi energy moves away from the charge neutrality point. The increase in phonon energy is rather small, up to 10-15 cm^{-1}, and the rate of that increase depends on the specific filling factor value. Characteristic sudden changes in the first derivative of the G band energies is observed at $\nu = ..., -10, -6, -2, 2, 6, 10, ...$ These filling factors correspond to the situation when the effective oscillator strength enables/disables a given excitation due to Pauli blocking. That instantaneously changes the number of electronic excitations that contribute to the phonon energy renormalization.

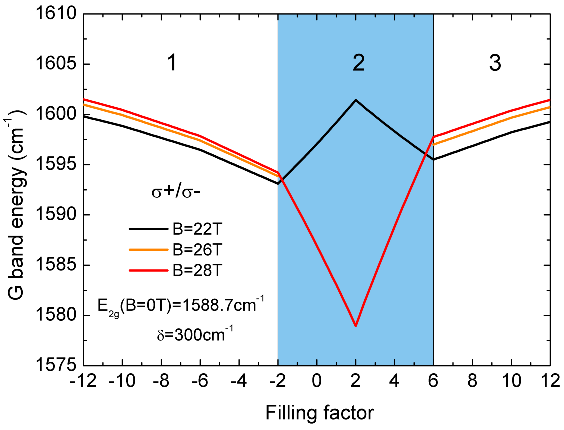

Figure 9.4: G band energy as a function of filling factor at chosen values of magnetic field, in $\sigma+/\sigma-$ configuration, as calculated from the model of *Ando* [137]. The blue shaded area shows range of filling factor when $L_{0,1}$ excitation is active.

The changes in the G band energy in regions 1 and 3 are much smaller than the changes observed for filling factor between $-2 < \nu < +6$ (region 2). Curves in Fig. 9.4 were calculated with an electronic broadening parameter $\delta = 300$ cm^{-1}. This value is about three times larger than the realistic one, but was used to decrease the amplitude of the G band shift in the resonant $-2 < \nu < +6$ range, just to present the qualitative changes in the G band energy on the same scale, in the whole $-12 < \nu < +12$ range. Moreover, the calculated curves in regions 1 and 3 show very similar behaviour for all magnetic fields in the range from 22 T to 28 T. This is a manifestation of the fact, that close to the resonance at $B \sim 25$ T the Γ phonon energy is primarily determined by the interaction with $L_{0,1}$ excitation. Once this interaction is quenched, which is the case when filling factor $\nu < -2$ (all initial states are empty) or $\nu > +6$ (all final states are occupied), the phonon energy is determined by a total effect of interaction with all the others excitations, which at so high fields is almost field independent. Evolution of phonon energy with the Fermi energy position in this high doping regime is a close reminiscence of the same dependence in the absence of the magnetic field. In the latter case the phonon energy is renormalized due to interaction with a continuum of electron-hole excitations with energies larger than $2E_F$. Increasing the E_F continuously decreases the number of possible excitations, which tends to increase the phonon energy. In the case of a highly doped system, the phonon energy is determined by the interaction with discrete inter-LLs excitations which also tends to lower the phonon energy. As the E_F increases, more and more of such excitations are blocked, which increases the phonon energy. Since the energy of LLs is quantized, the rate at which the phonon energy changes with filling factor shows a sudden change every time some excitation is fully blocked (filling factor crosses $\nu = \pm 2 + 4n$). This is seen in Fig. 9.4 as a sudden change in the curves slope at $\nu = -10, -6, -2, +6, +10$.

In the filling factor range $-2 < \nu < +6$ the Γ phonon energy is entirely dominated by the resonant interaction with $L_{0,1}$ excitation, which largely overwhelms the effect of all the other excitations. Depending on the value of magnetic field with respect to the resonance at ~ 25 T, the phonon energy is either increased (for $B < 25$ T) or decreased (for $B > 25$ T). This effect is illustrated in the blue-shaded part of Fig. 9.4. Since the Γ phonon shift due to magneto-phonon resonance is usually order of magnitude larger than a shift for filling factor in the range 1 and 3, a three times higher ($\delta = 300$ cm^{-1}) than realistic value of electronic excitation broadening parameter δ was used in the calculation. The magnitude of the shift continuously increases as the oscillator strength of $L_{0,1}$ rises, when the initial $n = 0$ LL begins to be populated at $\nu = -2$. It reaches a maximum when $n = 0$ LL is fully occupied at $\nu = +2$, and starts to decrease as the number of available empty states in the final $n = +1$ LL decreases at $\nu > +2$. Then $L_{0,1}$ excitation is completely blocked as filling factor reaches $\nu = +6$, when final state $n = +1$ LL is fully occupied, and the oscillator strength of that transition goes down to zero.

9.4.2 Tuning the Gamma phonon energy – experiment

First, a gate voltage was applied to the graphene sample to tune the carrier density to a level that enabled the $L_{0,1}$ excitation. Then in the $\sigma+/\sigma-$ configuration, a MPR was observed (see Fig. 9.5). At $B \approx 25$ T a clear anti-crossing appears, when the $L_{0,1}$ excitation crosses the phonon energy.

At selected values of the magnetic field indicated by the blue arrows in Fig. 9.3: Right we have tuned the Fermi energy – from the valence to the conduction band while measuring the Raman scattering response. The selected values of magnetic field correspond to the different regimes of coupling the $L_{-1,0}$ and $L_{0,1}$ excitations to the Γ phonon. At $B = 14$ T, the electron-phonon interaction is not resonant, but the observed phonon energy is sensitive to the $L_{-1,0}/L_{0,1}$ excitations which, whenever they are active, tend to increase slightly the phonon energy with respect to its $B = 0$ value. Those two particular electronic excitations are tuned to the phonon energy at $B \sim 25$ T. We have tuned the Fermi energy at $B = 22$, 26 and 28 T, which represents

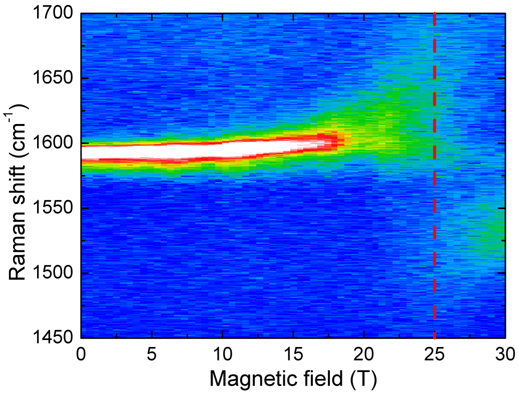

Figure 9.5: False colour map of the MPR in gated CVD graphene. The red, dashed line indicates the field $\sim$ 25T at which the $L_{0,1}$ excitation is in resonance with Γ point phonon.

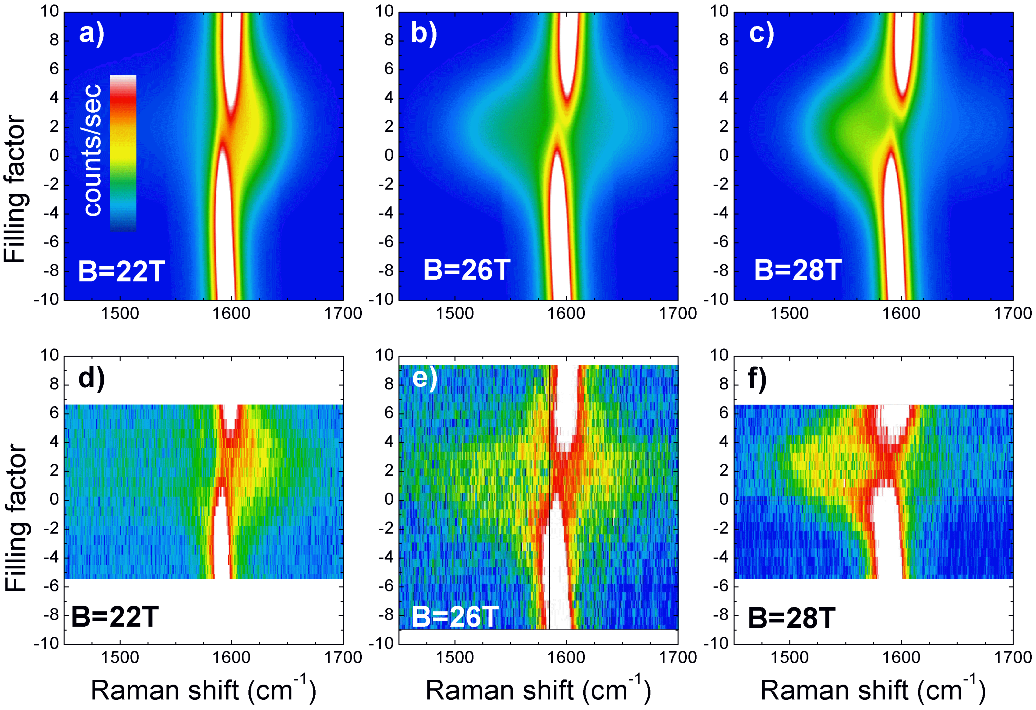

Figure 9.6: Upper row: false colour maps of the calculated phonon spectral function in the $\sigma+/\sigma-$ polarization configuration as a function of the filling factor for a) B=22 T, b) B=26 T c) B=28 T. Spectra have been convoluted with a gaussian-type distribution of carrier density with a standard deviation of 1.4×10^{12}. Lower row: false colour maps of the Raman scattering intensity measured while changing the filling factor by applying a gate voltage to graphene sample, performed at d) B=22 T, e) B=26 T f) B=28 T.

three different cases: just below, at the resonance, and slightly above the resonance, respectively. The expected changes in the phonon energy when the $L_{-1,0}$ or $L_{0,1}$ is turned on or off by tuning the Fermi energy are completely different in these three regimes. Below the resonance, the phonon energy is expected to increase when $L_{-1,0}$ or $L_{0,1}$ is turned on. Close to the resonance, the phonon should split into two components in clean enough systems, one with an increased energy and the other with a reduced energy. Finally above the resonance, the phonon energy is expected to decrease.

The measured Raman scattering spectra obtained while changing the gate voltage are in very good agreement with those expectations. Fig. 9.6d), e) and f) shows in the form of a false colour maps the intensity of the scattered light as a function of filling factor and an energy of the scattered light. The measurements performed in the $\sigma+/\sigma-$ configuration show a distinctively different behaviour at magnetic fields below, at and above the resonance with $L_{0,1}$ excitation. The fine structure developing on the side of phonon feature in filling factor range $-2 > \nu > +6$ is representative of the magneto-phonon resonance with shifts of the phonon energy as large as 60 cm^{-1}. Depending on the strength of the magnetic field with respect to the resonant field for the $L_{-1,0}$ excitation, the fine structure appears either on lower energy side, or on higher or on both sides simultaneously as is expected from the Γ phonon exhibiting a magneto-phonon resonance. This behavior can

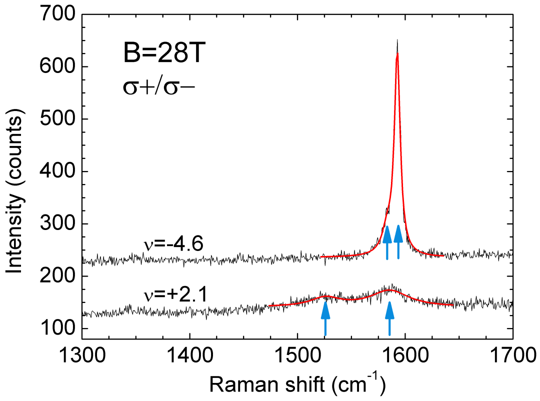

Figure 9.7: Raman scattering spectra of G band in graphene measured at magnetic field B=28 T, in $\sigma+/\sigma-$ configuration, at two different filling factors: at $\nu = -4.6$ when effective oscillator strength of $L_{0,1}$ excitation is zero, and at $\nu = +2.1$ when its effective oscillator strength is close to the maximum. Blue arrows indicates position of the center of two Lorentzian fits. Curves were vertically shifted for a better clarity.

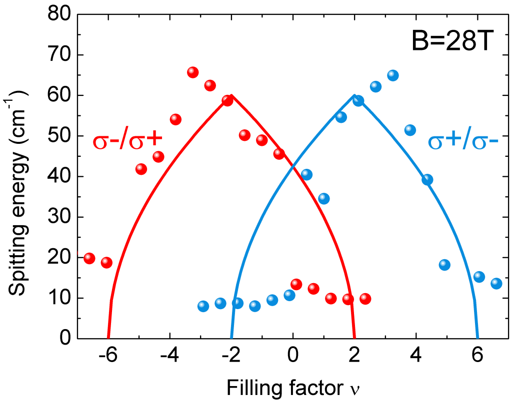

Figure 9.8: Evolution of the phonon energy as a function of the filling factor in the $\sigma-/\sigma+$(red dots) and $\sigma+/\sigma-$(blue dots) configurations, together with the expected $\sqrt{\tilde{\nu}_n}$ dependence (solid lines).

be very well reproduced by calculating the phonon spectral function, using Eq. 9.1 and 9.2. Fig. 9.6 a), b) and c) show results of such calculations made at the same values of magnetic fields as those that were explored in the experiment. Both experimental results, and calculations show that the largest shift of the phonon feature occurs at filling factor $\nu = +2$, when the oscillator strength of the $L_{0,1}$ excitation reaches its maximum value.

In all three ranges of magnetic fields (below, at and above resonance), the Γ phonon evolution with the applied gate voltage can be easily divided into two different regimes. The first regime is, when the filling factor is lower than $\nu = -2$ or when it is higher than $n = +6$. In that regime, the effective oscillator strength of the $L_{0,1}$ excitation is quenched and the G band peak has an energy and shape characteristic for the non interacting Γ phonon. The Raman scattering feature observed at ~ 1590 cm^{-1} has an intense and sharp (FWHM=7cm^{-1}) Lorentzian shape. It also has a small asymmetry on the low energy side which can be fitted with an additional Lorentzian peak (see uper curve in Fig. 9.7). Position and shape of this low energy peak is almost independent on the applied gate voltage and we are convinced that it originates from small puddles of electric charge that can be found in the whole illuminated area ($\sim 1\mu m$ laser spot). Those local puddles remained charged even after the Fermi energy, defined as an average value across the sample, was swept from -250 meV to $+250$ meV. These highly doped regions of graphene contribute to the Raman scattering spectrum by giving a peak at an energy corresponding to a Γ phonon, with all electron-phonon interactions being suppressed.
The second filling factor range comprises $-2 < \nu < +6$, when the $L_{0,1}$ excitations has a non-zero effective oscillator strength (lower curve in Fig. 9.7). The main G band peak, in

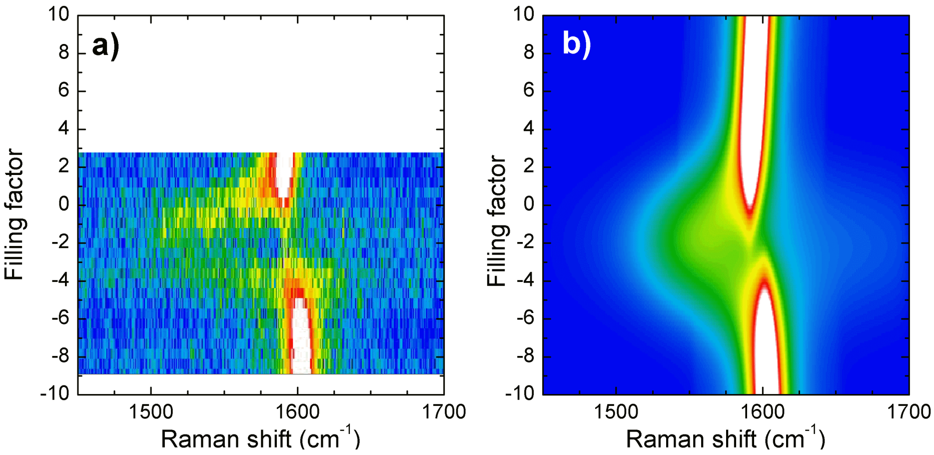

Figure 9.9: False colour maps of the: a) measured scattered intensity and b) calculated phonon spectral function at B=28T, in the $\sigma-/\sigma+$ polarization configuration as a function of the filling factor. The calculated spectra have been convoluted with a gaussian-type distribution of carrier density with a standard deviation of 1.4×10^{12}.

this range, broadens and shifts in energy in a direction which depends, whether the magnetic field value is below, at, or above the resonance field. At B=28 T this shift occurs towards lower energy (up to 1526 cm^{-1}) and the peak broadens up to FWHM$\approx$ 60 cm^{-1} which is a clear hallmark of the magneto-phonon resonance. On the other hand the second Raman peak corresponding to G band from graphene regions with a high charge density fluctuations remains at almost constant size and energy around 1582 cm^{-1}, which shows that the applied gate voltage in the range from -80 V to +80 V was not high enough to significantly change the carrier concentration in those highly doped domains. As can be seen in Fig. 9.9 in the $\sigma-/\sigma+$ configuration, a similar behavior is observed but the splitting has now a maximum value at filling factor $\nu=-2$, when oscillator strength of the $L_{-1,0}$ electronic excitation, active in this configuration is at its maximum. Similar results have also been obtained at $B=14$, 22 and 26 T.
These experiments unambiguously demonstrate the coupling of electronic excitations and optical phonons in graphene, both excitations having a similar angular momentum ±1. At $B=28$ T, we have determined the energy split of the phonon feature which is presented in Fig. 9.8 as a function of the filling factor, together with the expected $\sqrt{\tilde{\nu}_n}$ dependence(solid lines), where $0\leq\tilde{\nu}_n\leq1$ is the partial filling factor of the nthLL, as defined in ref. [138]. This energy difference represents half of the total energy split, because at $B=28$ T, only the low energy component of the coupled magneto-exciton-phonon mode is observed. The overall agreement between these data and existing theories is very good and such experiment offers the possibility to trigger the resonant electron-phonon interaction by electrical means and to gradually reach a strongly interacting regime.

Gate dependence at high filling factors When filling factor is tuned to high values so that the $L_{-1,0}$ or $L_{0,1}$ excitations are blocked due to Pauli principle, the contribution of the electron-phonon interaction to the phonon energy is determined by two types of electronic excitations. First are the interband electronic excitations, involving LLs with

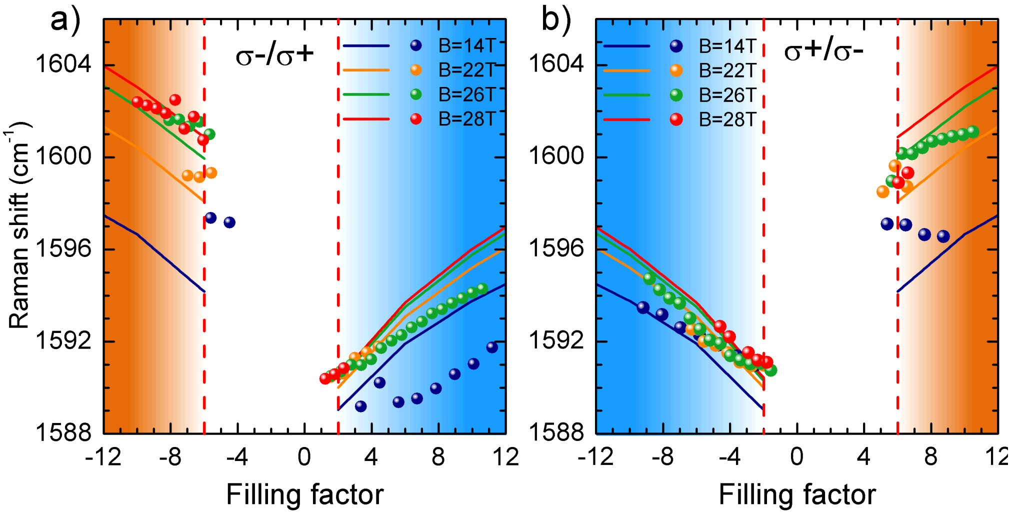

Figure 9.10: Evolution of phonon energy in the: a) $\sigma-/\sigma+$ and b) $\sigma+/\sigma-$ configuration, as a function of the filling factor for different values of the magnetic field(points) together with theoretical expectations including intra-band excitations (solid lines).

high index n, and with energy much higher than the phonon energy, while the others are the intraband excitations. Gradually quenching such interband excitations by increasing the Fermi energy, leads to an increase in the phonon energy. In the range of magnetic fields addressed in this study, the intraband excitations have an energy much lower than the phonon energy (at B=26 T, $L_{1,2}/L_{-2,-1}$=670 cm^{-1} and $L_{2,3}/L_{-3,-2}$=510 cm^{-1}) but they participate to the phonon renormalization by increasing the phonon energy. This effect is more pronounced as the magnetic field is increased and it can be seen in Fig. 9.10 in both polarization configurations. The solid lines in the figure represent the expected phonon energy at different values of magnetic field, as a function of the filling factor. They were calculated by solving for poles of denominator in Eq. 9.2 using the same set of parameters, corresponding to experimental conditions, as used before. When the intraband excitation is not active (for $\nu > +2$ in $\sigma-/\sigma+$ configuration and for $\nu < -2$ in $\sigma-/\sigma+$ configuration) there is a good agreement between theoretical expectations and the experimentally determined behaviour. The situation is rather different when going in the opposite range of filling factor. The effect of intraband excitations is clearly visible when comparing spectra obtained at $\nu = +2$ and $\nu = -6$ in the $\sigma-/\sigma+$ configuration and spectra at $\nu = -2$ and $\nu = +6$ in the $\sigma+/\sigma-$. Without considering intraband excitations, these spectra should be identical, because they correspond to situations when only the fundamental interband excitation is quenched while higher energy excitations are allowed in both polarization configuration and have the same energy (neglecting the electron-hole asymmetry and the trigonal warping [29]). Fig. 9.11 clearly shows that the phonon energy measured at these particular values of the filling factor is different and that there is a correspondence between spectra measured in the $\sigma-/\sigma+$ at $\nu = -6$ and those measured in the $\sigma+/\sigma-$ configuration at $\nu = +6$. In these two situations, the filling factor is such that the intraband excitation ($L_{-2,-1}$ and $L_{1,2}$) has a maximized and identical oscillator strength.

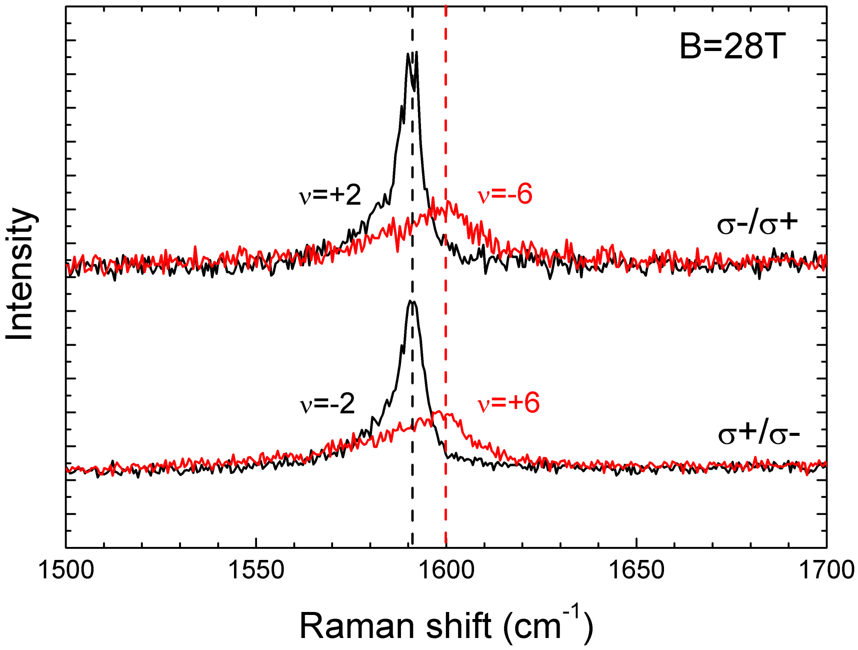

Figure 9.11: Raman scattering spectra of a gated monolayer graphene measured in two different polarization configurations at these filling factors in each polarization that only the fundamental interband electronic excitatation is blocked, while all other are still active. The black curves correspond to filling factors when the $L{-2,-1}$ (or $L1,2$) interband excitation is blocked, while red curved to filling factor when it is active.

9.5 Conclusion

We have shown that the resonant interaction between magneto-excitons and optical phonons in graphene can be switched on and off by controlling the position of the Fermi level, and hence, quenching or allowing specific electronic excitations through Pauli blocking. We have explored the three regimes for which the electronic excitation lies below, is degenerated with or is above the optical phonon energy. These three regimes have distinct signatures when monitoring the position of the Fermi level. In the resonant regime, satellite peaks appear when the $L_{-1,0}$ or $L_{0,1}$ excitation is active and energy shifts of the phonon feature up to 60 cm^{-1} have been observed, together with the expected $\sqrt{\tilde{\nu}_n}$ evolution of the splitting. Experimental results in the resonant regime are well reproduced by existing theories. Our polarization resolved measurements have revealed the renormalization of the phonon energy by either $\Delta|n| = +1$ or $\Delta|n| = -1$ electronic excitations. Such experiments offer a new insight into the electron-phonon interaction in graphene that could be used to continuously tune the electron-phonon system from a weakly to strongly interacting regime and could be extended to multilayer graphene systems or to hybrid graphene/2D materials heterostructures.

Chapter 10

Summary

10.1 Summary (English)

Despite a large scientific effort in the past few years and an enormous progress of our knowledge about the properties of the first atomically-thin, two-dimensional system: the monolayer graphene, this material does not cease to surprise us. In this work we have studied the magneto-optical properties of three different, graphene based systems. Even though all of them consist of the same 2D carbon crystal, the method of production and the nearest environment largely affect the optical and electronic properties of graphene. The **original results** obtained in the course of this work have been **reported in Chapters 7,8 and 9** and are summarized below.

In **Chapter 7**, we have presented the **magneto-optical studies** of the graphene system, which, in our opinion, shows the highest electronic and structural quality among all, ever investigated graphene structures. This unique but yet rather unexplored system consist of graphene inclusions which can be found on freshly cleaved surfaces of graphite. Graphite is a structurally perfect substrate for graphene but unfortunately it makes graphene "invisible" for optical microscopy (weak interference contrast) and difficult to be selectively contacted (conducting substrate) for the sake of electric transport measurements. On the other hand, **graphene on graphite** can be effectively studied with spectroscopy methods and, in particular, with micro-magneto Raman scattering techniques, as demonstrated in the present work.
The outstanding "electronic quality" of graphene on graphite allows us to observe its characteristic electronic response (inter Landau level excitations) in magneto-Raman scattering experiments. Mapping this response, with micron scale resolution, is shown to be a functional method to identify (imaging) the graphene flakes on graphite. In addition, we have shown that the graphene locations on graphite are also characterized by a distorted form of the phonon 2D band: the observation of the distorted form of the 2D band correlates with the appearance of the characteristic electronic response. The identification of graphene flakes on graphite is therefore possible even without applications of magnetic fields.

Next, the magneto-Raman scattering response of graphene on graphite has been analyzed in more details, with the main focus on the effects which fall beyond the simplistic expectations. The inter-Landau level (LL) excitations were observed on few different graphene flakes, using different laser excitations and at different: room and liquid helium temperatures. Characteristic features of electronic magneto-Raman scattering response are briefly discussed. An unexpected splitting of the Raman peaks related to the electronic, inter-LL excitations has been observed and interpreted in terms of a weak coupling of graphene flakes to the graphite substrate. The observation of the fine structure of the hybrid, LL excitation – E_{2g} phonon, modes in the vicinity of the fundamental magneto-phonon resonance ($B \sim 25$T) has been attributed to the effects of charge doping and/or electron-hole asymmetry of the electronic bands of graphene.
One of the main results of this work is presented in **Section 7.5**. There, we report on the observation of a **new class of magneto-phonon resonances**. The conventional magneto-phonon resonance in graphene is understood in terms of the hybridization between the E_{2g} - phonon mode and the inter-LL excitation. These conventional resonances are traced in an experiment when investigating the evolution of the E_{2g}-phonon (Raman G-band) as a function of the magnetic field. In contrast, our new magneto-phonon resonances manifest themselves as the magneto-resonant deformations (broadening and/or splitting) of the electronic, inter-LL, Raman scattering peaks. Those new effects appear when a given inter-LL excitation is in resonance with a double excitation mode, i.e., the combined electron and phonon and/or two phonon excitation mode. This is in contrast to a conventional magneto-phonon resonance which implies the hybridization of only two, single particle excitation modes. Our new class of magneto-phonon resonances involves phonons from the Gamma- as well as from the K-point of the Brillouin zone; the relevant electronic excitations imply either inter- or intra-valley processes. The phenomenological interpretation of this new class of magneto-phonon resonances is given in terms of resonant shortening of the lifetime (spectral broadening) for the electrons and/or holes excited in the electronic Raman scattering process. Furthermore, a more accurate model which refers to the scheme of interactions, and which better accounts for the experimental observations (peak splitting), is presented.

The most studied graphene structures are those exfoliated on Si/SiO$_2$ substrates, albeit they suffer rather moderate electronic quality (mobility). Hexagonal boron nitride (hBN), which is well lattice-matched to graphene, was expected to be a better choice for the graphene substrate. This expectation has been indeed confirmed in a number of electric transport experiments. In this work **(Chapter 8)** we have examined the properties of **graphene on hBN** with respect to its response in Raman scattering and **magneto-Raman scattering** experimental probes. The intentionally fabricated structure was a graphene sandwiched in between two hBN layers, altogether deposited on a Si/SiO$_2$ substrate. This was indeed the central part of the investigated structure, outside of which we could, however, find other regions, such as, graphene on Si/SiO$_2$ and graphene on hBN (uncapped by the upper hBN layer). Those different regions were well identified experimentally by comparing the optical microscope images of the investigated structure with its mapping by Raman scattering signals. A spurious and often large background signal in the Raman scattering response from regions which include the hBN layers is a clear disadvantage with respect to our optical experiments. The origin of this background signal remains to be firmly explained; we speculate it might be associated to the specific properties of the BN source material or it might arise from the contaminations brought by chemical compounds which were used in the process of layer transfer.

Nevertheless, our Raman scattering experiments confirm that in contrast to the graphene on a Si/SiO_2 substrate, the graphene on hBN and/or graphene sandwiched in between hBN layers show weaker charge doping and a superior electronic quality. This is proved by the observation of conventional magneto-phonon resonances (hybridization of the E_{2g}-phonon with inter-LL excitations) which have been traced down to the relatively low magnetic fields ($B \sim 1$ T) both in case of graphene on hBN and graphene sandwiched in between the hBN layers. Notably, the graphene on hBN, with smaller background signal, shows also the electronic response (fundamental inter-LL transition) in our magneto-Raman scattering experiments. Both observations, of rich in features magneto-phonon effect and of electronic Raman scattering, have not been reported so far for any other graphene system, except graphene on graphite.

An intriguing conclusion which follows our data modelling is that a single value for the Fermi velocity, which is the main parameter defining the dispersion of electronic states of graphene, cannot be used to explain an ensemble of our experimental results. To this end, the Fermi velocity must be assumed as a parameter which depends on the type of graphene's substrate and which also weakly varies with the magnetic field. Those changes in the Fermi velocity are attributed to the effects of electron-electron interactions, which indeed largely contribute to the apparent values of the Fermi energy in graphene. The dependence of the mean Fermi velocity on the substrate can be understood in terms of the effect of different dielectric screening. The "proximity" screening in the substrate modifies the strength of electron-electron interactions within the graphene sheet, and in turns modifies the Fermi velocity. We confirm here the results of previous studies [218, 170] and show that the apparent Fermi velocity correlates well with the inverse of the dielectric constant of the substrate material. Subsequently, the substrate dependent Fermi velocity can very well explain the observed shift in the 2D band position, in graphene deposited on different substrates.

The changes of the Fermi velocity as a function of the magnetic field remain to be firmly interpreted; we speculate that they may reflect the characteristic for graphene interplay between the Coulomb attraction and the exchange repulsion for electron-hole pairs excited into discrete Landau levels (inter LL magneto-excitons).

Investigations of the conventional **magneto-phonon resonance** (hybridization of optical E_{2g}-phonon with inter-LL excitations) but on a **gated graphene structure** are reported in **Chapter 9**. The graphene used in these studies has been initially grown on copper using the method of chemical vapor deposition (CVD) and afterwards transferred and processed on a Si/SiO_2 substrate. Notably, the properties of the CVD-grown graphene are of particular interest since the CVD growth is among the most promising technique for the industrial production of graphene.

The optical phonon of graphene couples to a continuum of electronic excitations in the absence of the magnetic field, but it resonantly hybridizes with discrete inter-LL excitations when the magnetic field is applied. In the absence of magnetic fields, tuning the gate voltage, and therefore the Fermi energy (and thus the available spectrum of excitations), results in a rather smooth evolution of the phonon energy and its broadening. Our experiment shows, that when tuning the Fermi energy in a magnetic field, and particularly in the proximity of the fundamental magneto-phonon resonance, the phonon response can be modified in a very spectacular way: the effect of resonant hybridization can be switched to be apparent or completely absent. This "on" and "off" switching of the resonant hybridization is the result of changing, with the gate voltage, the population of LLs (filling factor). Depending on the LL filling factor, we activate or block a given inter-LL transition which, potentially, couples to the optical phonon. The presented results of the studies of the phonon response as a function of the gate voltage (filling factors) at different magnetic fields (distinct conditions: below, at and above the fundamental, $B \sim 25$ T resonance) are well accounted by a theoretical modelling. The accurate description of the experimental data required the improved version of the existing theoretical models of the magneto-phonon resonance. Those latter models neglected some terms, related to intraband inter-LL excitations (cyclotron resonance mode), which on the other hand appeared to be essential for the interpretation of our experimental results.

10.2 Conclusions (français)

Malgré les nombreux efforts scientifiques au cours des dernières années et l'énorme avancée de nos connaissances sur les propriétés du premier système de l'épaisseur d'un atome, donc purement bidimensionnels, le graphène monocouche, ce matériau ne cesse de nous surprendre. Dans ce travail, nous avons étudié les propriétés magnéto-optiques de trois différents systèmes de type graphène. Même si tous sont constitués du même cristal de carbone 2D, la méthode de production ainsi que l'environnement le plus proche, affectent grandement ses propriétés optiques et électroniques. Les résultats originaux obtenus dans le cadre de ce travail sont décrits dans les chapitres 7, 8 et 9 et sont résumées ci-dessous.
Dans le Chapitre 7, nous présentons les résultats d'études magnéto-optiques d'un système de type graphène, qui, à notre avis, présente des qualités électroniques et structurelles les plus élevées parmi toutes les structures de graphène jamais étudiés. Ce système unique, mais encore trop peu exploré, se présente sous forme d'inclusions de graphène qui peuvent être trouvées sur des surfaces fraîchement clivées de graphite. Le graphite est un substrat structurellement parfait pour le graphène, mais malheureusement, il rend le graphène "invisible" pour la microscopie optique (à cause d'un trop faible contraste d'interférence) et difficile à contacter de manière sélective (à cause du substrat conducteur) pour des mesures de transport électrique. Par contre, le graphène sur graphite peut être étudié de manière efficace par des méthodes de spectroscopie et, en particulier, avec des techniques de diffusion micro-magnéto Raman, comme il est démontré dans ce travail.
La "qualité électronique" exceptionnelle du graphène sur graphite nous permet d'observer sa réponse électronique caractéristique (excitations inter niveau Landau) par des expériences de diffusion Raman sous champ magnétique. Nous démontrons que la cartographie de cette réponse, avec une résolution spatiale de l'ordre du micromètre, est une méthode efficace pour identifier (imager) les flocons de graphène sur graphite. En outre, nous avons montré que les emplacements de graphène sur graphite sont également caractérisés par une forme anormale de la bande 2D du spectre de diffusion Raman: l'observation de cette forme particulière de la bande 2D est corrélée avec l'observation de la réponse électronique caractéristique du graphène. L'identification des flocons de graphène sur graphite est donc possible, même sans application de champs magnétiques. Ensuite, la réponse magnéto-Raman du graphène sur graphite est analysée plus en détail, avec un accent porté sur les effets qui dépassent les attentes simplistes. Les excitations inter-niveaux de Landau (LLs) ont été observé sur quelques flocons différents de graphène, en utilisant différentes énergies d'excitations et différentes températures (température ambiante et l'hélium liquide). Les caractéristiques principales de la réponse électronique de observée par diffusion magnéto-Raman sont brièvement discutées. Une séparation inattendue des pics Raman liés aux excitations, inter-LL électroniques a été observé et interprété en termes de faible couplage des flocons de graphène avec substrat de graphite. L'observation d'une structure fine des modes hybride, excitation électronique- phonon E_{2g}, proche de la résonance magnéto-phonon fondamentale ($B \sim 25$ T), est attribuée aux effets du dopage de charge et / ou d'asymétrie électron-trou dans le graphène.
L'un des principaux résultats de ce travail est présenté à la Section 7.5. Là, nous rapportons l'observation d'une nouvelle classe de résonances magnéto-phonon. La résonance magnéto-phonon classique dans le graphène est comprise en termes de l'hybridation entre

le mode phonon E_{2g} et les excitations inter-LL. Ces résonances classiques sont observées dans une expérience où l'on étudie l'évolution du phonon E_{2g} (bande G) en fonction du champ magnétique. En revanche, nos nouvelles résonances magnéto-phonon se manifestent par des déformations magnéto-résonnantes (élargissement et / ou dédoublement) des pics de diffusion magneto-Raman qui correspondent aux excitations électroniques inter-LLs. Ces nouveaux effets apparaissent lorsque une des excitations inter-LLs est en résonance avec un mode d'excitation double, c'est à dire, un mode combiné électron et phonon et /ou un mode d'excitation à deux phonons. Ceci est en contraste avec une résonance magnéto-phonon conventionnelle qui implique l'hybridation de deux modes d'excitation à une particule uniquement. Cette nouvelle classe de résonances magnéto-phonon implique des phonons au point Γ ainsi qu'au point K de la zone de Brillouin ; les excitations électroniques pertinentes impliquent des processus inter- ainsi que intra-vallée. L'interprétation phénoménologique de cette nouvelle classe de résonance magnéto-phonon est donnée en termes de diminution résonante du temps de vie (de l'élargissement spectral) pour les électrons et / ou trous excités dans le processus de diffusion Raman électronique. De plus, un modèle plus précis qui se réfère aux processus d'interactions, et qui rend mieux compte des observations expérimentales (séparation de pics), est présentée.

Les structures de graphène, le plus étudiés, sont ceux exfoliée sur des substrats Si/SiO$_2$, mais ils présentent une qualité électronique modérée (mobilité). Le nitrure de bore hexagonal (hBN), qui a un réseau cristallin similaire à celui du graphène, apparait comme étant un meilleur choix de substrat pour le graphène. Cette attente a été en effet confirmée dans un certain nombre d'expériences de transport électriques. Dans ce travail (Chapitre 8), nous avons examiné les propriétés du graphène sur hBN par rapport à sa réponse en diffusion Raman et magnéto- Raman. La structure fabriquée est composée d'une couche de graphène en sandwich entre deux couches de hBN, le tout étant déposé sur un substrat de Si/SiO$_2$. Ce fut, en effet, la partie centrale de la structure étudiée, en dehors de laquelle nous avons pu, toutefois, trouver d'autres régions, telles que du graphène sur Si/SiO$_2$ et du graphène sur hBN (non encapsulé). Ces différentes régions ont été identifiées expérimentalement en comparant les images de microscopie optique de la structure étudiée avec sa cartographie par diffusion Raman. Un signal de fond parasite et souvent très intense a été observé dans la réponse de diffusion Raman des régions qui comprennent des couches de hBN. Ce signal nuit fortement à nos expériences d'optique. L'origine de ce bruit de fond reste à être expliquée. Nous supposons qu'il pourrait être associé à des propriétés spécifiques du matériau source de BN ou à des contaminations apportées par les composés chimiques utilisés dans le processus de transfert.
Néanmoins, nos expériences de diffusion Raman confirment que, contrairement au graphène sur substrat de Si/SiO$_2$, le graphène sur hBN et/ou de graphène pris en sandwich entre des couches de hBN montrent un dopage plus faible et une qualité électronique supérieure. Ceci est prouvé par l'observation des résonances magnéto-phonon classiques (hybridation des phonons E2g avec les excitations inter-LL) qui ont été observés jusqu'aux champs magnétiques relativement faibles ($\sim$ 1 T) à la fois dans le cas du graphène sur hBN et du graphène encapsulé. Notamment, le graphène sur hBN, avec un plus petit signal de fond, montre également dans nos expériences de diffusion magnéto-Raman, une réponse liée à des excitations purement électroniques. Ces deux observations, de l'effet magnéto-phonon

et de la diffusion Raman des excitations électroniques, n'avaient jusqu'à présent jamais été rapporté pour d'autres systèmes de type graphène que le graphène sur graphite.
Une conclusion intéressante, qui fait suite à notre analyse des données, est qu'une valeur unique pour la vitesse de Fermi, le paramètre principal qui définit la dispersion des états électroniques du graphène, ne peut pas être utilisé pour expliquer l'ensemble de nos résultats expérimentaux. La vitesse de Fermi doit être considérée comme un paramètre qui dépend du type de substrat, et qui varie avec le champ magnétique. Ces changements dans la vitesse de Fermi sont attribués aux effets des interactions électron-électron. La dépendance de la vitesse de Fermi moyenne en fonction du substrat peut être comprise en termes d'effet d'écrantage diélectrique. L'écrantage par le substrat, modifie la force des interactions électron-électron dans un feuillet de graphène, et à son tour modifie la vitesse de Fermi. Nous confirmons ici les résultats d'études précédentes [218, 170] et nous montrons que la vitesse de Fermi apparente varie bien comme l'inverse de la constante diélectrique du matériau substrat. Par la suite, la dépendance de la vitesse Fermi par rapport au substrat peut très bien expliquer le décalage observé dans la position de la bande 2D, mesuré sur des graphènes déposés sur des substrats différents. Les changements de la vitesse de Fermi en fonction du champ magnétique restent à être interprété; nous supposons qu'ils peuvent refléter la différence entre l'interaction attractive de Coulomb et la répulsion lié à l'interaction d'échange des paires électrons-trous excités dans les niveaux de Landau discrets (inter-LL magnéto-excitons).

Les études de la résonance magnéto-phonon classique (hybridation des phonons optique E_{2g} avec les excitations inter-LL), mais sur une structure de graphène avec une grille électrostatique, sont présentés dans le Chapitre 9. Le graphène utilisée dans ces études a été initialement développée sur du cuivre en utilisant le procédé de dépôt chimique en phase vapeur (CVD), et qui a ensuite été transféré sur un substrat de Si/SiO$_2$. Notamment, les propriétés du graphène CVD sont d'un intérêt particulier puisque la croissance CVD est parmi les techniques les plus prometteuses pour la production industrielle du graphène. Le phonon optique de graphène est couplé à un continuum d'excitations électroniques en l'absence de champ magnétique, mais il s'hybride de manière résonante avec des excitations discrètes inter- LL lorsqu'un champ magnétique est appliqué. En l'absence de champ magnétique, le control de la tension de grille, et par conséquent de l'énergie de Fermi (ainsi que du spectre d'excitations disponible), se traduit par une évolution assez lisse de l'énergie des phonons et de leur élargissement spectrale. Notre expérience montre que lorsque l'on ajuste l'énergie de Fermi dans un champ magnétique, et en particulier au voisinage de la résonance magnéto-phonon fondamentale, la réponse des phonons peut être modifiée de façon très spectaculaire: l'hybridation peut être activée et désactivée. Cette commutation entre "marche" et "arrêt" de l'hybridation est le résultat de l'évolution, avec la tension de grille, l'occupation des LLs (facteur de remplissage). Selon le facteur de remplissage des LLs, nous activons ou bloquons une transition inter-LL qui, potentiellement, se couple au phonon optique. Les résultats présentés de l'étude de la réponse de phonons en fonction de la tension de grille (facteurs de remplissage) à différentes valeurs du champ magnétique (conditions distinctes: au-dessous, égale à et au-dessus de la résonance fondamentale à $B \sim 25$ T) sont bien décris par un modèle théorique. La description précise des données expérimentales nécessite une version améliorée des modèles théoriques existants de la résonance magnéto-phonon. Ces modèles négligeaient certains termes, liés aux excitations intra-bande inter-LL (mode de résonance cyclotron) qui sont en revanche essentielle pour l'interprétation de nos résultats expérimentaux.

Bibliography

[1] P. R. Wallace. *The band theory of graphite.* **Phys. Rev. 71(9)**:622, 1947. [cited at p. ix, xiii, 2, 4, 8, 10]

[2] J. C. Slonczewski and P. R. Weiss. *Band structure of graphite.* **Phys. Rev. 109(2)**:272, 1958. [cited at p. ix, xiii, 4, 8, 10, 52]

[3] J. W. McClure. *Band structure of graphite and de Haas-van Alphen effect.* **Phys. Rev. 108(3)**:612, 1957. [cited at p. ix, xiii, 4, 10, 52]

[4] M. S. Dresselhaus, G. Dresselhaus, and R. Saito. *Carbon fibers on* C_{60} *and their symmtery.* **Phys. Rev. B**. **45(11)**:6234, 1992. [cited at p. ix, xiii, 4]

[5] K. S. Novoselov, D. Jiang, F. Schedin, T. J. Booth, V. V. Khotkevich, S. V. Morozov, and A. K. Geim. *Two-dimensional atomic crystals.* **PNAS**. **102(30)**:10451, 2005. [cited at p. ix, xiii, 59, 60]

[6] L. D. Landau. *Zur theorie der phasenumwandlungen II.* **Phys. Z. Sowjetunion**. **11**:26–35, 1937. [cited at p. ix, xiii]

[7] R. E. Peierls. *Quelques proprietes typiques des corpses solides.* **Ann. I. H. Poincare**. **5**:177–222, 1935. [cited at p. ix, xiii]

[8] J. A. Venables, G. D. T. Spiller, and M. Hanbucken. *Nucleation and growth of thin films.* **Rep. Prog. Phys. 47**:399, 1984. [cited at p. ix, xiii]

[9] J. W. Evans, P. A. Thiel, and M. C. Bartelt. *Morphological evolution during epitaxial thin film growth: Formation of 2d islands and 3d mounds.* **Sur. Sci. Rep. 61**:1–128, 2006. [cited at p. ix, xiii]

[10] K. S. Novoselov, A. K. Geim, S. V. Morozov, D. Jiang, Y. Zhang, S. V. Dubonos, I. V. Grigorieva, and A. A. Firsov. *Electric field effect in atomically thin carbon films.* **Science**. **306**:666, 2004. [cited at p. ix, xiii]

[11] Ch. Lee, X. Wei, J. W. Kysar, and J. Hone. *Monolayer graphene measurement of the elastic properties and intrinsic strength of monolayer graphene.* **Science**. **321**:385, 2008. [cited at p. ix, xiii]

[12] A. S. Mayorov, R. V. Gorbachev, S. V. Morozov, L. Britnell, R. Jalil, L. A. Ponomarenko, P. Blake, K. S. Novoselov, K. Watanabe, T. Taniguchi, and A. K. Geim. *Micrometer-scale ballistic transport in encapsulated graphene at room temperature.* **Nano Lett. 11(6)**:2396–2399, 2011. [cited at p. x, xiv]

[13] P. Neugebauer, M. Orlita, C. Faugeras, A.-L. Barra, and M. Potemski. *How perfect can graphene be?* **Phys. Rev. Lett. 103**:136403, 2009. [cited at p. x, xiv, 12, 29, 52, 55, 57, 61, 71, 74, 88, 91]

[14] David R. Lide. *CRC Handbook of Chemistry and Physics.* CRC Press, Boca Raton, FL, internet version 2005 edition, 2005. [cited at p. 1]

[15] M. O. Goerbig. *Electronic properties of graphene in a strong magnetic field.* **Rev. Mod. Phys. 83**:1193, 2011. [cited at p. 1, 2, 4, 5, 12, 88]

[16] L. Pauling. *The Nature of Chemical Bonds.* Cornell University Press, Ithaca, 1960. [cited at p. 3]

[17] N. Hamada, Sh. Sawada, and A. Oshiyama. *New one-dimensional conductors: graphitic microtubules.* **Phys. Rev. Lett. 68(10)**:1579, 1992. [cited at p. 4]

[18] J. W. Mintmire, B. I. Dunlap, and C. T. White. *Are fullerene tubules metallic?* **Phys. Rev. Lett. 68(5)**:631, 1992. [cited at p. 4]

[19] R. Saito, M. Fujita, G. Dresselhaus, and M. S. Dresselhaus. *Electronic structure of graphene tubules based on C_60.* **Phys. Rev. Lett. 46(3)**:1804, 1992. [cited at p. 4]

[20] T. Ando. *Theory of electronic states and transport in carbon nanotubes.* **J. Phys. Soc. Jap. 74(3)**:777, 2005. [cited at p. 4, 7, 12]

[21] A. H. Castro Neto, F. Guinea, N. M. R. Peres, K. S. Novoselov, and A. K. Geim. *The electronic properties of graphene.* **Rev. Mod. Phys. 81**:109, 2009. [cited at p. 4, 5, 6, 88]

[22] S. Reich, C. Thomsen, and J. Maultzsch. *Carbon nanotubes: Basic concepts and physical properties.* Wiley-VCH Verlag GmbH & Co. KGaA, 2004. [cited at p. 4]

[23] B. Partoens and F. M. Peeters. *From graphene to graphite: electronic structure around the K point.* **Phys. Rev. B. 74**:075404, 2006. [cited at p. 4, 10, 13, 24]

[24] N. M. R. Peres, F. Guinea, and A. H. Castro Neto. *Electronic properties of disordered two-dimensional carbon.* **Phys. Rev. B. 73**:125411, 2006. [cited at p. 6, 82]

[25] M. Orlita and M. Potemski. *Dirac electronic states in graphene systems: optical spectroscopy studies.* **Semicond. Sci. Technol. 25**:063001, 2010. [cited at p. 6, 8, 82]

[26] Y. Zhang, Y.-W. Tan, H. L. Stormer, and P. Kim. *Experimental observation of the quantum Hall effect and Berry's phase in graphene.* **Nature. 438**:201, 2005. [cited at p. 6, 11]

[27] Z. Jiang, Y. Zhang, Y.-W. Tan, H.L. Stormer, and P. Kim. *Quantum Hall effect in graphene.* **Solid State Comm. 143**:14, 2007. [cited at p. 6]

[28] Z. Jiang, E.A. Henriksen, L. C. Tung, Y. J. Wang, M. E. Schwartz, M. Y Han, P. Kim, and H. L. Stormer. *Infrared spectroscopy of Landau levels in graphene.* **Phys. Rev. Lett. 98**:197403, 2007. [cited at p. 6, 12, 45, 127]

[29] P. Plochocka, C. Faugeras, M. Orlita, M. L. Sadowski, G. Martinez, M. Potemski, M. O. Goerbig, J.-N. Fuchs, C. Berger, and W. A. de Heer. *High-energy limit of massless Dirac fermions in multilayer graphene using magneto-optical transmission spectroscopy.* **Phys. Rev. Lett. 100**:087401, 2008. [cited at p. 6, 12, 94, 138]

[30] S. Reich, J. Maultzsch, C. Thomsen, and P. Ordejón. *Tight-binding description of graphene.* **Phys. Rev. Lett. 66**:035412, 2002. [cited at p. 6]

[31] O. Kashuba and V. I. Fal'ko. *Signature of electronic excitations in the Raman spectrum of graphene.* **Phys. Rev. B. 80**:241404, 2009. [cited at p. 7, 45, 46, 49, 50, 51, 79, 83, 119, 129]

[32] M. Kühne, C. Faugers, P. Kossacki, A. A. L. Nicolet, M. Orlita, Yu. I. Latyshev, and M. Potemski. *Polarization-resolved magneto-Raman scattering of graphenelike domains on natural graphite*. **Phys. Rev. B**. **85**:195406, 2012. [cited at p. 7, 12, 33, 39, 45, 51, 52, 58, 71, 79, 86, 95, 96, 114, 115, 118, 119]

[33] K. S. Novoselov, E. McCann, S. V. Morozov, V. I. Fal'ko, M.I.Katnelson, D. Jiang U. Zeitler, F. Schedin, and A. Geim. *Unconventional quantum Hall effect and Berry's phase of 2π in bilayer graphene*. **Nature phys.** **2**:177, 2006. [cited at p. 8, 12]

[34] E. McCann. *Asymmetry gap in the electronic band structure of bilayer graphene*. **Phys. Rev. B**. **74**:161403, 2006. [cited at p. 8]

[35] M. Koshino and T. Ando. *Orbital diamagnetism in multilayer graphene: Systematic study with the effective mass approximation*. **Phys. Rev. B**. **76**:085425, 2007. [cited at p. 9, 13]

[36] M. Koshino and T. Ando. *Magneto-optical properties of multilayer graphene*. **Phys. Rev. B**. **77**:115313, 2008. [cited at p. 10, 12, 13, 14, 53]

[37] B. Partoens and F. M. Peeters. *Normal and Dirac fermions in graphene multilayers: tight-binding description of the electronic structure*. **Phys. Rev. B**. **75**:193402, 2007. [cited at p. 10, 23]

[38] Y. Zheng and T. Ando. *Hall conductivity of a two dimensional graphite system*. **Phys. Rev. B**. **65**:245420, 2002. [cited at p. 11]

[39] K. S. Novoselov, A. K. Geim, S. V. Morozov, D. Jiang, M. I. Katnelson, I. V. Grigorieva, S. V. Dubonos, and A. A. Firsov. *Two-dimensional gas of massless Dirac fermions in graphene*. **Nature**. **438**:197, 2005. [cited at p. 11]

[40] M. L. Sadowski, G. Martinez, M. Potemski, C. Berger, and W. A. de Heer. *Landau level spectroscopy of ultrathin graphite layers*. **Phys. Rev. Lett.** **97**:266405, 2006. [cited at p. 12, 42, 45, 127]

[41] R. S. Deacon, K.-C. Chuang, R. J. Nicholas, K. S. Novoselov, and A. K. Geim. *Cyclotron resonance study of the electron and hole velocity in graphene monolayers*. **Phys. Rev. B**. **76**:081406, 2007. [cited at p. 12]

[42] V. P. Gusynin, S.G. Sharapov, and J. P. Carbotte. *Anomalous absorption line in the magneto-optical response of graphene*. **Phys. Rev. Lett.** **98**:157402, 2007. [cited at p. 12]

[43] V.P. Gusynin, S. G. Sharapov, and J P Carbotte. *Magneto-optical conductivity in graphene*. **J. Phys.: Condens. Matter**. **19**:026222, 2007. [cited at p. 12]

[44] C. Faugeras, M. Amado, P. Kossacki, M. Orlita, M. Kühne, A. A. Nicolet, Yu. I. Latyshev, and M. Potemski. *Magneto-Raman scattering of graphne on graphite: electronic and phonon excitations*. **Phys. Rev. Lett.** **107**:036807, 2011. [cited at p. 12, 15, 29, 39, 45, 52, 58, 71, 86, 88, 96, 114, 118]

[45] P. Kossacki, C. Faugeras, M. Kühne, M. Orlita, A. A. L. Nicolet, J. M. Schneider, D. M. Basko, Yu. Latyshev, and M. Potemski. *Electronic excitations and electron-phonon coupling in bulk graphite through Raman scattering in high magnetic fields*. **Phys. Rev. B**. **84**:235138, 2011. [cited at p. 12, 33, 39, 45, 52, 58, 79, 114, 118, 129]

[46] Y. Kim, Y. Ma, A. Imambekov, N. G. Kalugin, A. Lombardo nad A. C. Ferrari, J. Kono, and D. Smirnov. *Magnetophonon resonance in graphite: High-field Raman measurements and electron-phonon coupling contributions*. **Phys. Rev. B**. **85**:121403, 2012. [cited at p. 12, 39, 45, 52, 114]

[47] E. McCann and V. I. Fal'ko. *Landau-level degeneracy and quantum Hall effect in graphite bilayer.* **Phys. Rev. Lett. 96**:086805, 2006. [cited at p. 12, 13]

[48] G. Dresselhaus and M. S. Dresselhaus. *Spin-orbit interaction in graphite.* **Phys. Rev. 140**:A401, 1965. [cited at p. 14]

[49] J. W. McClure. *Theory of diamagnetizm of graphite.* **Phys. Rev. 119(2)**:606, 1960. [cited at p. 14]

[50] M. Inoue. *Landau levels and cyclotron resonance in graphite.* **J.Phys. Soc. Jap. 17(5)**:808, 1962. [cited at p. 14]

[51] Kenji Nakao. *Landau level structure and magnetic breakthrough in graphite.* **J. Phys. Soc. Jap. 40(3)**:761, 1976. [cited at p. 14, 52]

[52] M. Koshino and T. Ando. *Electronic structures and optical absorption of multilayer graphenes.* **Solid State Comm. 149(27)**:1123, 2009. [cited at p. 14]

[53] M. Orlita, C. Faugeras, J. M. Schneider, G. Martinez, D.K. Maude, and M. Potemski. *Graphite from the viewpoint of Landau level spectroscopy: An effective graphene bilayer and monolayer.* **Phys. Rev. Lett. 102**:166401, 2009. [cited at p. 14, 53]

[54] C. V. Raman and K. S. Krishnan. *A new type of secondary radiation.* **Nature**. **121(3048)**:501, 1928. [cited at p. 15]

[55] R. Loudon. *The Raman effect in crystals.* **Adv. Phys. 50(7)**:813–864, 1964. reprint from: ibid. 13(52): 423-482, 1964. [cited at p. 18, 102]

[56] M. Cardona and G. Güntherodt. *Light scattering in solids II: Basic concepts and instrumentation*, volume 50 of *Topics in applied physics.* Springer-Verlag, 1982. [cited at p. 18]

[57] D. A. Long. *Quantum Mechanical Theory of Rayleigh and Raman Scattering, in The Raman Effect: A Unified Treatment of the Theory of Raman Scattering by Molecules.* John Wiley & Sons, Ltd, Chichester, UK., 2002. [cited at p. 18]

[58] D. M. Basko. *Theory of resonant multiphonon Raman scattering in graphene.* **Phys. Rev. B**. **78**:125418, 2008. [cited at p. 18, 79]

[59] A. C. Ferrari and D. M. Basko. *Raman spectroscopy as a versatile tool for studying the properties of graphene.* **Nature nanotechnology**. **8**:235, April 2013. [cited at p. 20, 31, 129]

[60] A. C. Ferrari and J. Robertson. *Resonant Raman spectroscopy of disordered, amorphous and diamondlike carbon.* **Phys. Rev. B**. **64**:075414, 2001. [cited at p. 20]

[61] F. Tuinstra and J. L. Koenig. *Raman spectrum of graphite.* **J. Chem. Phys. 53(3)**:1126, 1970. [cited at p. 20]

[62] C. Thomsen and S. Reich. *Double resonant Raman scattering in graphite.* **Phys. Rev. Lett. 85(24)**:5214, 2000. [cited at p. 20, 124]

[63] D. M. Basko, S. Piscanec, and A. C. Ferrari. *Electron-electron interactions and doping dependence of the two-phonon Raman intensity in graphene.* **Phys. Rev. B**. **80**:165413, 2009. [cited at p. 21, 22, 32, 33, 34, 104, 108]

[64] J. Maultzsch, S. Reich, and C. Thomsen. *Double-resonant Raman scattering in graphite: interference effects, selection rules, and phonon dispersion.* **Phys. Rev. B**. **70**:155403, 2004. [cited at p. 21, 22, 36]

[65] M. Ramsteiner and J. Wagner. *Resonant Raman scattering of hydrogenated amorphous carbon: evidence for π-bonded carbon clusters.* **Appl. Phys. Lett. 51(17)**:1355, 1987. [cited at p. 20, 83]

[66] Istvan Pócsik, Martin Hundhausen, Margit Koós, and Lothar Ley. *Origin of the D peak in the Raman spectrum of microcrystalline graphite.* **J. Non-Cryst. Solids**. **227-230**:1083 – 1086, 1998. [cited at p. 20, 83]

[67] M. J. Mathhews, M. A. Pimenta, G. Dresselhaus, M. S. Dresselhaus, and M. Endo. *Origin of dispersive effects of the Raman D band in carbon materials.* **Phys. Rev. B**. **59(10)**:R6585, 1999. [cited at p. 20, 31, 83]

[68] S. Reich and Ch. Thomsen. *Raman spectroscopy of graphite.* **Phil. Trans. R. Soc. Lond. A**. **362**:2271–2288, 2004. [cited at p. 20, 30, 31, 124]

[69] A. C. Ferrari, J. C. Meyer, V. Scardaci, C. Casiraghi, M. Lazzeri, F. Mauri, S. Piscanec, and D. Jiang. *Raman spectrum of graphene and graphene layers.* **Phys. Rev. Lett. 97**:187401, 2006. [cited at p. 23, 24, 33, 52, 74, 75, 113, 129]

[70] L. M. Malard, M. A. Pimenta, G. Dresselhaus, and M. S. Dresselhaus. *Raman spectroscopy in graphene.* **Physics Reports**. **473**:51–87, 2009. [cited at p. 23, 30, 31, 34]

[71] S. Latil, V. Meunier, and L. Henrard. *Massless fermions in multilayer graphitic systems with misoriented layers: Ab initio calculations and experimental fingerprints.* **Phys. Rev. B**. **76**:201402(R), 2007. [cited at p. 24, 25]

[72] J. M. B. Lopes dos Santos, N. M. R. Peres, and A. H. Castro Neto. *Graphene bilayer with a twist: electronic structure.* **PRL**. **99**:256802, 2007. [cited at p. 24]

[73] A. Sagar, E. J. H. Lee, and K.Balasubramanian. *Effect of stacking order on the electric-field induced carrier modulation in graphene bilayers.* **Nano Lett. 9(9)**:3124–3128, 2009. [cited at p. 24]

[74] A. Luican, G. Li, J. Kong, R. R. Nair, K. S. Novoselov, A. K. Geim, and E. Y. Andrei. *Single-layer behavior and its breakdown in twisted graphene layers.* **Phys. Rev. Lett. 106**:126802, 2011. [cited at p. 24]

[75] P. Poncharal, A. Ayari, T. Michel, and J.-L. Sauvajol. *Raman spectra of misoriented bilayer graphene.* **Phys Rev. B**. **78**:112407, 2008. [cited at p. 24, 86]

[76] L. G. Cancado, M. A. Pimenta, R. Saito, A. Jorio, L. O. Ladeira, A. Grueneis, A. G. Souza-Filho, G. Dresselhaus, and M. S. Dresselhaus. *Stokes and anti-Stokes double resonance Raman scattering in two-dimensional graphite.* **Phys. Rev. B**. **66**:035415, 2002. [cited at p. 24]

[77] D. L. Mafra, G. Samsonidze, L. M. Malard, D. C. Elias, J.C. Brant, F. Plentz, E.S. Alves, and M. A. Pimenta. *Determination of LA and TO phonon dispersion relations of graphene near the Dirac point by double resonance Raman scattering.* **Phys. Rev. B**. **76**:233407, 2007. [cited at p. 24]

[78] J.-C. Charlier, X. Gonze, and J.-P. Michenaud. *First-principles study of the stacking effect on the electronic properties of graphite(s).* **Carbon**. **32**:289–299, 1994. [cited at p. 25]

[79] F. Guinea, A. H. Castro Neto, and N. M. R. Peres. *Electronic states and Landau levels in graphene stacks.* **Phys. Rev. B**. **73**:245426, 2006. [cited at p. 25]

[80] V. M. Pereira, A. H. Castro Neto, and N. M. R. Peres. *Tight-binding approach to uniaxial strain in graphene.* **Phys. Rev. B**. **80**:045401, 2009. [cited at p. 25]

[81] F. Liu. *Ab initio calculation of ideal strength and phonon instability of graphene under tension.* **Phys. Rev. B**. **76**:064120, 2007. [cited at p. 25]

[82] F. Guinea, M. I. Katsnelson, and A. K. Geim. *Energy gaps and a zero-field quantum Hall effect in graphene by strain engineering.* **Nature Phys.** **6**:30, January 2010. [cited at p. 25]

[83] F. Guinea, B. Horovitz, and P. Le Doussal. *Gauge field induced by ripples in graphene.* **Phys. Rev. B**. **77**:205421, 2008. [cited at p. 26]

[84] T. M. G. Mohiuddin, A. Lombardo, R. R. Nair, A. Bonetti, G. Savini, R. Jalil, N. Bonini, D. M. Basko, C. Galiotis, N. Marzari, K. S. Novoselov, A. K. Geim, and A. C. Ferrari. *Uniaxial strain in graphene by Raman spectroscopy: G peak splitting, Grüneisen parameters, and sample orientation.* **Phys. Rev. B**. **79**:205433, 2009. [cited at p. 26]

[85] O. Frank, M. Mohr, J. Maultzsch, Ch. Thomsen, I. Riaz, R. Jalil, K. S. Novoselov, G. Tsoukleri, J. Parthenios, K. Papagelis, L. Kavan, and C. Galiotis. *Raman 2D-band splitting in graphene: theory and experiment.* **ACS Nano**. **5(3)**:2231–2239, 2011. [cited at p. 26]

[86] A. Das, S. Pisana, B. Chakraborty, S. Piscanec, S. K. Saha, U. V. Waghmare, K. S. Novoselov, H.R Krishnamurthy, A. K. Geim, A. C. Ferrari, and A. K. Sood. *Monitoring dopants by Raman scattering in an electrochemically top-gated graphene transistor.* **Nature Nanotech.** **3**:210, April 2008. [cited at p. 27, 33, 36]

[87] Z. Yao, C. L. Kane, and C. Dekker. *High-field electrical transport in single-wall carbon nanotubes.* **Phys. Rev. Lett.** **84(13)**:2941–2944, 2000. [cited at p. 29]

[88] J.-Y. Park, S. Rosenblatt, Y. Yaish, V. Sazononva, H. Üstünel, S. Braig, T.A. Arias, P. W. Brouwer, and P.L. McEuen. *Electron-phonon scattering in metallic single-walled carbon nanotubes.* **Nano Letters**. **4**:517–520, 2004. [cited at p. 29]

[89] M. Lazzeri, S. Piscanec, F. Mauri, A. C. Ferrari, and J. Robertson. *Electron transport and hot phonons in carbon nanotubes.* **Phys. Rev. Lett.** **95**:236802, 2005. [cited at p. 29]

[90] V. Perebeinos, J. Tersoff, and Ph. Avouris. *Electron-phonon interaction and transport in semiconducting carbon nanotubes.* **Phys. Rev. Lett.** **94**:086802, 2005. [cited at p. 29]

[91] A. Javey, J. Guo, M. Paulsson, Q. Wang, D. Mann, M. Lundstrom, and H. Dai. *High-field quasiballistic transport in short carbon nanotubes.* **Phys. Rev. Lett.** **92(10)**:106804, 2004. [cited at p. 29]

[92] S. Berciaud, S. Ryu, L. E. Brus, and T. F. Heinz. *Probing the intrinsic properties of exfoliated graphene: Raman spectroscopy of free-standing monolayers.* **Nano Lett.** **9(1)**:346, 2009. [cited at p. 29, 33]

[93] G. Giovanetti, P. A. Khomyakov, Geert Brocks, P. J. Kelly, and J. van den Brink. *Substrate-induced band gap in graphene on hexagonal boron nitride: Ab initio density functional calculations.* **Phys. Rev. B**. **76**:073103, 2007. [cited at p. 29, 60]

[94] M. P. Levendorf, Ch.-J. Kim, L. Brown, P. Y. Huang, R. W. Havener, D. A. Muller, and J. Park. *Graphene and boron nitride lateral heterostructures for atomically thin circuitry.* **Nature**. **488**:627, 2012. [cited at p. 29, 61]

[95] C. Dean, A. F. Young, L. Wang, I. Meric, G.-H. Lee, K. Watanabe, T. Taniguchi, K. Shepard, P. Kim, and J. Hone. *Graphene based heterostructures.* **Solid State Comm.** **152**:1275–1282, 2012. [cited at p. 29, 60, 61]

[96] G. Li, A. Luican, and E. Y. Andrei. *Scanning tunneling spectroscopy of graphene on graphite.* **Phys. Rev. B**. **102**:176804, 2009. [cited at p. 29, 55, 56, 74]

[97] M. Lazzeri, C. Attaccalite, L. Wirtz, and F. Mauri. *Impact of the electron-electron correlation on phonon dispersion: Failure of LDA and GGA DFT functionals in graphene and graphite.* **Phys. Rev. B. 78**:081406(R), 2008. [cited at p. 30, 32, 33]

[98] R.J. Nemanich, G. Lucovsky, and S.A. Solin. *Infrared active optical vibrations of graphite.* **Solid State Comm. 23(2)**:117, 1977. [cited at p. 30, 31]

[99] J. Maultzsch, S. Reich, C. Thomsen, H. Requardt, , and P. Ordejón. *Phonon dispersion in graphite.* **Phys. Rev. Lett. 92(7)**:075501, 2004. [cited at p. 30, 31, 33, 36]

[100] A. Grüneis, R. Saito T. Kimura, L. G. Cançado, M. A. Pimenta, A. Jorio, A. G. Souza Filho, G. Dresselhaus, and M. S. Dresselhaus. *Determination of two-dimensional phonon dispersion relation of graphite by Raman spectroscopy.* **Phys. Rev. B. 65**:155405, 2002. [cited at p. 31, 38]

[101] R. Saito, A. Jorio, A. G. Souza Filho, G. Dresselhaus, M. S. Dresselhaus, and M. A. Pimenta. *Probing phonon dispersion relations of graphite by double resonance Raman scattering.* **Phys. Rev. Lett. 88(2)**:027401, 2002. [cited at p. 31, 36]

[102] C. Mapelli, C. Castiglioni, G. Zerbi, and K. Müllen. *Common force field for graphite and polycyclic aromatic hydrocarbons.* **Phys. Rev. B. 60(18)**:12 710, 1999. [cited at p. 31]

[103] S. Piscanec, M. Lazzeri, F. Mauri, A. C. Ferrari, and J. Robertson. *Kohn anomalies and electron-phonon interactions in graphite.* **Phys. Rev. Lett. 93(18)**:185503, 2004. [cited at p. 31, 32, 33, 35, 38, 39, 42, 105, 107, 108, 127]

[104] P. Y. Yu and M. Cardona. *Fundamentals of semiconductors - physics and materials properties.* Springer-Verlag, 4th edition, 2010. [cited at p. 32]

[105] M. Lazzeri, S. Piscanec, F. Mauri, A. C. Ferrari, and J. Robertson. *Phonon linewidths and electron-phonon coupling in graphite and nanotubes.* **Phys. Rev. B. 73**:155426, 2006. [cited at p. 32, 33, 35]

[106] J. Yan, Y. Zhang, P. Kim, and A. Pinczuk. *Electric field effect tuning of electron-phonon coupling in graphene.* **Phys. Rev. Lett. 98**:166802, 2007. [cited at p. 32, 33, 36, 37, 112, 128, 130]

[107] S. Pisana, M. Lazzeri, C. Casiraghi, K. S. Novoselov, A. K. Geim, A. C. Ferrari, and F. Mauri. *Breakdown of the adiabatic Born-Oppenheimer approximation in graphene.* **Nature Mat. 6**:198, March 2007. [cited at p. 32, 33, 36, 37, 128, 130]

[108] C. Faugeras, M. Amado, P. Kossacki, M. Orlita, M. Sprinkle, C. Berger, W.A. de Heer, and M. Potemski. *Tuning the electron-phonon coupling in multilayer graphene with magnetic fields.* **Phys. Rev. Lett. 103**:186803, 2009. [cited at p. 33, 39, 88, 114, 115, 118]

[109] J. Yan, S. Goler andT. D. Rhone, M. Han, R. He, Ph. Kim, V. Pellegrini, and A. Pinczuk. *Observation of magneto-phonon resonance of Dirac fermions in graphite.* **Phys. Rev. Lett. 105**:227401, 2010. [cited at p. 33, 39, 58, 88, 114]

[110] A. Das, B. Chakraborty, S. Piscanec, S. Pisana, A. K. Sood, and A. C. Ferrari. *Phonon renormalization in doped bilayer graphene.* **Phys. Rev. B. 79**:155417, 2009. [cited at p. 33, 36]

[111] P.H. Tan, Ch.Y. Hu, J. Dong, W.C. Shen, and B.F. Zhang. *Polarization properties, high-order Raman spectra, and frequency asymmetry between Stokes and anti-Stokes scattering of Raman modes in a graphite whisker.* **Phys. Rev. Lett. 64**:214301, 2001. [cited at p. 33]

[112] A. Grüneis, C. Attaccalite, T. Pichler, V. Zabolotnyy, H. Shiozawa, S. L. Molodtsov, D. Inosov, A. Koitzsch, M. Knupfer, J. Schiessling, R. Follath, R. Weber, P. Rudolf, L. Wirtz, and A. Rubio. *Electron-electron correlation in graphite: A combined angle-resolved photoemission and first-principles study.* **Phys. Rev. Lett. 100**:037601, 2008. [cited at p. 33]

[113] A. Grüneis, J. Serrano, A. Bosak, M. Lazzeri, S. L. Molodtsov, L. Wirtz, C. Attaccalite, M. Krisch, A. Rubio, F. Mauri, and T. Pichler. *Phonon surface mapping of graphite: Disentangling quasi-degenerate phonon dispersions.* **Phys. Rev. Lett. 80**:085423, 2009. [cited at p. 33, 36]

[114] S. Y. Zhou, D. A. Siegel, A. V. Fedorov, and A. Lanzara. *Kohn anomaly and interplay of electron-electron and electron-phonon interactions in epitaxial graphene.* **Phys. Rev. B**. **78**:193404, 2008. [cited at p. 32, 33, 36, 38, 42]

[115] M. Calandra and F. Mauri. *Electron-phonon coupling and electron self-energy in electron-doped graphene: calculation of angular-resolved photoemission spectra.* **Phys. Rev. B**. **76**:205411, 2007. [cited at p. 32, 38, 39, 122, 123, 124]

[116] M. Lazzeri and F. Mauri. *Nonadiabatic Kohn anomaly in a doped graphene monolayer.* **Phys. Rev. Lett. 97**:266407, 2006. [cited at p. 32, 37]

[117] T. Ando. *Anomaly of optical phonon in monolayer graphene.* **J. Phys.Soc. Jap. 75**:124701, 2006. [cited at p. 32, 35, 39, 40, 88, 131]

[118] W. Kohn. *Image of the Fermi suraface in the vibration spectrum of a metal.* **Phys. Rev. Lett. 2(9)**:393, 1959. [cited at p. 34]

[119] R. Nicklow, N. Wakabayashi, and H. G. Smith. *Lattice dynamics of pyrolitic graphite.* **Phys. Rev. B**. **5(12)**:4951, 1972. [cited at p. 36]

[120] J.L.Wilkes, R.E. Palmer, and R.F.Willis. *Phonons in graphite studied by EELS.* **J. Electron Spectrosc. Relat. Phenom. 44**:355, 1987. [cited at p. 36]

[121] C. Oshima, T. Aizawa, R. Souda, Y. Ishizawa, and Y. Sumiyoshi. *Surface phonon dispersion curves of graphite (0001) over the entire energy region.* **Solid State Commun. 65**:1601, 1988. [cited at p. 36]

[122] K.-H. Rieder S. Siebentritt, R. Pues. *Surface phonon dispersion in graphite and in a lanthanum graphite intercalation compound.* **Phys. Rev. B**. **55(12)**:7927, 1997. [cited at p. 36]

[123] M. Mohr, J. Maultzsch, E. Dobardžic, S. Reich, I. Miloševic, M. Damnjanovic, A. Bosak, M. Krisch, and C. Thomsen. *Phonon dispersion of graphite by inelastic x-ray scattering.* **Phys. Rev. B**. **76**:035439, 2007. [cited at p. 36]

[124] C. Casiraghi, S. Pisana, K. S. Novoselov, A. K. Geim, and A. C. Ferrari. *Raman fingerprint of charged impurities in graphene.* **Appl. Phys. Lett. 91**:233108, 2007. [cited at p. 36]

[125] G.-J. Kroes, A. Gross, E.-J. Baerends, M. Scheffler, and D. A. McCormac. *Quantum theory of dissociative chemisorption on metal surfaces.* **Acc. Chem. Res. 35(3)**:193–200, 2002. [cited at p. 37]

[126] D. Alfe, M. J. Gillan, and G. D. Price. *The melting curve of iron at the pressures of the Earth's core from ab initio calculations.* **Nature**. **401**:462–464, 1999. [cited at p. 37]

[127] B. G. Walker, C. Molteni, and N. Marzari. *Ab initio molecular dynamics of metal surfaces.* **J. Phys. Condens. Matter**. **16**:S2575–S2596, 2004. [cited at p. 37]

[128] G. V. Chester. *The theory of interaction of electrons with lattice vibrations in metals.* **Adv. Phys. 10**:357–400, 1961. [cited at p. 37]

[129] S. Baroni, S. de Gironcoli, A. Dal Corso, and P. Giannozzi. *Phonons and related crystal properties from density functional perturbation theory.* **Rev. Mod. Phys. 73**:515–562, 2001. [cited at p. 37]

[130] S. Y. Savrasov and D. Y. Savrasov. *Electron-phonon interactions and related physical properties of metals from linear-response theory.* **Phys.Rev.B**. **54**:16487–16501, 1996. [cited at p. 37]

[131] Y. S. Ponosov, G. A. Bolotin, C. Thomsen, and M. Cardona. *Raman scattering in Os: Nonadiabatic renormalization of the optical phonon self energies.* **Phys. Status Solidi B**. **208**:257–269, 1998. [cited at p. 37]

[132] J. D. White, J. Chen, D. Matsiev, D. J. Auerbach, and A. M. Wodtke. *Conversion of large-amplitude vibration to electron excitation at a metal surface.* **Nature**. **433**:503–505, 2005. [cited at p. 37]

[133] A. Grüneis, C. Attaccalite, A. Rubio, D. V. Vyalikh, S. L. Molodtsov, J. Fink, R. Follath, W. Eberhardt, B. Büchner, and T. Pichler. *Electronic structure and electron-phonon coupling of doped graphene layers in* KC_8. **Phys. Rev. B**. **79**:205106, 2009. [cited at p. 38, 42]

[134] CH.-H. Park, F. Giustino, M. L. Cohen, and S. G. Louie. *Velocity renormalization and carrier lifetime in graphene from the electron-phonon interaction.* **Phys. Rev. Lett. 99**:086804, 2007. [cited at p. 39]

[135] D. A. Siegel, Ch.-H. Park, Ch. Hwang, J. Deslippe, A. V. Federov, S. G. Louie, and A. Lanzzara. *Many-body interactions in quasi-freestanding graphene.* **PNAS**. **108(28)**:11365–11369, 2011. [cited at p. 39, 122]

[136] A. Bostwick, T. Ohta, T. Seyller, K. Horn, and E. Rotenberg. *Quasiparticle dynamics in graphene.* **Nature Phys. 3**:36, January 2007. [cited at p. 39]

[137] T. Ando. *Magnetic oscillation of optical phonon in graphene.* **J. Phys. Soc. Jap. 76(2)**:024712, 2007. [cited at p. 39, 40, 86, 88, 91, 115, 128, 131, 133]

[138] M. O. Goerbig, J.-N. Fuchs, K. Kechedzhi, and V. I. Fal'ko. *Filling-factor-dependent magnetophonon resonance in graphene.* **Phys. Rev. Lett. 99**:087402, 2007. [cited at p. 39, 40, 86, 88, 91, 128, 131, 137]

[139] P. Kossacki, C. Faugeras, M. Kühne, M. Orlita, A. Mahmood, E. Dujardin, R. R. Nair, A. K. Geim, and M. Potemski. *Circular dichroism of magnetophonon resonance in doped graphene.* **Phys. Rev. B**. **86**:205431, 2012. [cited at p. 39, 114, 118]

[140] C. Faugeras, P. Kossacki, A. Nicolet, M. Orlita, M. Potemski, and D. Basko. *Probing the band structure of quadri-layer graphene with magneto-phonon resonance.* **New J. of Phys. 14**:095007, 2012. [cited at p. 39]

[141] Y. Kim, J. M. Poumirol, A. Lombardo, N. G. Kalugin, T. Georgiou, Y. J. Kim, K. S. Novoselov, A. C. Ferrari, J. KOno, O. Kashuba, V. I. Fal'ko, and D. Smirnov. *Measurement of filling-factor-dependent magnetophonon resonances in graphene using Raman spectroscopy.* **Phys. Rev. Lett. 110**:227402, 2013. [cited at p. 39, 88]

[142] K. Ishikawa and T. Ando. *Optical phonon interacting with electrons in carbon nanotubes.* **J. Phys. Soc. Jap. 75(8)**:084713, 2006. [cited at p. 40]

[143] M. Orlita, L. Z. Tan, M. Potemski, M. Sprinkle, C. Berger, W. A. de Heer, S. G. Louie, and G. Martinez. *Resonant excitation of graphene K-phonon and intra-Landau-level excitons in magneto-optical spectroscopy.* **Phys. Rev. Lett. 108**:247401, 2012. [cited at p. 42, 43, 97]

[144] T. Ohta, A. Bostwick, Th. Seyller, K. Horn, and E. Rotenberg. *Controlling the electronic bandstructure of bilayer graphene.* **Science**. **313**:951, 2006. [cited at p. 45]

[145] A. B. Kuzmenko, E. van Heumen, and D. van der Marel. *Infrared spectroscopy of electronic bands in bilayer graphene.* **Phys. Rev. B**. **79**:115441, 2009. [cited at p. 45]

[146] L. M. Zhang, Z. Q. Li, D. N. Basov, M. M. Fogler, Z. Hao, and M. C. Martin. *Determination of the electronic structure of bilayer graphene from infrared spectroscopy.* **Phys. Rev. B**. **78**:235408, 2008. [cited at p. 45]

[147] A. B. Kuzmenko, I. Crassee, D. van der Marel, P. Blake, and K. S. Novoselov. *Determination of the gate-tunable bandgap and tight-binding parameters in bi-layer graphene using infrared spectroscopy.* **Phys. Rev. B**. **80**:165406, 2009. [cited at p. 45]

[148] E. A. Henriksen, Z. Jiang, L.-C. Tung, M. E. Schwartz, M. Takita, Y.J. Wang, P. Kim, and H. L. Stormer. *Cyclotron resonance in bilayer graphene.* **Phys. Rev. Lett.** **100**:087403, 2008. [cited at p. 45]

[149] M. Mucha-Kruczynski, O. Kashuba, and V. I. Fal'ko. *Spectral features due to inter-Landau-level transitions in the Raman spectrum of bilayer graphene.* **Phys. Rev. B**. **82**:045405, 2010. [cited at p. 45]

[150] O. Kashuba and V. I. Fal'ko. *Role of electronic excitations in magneto-Raman spectra of graphene.* **New J. Phys.** **14**:105016, 2012. [cited at p. 45, 46, 47, 48, 49, 50, 51]

[151] R. E. Slusher, C. K. N. Patel, and P. A. Fleury. *Inelastic light scattering from Landau-level electrons in semiconductors.* **Phys. Rev. Lett.** **18(3)**:77, 1967. [cited at p. 45]

[152] C. K. N. Patel and R. E. Slusher. *Light scattering by plasmons and Llandau levels of electron gas in inas.* **Phys. Rev.** **167(2)**:167, 1968. [cited at p. 45]

[153] A. Wysmołek, D. Plantier, M. Potemski, T. Słupinski, and Z. R. Żytkiewicz. *Coupled plasmon-LO-phonon modes at high-magnetic fields.* **Phys. Rev. B**. **74**:165206, 2006. [cited at p. 45]

[154] J.M. Worlock, A. Pinczuk, Z.J. Tien, C.H. Perry, H. Störmer, R. Dingle, A.C. Gossard, and W. Wiegmann. *Spectroscopy of Landau transitions of two-dimensional electron gases.* **Solid State Comm.** **40(9)**:867–871, 1981. [cited at p. 45]

[155] Z.J. Tien, J.M. Worlock, C.H. Perry A. Pinczuk, R.L. Aggarwal, H.L. Störmer, A.C. Gossard, and W. Wiegmann. *Light scattering from two-dimensional electron systems in strong magnetic fields.* **Surf. Sci.** **113**:89, 1982. [cited at p. 45]

[156] A. Fainstein, T. Ruf, , M. Cardona, V. I. Belitsky, and A. Cantarero. *Electronic and acoustic-phonon inter-Landau-level Raman scattering in GaAs/*$Al_xGa_{1-x}As$ *multiple quantum wells.* **Phys. Rev. B**. **51(11)**:7064, 1995. [cited at p. 45]

[157] D. Richards. *Inelastic light scattering from inter-Landau level excitations in a two-dimensional electron gas.* **Phys. Rev. B**. **61(11)**:7517, 2000. [cited at p. 45]

[158] A. F. Garcia-Flores, H. Terashita, E. Granado, and Y. Kopelevich. *Landau levels in bulk graphite by Raman spectroscopy.* **Phys. Rev. B**. **79**:113105, 2009. [cited at p. 52, 58]

[159] M. Orlita, C. Faugeras, G. Martinez, D.K. Maude, M. L. Sadowski, and M. Potemski. *Dirac fermions at the H point of graphite: Magnetotransmission studies.* **Phys. Rev. Lett.** **100**:136403, 2008. [cited at p. 53]

[160] P. Sabatier. *La catalyse en chimie organique.* C. Béranger, 1913. [cited at p. 55]

[161] H. Ibach. *Physics of surfaces and interfaces.* Springer, 2006. [cited at p. 55]

[162] R. P. Gupta. *Lattice relaxation at metal surface.* **Phys. Rev. B**. **23**:6265–6270, 1981. [cited at p. 55]

[163] R. B. Doak, U. Harten, and J. P. Toeninies. *Anomalous surface phonon dispersion relations for Ag(111) measured by inelastic scattering of He atoms.* **Phys. Rev. Lett. 51**:578–581, 1983. [cited at p. 55]

[164] G> Benedek, M. Bernasconi, V. Chis, E. Chulkov, P. M. Echenique, B. Hellsing, and J. P. Toennies. *Theory of surface phonons at metal surfaces: recent advances.* **J.Phys.: Cond. Matt. 22**:084020, 2010. [cited at p. 55]

[165] R. H. Ritchie. *Plasma losses by fast electrons in thin films.* **Phys. Rev. 106(5)**:874–881, 1957. [cited at p. 55]

[166] W. L. Barnes, A. Dereaux, and T. W. Ebbesen. *Surface plasmon subwavelength optics.* **Nature**. **424**:824, 2003. [cited at p. 55]

[167] H. Zhang, Ch.-X. Liu, X.-L. Qi, X. Dai, Zh. Fang, and Sh.-Ch. Zhang. *Topological insulators in Bi_2Se_3, Bi_2Te_3 and Sb_2Te_3 with a single Dirac cone on the surface.* **Nature physics**. **5**:438, 2009. [cited at p. 55]

[168] I. A. Luk'yanchuk, Y. Kopelevich, and M. El Marssi. *Dirac fermions in graphite: the state of art.* **Phys. B: Cond. Matt. 404(3-4)**:404–406, 2009. [cited at p. 55, 58, 59]

[169] K. I. Bolotin, K. J. Sikes, J. Hone, H. L. Stormer, and P. Kim. *Temperature-dependent transport in suspended graphene.* **Phys. Rev. Lett. 101**:096802, 2008. [cited at p. 57, 61]

[170] D. C. Elias, R. V. Gorbachev, A. S.Mayorov, S. V.Morozov, A. A. Zhukov, P. Blake, L. A. Ponomarenko, I. V. Grigorieva, K. S. Novoselov, F. Guinea, and A. K. Geim. *Dirac cones reshaped by interaction effects in suspended graphene.* **Nature phys. 7**:701, 2011. [cited at p. 57, 123, 124, 143, 147]

[171] W. A. de Heer, C. Berger, X. Wu, P. N. First, E. H. Conrad, X. Li, M. Sprinkle, J. Hass, M. L. Sadowski, M. Potemski, and G. Martinez. *Epitaxial graphene.* **Sol. State Comm. 143**:92–100, 2007. [cited at p. 57]

[172] J. A. Wilson and A. D. Yoffe. *The transition metals dichalcogenides. Discussion and interpretation of the observed optical, electrical and structural properties.* **Adv.Phys. 18**:193, 1969. [cited at p. 59]

[173] R Coehoorn, C. Haas, J. Dijkstra, and C. J. F. Flipse. *Electronic structure of $MoSe_2$, MoS_2, and WSe_2. I. Band-structure calculations and photoelectron spectroscopy.* **Phys. Rev. B**. **35(12)**:6195, 1987. [cited at p. 59]

[174] B. L. Evans and P. A. Young. *Exciton spectra in thin crystals: the diamagnetic effect.* **Proc. Phys. Soc. 91**:475, 1967. [cited at p. 59]

[175] H. Fukutani M. Tanaka and Goro Kuwabara. *Excitons in VI B transition metal dichalcogenides.* **J. Phys. Soc. Jap. 45(6)**:1899, 1978. [cited at p. 59]

[176] G. Jones and J. L. Brebner. *The behaviour of Wanier excitons in very thin crystals.* **J. Phys. C: Solid St. Phys. 4**:723, 1971. [cited at p. 59]

[177] R. F. Frindt. *Optical absorption of a few unit-cell layers of MoS_2.* **Phys. Rev. 140(2A)**:A536, 1965. [cited at p. 59]

[178] S. J. Sandoval, D. Yang, R. F. Frindt, and J. C. Irwin. *Raman study and lattice dynamics of single molecular layers of MoS_2.* **Phys. Rev. B**. **44(8)**:3955, 1991. [cited at p. 59]

[179] M. S. Dresselhaus and G. Dresselhaus. *Intercalation compounds of graphite.* **Adv. Phys. 51(1)**:1–186, 2002. [cited at p. 60]

[180] J. H. Warner, M. H. Rümmeli, A. Bachmatiuk, and B. Büchner. *Atomic resolution imaging and topography of boron nitride sheets produced by chemical exfoliation.* **ACS Nano**. **4(3)**:1299–1304, 2010. [cited at p. 60]

[181] J. C. Meyer, A. Chuvilin, G. Algara-Siller, J. Biskupek, and U. Kaiser. *Selective sputtering and atomic resolution imaging of atomically thin boron nitride membranes.* **Nano Lett. 9(7)**:2683–2689, 2009. [cited at p. 60]

[182] A. J. Van Bommel, J. E. Crombeen, and A. van Tooren. *LEED and Auger electron observations of the SiC (0001) surface.* **Surf. Sci. 48(2)**:463–472, 1975. [cited at p. 60]

[183] C. Berger, Zh. Song, T. Li, X. Li, A. Y. Ogbazghi, R. Feng, Zh. Dai, A. N. Marchenkov, E. H. Conrad, P. N. First, and W.A. de Heer. *Ultrathin epitaxial graphite-2D electron gas properties and a route toward graphene-based nanoelectronics.* **J. Phys. Chem. B**. **108(52)**:19912–19916, 2004. [cited at p. 60]

[184] K. S. Kim, Y. Zhao, H. Jang, S. Y. Lee, J. M. Kim, K. S. Kim, J.-H. Ahn, Philip Kim J.-Y. Choi, and B. H. Hong. *Large-scale pattern growth of graphene films for stretchable transparent electrodes.* **Nature**. **457**:706–710, 2009. [cited at p. 60, 62, 63]

[185] Z. Sun, Z. Yan, J. Yao, E. Beitler, Y. Zhu, and J. M. Tour. *Growth of graphene from solid carbon sources.* **Nature**. **468**:549, 2010. [cited at p. 60]

[186] K. S. Novoselov and A. H. Castro Neto. *Two-dimensional crystals-based heterostructures: materials with tailored properties.* **Phys. Scr. T146(014006)**, 2012. [cited at p. 60]

[187] L. Britnel, R. V. Gorbachev, R. Jalil, B. D. Belle, F. Scheidin, A. Mishchenko, T. Georgiou, M. I. Katsnelson, L. Eaves, S. V. Morozov, N. M. R. Peres, J. Leist, A. K. Geim, K. S. Novoselov, and L. A. Ponomarenko. *Field-effect tunneling transistor based on vertical graphene heterostructures.* **Nature**. **335**:947, 2012. [cited at p. 60]

[188] W. J. Yu, Zh. Li, H. Zhou, Y. Chen Y. Wang, Y. Huang, and X. Duan. *Vertically stacked multi-heterostructures of layered materials for logic transistors and complementary inverters.* **Nature mat. 12**:246, 2012. [cited at p. 60, 62]

[189] K. Watanabe, T. Taniguchi, and H. Kanda. *Direct-bandgap properties and evidence for ultraviolet lasing of hexagonal boron nitride single crystal.* **Nature mat. 3**:404, 2004. [cited at p. 60]

[190] C. R. Dean, A.F. Young, I. Meric, C. Lee, L. Wang, S. Sorgenfrei, K. Watanabe, T. Taniguchi, P. Kim, K.L. Shepard, and J. Hone. *Boron nitride substrates for high-quality graphene electronics.* **Nature nano. 5**:722, 2010. [cited at p. 61]

[191] X. Hong, K. Zou, and J. Zhu. *Quantum scattering time and its implications on scattering sources in graphene.* **Phys. Rev. B**. **80**:241415(R), 2009. [cited at p. 61]

[192] W. Gannett, W. Regan, K. Watanabe, T. Taniguchi, M. F. Crommie, and A. Zettl. *Boron nitride substrate for high mobility chemical vapor deposited graphene.* **Appl. Phys. Lett. 98(98)**:242105, 2011. [cited at p. 61]

[193] M. Wang, S. K. Jang, W.-J. Jang, M. Kim, S.-Y. Park, S.-W. Kim, S.-J. Kahng, J.-Y. Choi, R. S. Ruoff, and Y. J. Song. *A platform for large-scale graphene electronics - CVD growth of single-layer graphene on CVD-grown hexagonal boron nitride.* **Adv. Matt. 25**:2746–2752, 2013. [cited at p. 61]

[194] F. Forster, A. Molina-Sanchez, S. Engels, A. Epping, K. Watanabe, T. Taniguchi, L. Wirtz, and C. Stampfer. *Confocal raman spectroscopy of graphene on hexagonal boron nitride.* arXiv:1212.3993 [cond-mat.mes-hall], 2012. [cited at p. 61]

[195] R. V. Gorbachev, I. Riaz, R. R. Nair, R. Jalil, L. Britnell, B. D. Belle, E. W. Hill, K. S. Novoselov, K. Watanabe, T. Taniguchi, A. K. Geim, and P. Blake. *Hunting for monolayer boron nitride: Optical and raman signatures.* **Small**. **7(4)**:465–468, 2011. [cited at p. 61]

[196] M.C. Lemme, T.J. Echtermeyer, M. Baus, B.N. Szafranek, J. Bolten, M. Schmidt, T. Wahlbrink, and H. Kurz. *Mobility in graphene double gate field effect transistors.* **Solid State Electron. 52(4)**:514, 2008. [cited at p. 62]

[197] S. Kim, J. Nah, I. Jo, D. Shahrjerdi, L. Colombo, Z. Yao, E. Tutuc, and S. K. Banerjee. *Realization of a high mobility dual-gated graphene field-effect transistor with* Al_2O_3 *dielectric.* **Apl. Phys. Lett. 94**:062107, 2009. [cited at p. 62]

[198] X. Wang, L. Zhi, and K. Müllen. *Transparent, conductive graphene electrodes for dye-sensitized solar cells.* **Nano Lett. 8(1)**:323, 2008. [cited at p. 62]

[199] P. Blake, P. D. Brimicombe, R. R. Nair, T. J. Booth, D. Jiang, F. Schedin, L. A. Ponomarenko, S. V. Morozov, H. F. Gleeson, E. W. Hill, A. K. Geim, and K. S. Novoselov. *Graphene-based liquid crystal device.* **Nano Lett. 8(6)**:1704, 2008. [cited at p. 62]

[200] R. R. Nair, P. Blake, A. N. Grigorenko, K. S. Novoselov, T. J. Booth, T. Stauber, N. M. R. Peres, and A. K. Geim. *Fine structure constant defines visual transparency of graphene.* **Science**. **320**:1308, 2008. [cited at p. 62]

[201] Qingkai Yu, J. Lian, S. Siriponglert, H. Li, Y. P. Chen, and Sh.-Sh. Pei. *Graphene segregated on Ni surfaces and transferred to insulators.* **Appl. Phys. Lett. 93**:113103, 2008. [cited at p. 62]

[202] A. Reina, X. Jia, J. Ho, D. Nezich, H. Son, V. Bulovic, M. S. Dresselhaus, and J. Kong. *Large area, few-layer graphene films on arbitrary substrates by chemical vapor deposition.* **Nano Lett. 9(1)**:30, 2009. [cited at p. 62]

[203] X. Li, W. Cai, J. An, S. Kim, J. Nah, D. Yang, R. Piner, A. Velamakanni, I. Jung, E. Tutuc, S. K. Banerjee, L. Colombo, and R. S. Ruoff. *Large-area synthesis of high-quality and uniform graphene films on copper foils.* **Science**. **324**:1312, 2009. [cited at p. 62, 63, 128]

[204] H. I. Rasool, E. B. Song, M. J. Allen, J. K. Wassei, R. B. Kaner, K. L. Wang, B. H. Weiller, and James K. Gimzewski. *Continuity of graphene on polycrystalline copper.* **Nano Lett. 11**:251, 2011. [cited at p. 62]

[205] S. Bae, H. Kim, Y. Lee, X. Xu, J.-S. Park, Y. Zheng, J. Balakrishnan, T. Lei, H. R. Kim, Y. I. Song, Y.-J. Kim, K. S. Kim, B. Ozyilmaz, J.-H. Ahn, B. H. Hong, and S. Iijima. *Roll-to-roll production of 30-inch graphene films for transparent electrodes.* **Nature nano. 5**:574, 2010. [cited at p. 62]

[206] X. Li, C. W. Magnuson, A. Venugopal, J. An, J. W. Suk, B. Han, M. Borysiak, W. Cai, A. Velamakanni, Y. Zhu, L. Fu, E. M. Vogel, E. Voelkl, L. Colombo, and R. S. Ruoff. *Graphene films with large domain size by a two-step chemical vapor deposition process.* **Nano Lett. 10**:4328, 2010. [cited at p. 63]

[207] K. Kim, Z. Lee, W. Regan, C. Kisielowski, M. F. Crommie, and A. Zettl. *Grain boundary mapping in polycrystalline graphene.* **ACS Nano**. **5(3)**:2142, 2011. [cited at p. 63]

[208] P. Y. Huang, C. S. Ruiz-Vargas, A. M. van der Zande, W. S. Whitney, M. P. Levendorf, J. W. Kevek, S. Garg, J. S. Alden, C. J. Hustedt, Y. Zhu, J. Park, P. L. McEuen, and D. A. Muller. *Grains and grain boundaries in single-layer graphene atomic patchwork quilts.* **Nature**. **469**:389, 2011. [cited at p. 63]

[209] O. V. Yazev and S. G. Louie. *Electronic transport in polycrystalline graphene.* **Nature mat.** **9**:806, 2010. [cited at p. 63]

[210] Q. Yu, L. A. Jauregui, W. Wu, R.Colby, J. Tian, Zh. Su, H. Cao, Zh. Liu, D. Pandey, D. Wei, T. F. Chung, P. Peng, N. P. Guisinger, E. A. Stach, J. Bao, Sh.-Sh. Pei, and Yong P. Chen. *Control and characterization of individual grain and grain boundaries in graphene grown by chemical vapour deposition.* **Nature mat.** **10**:443, 2011. [cited at p. 63]

[211] R. Grantab, V. B. Shenoy, and R. S. Ruoff. *Anomalous strength characteristics of tilt grain boundaries in graphene.* **Science**. **330**:946, 2010. [cited at p. 63]

[212] Zh.Han, A. Kimouche, A. Allain, H. Arjmandi-Tash, A. Reserbat-Plantey, S. Pairis, V. Reita, N. Bendiab, J. Coraux, and V. Bouchiat. *Suppression of multilayer graphene patches during graphene growth.* arXiv:1205.1337 [cond-mat.mes-hall], 2012. [cited at p. 63, 64]

[213] P. Blake, E. W. Hill, A. H. Castro Neto, K. S. Novoselov, D. Jiang, R. Yang, T. J. Booth, and A. K. Geim. *Making graphene visible.* **Appl. Phys. Lett.** **91**:063124, 2007. [cited at p. 73]

[214] C. Faugers, P. Kossacki, D. M. Basko, M. Amado, M. Sprinkle, C. Berger, W. A. de Heer, and M. Potemski. *Effect of a magnetic field on two-phonon Raman scattering in graphene.* **Phys. Rev. B**. **81**:155436, 2010. [cited at p. 79]

[215] I. Calizo, A. A. Balandin, W. Bao, F. Miao, and C. N. Lau. *Temperature dependence of the Raman spectra of graphene and graphene multilayers.* **Nano Lett.** **7(9)**:2645, 2007. [cited at p. 82]

[216] D. M. Basko. *Calculation of the Raman G peak intensity in monolayer graphene: role of Ward identities.* **New Journ. Phys.** **11**:095011, 2009. [cited at p. 83]

[217] R. W. Lynch and H. G. Drickamer. *Effect of high pressure on the lattice parameters of diamond, graphite and hexagonal boron nitride.* **Journ. Chem. Phys.** **44(1)**:181, 1966. [cited at p. 109]

[218] Ch. Hwang, D. A. Siegel, S.-K. Mo, W. Regan, A. Ismach, Y. Zhang, Alex Zettl, and A. Lanzara. *Fermi velocity engineering in graphene by substrate modification.* **Sci. Rep.** **2(590)**, 2012. [cited at p. 121, 124, 143, 147]

[219] P. E. Trevisanutto, Ch. Giorgetti, L. Reining, M. Ladisa, and V. Olevano. *Ab Initio GW many-body effects in graphene.* **Phys. Rev. Lett.** **101**:226405, 2008. [cited at p. 122, 123, 124]

[220] V. N. Kotov, B. Uchoa, V. M. Pereira, F. Guinea, and A.H. Castro Neto. *Electron-electron interactions in graphene: Current status and perspectives.* **Rev. Mod. Phys.** **84**:1067, Jul.-Sept. 2012. [cited at p. 122]

[221] Ch.-H. Park, L. Yang, M. L. Cohen Y.-W. Son, and S. G. Louie. *Anisotropic behaviours of massless Dirac fermions in graphene under periodic potentials.* **Nat. Phys.** **4**:213, 2008. [cited at p. 122]

[222] A. Raoux, M. Polini, R. Asgari, A. R. Hamilton, R. Fazio, and A. H. MacDonald. *Velocity-modulation control of electron-wave propagation in graphene.* **Phys. Rev. B**. **81**:073407, 2010. [cited at p. 122]

[223] C. Jang, S. Adam, J.-H. Chen, E.D. Williams, S. Das Sarma, and M. S. Fuhrer. *Tuning the effective fine structure constant in graphene: Opposing effects of dielectric screening on short - and long-range potential scattering.* **Phys. Rev. Lett.** **101**:146805, 2008. [cited at p. 122]

[224] Z. Q. Li, E. A. Henriksen, Z. Jiang, Z. Hao, M. C. Martin, P. Kim, H. L. Stormer, and D. N. Basov. *Dirac charge dynamics in graphene by infrared spectroscopy.* **Nature Phys.** **4**:532, 2009. [cited at p. 127]

[225] V. Carozo, C. M. Almeida, E. H. M. Ferreira, L. G. Conçado, C. A. Achete, and A. Jorio. *Raman signature of graphene superlattices.* **NanoLett.** **11**:4527, 2011. [cited at p. 129]

[226] R. He, T.-F. Chung, C. Delaney, C. Keiser, L. A. Jauregui, P. M. Shand, C. C. Chancey, Y. Wang, J. Bao, and Y. P. Chen. *Observation of low energy Raman modes in twisted bilayer graphene.* **NanoLett.** **13**:3594, 2013. [cited at p. 129]